https://doi.org/10.15388/vu.thesis.191
https://orcid.org/0000-0003-2589-1447

VILNIUS UNIVERSITY
CENTER FOR PHYSICAL SCIENCES AND TECHNOLOGY

Andrius
AUKŠTUOLIS

Charge carrier transport and recombination in organic semiconductors thin film structures

DOCTORAL DISSERTATION

Technological Sciences,
Materials Engineering (T 008)

VILNIUS 2021

This dissertation was written between 2014 and 2020 at the Institute of Chemical Physics, Vilnius University and at the Faculty of Sciences, University of Angers.

Academic supervisor:
Doc. dr. Nerijus Nekrašas (Vilnius University, Natural Sciences, Physics – N 002).

Dissertation Defence Panel:
Chairman – Prof. dr. Saulius Juršėnas (Vilnius University, Natural Sciences, Physics – N 002).
Members:
Prof. dr. Vytautas Getautis (Kaunas University of Technology, Natural Sciences, Chemistry – N 003).
Prof. dr. Vidmantas Gulbinas (Center for Physical Sciences and Technology, Natural sciences, Physics – N 002).
Prof. dr. Diana Mihaela Mardare (Alexandru Ioan Cuza University of Iasi, Romania, Natural sciences, Physics – N 002).
Prof. dr. Nerija Žurauskienė (Vilnius University, Technological Sciences, Materials Engineering – T 008).

The dissertation shall be defended at a public meeting of the Dissertation Defence Panel at 13:00 on 13 September 2021 in the meeting room B336 of the Center for Physical Sciences and Technology.
Address: Saulėtekio av. 3, meeting room B336, Vilnius, Lithuania
Tel. +370 5 264 8884; e-mail: office@ftmc.lt

The text of this dissertation can be accessed at the libraries of Vilnius University and the Center for Physical Sciences and Technology, as well as on the website of Vilnius University: www.vu.lt/lt/naujienos/ivykiu-kalendorius.

https://doi.org/10.15388/vu.thesis.191
https://orcid.org/0000-0003-2589-1447

VILNIAUS UNIVERSITETAS
FIZINIŲ IR TECHNOLOGIJOS MOKSLŲ CENTRAS

Andrius
AUKŠTUOLIS

Krūvininkų pernaša ir rekombinacija plonasluoksniuose organinių puslaidininkių dariniuose

DAKTARO DISERTACIJA

Technologijos mokslai,
Medžiagų inžinerija (T 008)

VILNIUS 2021

Disertacija rengta 2014– 2020 metais Vilniaus universiteto Cheminės Fizikos Institute ir Anžė universiteto Gamtos Mokslų Fakultete.

Mokslinis vadovas:
doc. dr. Nerijus Nekrašas (Vilniaus universitetas, gamtos mokslai, fizika – N 002).

Gynimo taryba:
Pirmininkas – prof. dr. Saulius Juršėnas (Vilniaus universitetas, gamtos mokslai, fizika – N 002).
Nariai:
prof. dr. Vytautas Getautis (Kauno technologijos universitetas, gamtos mokslai, chemija – N 003).
prof. dr. Vidmantas Gulbinas (Fizinių ir technologijos mokslų centras, gamtos mokslai, fizika – N 002).
prof. dr. Diana Mihaela Mardare (Alexandru Ioan Cuza University of Iasi, Rumunija, gamtos mokslai, fizika – N 002).
prof. dr. Nerija Žurauskienė (Vilniaus universitetas, technologijų mokslai, medžiagų inžinerija – T 008).

Disertacija ginama viešame Gynimo tarybos posėdyje 2021 m. rugsėjo mėn. 13 d. 13:00 val. Nacionalinio fizinių ir technologijos mokslų centro B336 auditorijoje.
Adresas: Saulėtekio al. 3, B336, Vilnius, Lietuva.
Tel. +370 5 264 8884; el. pastas: office@ftmc.lt.

Disertaciją galima peržiūrėti Vilniaus universiteto bibliotekose ir VU interneto svetainėje adresu: https://www.vu.lt/naujienos/ivykiu-kalendorius

TABLE OF CONTENT

ABBREVIATIONS

P3HT – poly(3-hexylthiophene-2,5-diyl);

RR-P3HT – regioregular poly(3-hexylthiophene-2,5-diyl);

A – voltage increment rate in CELIV measurement techniques;

PCPDTBT – poly[2,6-(4,4-bis-(2-ethylhexyl)-4H-cyclopenta [2,1-b;3,4-b′]dithiophene)-alt-4,7(2,1,3-benzothiadiazole)];

PCBM – [6,6]-Phenyl C61 (or C71) butyric acid methyl ester;

PBDTTPD – poly[(5,6-dihydro-5-octyl-4,6-dioxo-4H-thieno[3,4-c]pyrrole-1,3-diyl)[4,8-bis[(2-ethylhexyl)oxy]benzo[1,2-b:4,5-b′]dithiophene-2,6-diyl]];

OFET – organic field effect transistor;

L – organic field effect transistor channel length;

W – organic field effect transistor channel width;

photo-CELIV – photogenerated charge extraction by linearly increasing voltage;

$t_{\max}$ – time when photo-CELIV current density transient reaches its peak value;

i-CELIV – injected charge extraction by linearly increasing voltage;

$j(0)$ – initial current density step in photo-CELIV and i-CELIV experiments;

FTO – fluorine doped tin oxide;

ITO – indium tin oxide;

Spiro-MeOTAD – 2,2',7,7'-Tetrakis[N,N-di(4-methoxyphenyl)amino]-9,9'-spirobifluorene;

TiO_2 – titanium dioxide;

$CH_3NH_3PbI_3$ – methylammonium halide perovskite;

HTM – hole transporting material;

DMF – dimethylformamide;

rpm – revolutions per minute;

PbI_2 – lead (II) iodide;

CB – chlorobenzene;

TOF – time of flight technique;

μ – charge carrier (electron or hole) mobility;

μ_0 – mobility prefactor;

τ_σ – Maxwell relaxation time;

SEM – scanning electron microscopy;

XRD – X-ray diffraction spectroscopy;

DSC – differential scanning calorimetry;

GDM – Gaussian disorder model;
SCLC – space charge limited current;
DOS – density of states;
T_{g} – glass transition temperature;
t_{tr} – charge carrier transit time;
ε_0 – vacuum permittivity;
F – electric field;
σ – energetic disorder parameter;
k – Boltzmann constant;
AFM – atomic force microscopy;
OTS – trichloro(octyl)silane;
α – light absorption coefficient;
B_{L} – Langevin type recombination coefficient;
t_{del} – delay time between laser light and ramp pulse;
$n(t)$ – charge carrier density;
MIS – metal-insulator-semiconductor;
HOMO – highest occupied molecular orbital;
LUMO – lowest unoccupied molecular orbital;
PCE – power conversion efficiency;
PVA – polyvinyl alcohol;
PMMA – poly(methyl methacrylate);
CYTOP – fluoropolymer used as insulator in field-effect transistors;
MOS – metal-oxide-semiconductor.

INTRODUCTION

Organic semiconductors already play a very significant role in today's world of electronics. For example, electrophotographic image recording now mainly relies on organic materials and increasingly industrial screen manufacturers are offering OLED (organic light emitting diode) panels in their portfolio (examples: Samsung, LG, BOE and others). The benefit of possible mechanical flexibility of organic semiconductors in the applications was repeatedly mentioned in the reports **[1- 3]** and now the first widely available products with flexible (not curved or bent) OLED screens emerge in the stores around the world (smartphones-tablets, laptops). This shows the true potential and growing interest in organic semiconductor materials and they are becoming more important for applications in OFETs (organic field-effect transistors) and in organic solar cells as well (Fig. 1). Quite recently, organic solar cells field partly shifted to the research of perovskite type materials which together with the organic materials promise new heights in efficiency of the solar cells (Fig. 2) **[4, 5]**.

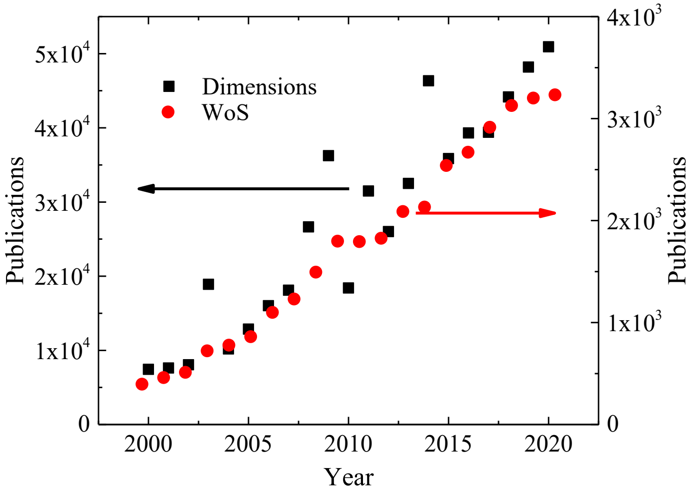

Fig. 1. Number of publications under the keyword "organic semiconductor" in "Dimensions" database (black squares) and in "Web of Science" database (red circles) **[7, 8]**.

Charge transport properties of organic semiconductors are decisive factor for the applications and devices mentioned above, therefore, the study of charge transport was and is one of the main topics in this research field.

Growing attention to the organic semiconductors research field brings more funding and people. Consequently, over the last decade the number of research groups that work in the research of organic semiconductors has increased greatly **[6]**. This includes graduate training programs, specific courses, summer schools, grants to MSc, PhD, and postdoctoral research students.

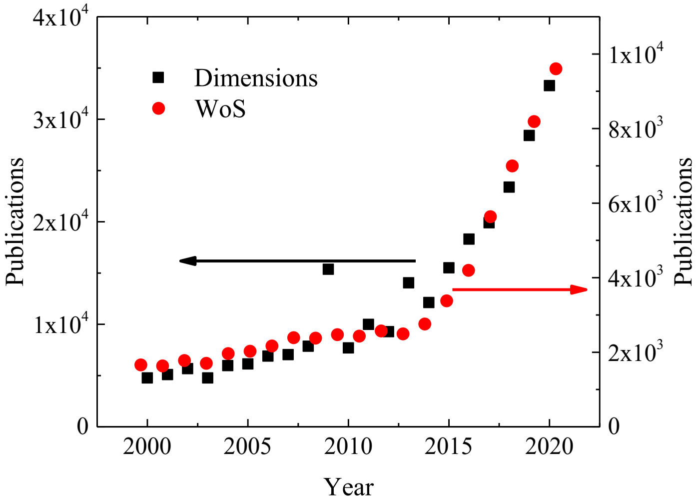

Fig. 2. Number of publications under the keyword “perovskite” in “Dimensions” database (black squares) and in “Web of Science” database (red circles) **[7, 8]**.

The main focus of this thesis is on charge carrier transport and recombination in various organic semiconductor structures. Since the first article about perovskite solar cells **[9]** a lot of research is done to investigate charge carrier transport in these novel perovskite materials. However, despite extremely fast progress in solar cell efficiency, the exact electronic properties of this type of materials are relatively little understood. Moreover, obtained research data strongly depends on the preparation method, purity of the materials which can lead to uncontrolled morphological variations of the samples and poor reproducibility of photovoltaic performance.

Theoretical calculations of charge transport in hybrid perovskites suggest very high charge carrier mobility which is unusual in organic solar cells research field. However, experimentally obtained charge carrier mobility in perovskite layers suggest that charge carrier mobility is greatly lower than theoretically calculated and that it has strong dependence on morphology and temperature **[10-12]**. In this work hole mobility in $CH_3NH_3PbI_3$ perovskite solar cell structure was evaluated by photo-CELIV (photogenerated charge extraction by linearly increasing voltage) technique to better understand charge transport properties in this type of materials.

One of the biggest differences between traditional semiconductors and organic semiconductors is that organics usually are in the amorphous state due to weak interaction between the molecules. This feature can be considered as an advantage (flexibility, easy manufacturing) as well as a disadvantage (low mobility, poor reproducibility). By manipulating the morphology of organic semiconductors, the performance in the devices can be significantly increased **[13]**. Also, morphology of some of the long chain polymers can be significantly altered by layer casting procedure showing the sensibility of electrical properties to morphology and possible variations of the same material as well **[14]**. In this work charge carrier transport in OFET structure fabricated with neat PCPDTBT (poly[2,6-(4,4-bis-(2-ethylhexyl)-4H-cyclopenta [2,1-b;3,4-b′]dithiophene)-alt-4,7(2,1,3-benzothiadiazole)]) active layer was investigated. PCPDTBT material has potential to be used in organic solar cells, as it is usually mixed with PCBM to form bulk heterojunction **[15, 16]**. However, in this work PCPDTBT was employed as an active layer in OFET structure allowing to investigate charge carrier transport in different directions of the structure, thus allowing to investigate anisotropy of charge carrier transport in PCPDTBT. To achieve that the quite novel i-CELIV and OFET current transients techniques were used.

In OFET structures dielectric layer surface plays important role in charge transport, because it is a foundation with which organic active layer forms interface which is essential to charge carrier transport in the OFET channel. Dielectric layer surface can be modified before casting organic active layer and like so charge carrier transport can be improved **[17, 18]**. Thus, it is important to investigate, how dielectric surface can influence charge carrier transport in particular material or OFET structure. In this work PBDTTPD material commonly used as hole transport material in blends with PCBM to form solar cell structures **[19]**, was employed as an active layer in OFET structures for investigation of charge carrier transport and how dielectric surface influences charge carrier transport.

Recombination of photogenerated charge carriers is one of the most important characteristics of organic semiconductors used in solar cells application. Therefore, in this work neat PBDTTPD was employed as an active layer in sandwich structure to investigate charge carrier transport and recombination in this material. Investigation of single material instead of blends gives more information about the material itself and its performance, where investigation of blends focuses more on optimal ratios, thicknesses and other characteristics to get the best possible properties like efficiency, stability and overall performance **[20, 21]**. PBDTTPD sandwich structures were investigated by time of flight (TOF) and photo-CELIV techniques. Both techniques can be used for evaluation of charge carrier mobility, moreover photo-CELIV technique also allows to estimate recombination rate and Langevin recombination coefficient in photogenerated charge carrier decay experiment **[22-24]**.

MAIN GOALS AND TASKS OF THE THESIS

The main goals of this thesis are investigation of charge carrier transport in solar cell structures with $CH_3NH_3PbI_3$ perovskite layer, in OFET structures with PCPDTBT and PBDTTPD active layers and recombination in neat PBDTTPD layer employed in sandwich structure. This includes fabrication of the samples necessary for investigation of charge carrier transport, choosing and applying measurement techniques which are capable of measuring needed charge carrier parameters. Therefore, main tasks of this thesis were formulated accordingly:

1. To apply photo-CELIV technique to measure charge carrier mobility in $CH_3NH_3PbI_3$ perovskite solar cell structure.
2. To fabricate OFET structures with PCPDTBT active layer, apply i-CELIV and OFET current transients techniques allowing to measure charge carrier transport in different directions of OFET structure.
3. To fabricate OFET structures with PBDTTPD active layer on differently treated dielectric layer surfaces and to investigate dielectric surface influence on charge carrier transport.
4. To fabricate sandwich structures with PBDTTPD active layer and to investigate photogenerated charge carrier transport and recombination.

NOVELTY OF THE WORK

In the each of the experiments presented in this work scientific novelty is demonstrated and it is expressed by the following statements:

- After applying photo-CELIV technique for the first time to investigate charge carrier mobility in $CH_3NH_3PbI_3$ perovskite solar cell structure, in which holes were extracted from $CH_3NH_3PbI_3$ perovskite and

Spiro-OMeTAD layers together, it was shown that layers morphology impedes hole extraction from the structure.

- After applying i-CELIV and OFET current transients techniques for charge carrier transport investigation in perpendicular and parallel directions in neat PCPDTBT OFET structures, it was shown that hole transport exhibits anisotropy.
- After investigating OFET structures for the first time fabricated with neat PBDTTPD layer with i-CELIV and OFET current transients techniques, it was demonstrated how dielectric surface influences hole transport.
- After investigation of photogenerated charge carrier recombination in neat PBDTTPD layer, it was shown that bimolecular recombination in PBDTTPD material is reduced.

STATEMENTS TO DEFEND

1. Grain boundaries of $CH_3NH_3PbI_3$ perovskite layer and perovskite-organic layers interface impede hole extraction out of the solar cell structure by increasing density of trap states.
2. PCPDTBT OFET structures have anisotropy of hole transport in perpendicular and in parallel to the substrate directions and exhibit morphology change of PCPDTBT layer at higher than room temperatures, thus influencing hole transport.
3. SiO_2 surface modification in PBDTTPD OFET structures reduces interface energetic disorder parameter σ by reducing SiO_2 surface defects influence on hole transport and thus improves hole transport conditions near dielectric layer.
4. PBDTTPD sandwich structures exhibit bimolecular-type recombination rate 6 times lower than Langevin recombination rate calculated from obtained charge carrier mobility due to part of photogenerated holes escaping from recombination area.

LIST OF PUBLICATIONS AND AUTHOR‘S CONTRIBUTION

List of publications

1. Andrius Aukštuolis, Mihaela Girtan, George A. Mousdis, Romain Mallet, Marcela Socol, Mohamed Rasheed, Anca Stanculescu. Measurement of charge carrier mobility in perovskite nanowire films by photo-CELIV method, *Proceedings of the Romanian Academy, Series A*, 18, 1, 34–41 (2017).
2. Andrius Aukštuolis, Nerijus Nekrašas, Kristijonas Genevičius, Jūratė Jonikaitė-Švėgždienė. Anisotropy of charge carrier transport in PCPDTBT field-effect transistor structures, *Synthetic Metals*, 264, 116382 (2020), https://doi.org/10.1016/j.synthmet.2020.116382.
3. Andrius Aukštuolis, Nerijus Nekrašas, Kristijonas Genevičius, Giedrius Juška, Investigation of charge carrier mobility and recombination in PBDTTPD thin layer structures, *Organic Electronics*, 90, 106066 (2021), https://doi.org/10.1016/j.orgel.2021.106066.

Author’s contribution

1st publication. Author measured samples provided by co-authors with photo-CELIV technique, gathered experimental data and organized it for publication. Also, author contributed to writing few segments of the article and edited the text for publication.

2nd publication. Author fabricated the samples for the experiments, measured them with i-CELIV and OFET current transients techniques, gathered experimental data and organized it for publication. Author together with N. Nekrašas wrote original draft for publication and together with K. Genevičius ir N. Nekrašas made revisions necessary for publication.

3rd publication. Author fabricated the samples for the experiments, measured them with i-CELIV and OFET current transients techniques, together with N. Nekrašas measured samples with TOF, photo-CELIV techniques, gathered experimental data and organized it for publication. Author also together with N. Nekrašas and K. Genevičius wrote original draft for publication and made revisions necessary for publication.

PRESENTATIONS IN THE INTERNATIONAL CONFERENCES

1. Mihaela Girtan*, G. Mousdis, A. Aukštuolis, M. Rasheed, R. Mallet, Studies of the physical properties $CH_3NH_3PbI_3$ nanowires thin films prepared by spin-coating, EMRS 2016 (May 2-6), Lille, France. Poster presentation.
2. Andrius Aukštuolis*, George A. Mousdis, Romain Mallet, Mihaela Girtan*, Measurement of charge carrier mobility in $CH_3NH_3PbI_3$ perovskite thin films systems by photo-CELIV method, 3èmes Journées Pérovskites Hybrides (JPH) 2017 (May 9-10), Angers, France. Poster presentation.
3. A. Aukštuolis*, N. Nekrašas, K. Genevičius, M. Girtan, G. Juška, Charge carrier transport properties in PBDTTPD organic solar cell structure, 12th Conference on Hybrid and Organic Photovoltaics, HOPV20 Online Conference, 2020 (May 26-29). Poster presentation.
4. Andrius Aukštuolis*, Nerijus Nekrašas, Kristijonas Genevičius, Jūratė Jonikaitė-Švėgždienė, Giedrius Juška, Charge carrier transport properties in thin film hybrid field effect transistor structures, 28th in the series of Condensed Matter General conferences, CMD2020GEFES, 2020 (August 31 – September 4), Online conference. Oral presentation.
5. Andrius Aukštuolis*, Nerijus Nekrašas, Kristijonas Genevičius, Jūratė Jonikaitė-Švėgždienė, Giedrius Juška, Charge carriers transport properties in PCPDTBT thin film transistor structures, Functional materials and Nanotechnologies – 2020 (November 23-25), Online conference. Poster presentation.

* Presenter

1. Literature review

1.1 Organic semiconductors

Organic semiconductors are not “organic” in the terms that are mostly used today. They are not organically grown in the fields without pesticides, on the contrary, they are synthesized with desirable parameters by scientists in the laboratories around the world. The word organic comes from organic chemistry and from comparison with traditional materials (silicon, germanium, gallium arsenide) which were first used for semiconductor devices like diodes, transistors, solar cells and etc. In electronics field the term *organic semiconductors* implies that the material is made by mostly carbon and hydrogen atoms with often few heteroatoms like oxygen, nitrogen, sulfur or sometimes even silicon **[25]** and all the materials must exhibit typical properties for semiconductors materials. These properties are absorption and usually emission of electromagnetic waves in around the visible spectral range and some degree of conductivity which is sufficient enough for operation of semiconductor devices like solar cells, field-effect transistors and light emitting diodes. Although organic semiconductors can be used for operating devices, their semiconductor properties are similar to the ones of dielectric materials. If traditional semiconductors have low band gaps (0.7 – 1.4 eV) and dielectric permittivities as large as $\varepsilon_r = 11$, organic semiconductors have the properties that are similar to dielectric materials with band gaps in the range of 2 – 3 eV and dielectric permittivity of about $\varepsilon_r = 3.5$. Thus, these parameters disturb charge carriers creation by thermal excitation at room temperature, which is not an obstacle for non-organic doped semiconductors. The differences between mentioned parameters and inner structure of organic and non-organic semiconductors strongly affect charge transport properties and the nature itself, which will be discussed in later sections.

Research of organic solids began at the beginning of twentieth century when first reports on conductivity, photoconductivity and fluorescence were published **[26]**. However, the research was inconsistent and slow. It gained acceleration in the years from 1950 to 1980. In 1953 the report on electroluminescence of a cellulose film doped with acridine orange was published **[27]**. The big breakthrough in organic electronics probably belongs to the discovery that high conductivity could be achieved in doped π-conjugated polymers (up to 10^9 times higher than in undoped polymer) **[28]**. For this discovery of conductive polymers Nobel Prize in Chemistry was awarded in 2000.

The name "π-conjugation" comes from the name of the bond between atoms in the molecule. For explanation what kind of bond it is the simple system – molecule of ethene will be used as an example (Fig. 3). From all the six electrons of carbon atom only two can form covalent bonds in the ground state electron configuration. In this configuration two electrons are in a 1s orbital, two in a 2s orbital, the remaining two in the two of the three $2p_x$, $2p_y$ and $2p_z$ orbitals. Configuration can be written as $(1s)^2(2s)^2(2p_x)^1(2p_y)^1(2p_z)^0$ or in a shorter manner $1s^22s^22p_x^12p_y^1$. The ground state of carbon has only two electrons in 2p orbitals, thus only two covalent bonds can be created. However, promoting electron from 2s state to 2p state requires less energy than it is gained from biding energy by forming four covalent bonds, thus the promotion happens every time when carbon is not in elementary atomic form. If carbon atom has approaching atoms like another carbon or hydrogen to form a bond, external forces give energy sufficient enough to compensate the energy difference between 2s and 2p orbitals and to disintegrate them. As a consequence, the mixing of orbitals happens and it forms new so-called hybrid orbitals. If mixing happens between three orbitals, three new sp^2 orbitals are formed. Superscript this time refers not to the number of electrons in the orbital, but to the number of orbitals involved in the hybrid orbitals (in this case sp^2 means that two p orbitals are involved in hybrid orbitals). Three orbitals are distributed in one plane with an angle of 120° between them and the remaining not hybrid orbital is perpendicular to the plane of the hybrid orbitals. This form is typical for carbon in the molecule of ethene (Fig. 3). Each of the sp^2 orbitals forms σ-bonds with other atoms. Two of these bonds are with hydrogen atoms and one with other carbon atom. The electrons in the $2p_z$ orbitals of each carbon atom will be paired with one another in the molecule. Both $2p_z$ orbitals will be connected between two carbon atoms and will form π-orbital. The electrons in π-orbital have spatial probability density of being above and below molecular axis. The electrons in the molecule no longer belong to the atom they originally came from, but they belong to the both atoms of ethene molecule.

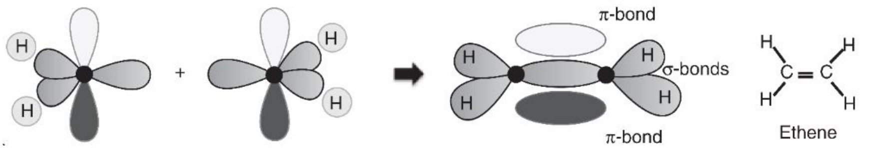

Fig. 3. Schematic view of four hydrogen atoms and two carbon atoms with sp^2 hybrid orbitals forming a molecule of ethene. σ-bonds of the molecule are coloured in grey and π-bonds are coloured in black and white. Adapted from **[29]**.

The molecular orbitals are different than atomic ones. In the molecule atomic orbitals interact with each other creating resonance integral with σ and π orbitals with the different energies. 1s orbitals are close to the core and their interaction creates σ bonding and σ^* anti-bonding orbitals with low energy gap between them. One of the three $2sp^2$ hybrid orbitals of each carbon atom points along the internuclear axis, thus their charge overlap leads to large resonance integral creating σ and σ^* orbitals that are separated by big energy gap (Fig. 4). The interaction of $2p_z$ orbitals takes place further from carbon nuclei and it forms π bonding and π^* anti-bonding orbitals with weaker splitting between them.

Each of the σ and σ^* orbitals created from 1s orbitals are filled with electrons leading to no net interaction. However, in the other pair of σ bonding and σ^* anti-bonding orbitals on the low-lying σ orbital is filled with electrons leaving σ^* empty. This results in strong attraction between the nuclei involved, meaning that σ-bonds are the backbone of the molecule holding it together. Also, π-bonding orbital is filled with two electrons while π^* anti-bonding orbital is empty. The π orbital contributes very little to attractive interaction between the nuclei in comparison with the σ orbital, because the overlap of electron density is further away from the internuclear axis. Thus, π-orbital is highest occupied molecular orbital (HOMO) of the ethene molecule and π^* orbital is lowest unoccupied molecular orbital (LUMO). The energy difference between these two orbitals is referred as band gap of the molecule and is equivalent to band gap between valence band and conduction band in non-organic semiconductors.

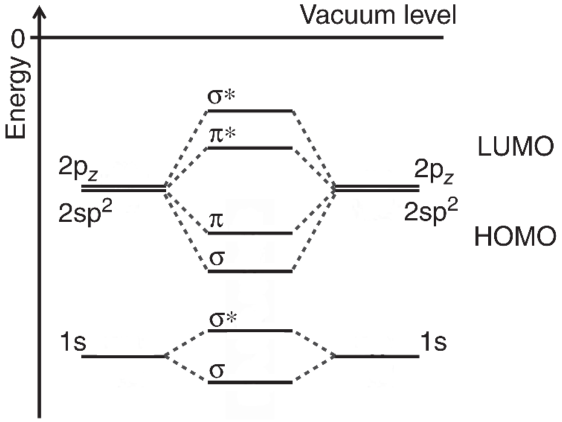

Fig. 4. Simplified energy level diagram of the ehtene molecule showing only the orbitals from carbon atoms interaction. Adapted from **[29]**.

HOMO and LUMO are also called frontier orbitals and they are crucial for optical and electrical properties of the molecule. Also, the energy levels of these orbitals determine, if electron or hole can be injected from metal electrodes and the energy levels of frontier orbitals can be chosen or tuned to be compatible with certain metals work function, thus allowing injection and transition of charge between the materials (Fig. 5). The band gap between π-orbitals is convenient for employing this kind of materials in solar cells or OLEDs as they absorb and emit light in the visible spectral range.

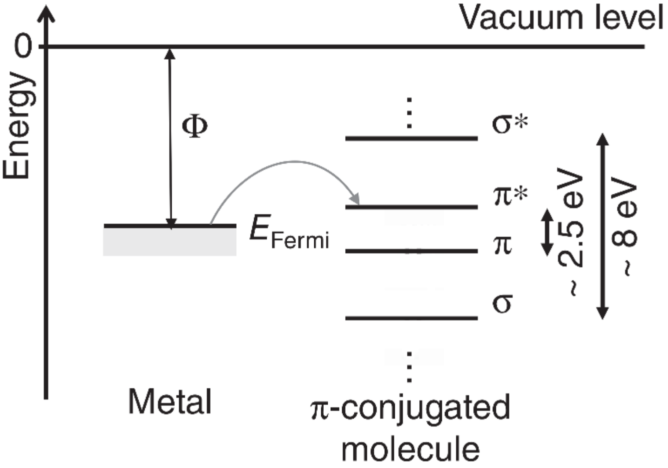

Fig. 5. Schematic view of typical energy levels of molecular orbitals in carbon-based material relative to metal work function. Adapted from **[6]**.

In the ethene molecule there is σ bonds holding molecule together and π bond which has electrons in π-orbital, but it adds little to the attraction force between the carbon nuclei. For example, in benzene molecule there are six σ bonds between carbon atoms and three π bonds. Benzene ring is Kekulé structure (named after August Kekulé) meaning that the place of π bonds constantly changes within the molecule creating delocalization of π orbitals and electrons in these orbitals. The electrons are not tied to the carbon atoms they originally came from, but they are “shared” between all six atoms in the ring. Delocalization of electrons in the molecule is the key to the conductivity in the organic semiconductors and it can be obtained in the polymers or smaller molecule organic materials (Fig. 6). Delocalization in organic semiconductors is achieved by creating single and double bonds which change each other in the molecule or backbone of the polymer. Materials which have single and double bonds changing each other in the molecule are called π-conjugated materials (sometimes just *conjugated materials*).

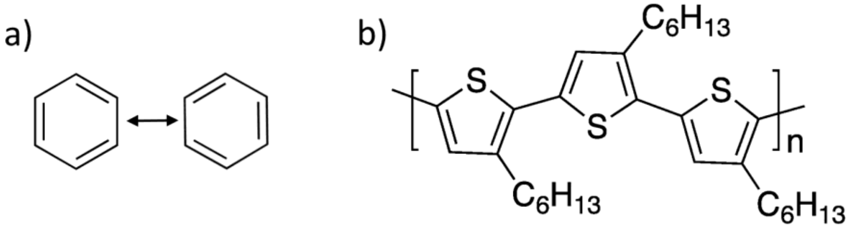

Fig. 6. a) Schematic view of benzene molecule and the interchanging π bond place; b) Schematic view of P3HT π-conjugated molecule.

In the benzene molecule electron delocalization is “full” meaning that all electrons in the π orbitals are shared equally between all the carbon atoms. This is not the same case in π-conjugated materials, especially in the polymers. Delocalization in polymers can be restricted due to defects in the molecule, twists, bends and knots of the molecule and the length of delocalization is usually much smaller than the length of the polymer itself, thus creating local states in many places through the polymer molecule. The length of local delocalization state is around 5-15 monomers and it strongly depends on the morphology of the casted layer **[30, 31]**. If in non-organic semiconductors charge carriers can move through the whole crystal via conduction and valence bands, in organic semiconductors charge carriers move by hopping through the local states in the casted layer **[32]**.

The majority of this chapter was prepared by mainly using the references **[6, 29, 33-35]**.

1.2 Charge transport in organic semiconductors

Probably the most influential paper about charge transport in disordered organic semiconductors was published by Heinz Bässler in 1993 **[32]**. It was cited more than 2200 times already according to CrossRef **[36]** and the transport model he proposed in the paper is still popular among researchers in the field **[37]**. By using Monte Carlo simulation H. Bässler showed that the density of states (DOS) in various different organic materials can be described by Gaussian shape (Fig. 7). Gaussian energy spectrum is described via formula:

$$g(E) = \frac{N}{\sigma\sqrt{2\pi}} \exp\left(-\frac{E^2}{2\sigma^2}\right) \quad , \tag{1.1}$$

where N is the density of randomly distributed localized states (localization states) through which charge carriers can hop, σ is energetic disorder parameter of DOS (see Fig. 7). Naturally, bigger value of σ means bigger disorder in the layer. Common value of σ in disordered organic materials is around 0.1 eV **[32]**.

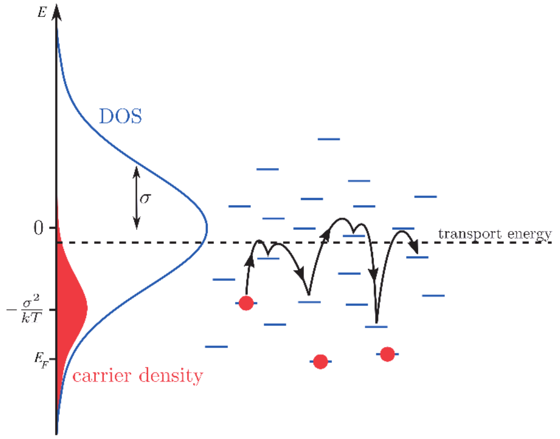

Fig. 7. Schematic view of Gaussian DOS in organic semiconductors. Adapted from **[38]**.

Charge carriers can travel via hopping in such disordered system by transitioning from occupied state *i* to an empty state *j* separated by the distance

r_{ij}. Hopping from one state to another requires a compensation of energy between the two states. That energy can be compensated, for example, by absorbing or emitting a phonon. The rate at which charge carriers make transitions between the states in described by Miller-Abrahams equation **[39]**:

$$\nu_{ij} = \nu_0 \exp\left(-\frac{2r_{ij}}{a} - \frac{|E_i - E_j| + |E_i - E_{\mathrm{F}}| + |E_j - E_{\mathrm{F}}|}{2kT} \right) , \quad (1.2)$$

where a is the localization length of charge carriers in the states (usually around 10^{-8} cm **[40]**), E_i and E_j are energies of charge carriers on sites i and j respectively, E_{F} is Fermi energy level, T is temperature, k is the Boltzman constant and ν_0 is frequency prefactor, which is called attempt-to-escape frequency. If charge carriers interact with phonons, frequency prefactor value is close to the phonon frequency value 10^{12} s^{-1} **[41]**.

By using Miller-Abrahams hopping rate and Monte Carlo simulation H. Bässler showed how charge carrier mobility depends on temperature and electric field in Gaussian DOS of disordered solids **[32]**:

$$\mu(T,F) = \mu_0 \exp(-\left(\frac{2}{3}\frac{\sigma}{kT}\right)^2) \begin{cases} \exp C\left(\left(\frac{\sigma}{kT}\right)^2 - \Sigma^2\right) F^{\frac{1}{2}} ;\ \Sigma \geq 1.5 \\ \exp C\left(\left(\frac{\sigma}{kT}\right)^2 - 2.25\right) F^{\frac{1}{2}} ;\ \Sigma < 1.5 \end{cases} , \quad (1.3)$$

where μ_0 is mobility prefactor, C is a scaling factor from parametric fit, F is electric field and Σ is spatial disorder parameter.

Not all localized states act as transport states in organic semiconductors. Since the distribution of states is Gaussian shape, there are no distinct separation between states that act as transport states and the ones that act as trap states. Transport energy level in DOS is analogous to band edge or mobility edge in traditional non-organic semiconductors and it describes which states act as transport states and which states act as trap states **[42, 43]**. It has only a statistical meaning, because it marks the energy level of states from which charge carrier is most probably to be released to hop to neighboring state. Therefore, states below transport energy act as trap states and states above transport energy act as regular transport states. However, at lower temperatures the states that were trap states may become transport states, because transport energy level is dependent on the temperature **[33]**.

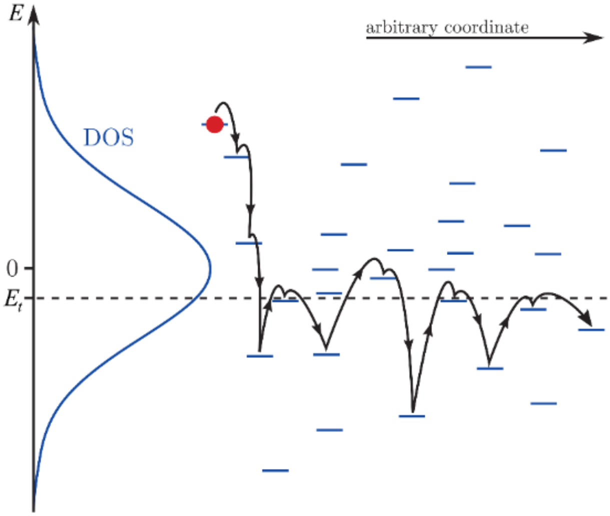

Fig. 8. Schematic view of charge carrier relaxation after injection or photogeneration. Adapted from **[44]**.

In organic solar cells and organic field-effect transistors charge carriers are photogenerated with light or injected with applied external voltage, thus charge carriers have higher energy and occupy higher energy states of organic semiconductor (Fig. 8). With time charge carriers redistribute through the DOS by relaxing to lower energy states (see Fig. 8). Relaxation of charge carriers reduces their hopping mobility, because with time more charge carriers occupy states that are below transport energy level. Another important factor for charge carrier mobility is the charge carrier density *n*, because it directly impacts Fermi level. The higher the density *n*, the closer Fermi level is to transport energy level, thus increasing the probability of hopping to neighboring state (Fig. 9) **[38, 45]**.

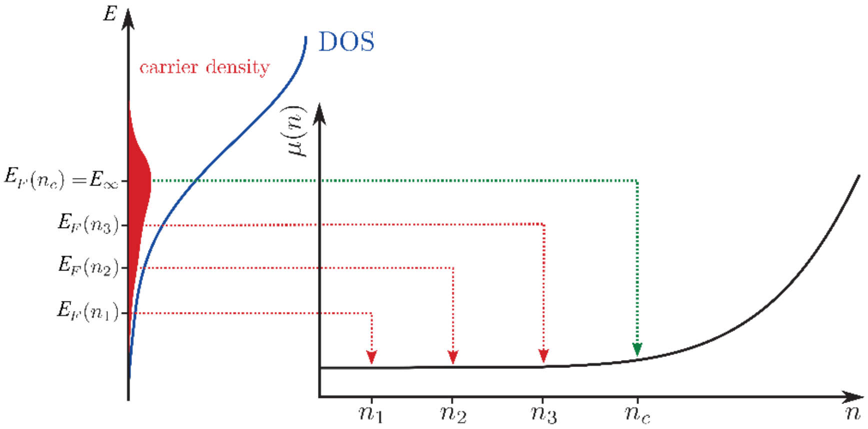

Fig. 9. Mobility and Fermi level dependencies on the density of charge carriers *n* in the Gaussian DOS. Adapted from **[38]**.

The distribution of DOS in the organic semiconductors may obtain different shapes, not only Gaussian. The other most common DOS shape in the organic semiconductors is exponential DOS distribution **[38]**. The shape of DOS in the material is found experimentally by measuring charge carrier mobility dependence on time, temperature and density of charge carriers. Also, organic systems that exhibit superposition of two different DOS distributions (for example, Gaussian + exponential) were reported in articles as well **[46, 47]**. The exponential tail of DOS in superposition is usually attributed to trap states in which charge carriers sink with more time they spend in the sample. The different shapes of DOS and different widths of DOS demonstrate the possible variety of organic semiconductors and the importance of morphology to charge carrier transport.

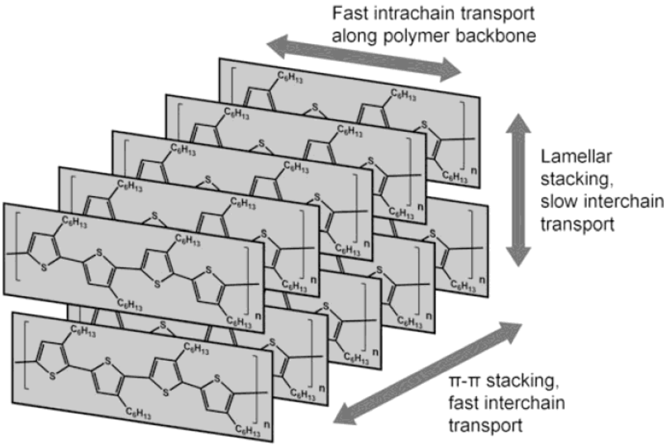

Fig. 10. Schematic view of P3HT chains ordering and possible slow and fast charge transport conditions. Adapted from **[31]**.

Usually an amorphous structure (especially π-conjugated polymers) by nature, organic semiconductors can obtain various structures under special layer casting conditions. For example, P3HT tends to form lamellar structure if casted layer is heated for around 10-15 minutes **[48]**, field-effect transistors of pentacene can be manufactured in a way, that pentacene acts as a single crystal material **[49]**. These examples show not only the importance of morphology of the layer to the charge carrier transport, but possible strong anisotropy of charge carrier mobility and transport conditions in different directions of the layer (Fig. 10). Charge carrier mobility may differ more than three orders of magnitude in the structures in which π stacking distance changes from 3.5 Å to 3.8 Å and charge carrier mobility obtained in the same structure, but in different directions may differ by two orders of magnitude **[13]**. All these specifics of charge carrier transport must be taken into account when fabricating device or choosing material for desired application.

The majority of this chapter was prepared by mainly using the references **[6, 31, 33, 34, 38]**.

1.3 Recombination

Recombination is the process that is inevitable in organic (and non-organic) semiconductors where both polarity charges are participating in the transport. It is the working principle of electroluminescence in OLEDs and it affects solar cells efficiency **[50]**. Therefore, recombination of charge carriers is one of the important parameters for the applications of organic semiconductors.

Photogenerated charge carriers travel to electrodes and in their paths they can recombine if they meet a charge carrier with opposite polarity. The continuity equation of photogenerated charge carriers can be expressed by **[33]**:

$$\frac{dn}{dt} = G - R - \frac{1}{q}\frac{\partial j}{\partial x} \quad , \tag{1.4}$$

where n is the density of charge carriers, t is time, G is generation rate, R is recombination rate and $\partial j/\partial x$ is a spatial diffusion current derivative. The recombination in organic semiconductors is typically a non-geminate process and it is usually bimolecular recombination of an electron and a hole **[51, 52]**. In this case recombination rate can be written as:

$$R = B(np - n_i p_i) \quad , \tag{1.5}$$

where n and p are densities of photogenerated electrons and holes respectively, n_i and p_i are densities of intrinsic electrons and holes respectively and B is bimolecular recombination coefficient.

Description of bimolecular recombination in organic semiconductors with low charge carrier mobilities (μ < 1 cm^2/Vs) is based on model proposed by Langevin **[53, 54]**. This model describes the recombination rate of two ions of opposite charges in an ion reservoir. In a reservoir without external electric field two ions can avoid recombination only if their kinetic energy is larger than their Coulomb attraction. In that case they will recombine if the distance between them is smaller than Coulomb radius r_C **[54]**:

$$r_\mathrm{C} = \frac{e^2}{4\pi\varepsilon\varepsilon_0 kT} \quad , \tag{1.6}$$

where e is elementary charge, ε_0 and ε are dielectric permittivities of vacuum and material (for example, organic semiconductor) respectively. Then eq. (1.5) can be written as follow:

$$R_\mathrm{L} = B_\mathrm{L}(np - n_i p_i) \quad , \tag{1.7}$$

where R_L Langevin bimolecular recombination rate and B_L is Langevin recombination coefficient which is proportional to the sum of mobilities of both charge carriers of the material:

$$B_{\mathrm{L}} = \frac{e(\mu_{\mathrm{p}} + \mu_{\mathrm{e}})}{\varepsilon\varepsilon_0} \quad , \tag{1.8}$$

where μ_{p} and μ_{e} are hole and electron mobilities respectively.

Reports on charge carrier recombination in organic semiconductors have shown that in bulk heterojunctions bimolecular recombination rate is much lower than the calculated recombination rate accordingly to Langevin's model **[55, 56]**. Heterojunctions are not homogenous materials, thus the conditions for recombination are different from the ones in homogenous materials for which Langevin proposed recombination model. Therefore, the main explanation why recombination rate is much slower than calculated from charge carrier mobilities is that charge carriers are spatially separated in different domains (different materials of bulk heterojunction) and can recombine only in the interfaces of the two domains. Also, there are reports showing that Langevin recombination rate is lower because of the influence of the lowest mobility charge carriers in the material **[57]** and because of extent of charge delocalization of holes and electrons in charge transfer state **[22]**. Thus, an additional coefficient ξ called Langevin reduction coefficient is often used in the reports on recombination studies and it can be found accordingly:

$$\xi = \frac{B}{B_L} \quad . \tag{1.9}$$

In the case of non-reduced Langevin recombination $\xi = 1$ and $\xi < 1$ if recombination rate is reduced. Usually, the range of Langevin reduction coefficient ξ is between 1 and 10^{-4} **[22, 50, 58]**.

There are many commonly used experimental techniques to evaluate the charge carrier recombination rate in organic semiconductors and their blends. Among others, widely used techniques are transient absorption (TA) **[59, 60]**, transient photovoltage and photocurrent (TPV/TPC) **[52]** and charge extraction by linearly increasing voltage (photo-CELIV) **[55, 61]**. The latter can be used for measuring not only the decay of photogenerated charge carriers, but charge carrier mobility as well.

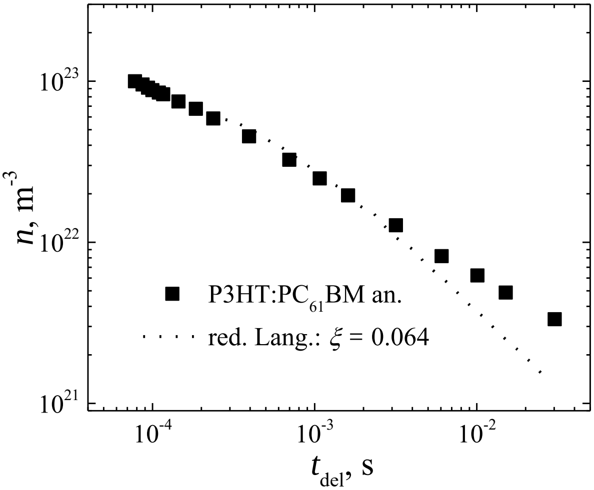

Fig. 11. Charge carrier density decay in P3HT:PCBM 1:0.8 bulk heterojunction solar cell at $T = 150$ K measured by photo-CELIV technique. Dashed line is a fit of reduced Langevin recombination with $\xi = 0.064$. Adapted from **[33]**.

A good example of reduced Langevin recombination in organic semiconductor blend can be seen in Fig. 11, where charge carrier density decay in P3HT:PCBM 1:0.8 bulk heterojunction solar cell at $T = 150$ K experimental data obtained by photo-CELIV is shown. Dashed line is fitted according to Langevin theory with experimentally obtained charge carrier mobility and additional reduction coefficient $\xi = 0.064$, showing that the part of charge carrier density decay is in accordance with reduced Langevin recombination rate.

The majority of this chapter was prepared by mainly using the references **[6, 33, 62, 63]**.

1.4 Perovskites

Originally $CaTiO_3$ mineral was called by the name *perovskite*. It was called after Russian mineralogist Count Lev Aleksevich von Petrovski when it was discovered by Prussian mineralogist Gustav Rose in 1839 in the mineral deposits in Ural Mountains **[64]**. Later the name *perovskite* was given to a family of compounds with the general formula close to or derived from the composition of ABX_3, where A is usually a large cation, B is usually medium size cation and X is an anion. Historically, the first reports of hybrid organic-inorganic perovskite structure compounds were published by Weber in 1978 **[65, 66]**. In following decades perovskite structure materials were studied in various fields for their unusual chemical and physical properties **[67-69]**. In 2009, first organic-inorganic hybrid perovskites ($CH_3NH_3PbI_3$ or $MAPbI_3$) usage as light absorber in dye-sensitized solar cells (DSSC) was demonstrated by Myiasaka and colleagues with the highest power conversion efficiency (PCE) of 3.81% achieved **[9]**. From this point the research in perovskite usage in solar cells application started to increase rapidly as it can be seen from the number of published research papers (see Fig. 2). The magnitude of the research led to the studies of new types of perovskites, to finding new types of organic materials used in solar cells together with perovskites and to abrupt increase in power conversion efficiency in perovskite solar cells as the current record holders reported efficiency of 25.5 % **[70]**. Organic-inorganic origin of persovskites used in solar cells brings new opportunities and new challenges as well. Perovskites have similarities to organic semiconductors in terms of sample manufacturing, light absorption and mostly the same measurement techniques can be used for charge transport investigation. But charge transport principle is different from the π-conjugated organic semiconductors. This alone is interesting from scientific point of view as well as important to better understand this type of materials and their prospects in future applications, because often perovkites are used together with organic materials in organic solar cells.

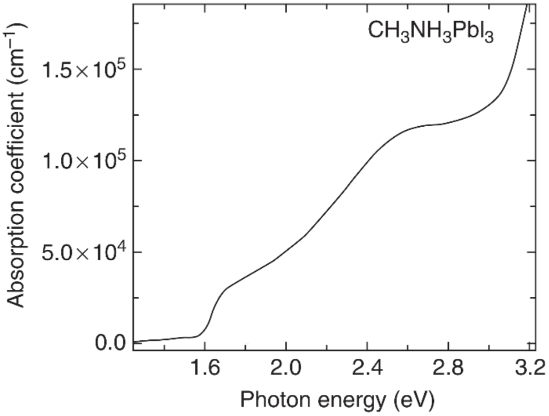

Fig. 12. Absorption spectrum of $CH_3NH_3PbI_3$ perovskite thin film at room temperature. Adapted from **[71]**.

One of the main reasons why perovskite materials are promising in solar cells application is broad absorption spectrum (Fig. 12). $CH_3NH_3PbI_3$ perovskite has large absorption coefficient which is similar to GaAs and about one order of magnitude higher than crystalline Si. Therefore, $CH_3NH_3PbI_3$ perovskite layer can be ten times thinner than Si and maintain same light absorption when used in solar cells application. Favorable absorption property of perovkskites comes from its structure (Fig. 13). With band gap E_g of 1.55 eV $CH_3NH_3PbI_3$ perovskite absorption edge reaches 800 nm with the direct transition between valence band and conduction band **[72]**.

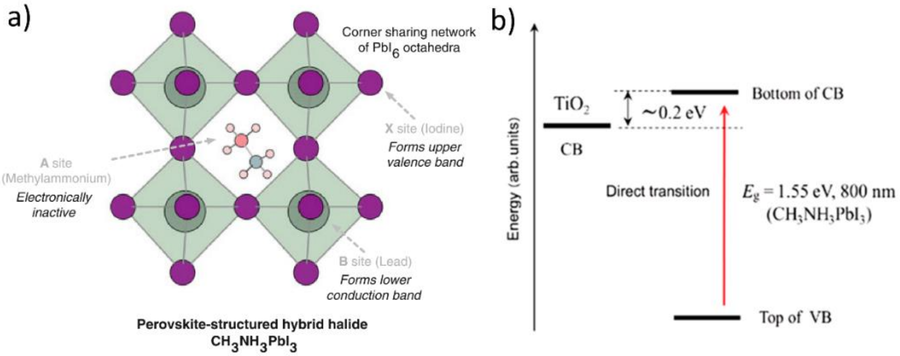

Fig. 13. a) Schematic view of $CH_3NH_3PbI_3$ pervoskite structure; b) band gap structure and energy levels of $CH_3NH_3PbI_3$ pervoskite in reference to TiO_2 energy level. Adapted from **[72, 73]**.

Light absorbers perovskites have to be implemented into solar cell structure in order to be used effectively in solar energy harvesting. $CH_3NH_3PbI_3$ pervoskite has ambipolar charge carrier mobility **[72]** and photogenerated charge carriers behave similarly to the ones in Si and GaAs and can migrate in absorber for long period of time **[74]**. However, for effective charge carrier extraction from perosvkite absorber to electrodes extra layer for hole transport is needed, as was shown by studies of perovskite solar cells **[72]**. This led to studies of new perovskite absorbers and their compatibility with hole transport materials. Probably the most studied solar cell structure with perovskite light absorber is the one with $CH_3NH_3PbI_3$ perovskite layer, spiro-MeOTAD (also used name spiro-OMeTAD) hole transport layer and TiO_2 electron transport layer (variations of dense and porous TiO_2 layers are used). Energy level diagram of this particular solar cell structure can be seen in Fig. 14. As in all multilayered solar cells, favorable transport conditions for electrons and holes must be created to have efficient cell. As it is shown in Fig. 14, choosing materials with favorable energy levels designs solar cell in a way that helps to separate electrons and holes and to transfer them to electrodes. This is typical n-i-p structure in which perovskite layer acts as intrinsic absorber. Even though this structure and working principle of perovskite solar cells is widely used and studied the processes of charge carrier generation and charge carrier transport in the solar cell and especially in the perovskite layer are not completely understood to this day.

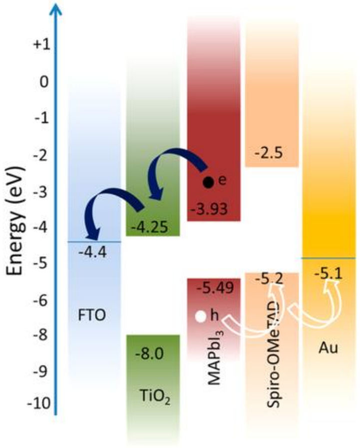

Fig. 14. Energy level diagram of perovskite solar cell with $CH_3NH_3PbI_3$ layer as light absorber, TiO_2 as electron transport layer, spiro-MeOTAD as hole transport layer, FTO as semitransparent electrode and Au as back electrode. Adapted from **[72]**.

Besides strong light absorption, the other convenient characteristics for solar energy harvesting is low exciton binding energy of $CH_3NH_3PbI_3$ perovskite **[75, 76]** and relatively high dielectric constant **[77]**. Therefore, electrons and holes can be rather easily separated in the perovskite film and then travel through their pathways to electrodes. However, this means that perovskite layer must provide favorable transport conditions for both types of charge carriers: electrons and holes, before they reach other layers (see Fig. 14). Recent studies have shown that holes and electrons exhibit very long diffusion lengths (up to 5 μm) in single crystal and polycrystalline films **[78, 79]**. In comparison, charge carrier diffusion lengths in the most of commonly used organic semiconductors (for example, P3HT and PCBM) are typically lower than 10 nm **[80]**.

Moreover, diffusion lengths are rather well balanced for both polarity charge carriers in perovskite solar cells **[81]**. However, the origin of these favorable properties for solar cells charge carrier transport in perovskite layers is still under scientific discussion, even though there are numerous characterizations of this type of materials. Diffusion length is tied with diffusion coefficient D of the material via formula: $L_{\mathrm{d}} = \sqrt{D\tau}$, where τ is the life time of charge carriers. Diffusion coefficient is mainly decided by the mobility of charge carriers: $D = \mu q / k_{\mathrm{B}} T$, thus it seems that long charge carrier diffusion lengths in perovskites should lead to high mobility. Theoretical calculations of charge carrier mobility show very high values for both: electrons and holes. At charge carrier concentrations of ~10^{16} cm^{-3} calculated electron mobility μ_e reaches 1500-3100 cm^2/Vs and calculated hole mobility μ_h reaches 500-800 cm^2/Vs in $CH_3NH_3PbI_3$ perovskite **[82]**. These theoretical values are orders of magnitude higher than the ones in organic polymers and can even be compared to the charge carrier mobilities of crystalline Si and GaAs. However, electron mobility experimentally obtained by Hall-effect measurements reaches “only” ~66 cm^2/Vs in $CH_3NH_3PbI_3$ perovskite **[83]**. In vapor grown polycrystalline $CH_3NH_3PbI_3$ perovskite film Hall-effect charge carrier mobility is even lower with μ ~ 8 cm^2/Vs (see Fig. 15 a)).

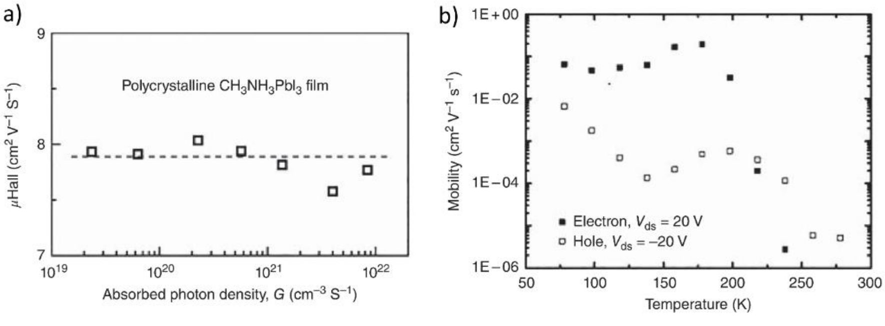

Fig. 15. a) Charge carrier mobility measured at different photo-excitation densities in polycrystalline $CH_3NH_3PbI_3$ film; b) Electron and hole mobilities measured at different temperatures in $CH_3NH_3PbI_3$ field effect transistors extracted from forward sweeping of transfer characteristics. Adapted from **[10, 11]**.

Discrepancies between theoretically calculated charge carrier mobility and experimentally obtained by Hall-effect measurements indicate that charge transport in perovskites is rather ambiguous. Scientific discussions about why perovskite materials exhibit such different charge carrier mobilities is still continuing as more data is gathered. Even though, perovskite materials are attractive in solar cell application, FET configuration is convenient for charge carrier transport investigation. Highest achieved values of charge carrier mobility in FETs were of the order of 0.5 cm^2/Vs (see Fig. 15 b)). These values were achieved at low temperature of 78 K. Authors state that around 150-170 K temperature $CH_3NH_3PbI_3$ perovskite has phase transition, which is partly responsible for charge carrier mobility decrease at higher temperatures. According to the report **[11]** $CH_3NH_3PbI_3$ perovskite FET mobilities at around room temperature are $4.8*10^{-6}$ cm^2/Vs for holes and $3*10^{-6}$ cm^2/Vs for electrons (Fig. 15 b)) which is comparable to the mobilities of commonly used amorphous organic semiconductors. Also, at all temperatures samples have hysteresis in measured transfer and output characteristics. There are still on-going discussions what causes hysteresis in perovskite films, as the reports mention possible ionic drift, ferroelectric behavior and possible influence of trap states.

Remarkable PCE efficiency of perovskite solar cells is tied with extraordinary perovskite properties such as high absorption coefficient, long charge carrier diffusion length and long charge carrier lifetime, moderate and in cases low charge carrier mobility. The investigations of these exceptional properties are still going on as do the scientific discussions about the origin of these interesting properties. Therefore, all the observations from different perspectives and diverse explanations proposed in the studies lead to vagueness of the nature of defects and charge carriers dynamics in perovskite materials and a simple and detailed understanding of all the processes of charge generation, charge carrier separation and transport is not available at the moment. Looks like the variety and complexity of growing studies about perovskites lie in the interconnection of many film characteristics as: grain boundaries, compositional non-uniformity, interfaces, compatibility and others. More studies are needed in order to better understand charge carrier dynamics and to better improve the performance of perovskite materials.

The majority of this chapter was prepared by mainly using the references **[64, 72, 76, 82, 84, 85]**.

1.5 Organic solar cell (sandwich) structures

Increasing research of the organic semiconductors led to a specific “standardization” of the measured sample structures. A wish to compare measured data between different laboratories and need for a simple manufacturing process brought simple solar cell-sandwich structure where layers are built on top of each other (Fig. 16). Few main components are always found in this type of structures: a transparent substrate, a transparent electrode, an active layer or investigated media, a top metal electrode. The substrate is the main body of the structure giving it physical support and it is the window for the light to go through, thus it has to be transparent to the wavelength that is absorbed by the active layer. Usually, glass is used because it is firm and clear for visible light, but plastic can be used as glass alternative for flexible samples. On top of the transparent substrate lays transparent electrode which has to be compatible with the wavelength of the light used in the experiment and its work function has to be compatible with valence and conduction bands (or LUMO and HOMO) energy levels of the active layer. Probably the most popular transparent electrodes are ITO (indium-tin-oxide) and FTO (fluorine-tin-oxide), because they can be put on the glass with various methods and can be relatively cheaply purchased from many suppliers ready to use. ITO and FTO transparencies in the visible light spectrum are very high **[86-88]**, their work functions are compatible with many commonly used organic semiconductors **[72]** and their sheet resistances are relatively low **[86-88]**. On top of the first electrode an active layer is casted. It is the layer where all the "magic" happens: photons are absorbed, charge is generated, charge carriers are separated and they are transported to the electrodes (Fig. 16). Active layer can be a single organic layer, heterojunction, perovskite layer, multilayered structure, tandem cell structure and more, depending on the experiment and the characteristics investigated. The convenience of the sandwich structure is that the active layer can be casted by using many different simple casting methods usually resulting in different morphologies, thus it gives freedom to use the best possible casting method for the sample. Commonly used methods are dropcasting, spincoating, vacuum evaporation, spraying, inkjet printing and more. The last layer is top metal (usually) electrode. As the transparent electrode, top metal electrode has to be compatible with valence and conduction bands (or LUMO and HOMO) energy levels. One of the most convenient and most used techniques for putting top electrode is evaporation through the pattern mask in vacuum chamber and the most used metals for top electrode are gold, silver, aluminium and copper.

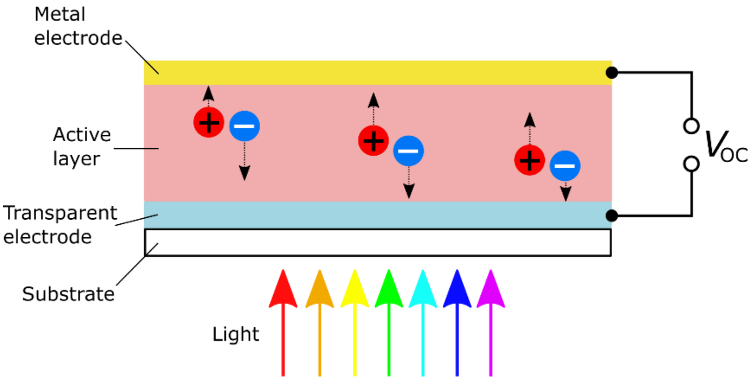

Fig. 16. Schematic view of solar cell (sandwich) structure.

The simplicity of the structure allows different materials and different configurations of the materials to be investigated in the active layer. A good example of bulk heterojunction active layer structures can be seen in Fig. 17. In this example bulk heterojunction of P3HT hole transport polymer and PCBM electron transport material was implemented into two different sandwich structures where each case had difference current direction. This kind of implementation allows to investigate not only key characteristics of solar cell: short circuit current I_{SC}, open circuit voltage V_{OC}, power conversion efficiency, but also optimal ratio of materials in bulk heterojunction, optimal thickness of active layer, recombination rate in bulk heterojunction, which current direction brings better performance, which metal electrodes work better, optimal thicknesses of electron blocking layer and hole blocking layer (PEDOT:PSS and ZnO in this case), which blocking layers work better and others. There are many reports, where optimal configurations of materials are investigated in order to get the best performance **[89-92]**.

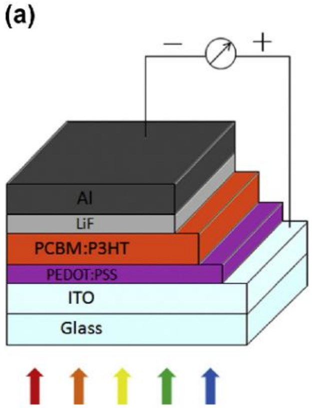
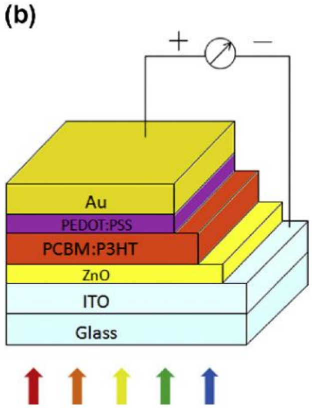

Fig. 17. Schematic view of PCBM:P3HT bulk heterojunction sandwich structures. a) structure with bottom electron blocking layer; b) structure with top electron blocking layer. Adapted from **[93]**.

Similar research approach was applied onto perovskite solar cells once they caught attention of the research labs investigating organic solar cells. Various sandwich structure architectures (see Fig. 18) are tested in the search of the best performance, the best materials, optimal ratio of precursors, optimal compatibility, favorable morphology and others **[94-100]**.

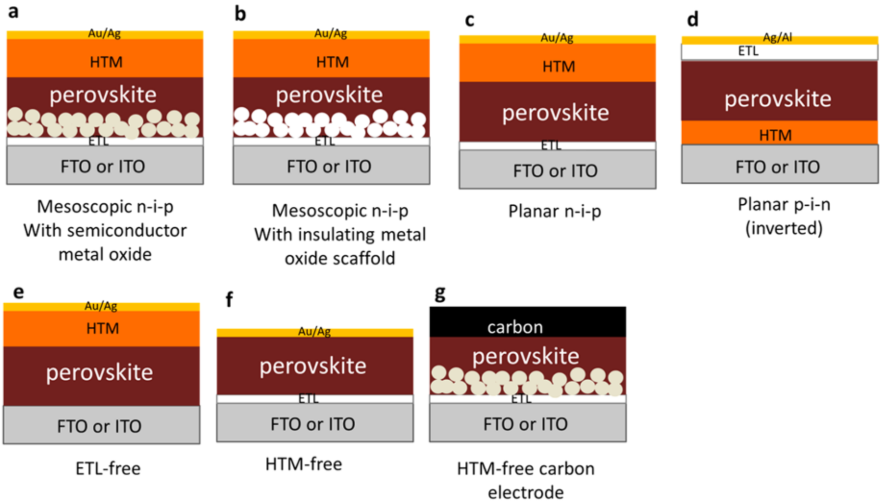

Fig. 18. Examples of possible sandwich structures with perovskite active layer. Adapted from **[72]**.

Studies of structures with blended materials or multilayered structures bring useful information about optimal ratio and thicknesses of the materials to get the best possible characteristics, efficiencies, stabilities. However, investigating single layer structures gives more detailed information about the material itself: possible morphologies at different layer casting methods, charge carrier mobility, recombination rate, characteristics of disorder in the material. These studies expose characteristics important for implementing organic semiconductors in various applications: solar cells, OFETs, OLEDs, sensors **[101-104]**.

1.6 Organic field-effect transistor structures

For the first time organic semiconductor was used as an active layer in the thin film field-effect transistor structure by Tsumura et al. in 1986 **[105]**. After that field-effect transistor structure was employed in numerous studies of the organic semiconductors. Driving forces of the research were few aspects: possibility to create flexible OFETs **[106]**, possible cost-efficient manufacturing process, many different organic materials to choose from. However, for the moment charge carrier mobility and stability of such devices are limiting factors for further integration into products. But the OFET structure became one of the most used structure in the research of organic semiconductors not for creating the best working transistor, but as a very convenient simple structure for the investigation of charge carrier transport. Even commonly used materials in organic solar cells like P3HT and PCBM are used in OFET structures for investigation of charge carrier transport **[31, 107]**.

The main components of OFET structure are a gate electrode, an insulator, an active layer and source-drain electrodes (Fig. 19). The active layer is always separated from gate electrode via insulator, while source and drain electrodes are always in contact with active layer. As a gate electrode can be used almost any metal as it used only to control OFET channel via applied voltage. Insulator layer is very important for OFET performance, because injected charge carriers move near the interface of active layer and insulating layer, thus every defect in insulator can affect morphology of organic semiconductor and also charge carrier transport. As an insulator often are used polymers such as PVA, PMMA, CYTOP and others **[108]**. Also, highly doped silicon wafers with thin silicon dioxide layer on top are frequently used as already made gate/insulator substrates for OFET structure manufacturing **[108-110]**. Planar architecture of OFET enables variation of active layer casting methods. Small molecule organic semiconductors like pentacene can be evaporated directly on top of the insulator layer **[111]**, polymers can be casted via solution-based methods like spincoating, doctor blading, dip coating, spraying, inkjet printing and others **[112, 113]**, but it is important to choose solvents correctly to not dissolve organic insulator if the latter is used. Source and drain electrodes are usually evaporated on top of active layer through patterned mask in vacuum chamber. To have effective injection of charge carriers into the active layer and extraction out of it, metal electrode work function energy has to be chosen accordingly to be compatible with HOMO and LUMO energy levels of the organic semiconductor **[114]**.

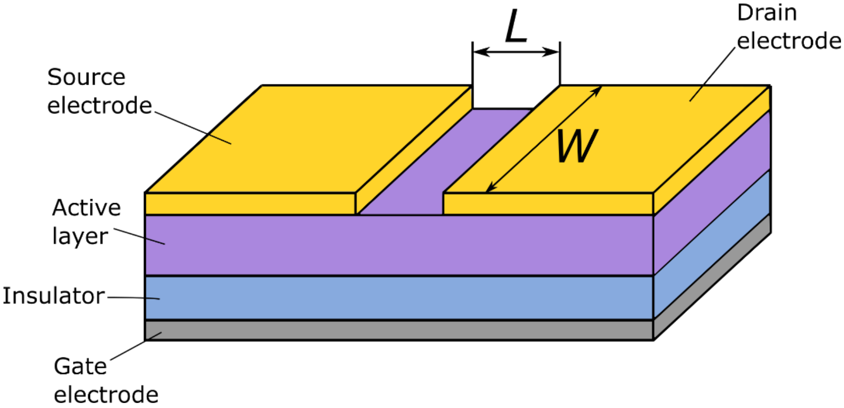

Fig. 19. Schematic view of organic field-effect transistor structure.

Few possible architectures of simple planar OFET structure can be seen in Fig. 20. Structures with SiO_2 layer as the dielectric usually are bottom gate OFET structures, because the silicon wafer acts as substrate giving physical support to the structure and other layers are put on top of it. Organic insulators are usually casted from solutions, thus they can be casted on top of active layer (see Fig. 20 a) and b)) or on top of gate electrode (see Fig. 20 c) and d)). Every architecture has its pros and cons and final one is chosen depending on the experiment and the materials. Highly doped silicon wafers with SiO_2 dielectric on top are often used, because of SiO_2 resistance to all solvents used for dissolving organic semiconductors and because of much simpler manufacturing process during which only single organic layer is casted on the cleaned substrate. However, SiO_2 surface can be modified with, for example, OTS (trichloro(octyl)silane) to improve the interface of the active layer and the dielectric and thus facilitate charge carrier transport **[17, 18, 115]**.

OFET structures with organic dielectric layer require substrate on which layers are built on top of each other. Thus, the usage of separate substrate allows more various architectures (Fig. 20), but the usage of organic dielectric brings its own disadvantages. First, dielectric material must be resistant to the solvent of organic semiconductor and vice versa, if the organic semiconductor layer is casted first. This can be achieved with dielectric polymers which can be modified with UV light or in water soluble polymers like PVA, but it still limits the number of materials which can be used in OFET structures **[116-118]**. Second, organic dielectric layer is usually spincoated so that necessary thickness is achieved and this can cause uneven layer thickness as well as different morphology of the dielectric layer in comparison to thermally grown SiO_2. However, there are many possible organic insulators and layer casting parameters (solution concentration, spincoating parameters) can be tuned accordingly and if chosen correctly they can give better charge carrier transport results in OFET structures than SiO_2 **[108]**.

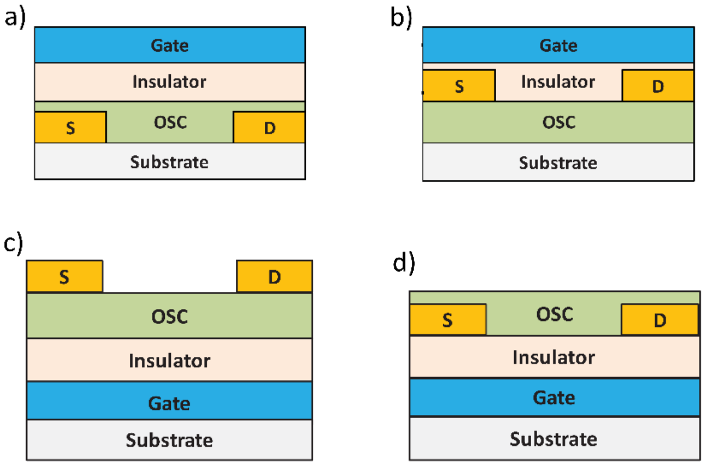

Fig. 20. Schematic view of various OFET structures. a) and b) are structures with top gate electrode; c) and d) are structures with bottom gate electrode. Adapted from **[119]**.

There are no the one most convenient OFET structure and choosing one for the experiment depends on many factors. Besides advantages and drawbacks mentioned above, the structure configurations like the ones in Fig. 20 a) and c) allow to investigate charge carrier transport in two directions: perpendicular to the dielectric direction and parallel to the dielectric direction, unlike the others configurations where charge carrier transport can be investigated in only in parallel to the dielectric direction. Possibility to investigate charge carrier transport in different directions is very convenient, because charge carrier transport is closely tied to the morphology of the layer in organic semiconductors and it could result in anisotropy of charge carrier mobility. Charge carrier transport in perpendicular to the substrate direction can be investigated with i-CELIV technique (more about it in 2nd chapter Experimental).

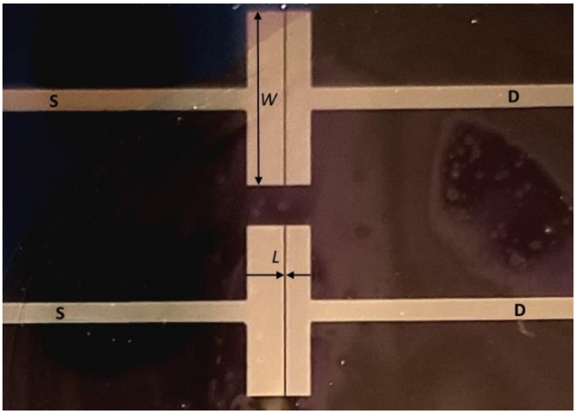

Fig. 21. Top view of OFET structure with bottom gate electrode and source-drain electrodes evaporated on top of organic layer.

Source and drain electrodes have to be formed not only from metal with compatible work function for effective charge injection, but the shape of electrodes is important as well. Capacitance of electrodes must be low for a faster OFET response to applied voltage, but channel width *W* has to be much longer than channel length *L* to have higher current in the channel. Thus, the electrode shape has to be adjusted accordingly to maintain long *W* but with as small electrode area as possible to reduce capacitance. One shape in particular is often used for source and drain electrodes for evaporation through the mask in the vacuum chamber (see Fig. 21).

2. Experimental

In this chapter all the experimental details of this work will be described. This includes the materials used in this work, details of sample fabrication and measurement techniques used in this work.

2.1 Materials

Mostly neat organic semiconductors were used in this work to fabricate the structures for charge carrier transport investigation (Fig. 22). Spiro-MeOTAD is hole transport material commonly used in solar cell application and together with $CH_3NH_3PbI_3$ perovskite were used to fabricate solar cell structures. PCPDTBT hole transport polymer was used as an active material in OFET structures. PBDTTPD hole transport polymer was used as an active material in sandwich and OFET structures.

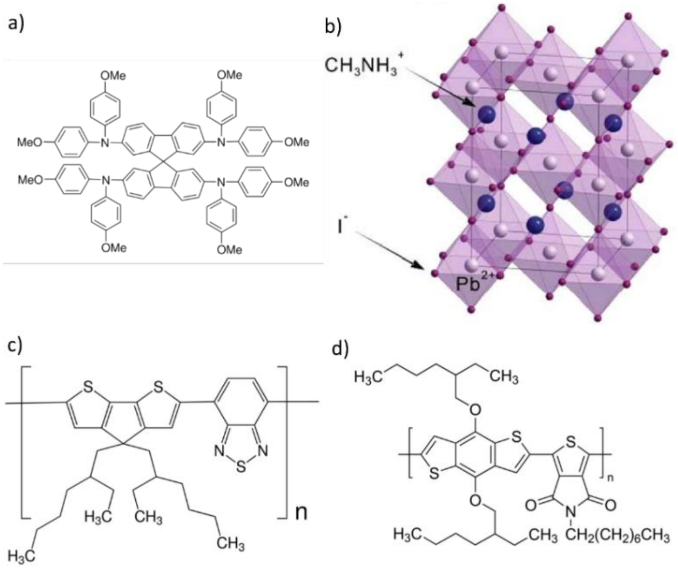

Fig. 22. Schematic view of the materials used in this work. a) Spiro-MeOTAD molecule; b) $CH_3NH_3PbI_3$ perovskite tetragonal lattice; c) PCPDTBT molecule; d) PBDTTPD molecule **[120]**.

2.2 Samples

The solar cell structure with $CH_3NH_3PbI_3$ perovskite layer used in photo-CELIV measurements is shown in Fig. 23. Structures were formed on commercially bought FTO covered glass substrates. Dense titanium dioxide (TiO_2) film of 30 nm was deposited by reactive sputtering method using a metallic titanium target in oxygen atmosphere. On top of TiO_2 perovskite layer was spincoated (1600 rpm for 30 s) from two equimolar solutions of 0.1983 g (1.25 mmole) CH_3NH_3I in 0.25 ml DMF solvent and 0.5785 g (1.25 mmole) PbI_2 in 25 ml DMF solvent which were mixed just before the spincoating.

CH_3NH_3I was prepared as follows: 20 ml of methylamine solution (Ferak 40% w/v) containing 8 g methylamine (257 mmol) was diluted in 80 ml of ethanol. To this solution a hydroiodic acid solution in water (Merck 57% w/v) was added slowly under stirring until the pH of solution turns to acidic (total about 60 ml of hydroiodic acid). The solution was stirred for 2 h at room temperature until the solvents evaporated. The solid remains were put into anhydrous diethylether and filtrated. After washing with anhydrous diethylether, copious amount of CH_3NH_3I white crystals was obtained which were later dried at 60 °C in a vacuum oven overnight.

PbI_2 was prepared as follows: 3.3 g (10 mmol) of $Pb(NO_3)_2$ (Serva anal. grade) were diluted with 50 ml of distilled water. To this solution, a solution of 3.3 g (20 mmol) of KI (Merck Reag. Ph. Eur.) in 50 ml distilled water was added slowly under stirring at room temperature. The obtained golden yellow precipitate was filtered and recrystallized from water to golden yellow crystals. The PbI_2 crystals were dried at 60 °C in a vacuum oven overnight.

On top of perovskite layer Spiro-MeOTAD (purchased from Merck) was used as hole transporting layer. Spiro-MeOTAD was dissolved in CB with the concentration of 75 mg in 0.3 ml and then it was spincoated at 3500 rpm for 20 s. Finally, the top gold electrode (of about 40 nm) was deposited by sputtering under vacuum.

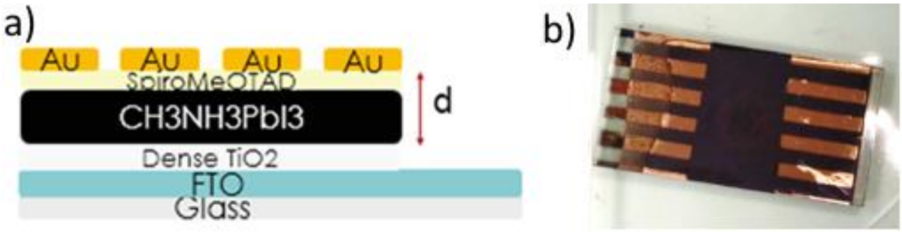

Fig. 23. a) Schematic drawing of solar cell structure with $CH_3NH_3PbI_3$ perovskite layer; b) photo of the solar cell structure sample.

OFET structures with PCPDTBT active layer were fabricated on commercially purchased Si/SiO$_2$ substrates of which SiO$_2$ layer (d_i = 100 nm) was used as dielectric of the OFET structure (Fig. 24). Silicon layer was heavily doped (n type) and used as gate electrode in i-CELIV and OFET current transients measurements. Substrates were cleaned in ultrasonic bath for 15 minutes in each of the solvents: distilled water, acetone and isopropanol and then they were treated by oxygen plasma for two minutes to remove organic residuals and to make surface more hydrophilic for organic layer deposition. PCPDTBT was bought from Sigma-Aldrich in form of dry powder with the average molecular weight M_w 7000-20000 g/mol and it was used as it is, without any additional purification. It was dissolved in chloroform with the concentration of 10 mg/ml under dry nitrogen atmosphere. Chloroform was chosen because of a good PCPDTBT solubility in it **[121]** and high evaporation rate, which are needed to produce thick enough layer for i-CELIV measurements. Solution was spincoated on Si/SiO$_2$ substrate under the same nitrogen atmosphere conditions as solution was made. First spincoating step was 500 rpm for 60 seconds to cast the layer and second step was 2000 rpm for 40 seconds to completely dry the sample and remove residuals of a solvent. These parameters resulted in getting d_s = 160 nm thickness of an active layer. After spincoating the polymer, gold source and drain electrodes with OFET channel length L of 30 μm were formed via evaporation. Structure with top electrodes was required for investigation of hole transport in perpendicular to the substrate direction by i-CELIV. Samples were not annealed prior to measurements.

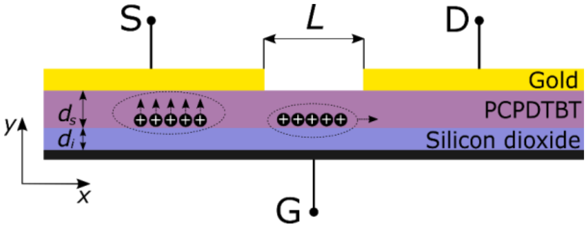

Fig. 24. Schematic view of PCPDTBT OFET structure used in this work.

PBDTTPD was used as an active layer in two types of sample structures: OFET and sandwich. Sandwich structures were made on glass/ITO substrates and OFET structures were made on Si/SiO$_2$ substrates on polished SiO$_2$ (d_i = 100 nm) side (see Fig. 25 and Fig. 26). Silicon layer was heavily doped (n type) and used as gate electrode in OFET structures. All of the substrates were cleaned in ultrasonic bath for 15 minutes in each of the solvents: distilled water, acetone and isopropanol. Cleaned substrates were treated by oxygen plasma for two minutes to remove organic residuals and to make surface more hydrophilic for casting the active layer. After cleaning, part of Si/SiO$_2$ substrates were submerged in 60 °C OTS/toluene solution of 10 mmol concentration for 15 min (OTS purchased from Sigma-Aldrich). After it they were washed in each of the solvents: hexane (for removing additional OTS layers), acetone, isopropanol.

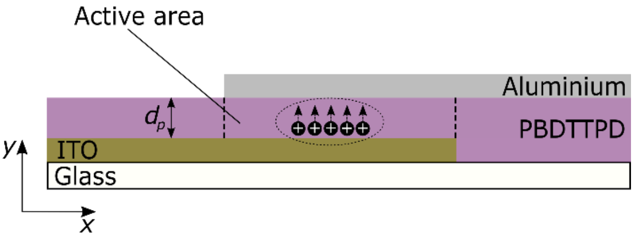

Fig. 25. Schematic drawing of sandwich structure with PBDTTPD active layer used for photo-CELIV and TOF measurements.

PBDTTPD was bought from Sigma-Aldrich in form of dry powder and was used as it is, without any additional purification. For sandwich structures PBDTTPD was dissolved in chlorobenzene with 10 mg/ml concentration. Layer was dropcasted under the dry nitrogen atmosphere conditions and the thickness of layer was $d_p = 1.2$ μm. After deposition aluminum electrodes were formed via thermal evaporation under vacuum.

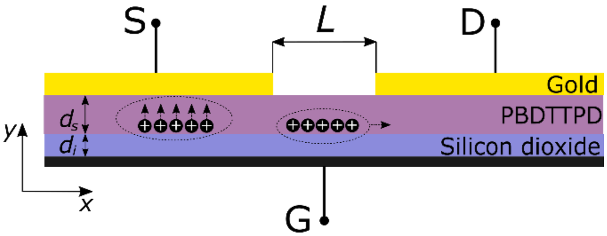

Fig. 26. Schematic drawing of an OFET structure with PBDTTPD active layer employed in our work.

For OFET structures PBDTTPD was dissolved in chloroform with 10 mg/ml concentration. Solution then was spincoated on Si/SiO$_2$ substrates under the dry nitrogen atmosphere conditions. The first spincoating step was 500 rpm for 60 seconds to cast the layer and the second step was 2000 rpm for

40 seconds to completely dry the sample and remove residuals of solvent. These parameters resulted in getting d_s = 135 nm thickness of the active layer. Gold source and drain electrodes were subsequently evaporated, resulting in OFET's channel length L of 30 μm. None of the samples were annealed prior to the measurements.

2.3 Measurement techniques

Together with new and improving materials in the organic semiconductors research field the techniques for investigation of the organic semiconductor properties are improving as well. Different types of structures give possibility to measure the properties of organic material in different configurations of the organic layer, but bring the question of comparison between the gathered results, especially results in different laboratories across the world. Organic layers are very sensitive to manufacturing conditions which may affect the experimental results, but experimental setup and experimental conditions themselves play important role as well. In this chapter the main measurement techniques used in this work will be presented. Advantages and drawbacks of each technique will be explained and compared between them in order to present clear picture how and in what conditions these techniques can be used and what properties can be measured by using them.

2.3.1 Time of Flight

For the first time Time of Flight (TOF) technique was demonstrated by W. E. Spear in 1957 **[122]**. The technique rapidly became one of the most used technique for investigation of moving charge in the non-organic and organic semiconductor layers and it is still used today as simple method to evaluate charge carrier mobility **[123, 124]**. The simplicity of the technique lies in the setup required for the experiment. Short light pulse source, square signal generator and oscilloscope are only needed to conduct an experiment (see Fig. 27). It is important that light source could generate light pulses shorter than charge relaxation time in the material and almost all short pulse lasers today are capable of doing that.

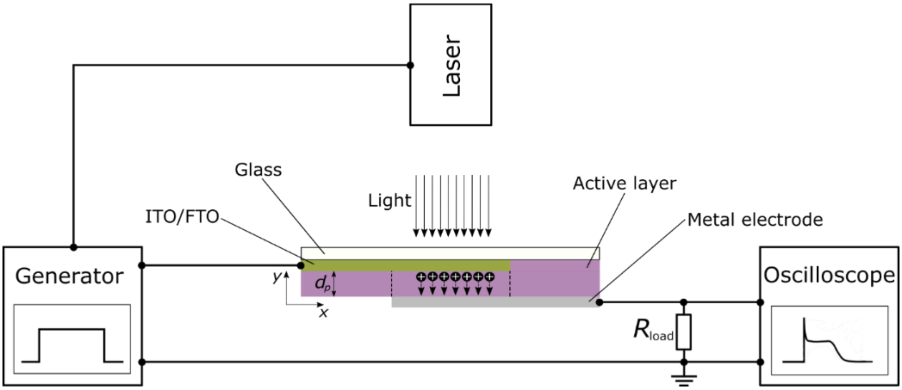

Fig. 27. Experimental setup of TOF technique.

Another important thing for every experiment and every measurement technique are the samples. Every technique measures different parameters of the material and thus the sample must be prepared accordingly to fit guidelines set by the technique. First, at least one electrode must be transparent or semitransparent for the light which is used in the experiment. Second, the sample must be thick enough to have surface light absorption conditions ($\alpha d > 1$) in order to evaluate charge carrier mobility. Thus, we encounter first drawback – TOF technique is unsuitable for the measurements of very thin layers. Usually organic semiconductors have strong absorption, but $\alpha d > 1$ condition is kept when the thickness of the layer is at least few hundred nanometers depending on the material **[125]**. Third, Maxwell's relaxation time τ_σ must be much higher than the transit time t_{tr} of the charge carriers, thus TOF technique is unsuitable for the measurement of relatively conductive materials.

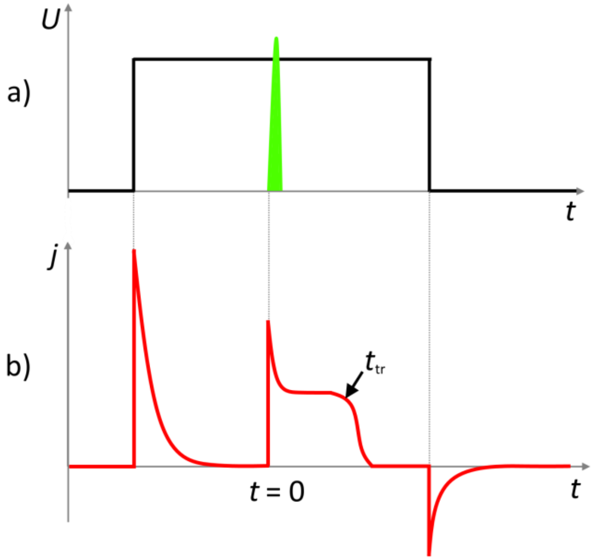

Fig. 28. Theoretical transients of TOF technique. a) Light pulse and square voltage pulse; b) TOF current density transient in the sample.

In the Fig. 28 there are shown theoretical current transient of the TOF technique. After photo excitation charge carriers are generated and they move in the electric field created by the applied square pulse. The advantage of TOF is that it can be conveniently measured hole and electron mobilities just by changing the polarity of the applied square pulse. Generated charge carriers move through the layer and reach the electrode after transit time t_{tr} which can be used for estimation of the mobility:

$$\mu = \frac{d_{\mathrm{p}}^2}{U t_{\mathrm{tr}}} \quad , \tag{2.1}$$

where d_{p} is thickness of the layer and U is voltage applied on the layer.

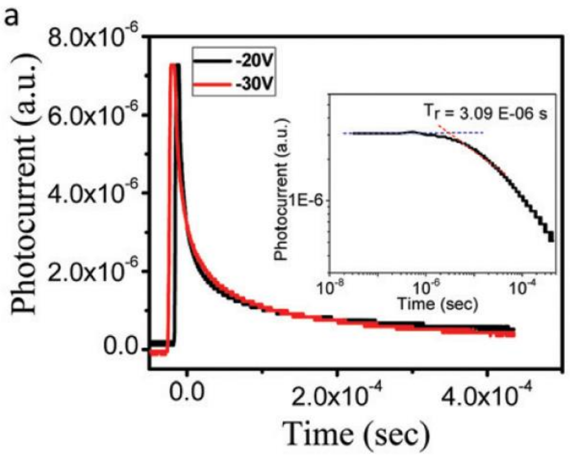

Fig. 29. Photocurrent transients of TOF technique without expressed kink. Inset presents the log-log scale for the finding of t_{tr}. Adapted from **[124]**.

Usually, the kink in the current transient at t_{tr} is easily visible and it facilitates finding transit time, but in case of very dispersive charge carrier transport nature in the material the kink could be not present and then transit time t_{tr} can be found in log(j)-log(t) coordinates (Fig. 29).

2.3.2 Photo-CELIV

The first ever technique of charge extraction by linearly increasing voltage (CELIV) was demonstrated by A. Petravičius et al. in 1975 as an alternative to TOF technique **[126]**. Later on, it was shown that CELIV technique is fully compatible and very convenient to investigate charge carrier transport in micro crystalline silicon layers and π-conjugated polymer layers **[61, 127]**. Modified CELIV technique was applied to investigate transport and recombination of the charge carriers generated with light pulse in light sensitive materials and it is called photo-CELIV **[55, 128]**. The measurement setup is very similar to the one of TOF: only generator, oscilloscope and light source are needed to perform the experiments (see Fig. 30). Light source and generator are synchronized in the way that the delay time t_{del} between the light pulse and ramp voltage could be altered to investigate time dependent charge carrier mobility and the recombination photogenerated charge carriers.

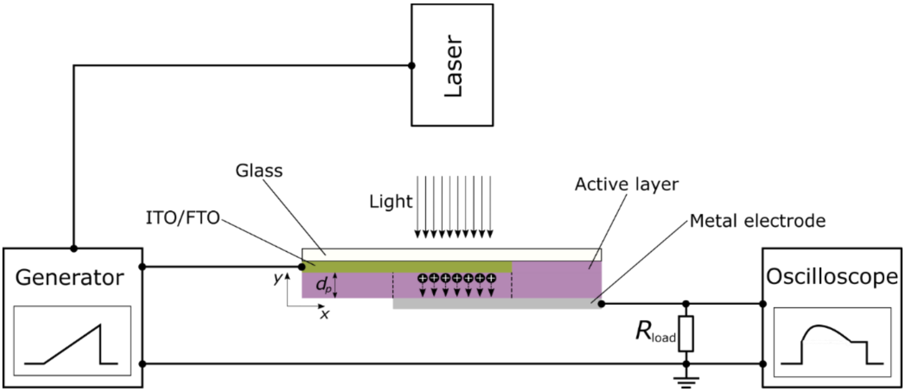

Fig. 30. Experimental setup of photo-CELIV technique.

The structure of the sample measured by photo-CELIV technique contains few layers as shown in Fig. 30. The simplest structure is of the single active layer between two electrodes and we call it sandwich structure. It has a geometrical capacitance of:

$$C = \frac{\varepsilon_0 \varepsilon_s S}{d_p} \tag{2.2}$$

or

$$C = \frac{Q}{U} \quad , \tag{2.3}$$

where S is area of overlapping electrodes, ε_s and ε_0 are dielectric permitivitties of active layer and vacuum respectively, d_p is the thickness of the active layer, Q is charge in the active layer.

By combining the two equation we get:

$$Q = \frac{U \varepsilon_0 \varepsilon_s S}{d_p} \quad . \tag{2.4}$$

Together with resistor R_{load} sandwich structure makes differentiating *RC* circuit which has a response of square shaped current density transient to applied ramp voltage (see Fig. 31). Initial current density step $j(0)$ of the sandwich structure can be expressed:

$$j(0)=\frac{I}{S}=\frac{1}{S}\frac{dQ}{dt}=\frac{1}{S}\frac{d(U\varepsilon_0\varepsilon_s S/d_\mathrm{p})}{dt}=\frac{\varepsilon_0\varepsilon_s}{d_\mathrm{p}}\frac{dU}{dt}=\frac{\varepsilon_0\varepsilon_s A}{d_\mathrm{p}}=\frac{CA}{S}\quad, \tag{2.5}$$

where I is the current and A is the voltage increment rate of the ramp pulse.

If light pulse is absorbed in the surface of the active layer ($\alpha d > 1$), then photogenerated charge carriers are extracted throughout all the thickness d_p when ramp voltage is applied.

$$\begin{gathered} d_\mathrm{p}=\int_0^{t_{tr}} v_{dr}\,dt=\int_0^{t_{tr}}\frac{\mu U}{d_\mathrm{p}}dt=\frac{\mu}{d_\mathrm{p}}\int_0^{t_{tr}}U\,dt=\frac{\mu}{d_\mathrm{p}}\int_0^{t_{tr}}At\,dt= \\ =\frac{\mu A}{d_\mathrm{p}}\int_0^{t_{tr}}t\,dt=\frac{\mu A t_{tr}^2}{2d_\mathrm{p}} \end{gathered}\quad, \tag{2.6}$$

where μ is charge carrier mobility, v_dr is charge carrier drift speed, t_tr is transit time of charge carriers.

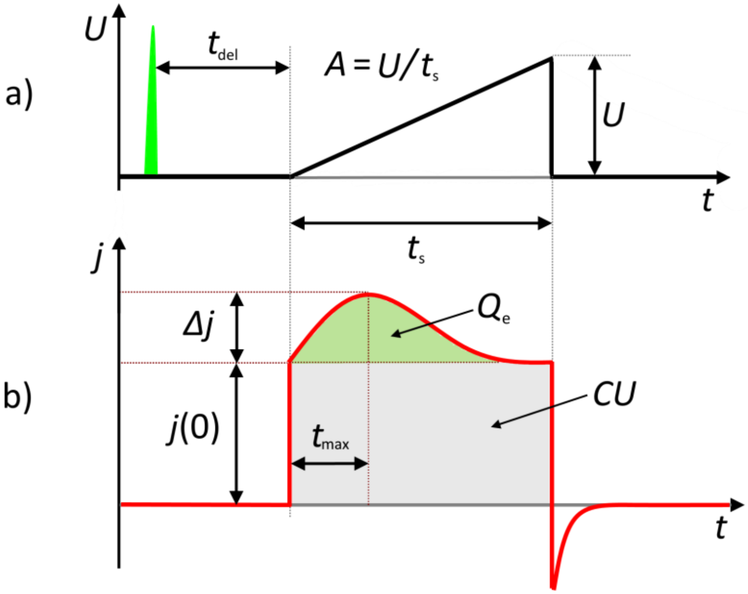

Fig. 31. Theoretical photo-CELIV transients. a) Light pulse and ramp voltage; b) photo-CELIV current density transient of the sample.

Current density transients of photo-CELIV have extraction current density Δj on top of the initial step $j(0)$. Extracted charge forms a peak in extraction current density at a time $t_{\max}$ which is equal to charge carrier transit time t_{tr}. Then eq. (2.6) can be rewritten and charge carrier mobility can be found:

$$\mu = \frac{2d_{\mathrm{p}}^2}{At_{\max}^2} \quad . \tag{2.7}$$

Equation (2.7) is valid only in certain case of experimental conditions. As more data was gathered using photo-CELIV technique during the years of experiments, more accurate equations were necessary for certain cases of experimental conditions (for example, absorption profile of the active layer). Theoretical calculations on various experimental conditions of photo-CELIV together with experimental results were made in order to make corrections in mobility calculation using extraction current density peak time $t_{\max}$ **[128]**. It was shown that equation (2.7) can be rewritten as:

$$\mu = K^2 \frac{2d_{\mathrm{p}}^2}{At_{\max}^2\left(1 + 0.36\left(\frac{\Delta j}{j(0)}\right)\right)} \quad , \tag{2.8}$$

where $K = t_{\max}/t_{\mathrm{tr}}$ is the correction factor. Depending on absorption coefficient αd of the active layer, K values vary from $1/\sqrt{3}$ ($\alpha d < 1$) to 1 ($\alpha d > 1$) (Fig. 32).

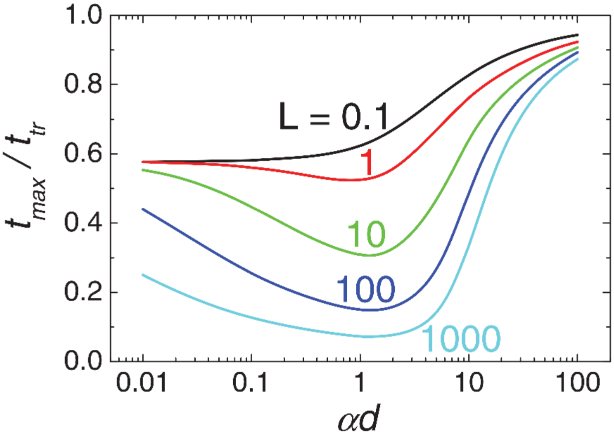

Fig. 32. Theoretical calculation of correction factor K dependence on absorption coefficient αd for various light pulse intensities. Adapted from **[128]**.

One of the biggest photo-CELIV advantages over TOF technique is possibility to measure relatively conductive materials. In TOF charge relaxation time τ_σ of the measured material has to be longer than the transit time t_{tr}, otherwise charge carriers cause electric field redistribution in the layer. In photo-CELIV τ_σ can be found from extraction transients at a time when current density reaches double the value of $j(0)$. Then using τ_σ value charge carrier mobility can be found accordingly:

$$\mu = \frac{\tau_\sigma d_{\mathrm{p}}^2}{t_{\mathrm{max}}^3 A} \quad . \tag{2.9}$$

Another useful photo-CELIV feature is the possible variation of time t_{del} between the light pulse and the extraction voltage. By variating t_{del}, charge carrier mobility dependence on time can be estimated. The time dependent charge carrier mobility measurements are important for disordered materials, because light excitation provides a lot of energy for charge carriers and they lose it through relaxation in DOS during the transport and during t_{del} which can ultimately affect their mobility and recombination rate.

For the investigation of photogenerated charge carrier recombination rate in the sample, photogenerated charge decay experiment by using photo-CELIV can be conducted. Extracted charge Q_e can be found by subtracting current density transient without light excitation from the one with light excitation $j - j(0) = \Delta j$. By integrating the area of the transient, we get extracted charge carrier density n and by increasing t_{del} we let charge carriers to recombine and we get the decay of extracted charge density $n(t)$. Bimolecular recombination coefficient B then can be found by fitting the formula:

$$n(t) = \frac{1}{Bt + \frac{1}{n(0)}} \tag{2.10}$$

onto the experimentally obtained decay of extracted charge carrier density.

2.3.3 i-CELIV

The measurement techniques mentioned above are dedicated to investigate sandwich structures and solar cell structures, where the active layer is between the two electrodes. One of the most popular and convenient structures for investigation of charge carrier transport in thin layers are OFET structures and MIS (metal-insulator-semiconductor) structures, containing dielectric layer. For this kind of structures, a technique called i-CELIV was demonstrated by G. Juška et al. in 2012 **[129]**. Technique is used to measure charge carrier mobility in perpendicular to the substrate (dielectric layer) direction (y direction in Fig. 33).

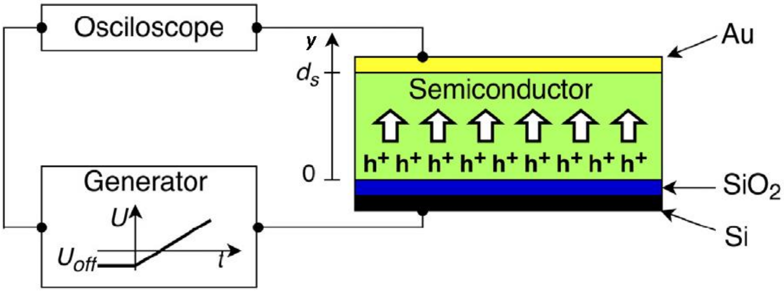

Fig. 33. MIS structure with hole transporting active layer and i-CELIV setup. Adapted from **[130]**.

After applying U_{off} voltage (see Fig. 33 and Fig. 34) to the MIS structure or to the OFET structure between gate and source (or gate and drain), charge carriers will drift through the active layer and will accumulate near dielectric layer. At the calm state the distribution of the charge carriers can be expressed by:

$$j = \mu kT\frac{dp(x)}{dx} + ep(x)\mu F(x) = 0 \quad , \tag{2.11}$$

where μ is hole mobility, k is Boltzmann constant, p is density of charge carriers, F is electric field, T is temperature and e is elementary charge.

By having Gauss' law:

$$\frac{dF(x)}{dx} = \frac{ep(x)}{\varepsilon_s\varepsilon_0} \quad , \tag{2.12}$$

where ε_0 and ε_s are dielectric permittivities of vacuum and semiconductor layer accordingly, we can rewrite the equation:

$$\frac{d^2F(x)}{dx^2} + \frac{e}{kT}F(x)\frac{dF(x)}{dx} = 0 \qquad . \qquad (2.13)$$

Then we can find solutions:

$$F(x) = \left(\frac{d_\mathrm{i}}{U_\mathrm{off}} + \frac{e}{2kT}x\right)^{-1} \qquad (2.14)$$

and

$$p(x) = p(0)\left(1 + \frac{eU_\mathrm{off}x}{2kTd_\mathrm{i}}\right)^{-2} \qquad , \qquad (2.15)$$

where d_i is the thickness of the dielectric layer.

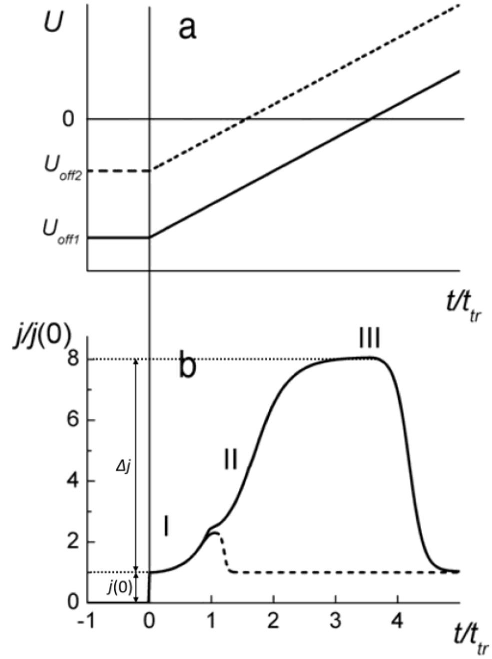

Fig. 34. Applied voltage in i-CELIV technique (a) and theoretical current density extraction transients (b). Adapted from **[129]**.

When $eU_\mathrm{off} >> kT$ and when the capacity of the dielectric layer is higher the capacity of the active layer, charge carriers will accumulate near the dielectric surface. This charge reservoir can be extracted with the ramp pulse which has voltage increment speed $A = dU/dt$. Space charge limited current (SCLS) density of the charge carriers can be expressed by:

$$j(t) = e\mu p(x,t) + \varepsilon_s\varepsilon_0 \frac{dF(x,t)}{dt} \quad . \tag{2.16}$$

To simplify the equation, we average SCLC transient in the active layer within the coordinates $0<x<d_s$ till the time t_{sc} (which represents the time needed for charge carriers to reach the opposite electrode) with given conditions $F = 0$ and $x = 0$:

$$j(t) = \frac{\varepsilon_s\varepsilon_0 A}{d_s} + \frac{\varepsilon_s\varepsilon_0\mu}{2d_s}F^2(d_s,t) = \varepsilon_s\varepsilon_0\frac{dF(d_s,t)}{dt} \quad , \tag{2.17}$$

where d_s is the thickness of the active layer.

As Fig. 34 (b) shows there are three distinct regions of the extraction current density transient of the i-CELIV technique. Solving eq. (2.17) in the I region gives solutions:

$$\frac{\Delta j(t)}{j(0)} = \tan^2\left(\frac{t}{t_{tr}}\right) \quad , \tag{2.18}$$

$$t_{sc} = 0.92 t_{tr} \quad , \tag{2.19}$$

where $j(0)$ is displacement current density, Δj is conductivity current density and t_{tr} is charge carriers transit time. If we have small charge extraction case, then:

$$t_{tr} = d_s\sqrt{\frac{2}{\mu A}\left(1 + \frac{\varepsilon_s d_i}{\varepsilon_i d_s}\right)} \quad , \tag{2.20}$$

where ε_i is dielectric permittivity of dielectric layer.

Then in the II region (Fig. 34 (b)) of extraction current density transient we will have:

$$\frac{\Delta j(t)}{j(0)} = \frac{9}{4}\frac{t^2}{t_{tr}^2} \quad . \tag{2.21}$$

Extraction current will always saturate to the charging current of dielectric layer capacitance C_i (region III in Fig. 34 (b)) and we get current density:

$$j_{\mathrm{sat}} = \varepsilon_{\mathrm{i}}\varepsilon_0 A/d_{\mathrm{i}} \quad . \tag{2.22}$$

If all of the charge reservoir is extracted, the current will decrease to its initial displacement current value $j(0)$.

When small charge is extracted ($\Delta j \leq j(0)$) the peak value of extraction current will occur at time t_{tr} (see Fig. 34 (b) dashed line) and charge carrier mobility can be calculated using eq. (2.20). When charge reservoir is bigger than the one in the electrodes at the time t_{tr}, we have SCLC conditions and current transient follows eq. (2.18). Current transient kink separating I and II regions in the extraction current (Fig. 34 (b)) usually is not visible due to dispersive transport nature of the organic semiconductors. In case of $\Delta j >> j(0)$ it is convenient to choose time t_1 for mobility calculation when current density reaches double the value of the initial step $j(0)$ (see Fig. 35):

$$t_1 = \frac{\pi}{4} t_{\mathrm{tr}} \quad . \tag{2.23}$$

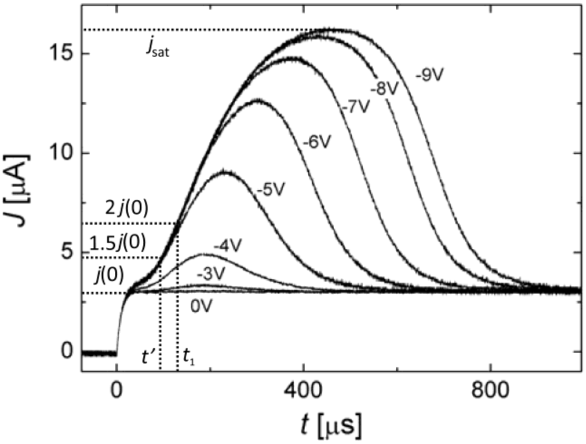

Fig. 35. Experimental i-CELIV current density transients with different injection voltages of structure with MEH-PPV active layer. Adapted from **[129]**.

If Δj is comparable to $j(0)$ (which usually means that the thickness of active layer is similar to the thickness of the dielectric layer), then time t_1 is not suitable to calculate mobility, because at that time started saturation of the transient causes inaccuracy in finding transit time of the charge carriers. In this case it is more convenient to choose time *t*' when current density reaches 1.5 of its initial value $j(0)$ (see Fig. 35). Transit time then can be found:

$$t' = \tan^{-1}\left(\frac{1}{\sqrt{2}}\right) t_{\mathrm{tr}} \quad . \tag{2.24}$$

In i-CELIV technique current density transients give information about geometrical capacitance of the measured sample $j(0) = C_g A$. Using ratio of the two capacitances (the active layer and the dielectric layer) we can estimate the thickness of the active layer without any additional measurements:

$$d_{\mathrm{s}} = \varepsilon_0 \varepsilon_{\mathrm{s}} A \left(\frac{1}{j(0)} - \frac{1}{j_{\mathrm{sat}}}\right) \quad . \tag{2.25}$$

2.3.4 OFET current transients

The first paper reporting delay time t_d of the drain current I_D after square voltage pulse in MOS (metal-oxide-semiconductor) transistors was published in 1969 **[131]**. Later on, this technique was conveniently applied in the research of thin films of organic semiconductors by employing them in OFET structures **[132-135]**. The technique can be used to investigate charge carriers moving along dielectric layer near the interface of dielectric and organic layers (x direction in Fig. 36 a)).

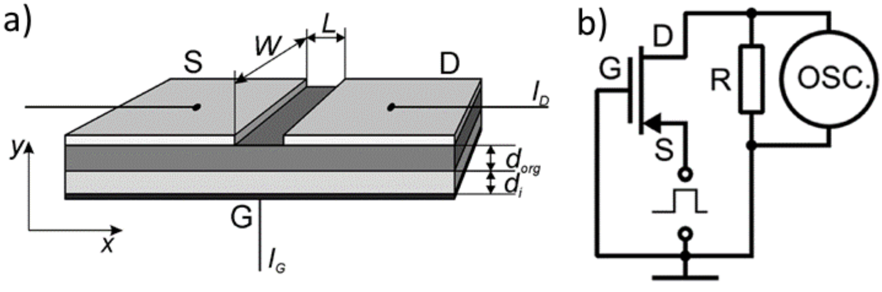

Fig. 36. Schematic view of OFET device structure (a) and of OFET current transients technique setup (b). Adapted from **[135, 136]**.

When field-effect transistor gate electrode is grounded and drain electrode is grounded via load resistor (Fig. 36 b)**)**, voltage step applied to source electrode will charge gate capacitance with the current accordingly:

$$I_{\mathrm{D}}(x,t) = \rho(x,t)\mu F(x,t)W \quad , \tag{2.26}$$

where $\rho(x, t)$ is charge surface density in the channel, $F(x, t)$ is x-component of electric field, W is width of the channel and μ is charge carrier mobility. The channel is formed by injected charge carriers from the source electrode. Then:

$$\rho(x,t) = \frac{\varepsilon_{\mathrm{i}}\varepsilon_0}{d_{\mathrm{i}}}U(x,t) \quad , \tag{2.27}$$

where $U(x, t)$ is electric potential, ε_{i} and ε_0 are dielectric and vacuum permittivities, d_{i} is thickness of the dielectric layer. From continuity equation:

$$\frac{d\rho(x,t)}{dt} = -\frac{dj_{\mathrm{D}}(x,t)}{dx} = -\mu\frac{d}{dt}\big(\rho(x,t)F(x,t)\big) \quad , \tag{2.28}$$

where $j_{\mathrm{D}}(x, t)$ is current density in the channel. After combining two equations we get:

$$\mu\frac{d}{dx}\left(U\frac{dU}{dx}\right) = \frac{dU}{dt} \quad . \tag{2.29}$$

For convenience we can normalize the variables: $x^* = x/L$, $t^* = t\mu U_{\mathrm{SD}}/L^2$, $U^* = U/U_{\mathrm{SD}}$. Therefore, we can rewrite the equation:

$$\frac{1}{2}\frac{d^2U^{*2}}{dx^{*2}} = \frac{dU^*}{dt^*} \quad . \tag{2.30}$$

Numerical solution of eq. (2.30) gives spatial distribution of the potential $U^*(x)$ at various time moments (see Fig. 37 (b)) by using the initial condition $U^*(0,0) = 1$. Drain current in the channel is shown in Fig. 37 (a). Time t_{d} at which charge carriers reach the drain can be used to evaluate the charge carrier mobility along the channel:

$$\mu = 0.38\frac{L^2}{t_{\mathrm{d}}U_{\mathrm{SD}}} \quad . \tag{2.31}$$

Charge carrier mobility obtained from eq. (2.31) represents mobility in low charge carrier density conditions, because mobility is calculated with the time t_{d} when first charge carriers reach drain electrode and their density in OFET channel is still low.

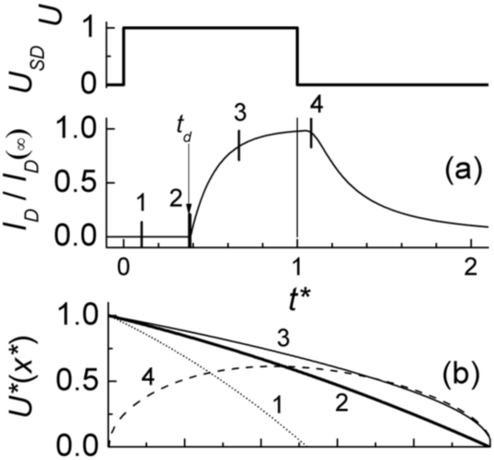

Fig. 37. Theoretical calculations of voltage pulse applied between source and drain. Current transient in the channel (a), the distribution of the potential U^* (b) at various time moments indicated in (a). Adapted from **[135]**.

OFET current transients technique is convenient for investigating field-effect transistor structures because it gives saturated current I_{D} value which can be used for mobility estimation as well. When current reaches its saturated value (see Fig. 37 (a) part 4) at a certain applied voltage, charge carrier mobility can be calculated:

$$\mu = \frac{d_{\mathrm{i}}L}{\varepsilon_{\mathrm{i}}\varepsilon_0 U_{\mathrm{SD}}W}\frac{\partial I_{\mathrm{D}}}{\partial U_{\mathrm{GS}}} \quad , \tag{2.32}$$

where U_{GS} is the voltage between the source and the gate. With saturated I_{D} value we have high charge carriers density condition, thus mobility obtained from eq. (2.32) represents mobility in high charge carrier density condition.

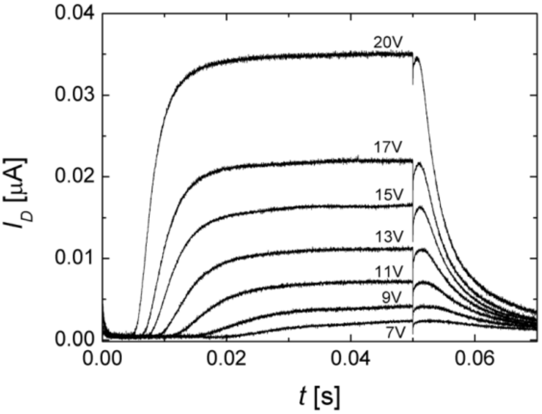

Fig. 38. Experimental drain current transients for different applied voltages U_{SD} of RR-P3HT OFET structures. Adapted from **[135]**.

Fig. 38 shows experimental current transients at different source-drain voltages applied in RR-P3HT layers. It can clearly be seen how channel opening time t_d and saturated drain current I_D correspond with increasing voltage.

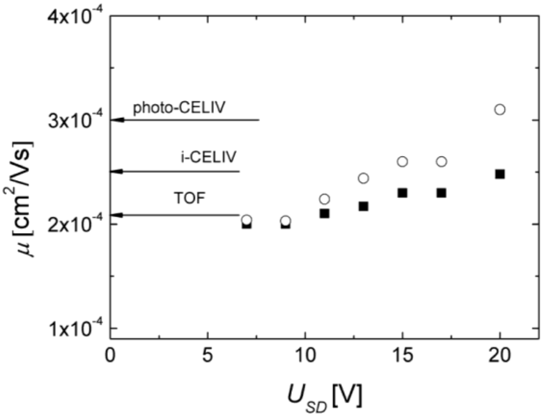

Fig. 39. Hole drift mobility dependence on applied source-drain voltage. Solid squares represent hole mobility obtained from channel opening time t_d, open circles represent hole mobility obtained from saturated drain current, arrows represent hole mobility obtained by TOF, i-CELIV and photo-CELIV techniques. Adapted from **[135]**.

Juška et al. **[135]** compared hole mobility obtained by OFET current transients technique with hole mobility obtained by other techniques in RR-

P3HT layers (see Fig. 39) in different directions (x direction and y direction in Fig. 36). Experimental results let to assume that OFET current transients technique is convenient and reliable technique for charge carrier transport investigation in the thin film organic layers.

3. Experimental results and discussion

3.1 Charge carrier transport in $CH_3NH_3PbI_3$ perovskite solar cell structures

Perovskites took organic solar cells research field with the storm (Fig. 2), but clear understanding about charge transport in the perovskites is still lacking. With every new publication and every new bit of information in this field a new block in the road towards clear understanding and more efficient solar cells is built.

Several studies have demonstrated that halide perovskites exhibit long charge carrier diffusion length **[78, 79, 81]**. $CH_3NH_3PbI_3$ (or MAPbI) perovskite layers prepared according to the recipe described in 2.2 chapter exhibit very long narrow crystals (longer than 200 µm, see Fig. 40 c)). Long diffusion lengths can then be explained by MAPbI perovskite ability to form extremely long crystals. However, in fig 41 b) there can be clearly seen polycrystal structure of the same layer. This type of structure, where on top of polycrystal perovskite base there are long narrow crystals, has uneven surface and it could affect layers deposited on top of it, as it can be seen in Fig. 40 d). Spiro-MeOTAD layer deposited on top of perovskite layer exposes how uneven is the surface of perovskite, therefore it causes uneven Spiro-MeOTAD deposition as well.

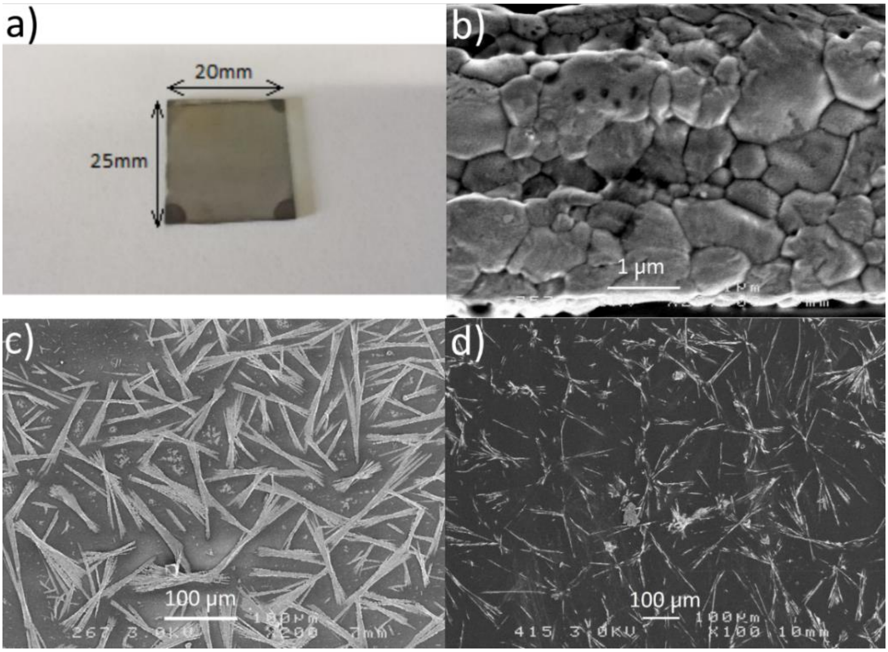

Fig. 40. $MAPbI_3$ perovskite film on glass substrate: a) sample photo; b) SEM image of the side cut of the perovskite film; c) SEM image of the top of perovskite film; d) SEM image of the top of the perovskite film after Spiro-OMeTAD deposition.

It was reported before that the methylammonium lead iodide ($MAPbI_3$) perovskite exists in the cubic Pm3m phase at high temperature above 330 K, below which it undergoes a phase transition to the tetragonal I4/mcm phase and then to the orthorhombic Pnma phase below 170 K **[12]**. The differences between the tetragonal and cubic phases are slight rotation of PbI_6 octahedra along the c-axis and a small energy levels difference. The XRD spectra of cubic and tetragonal phases are similar with slight differences that consist mainly from splitting of the peaks 100 and 200 of cubic phase to the 002, 110 and 004, 220 respectively of the tetragonal phase. Moreover, tetragonal phase exhibits two new peaks: 211 and 213. The most noticeable trait to distinguish the two mentioned peaks in XRD spectrum is minor diffraction from the (211) plane at $2\theta \sim 23.5°$.

Further investigation of $CH_3NH_3PbI_3$ layer was conducted using X-ray diffraction (see Fig. 41). The presence of a peak at $2\theta = 23.68°$ in the XRD spectrum indicates the tetragonal I4/mcm phase. Furthermore, the peak at $2\theta = 14.29°$ can be deconvoluted into two components at 14.14° and 14.29° attributed to the 002 and 110 diffractions respectively **[137]**. The XRD spectra of $CH_3NH_3PbI_3$ films on different substrates (glass, FTO, and TiO_2) confirm the tetragonal 3D structure and the space group I4/mcm. No peaks of PbI_2 are observed indicating that there is no excess of PbI_2 and the reaction of perovskite formation was fully completed.

The increase of the intensity of some peaks of XRD spectra in the perovskite film deposited on dense TiO_2 film indicates a better crystallization in comparison to the films deposited on FTO or glass. The crystallite size may influence the charge carrier transport as a better crystallization and larger crystallite size are usually tied with more favorable conditions for charge carrier transport.

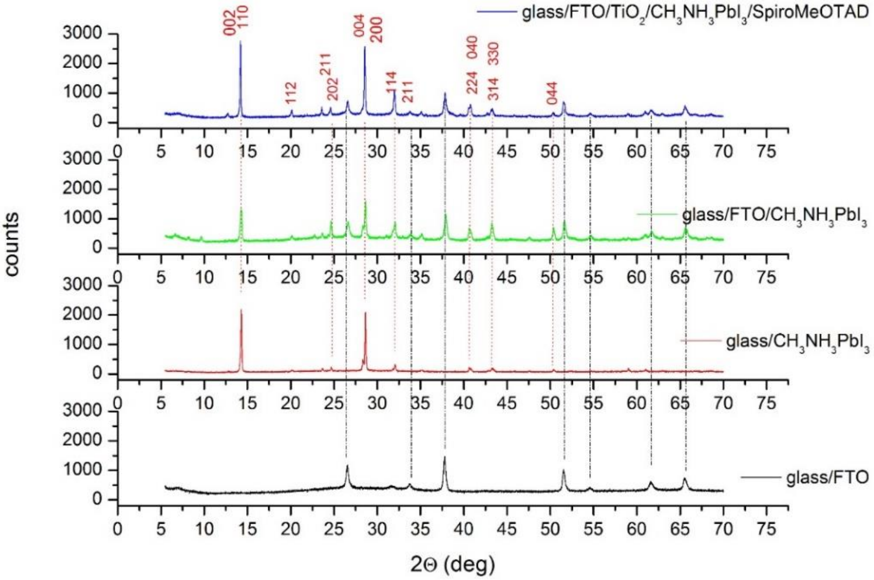

Fig. 41. XRD spectra of $MAPbI_3$ thin films deposited on various surfaces. The XRD spectrum of glass/FTO substrate is also given for reference.

Further investigation of $MAPbI_3$ perovskite solar cell structure (see Fig. 23 a)) was focused on charge carrier transport and it was conducted by using photo-CELIV technique. After applying ramp voltage pulse, it was observed that perovskite solar cell structure exhibit conductivity noticeable in the shape of current density transient. From obtained current density transient Maxwell's relaxation time τ_σ was estimated as it is the moment, when current density reaches double the value of the initial capacitance step $j(0)$ (see Fig. 42).

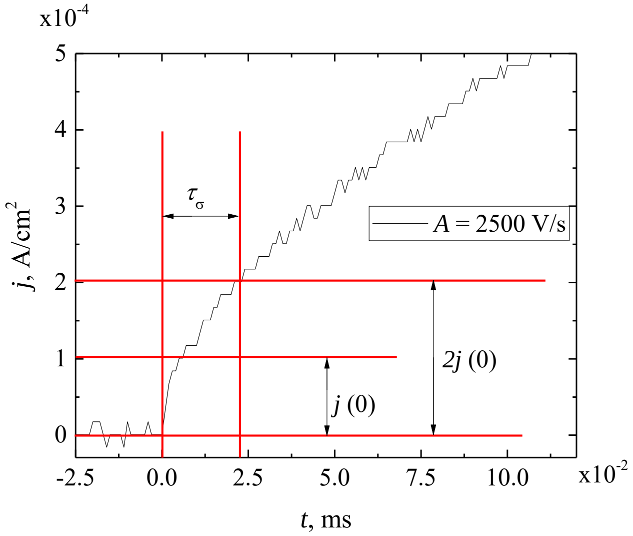

Fig. 42. Zoomed in beginning of photo-CELIV current density transient of $MAPbI_3$ perovskite solar cell structure.

$MAPbI_3$ perovskite has a strong absorption for $\lambda = 532$ nm **[71]** laser light which was used in Photo-CELIV experiment. The thickness of perovskite layer and Spiro-OMeTAD layer in the sample was $d = 1.2$ µm, therefore absorption profile of the solar cell structure was $\alpha d \sim 9.6$. This indicates that charge carriers are generated in the surface of perovskite layer and that extracted charge carriers travel the whole distance of $d = 1.2$ µm. The applied ramp voltage pulse polarity was chosen accordingly to extract holes through top gold electrode.

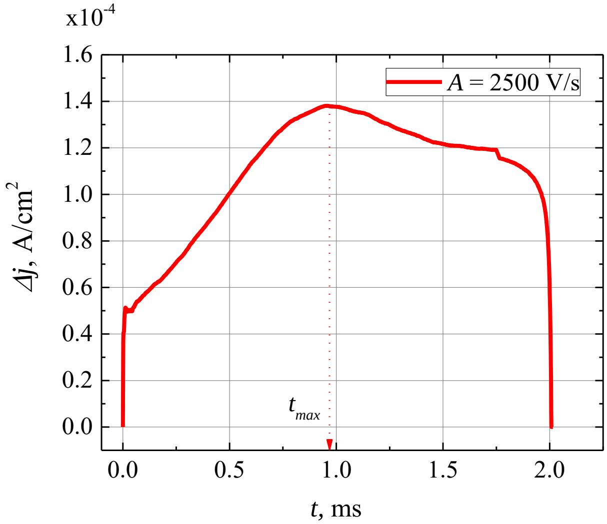

Fig. 43. Photo-CELIV current density transient *Δj* of $MAPbI_3$ perovskite solar cell structure.

Fig. 43 depicts photo-CELIV current density transient $\Delta j = j - j(0)$ at $A = 2500$ V/s. Transit time of holes was determined from the moment $t_{\max}$ when photogenerated current density value *Δj* reaches its peak value. Hole mobility was calculated by using eq. (2.9), because the shape of current density transient indicated conductivity of the measured layer. The obtained photo-CELIV hole mobility values were from $\mu = 5.2*10^{-7}$ cm^2/Vs to $\mu = 8.5*10^{-7}$ cm^2/Vs at different ramp voltage pulse increment rates *A* (Fig. 44). Hole mobility in single Spiro-OMeTAD material was previously reported with the values between $\mu = 1.69*10^{-6}$ cm^2/Vs and $\mu = 4*10^{-5}$ cm^2/Vs, where higher values were obtained in the spiro-OMeTAD layers with higher order. **[138, 139]**.

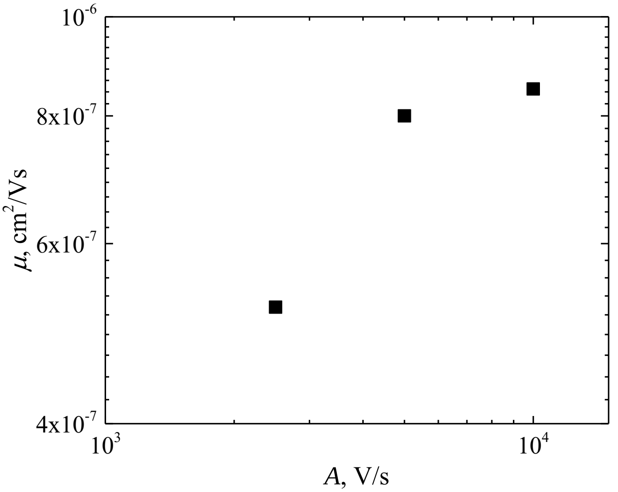

Fig. 44. Hole mobility in $CH_3NH_3PbI_3$ perovskite and Spiro-OMeTAD layers obtained by photo-CELIV technique at few different voltage increment rates *A*.

Hole mobility in $CH_3NH_3PbI_3$ perovskite varies greatly with hole mobilities reaching 500-800 cm^2/Vs in theoretical calculations of perovskite crystal structure, but rapidly decreasing in experimental results at room temperatures where hole mobility can be as low as $4.8*10^{-6}$ cm^2/Vs in perovskite FET configuration, as was discussed in 1.4 chapter of this thesis. Therefore, hole mobility strongly depends on the morphology of the perovskite layer.

In this work hole mobility in $CH_3NH_3PbI_3$ perovskite and Spiro-OMeTAD layers together was $\mu = 8.5*10^{-7}$ cm^2/Vs. Lower hole mobility than the ones reported in other studies in this case can be attributed to few sources presented in this work: the disorder of Spiro-OMeTAD layer, disorder and grain boundaries of polycrystalline perovskite film and the interface between perovskite nanowires and Spiro-MeOTAD layer (see Fig. 40). These unfavorable features of layers morphology increased density of trap states and therefore reduced hole mobility.

3.2 Investigation of anisotropy of charge carrier transport in PCPDTBT field-effect transistor structures

In this work PCPDTBT OFET structures were fabricated with top source-drain electrodes to enable measurements of charge carrier transport in two directions: perpendicular and parallel to the substrate (dielectric layer acts as a substrate in this case). For the investigation of charge carrier transport in perpendicular to the substrate direction i-CELIV technique was used and OFET current transients technique was used for the investigation of charge carrier transport in parallel to the substrate direction. Also, charge carrier transport dependence on temperature was measured to investigate energetic disorder in the layers. Experimental setup used in the charge carrier mobility measurements allows to measure mobilities at the temperatures up to 200 °C. PCPDTBT material is often used as hole transport material in bulk heterojunctions with PCBM **[15, 16]**, showing the importance of hole transport investigation in this material, therefore in OFET current transients and i-CELIV measurements polarity of injecting voltages were chosen accordingly to inject holes into the layer and to study hole transport.

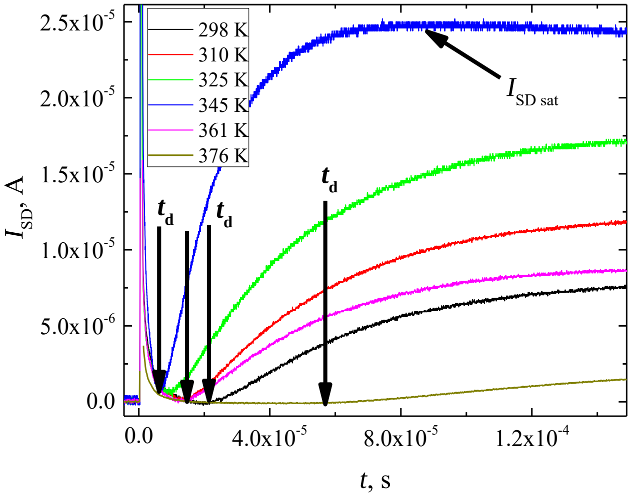

Fig. 45. PCPDTBT OFET structure current transients at different temperatures (obtained from OFET current transient technique).

In Fig. 45 there are presented few typical current transients of OFET structure with PCPDTBT active layer at different temperatures. Black arrows mark the saturated value $I_{\mathrm{SD\ sat}}$ of drain current and time t_{d} when holes reach drain contact. Further increase of the drain current after t_d is caused by increasing density of holes in the OFET channel until the current reaches saturation $I_{SD\ sat}$. OFET current transients technique has advantages over I-V characteristics. Firstly, mobility values obtained from t_d are not affected by high hole density, so comparison with i-CELIV results is more relevant. Secondly, first traveling holes are more sensitive to trapping states which can be affected by morphological changes in the film.

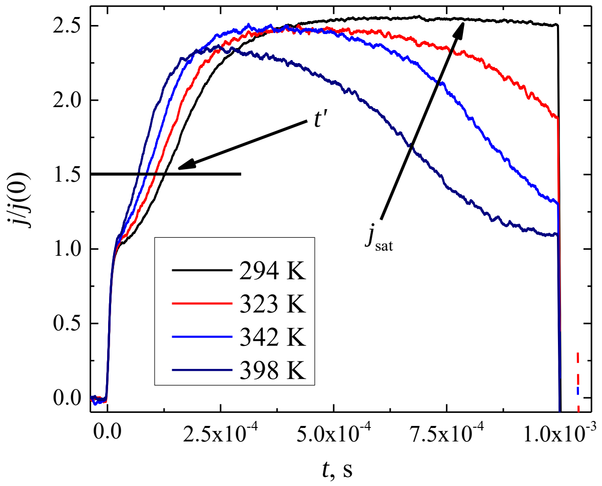

Fig. 46. PCPDTBT OFET structure normalized current density transients at different temperatures (obtained from i-CELIV technique).

Few examples of i-CELIV current density transients at different temperatures are presented in Fig. 46. After initial step $j(0)$ attributed to source-gate capacitance of the sample, extraction current density rises and the time value t' can be found for hole mobility estimation. The line marks time t' when the current density reaches 1.5 of the value of the initial capacitance step $j(0)$. The beginning of i-CELIV transients is superlinear indicating SCLC conditions in the measurement, thus holes are accumulated near the dielectric layer and they travel the entire thickness of the PCPDTBT layer during extraction by the increasing voltage pulse **[129]**.

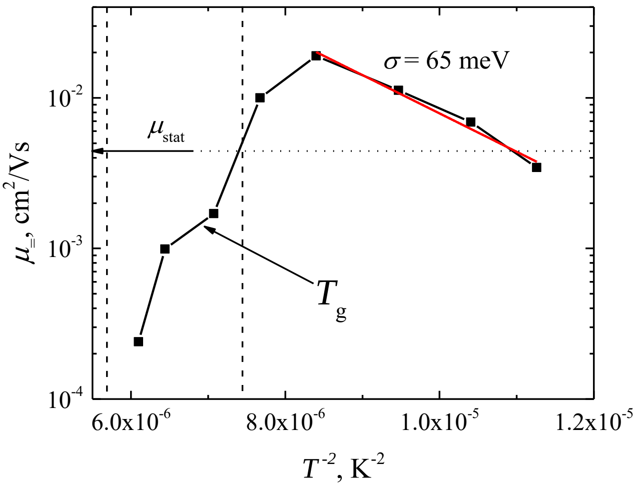

Fig. 47. Hole mobility dependence on temperature obtained by current transients measurement method.

In the Fig. 47 it is shown how temperature affects the hole mobility $\mu_=$ in parallel to the substrate direction. The axes in the figure were chosen according to Bässler's model of charge carrier hopping through energy states in order to obtain disorder parameters of the PCPDTBT **[32]**. PCPDTBT hole mobility in parallel to the substrate direction increases in the beginning of heating (see fitted region in Fig. 47). This is generally expected result in disordered organic materials according to Bässler's model because of temperature activated hopping rate **[32]**. When the temperature reaches 72 °C, the mobility and saturated current $I_{SD\ sat}$ value start to decrease (the decrease of saturated current can be seen in the Fig. 45). The decrease of the PCPDTBT:PCBM solar cell's performance in similar temperature range was reported before **[140]**. In this report authors state that short circuit current and efficiency had decreased due to the decrease of the conductivity of the active layer. Results of this study suggest that the conductivity could have been decreased because of the decrease in hole mobility in PCPDTBT. Hole mobility decrease is attributed to the change in PCPDTBT layer morphology in higher temperature and it will be discussed in later paragraphs. Also, for verification and comparison hole mobility μ_{stat} from measured current values $I_{SD\ sat}$ at room temperature was calculated (see Fig. 45). Similar values obtained from current transients technique and from $I_{SD\ sat}$ indicates that hole mobility has low dependence on hole density in the OFET channel.

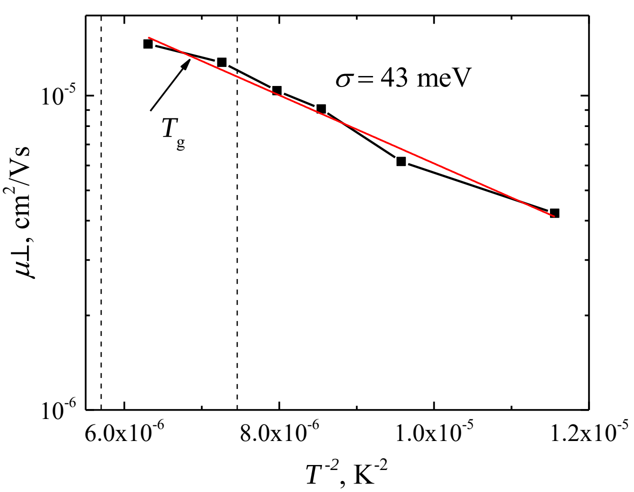

Fig. 48. Hole mobility dependence on temperature obtained by i-CELIV measurement method.

In contrast to the hole mobility dependence on temperature in parallel to the substrate direction $\mu_{=}$, hole mobility obtained by i-CELIV increases through all the heating range (see Fig. 48). Also, the value of hole mobility in perpendicular to the substrate direction is lower 800 times than in parallel to the substrate direction at room temperature. These results suggest different conditions for hole movement in different directions as well as different morphologies. To investigate the enegretic disorder in each of the directions the energetic disorder parameters σ were calculated using Bässler's formalism for disordered systems.

In eq. (1.3) there are two main parameters influencing charge carrier mobility: the temperature and the electric field. Energetic disorder parameters were found from the fit of hole mobility dependence on temperature (Fig. 47 and Fig. 48). Reliable value of positional disorder parameter Σ cannot be found because the exact value of electric field cannot be found neither in i-CELIV, nor OFET current transients techniques. Electric field's influence was neglected because the values of hole mobility were close to zero electric field condition in both of the experiments. For the parallel to the substrate direction zero electric field mobility values were extrapolated from mobility dependence on the voltage between source and drain (extrapolated hole mobility data can be found in Fig. S1 in Appendix 1). The mobility dependence on the voltage U_{SD} also indicates that hole mobility has a weak dependence on the electric field in the measured range. In OFET current transients technique applied voltage U_{SD} is proportional to the electric field in the layer but the exact value of the electric field cannot be found, because the electric field changes in time and in coordinate until $I_{\mathrm{SD\ sat}}$ is reached. In the perpendicular to the substrate direction (i-CELIV technique) electric field can be neglected because a significant part of the electric field is concentrated on the dielectric layer. Also, when the first holes are extracted at the time t_{tr} the voltage from the ramp pulse is still low and the electric field in PCPDTBT layer is very weak.

Charge carrier movement in the channel of the OFET is usually considered as 2D type movement. E.V. Emelianova et. al. **[141]** reported their theoretical calculations of the charge carrier movement in the channel and showed that when charge carriers are hopping through Gaussian DOS and their concentration is low, mobility dependence on the temperature is very similar to 3D case around the room temperature for the same energetic disorder parameter σ. OFET current transients technique measurements are performed in low concentration conditions and in 2D case calculated value of σ would be <10% smaller than in 3D case according to the Fig. 2 in the report **[141]**. Therefore, in this work found values of $\sigma_{=}$ = 65 meV for parallel to the substrate direction and $\sigma_{\perp}$ = 43 meV for perpendicular to the substrate direction can be compared with each other.

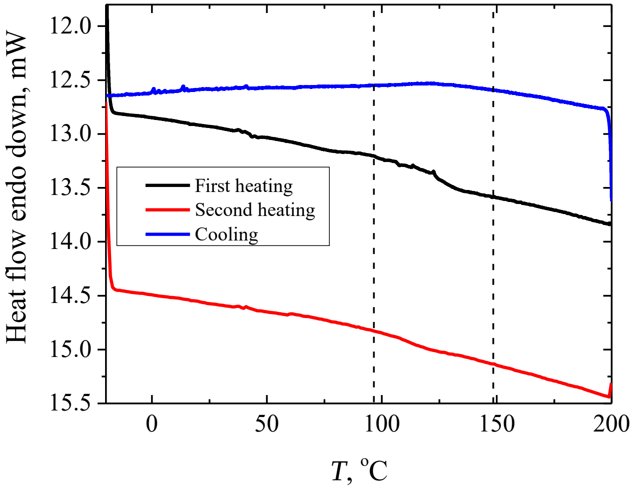

Fig. 49. DSC thermograms of PCPDTBT material.

To explain an abrupt change in hole mobility in parallel to the substrate direction with the increasing temperature, DSC measurements were performed in the temperature range from -20 °C to 200 °C (253 K to 473 K). Visible change in thermogram starts before 100 °C and ends above 120 °C and from the most abrupt change in the second heating curve the glass transition temperature T_g was found to be 112.5 °C (see Fig. 49 and Fig. 50). Indistinct and slow change in the thermogram is common feature for polymer materials because of their molecular weight, but hole mobility measurements show that the change in the morphology is crucial for the hole transport (see Fig. 47). From hole mobility $\mu_{=}$ measurements it can be assumed that structural changes in the PCPDTBT layer occurs at even lower temperatures than T_g and that these changes in morphology affect transport of the holes. Small shift in the DSC curve around glass transition temperature does not indicate that morphological transition in PCPDTBT is small. After heating in DSC measurements there were visible changes in the polymer state: from powder form before heating it changed to one piece glass/film type material after heating. Even though there were visible changes in PCPDTBT after heating in DSC measurements, spincoated layer did not have any visible changes after measurements. i-CELIV method allows to register active layer thickness (see eq. (2.25)) with every measurement made. There were no signs of any thickness or capacitance change in the PCPDTBT layer during the hole mobility measurements in different temperatures, thus heating did not cause any discontinuities in the layer.

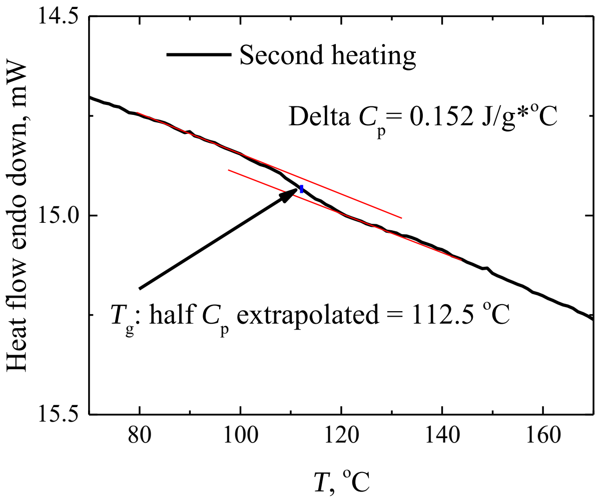

Fig. 50. Second heating thermogram with calculated glass transition temperature T_g.

DSC measurements indicate that the decrease of mobility at higher temperatures obtained by OFET current transients measurement was caused by morphology change in the film. Additional AFM (atomic force microscopy) measurements were performed on manufactured OFET structures before and after heating. The surface of spincoated PCPDTBT layer was very smooth before and after heating ($\Delta z \leq 5$ nm) and did not show any significant changes in the surface topology, only that heated layer became even smoother (roughness 1.2 nm of unheated layer to 0.3 nm of heated layer) which is expected result when heating material above T_g (AFM data can be found in Fig. S2 in Appendix 1). Thus, the inner morphological changes were not reflected on the surface of PCPDTBT. Also, additional measurement of the structure was done by grazing incidence X-ray diffraction technique (Fig. S3 in Appendix 1). Both heated and unheated PCPDTBT layers have single broad peaks around 20 degrees of 2θ. Thus, both layers are rather amorphous and do not have a distinct crystal structure.

At higher temperatures holes hopping rate increases due to temperature activated transport nature, but the change in PCPDTBT morphology causes modification of the DOS and affects hole transport. As a result, hole mobility decreases at higher temperatures in the parallel to the substrate direction (Fig. 47). For verification that hole mobility was affected by morphology, additional heating cycles were done (experimental data can be found in

Fig. S4 in Appendix 1). In the perpendicular to the substrate direction hole mobility steadily increases in the same temperature range, but the values of the mobility are much lower (Fig. 48). These results suggest that in PCPDTBT layer holes move in the different conditions in different directions (parallel and perpendicular to the substrate). This could be explained by morphology of polymer, in which (because of the interaction with SiO_2) the better conditions for the holes to move by the polymer/SiO_2 interface have formed (presumably, similar to “edge on” orientation). In this case the average π stacking distance decreases and therefore mobility of the holes is significantly higher. This difference in the mobility is hidden in the prefactor μ_0 which contains the probability for the holes to hop. Prefactor μ_0 is proportional to square of transfer integral and is determined by average coordinate intersite distance and molecular orientation **[142]**. It can be concluded that in parallel to the substrate direction average coordinate intersite distance and molecular orientation leads to more favorable conditions for the hole transport. From experimental results it follows, that these conditions are more susceptible to the heat. Higher temperature affects morphology in the way that molecules change their orientation more in the vicinity to the dielectric layer than in the volume. Similar tendency of difference in morphology in different directions was reported before **[13]**. In one report **[143]** authors showed that under some circumstances PCPDTBT could form nanoparticle quasicrystal structures in the chloroform solvent which could then result in similar morphology of the layer. The results demonstrated in this work are in agreement with other authors’ works **[13, 14, 144]** on PCPDTBT and it should be mentioned that changes in morphology of PCPDTBT triggered by heating should be considered when constructing devices, especially those, which are intended to work at higher ambient temperatures.

3.3 Charge carrier transport and recombination in PBDTTPD thin layer structures

In this study two types of structures were made with neat PBDTTPD as an active layer: OFET structures and sandwich structures (see Fig. 25 and Fig. 26). PBDTTPD material is often used as a hole transport material in blends with PCBM to make and investigate bulk heterojunction solar cells **[19]**, thus it is important to look closer into hole transport properties of this material. Therefore, in both sandwich and OFET structures in this study hole transport was investigated and voltages were chosen accordingly to inject and extract holes.

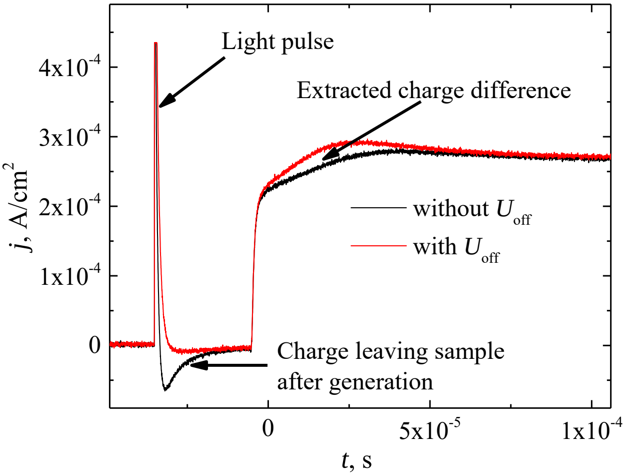

Fig. 51. photo-CELIV current density transients with and without U_{off}.

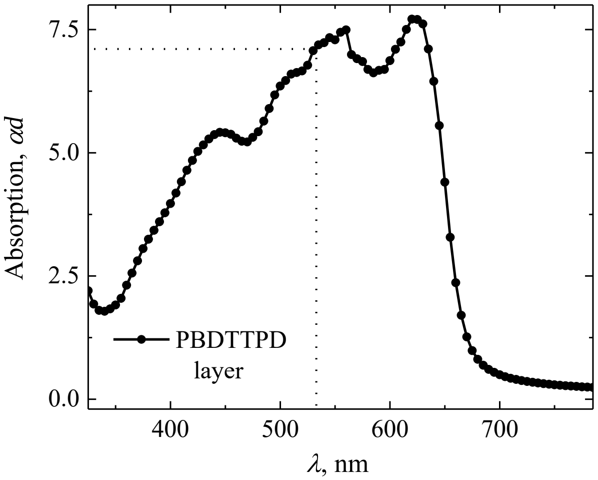

Fig. 52. Absorption spectrum of PBDTTPD layer. Dotted lines crossing marks absorption of wavelength used in photo-CELIV and TOF measurements.

The first goal of this study was to investigate hole mobility and recombination in sandwich structure with neat PBDTTPD layer and to achieve it photo-CELIV and TOF methods were employed. In photo-CELIV measurement external voltage $U_{\mathrm{off}} = 0.7$ V was applied to sandwich structure prior illumination to compensate built-in electric field and to stop photogenerated charge carriers from leaving the sample (Fig. 51). Also, PBDTTPD material has a strong absorption for the wavelength of the light used in TOF and photo-CELIV measurements (see Fig. 52), therefore it was took into account when estimating hole mobility. Few experimentally obtained photo-CELIV current density transients with different delay times t_{del} are depicted in Fig. 53. Black circle marks the "tails" where transients do not reach the initial capacitance step $j(0)$ indicating that some holes are very hard to extract by increasing ramp voltage from their occupied states. These "tails" are seen throughout the whole delay time t_{del} range and point to the dispersive character of hole transport in PBDTTPD layer which is connected to the redistribution of photogenerated holes in DOS with time **[145]**.

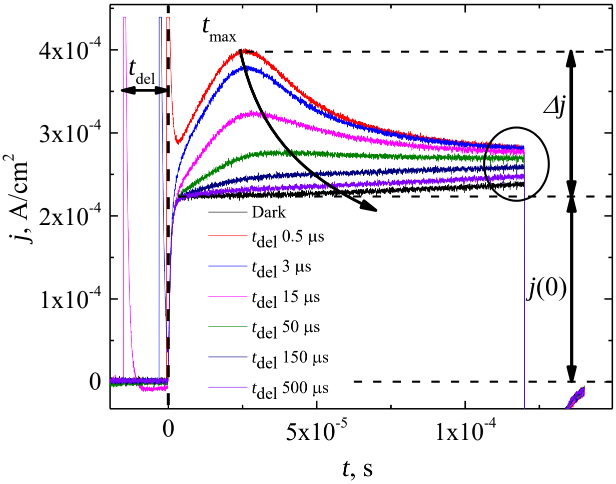

Fig. 53. photo-CELIV current density transients with increasing t_{del}.

Hole mobility in PBDTTPD layer obtained by photo-CELIV method was μ_{ph} = 4.8*10^{-4} cm^2/Vs and similar to already reported results elsewhere (1.4*10^{-4} cm^2/Vs – 7.5*10^{-4} cm^2/Vs) **[146-149]**. It should be considered that in mentioned reports blends of PBDTTPD were measured and different methods were used. With increasing t_{del} value the decrease of hole mobility in PBDTTPD was observed (see Fig. 54 and corresponding t_{max} increasing in fig 53). The decrease of hole mobility is caused by photogenerated holes redistribution in their states with time. With low t_{del} value (up to few μs) we have significant part of holes travelling relatively fast (μ_{ph} = 4.8*10^{-4} cm^2/Vs), forming pronounced current density peak with low t_{max} value (for example, see red and blue curves in Fig. 53) and relatively small amount of slower holes part of which cannot be extracted by applied ramp voltage (see "tails" of transients above $j(0)$). The increase of t_{del}, in addition to lowering the amount of holes due to recombination (see area of the photo-transient above the "dark" transient in Fig. 53), also causes the increased contribution of slower holes to the photo current with respect to the faster ones. We can assume that without t_{del} hole mobility would be higher and close to hole mobility μ_{tof} = 10^{-3} cm^2/Vs measured by TOF technique (TOF measurement data can be seen in Appendix 2 Fig. S5 and Fig. S6) as hole mobility obtained by photo-CELIV tends to saturate to TOF value (blue dashed line in Fig. 54). These results suggest that neat PBDTTPD material employed in sandwich structure exhibits much slower decay of DOS tail than in Gaussian DOS model. The holes in deep energy states barely contribute to the non-dispersive TOF current, but become "visible" in the photo-CELIV current when t_{del} is large and the most of photogenerated higher mobility holes have recombined or relaxed to deep energy states. Systems which exhibit superposition of two different DOS distributions (for example, Gaussian + exponential) was reported before **[47]**. It is worth mentioning, that combination of TOF and photo-CELIV techniques exposes hole transport properties discussed above that otherwise would be undetected and this emphasizes the importance of measurements in broad time scale.

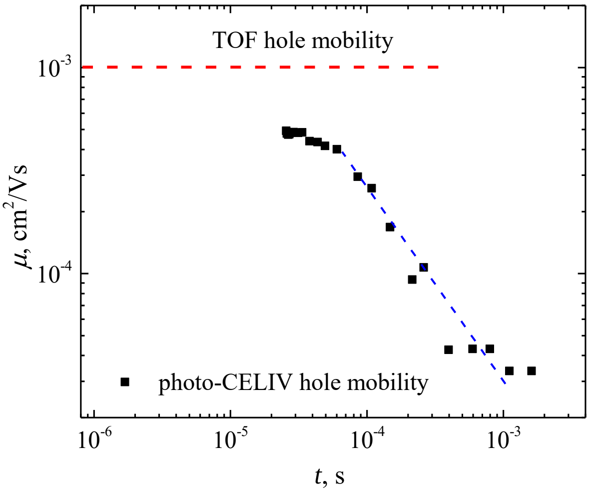

Fig. 54. Hole mobility in PBDTTPD sandwich structure. Time t in the bottom axis is $t_{\mathrm{del}} + t_{\mathrm{max}}$ which is the lifetime of the most holes from photogeneration to extraction.

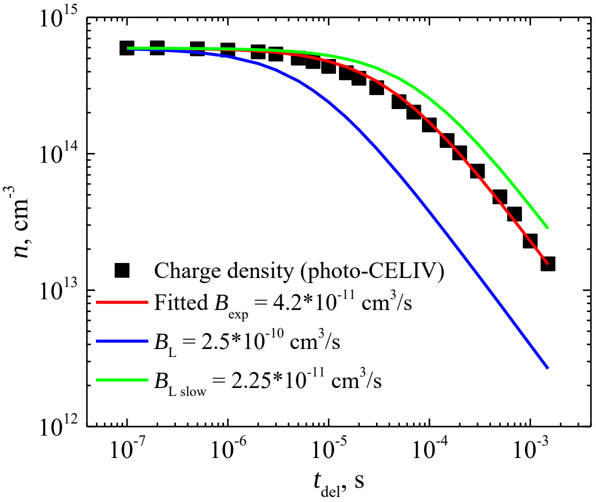

Fig. 55. Extracted charge carrier density decay in PBDTTPD sandwich structure.

Charge carrier density decay measured by photo-CELIV allows to investigate recombination rate in PBDTTPD sandwich structure (Fig. 55). Using eq. (2.10) bimolecular recombination coefficient B_{exp} can be found by fitting extracted charge carrier density dependence on time (red line in Fig. 55). Even though hole mobility changes by one order of magnitude with respect to t_{del}, the fitting of n(t_{del}) assuming B_{exp} = const is appropriate in all measured t_{del} range. From the experimental results obtained bimolecular recombination coefficient was B_{exp} = 4.2*10^{-11} cm^3/s. However, calculated Langevin recombination coefficient was B_L = 2.5*10^{-10} cm^3/s (for calculation hole mobility μ_{ph} = 4.8*10^{-4} cm^2/Vs was used), which means that recombination rate in the PBDTTPD sandwich structure was lower by almost 6 times. Usually, reduction of Langevin type recombination is observed in organic semiconductor bulk heterojunctions and is explained by the separation of the hole and electron pathways **[150, 151]**, by the influence of the lowest mobility charge carriers **[57]**, by the extent of charge delocalization of holes and electrons in charge transfer state **[22]**. However, these reasons explain reduction of recombination by few orders of magnitude in blends while in this case neat polymer layer was used and recombination is slowed down by 6 times only. As mentioned above, Fig. 53 and Fig. 54 indicate that photogenerated holes with the time relax and occupy lower energy states, hopping gets more difficult and average mobility decreases. Langevin recombination coefficient calculated by using the lowest measured hole mobility $\mu_{ph} = 4.35*10^{-5}$ cm^2/Vs was $B_{L\ slow} = 2.25*10^{-11}$ cm^3/s (green line in Fig. 55) and is about two times smaller than experimentally obtained recombination coefficient B_{exp}. It can be assumed that B_{exp} is tied to effective hole mobility in the layer which is close to the slowest measured mobility in photo-CELIV experiment, because part of holes with higher mobility escapes from photogeneration area before they can recombine and letting holes with lower mobility recombine, therefore reduced recombination coefficient is obtained.

Hole mobility in OFET structures with top source – drain gold electrodes were measured by OFET current transients and i-CELIV techniques. Though PBDTTPD is considered to be a promising hole transport polymer, only single work has been reported about using it in the OFET structure **[152]**. Authors investigated PBDTTPD mixed with P3HT in the active layer and found hole mobilities to be in range $4.36*10^{-4}$ cm^2/Vs – $8.69*10^{-3}$ cm^2/Vs at room temperature, mainly obtaining higher mobility values in the samples with bigger part of P3HT.

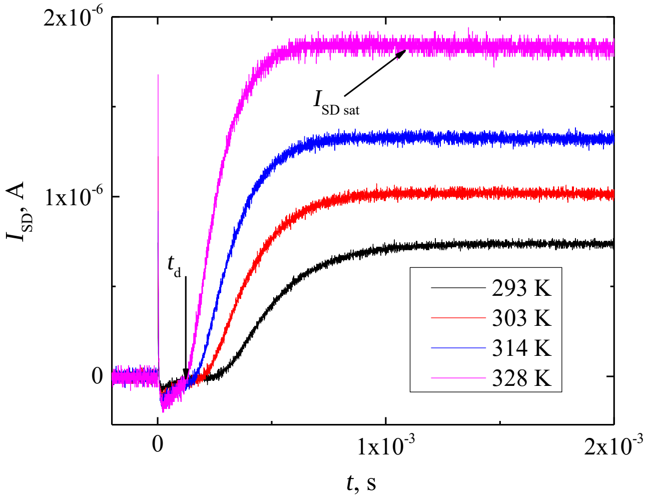

Fig. 56. Current I_{SD} transients at different temperatures obtained by OFET current transients method in PBDTTPD OFET structure with OTS treatment (U_{SD} = 80 V).

By using t_d value (Fig. 56) the estimated hole mobilities at room temperature were $\mu_{tr} = 9.3*10^{-5}$ cm^2/Vs in OFET structure without OTS treatment and $\mu_{tr} = 1.5*10^{-4}$ cm^2/Vs in OFET structure with OTS treatment.

Hole mobility values were extrapolated from the hole mobility dependence on applied voltage U_{SD} to get zero field hole mobility (experiment data is presented in Fig. S7 in Appendix 2). OFET current transients technique also gives opportunity to estimate hole mobility from IV characteristics using $I_{SD\ sat}$ value (Fig. 56) and for comparison hole mobility at room temperature of OFET structure with OTS treatment was calculated $\mu_{sat} = 1.1*10^{-4}$ cm^2/Vs (Fig. 57). Hole mobility calculated using t_d value represents mobility in low hole density conditions and hole mobility calculated using $I_{SD\ sat}$ value represents mobility in the high hole density in the OFET channel conditions. With both hole mobility values being similar it can be assumed that charge density does not affect mobility in PBDTTPD layers, therefore photo-CELIV hole mobility dependency on delay time t_{del} is caused by holes redistributing through energy states of DOS with the time and not by hole density reduction due to recombination.

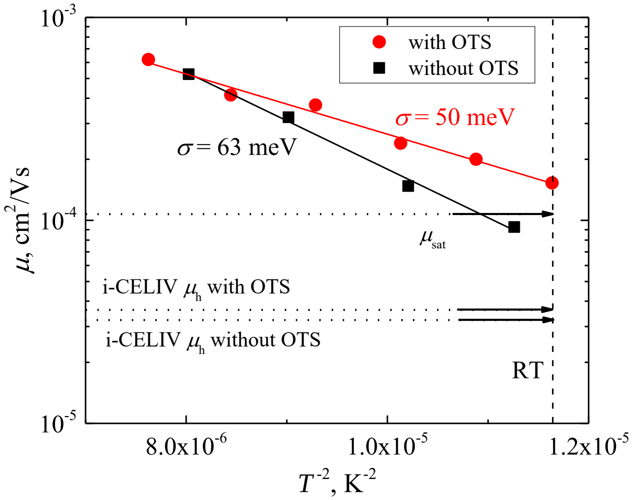

Fig. 57. Hole mobility dependence on temperature obtained from OFET current transients measurements. Arrows mark hole mobility values obtained from i-CELIV and IV characteristics at room temperature. Dashed line marks room temperature.

i-CELIV results of hole mobility do not show any significant difference between OFET structure without OTS treatment and OFET structure with OTS treatment ($\mu_h = 3.2*10^{-5}$ cm^2/Vs and $\mu_h = 3.4*10^{-5}$ cm^2/Vs respectively, Fig. 57). In i-CELIV experiment holes do not travel via OFET structure channel near dielectric/polymer interface, thus hole mobility is equal with and without OTS treatment, while hole mobility improved in OFET structure channel with OTS treatment. i-CELIV hole mobility is similar to the lowest photo-CELIV hole mobility, but is lower than calculated from t_d value (compare Fig. 54 and Fig. 57), because in i-CELIV injected holes are kept in the sample for a while before extraction, just as under photo-CELIV conditions with the highest t_{del} values, while in OFET current transients experiment holes travel instantly after voltage is applied.

From mobility dependence on temperature (Fig. 57) obtained disorder parameters show that energetic disorder parameter σ of dielectric/polymer interface DOS is smaller in OFET structure channel with OTS treatment than in OFET structure channel without OTS treatment (50 meV to 63 meV), thus via reduced interface energetic disorder (reduced influence of SiO_2 surface defects) hole transport conditions were improved and hole mobility increased. For verification that PBDTTPD does not have any phase shift which can also modify hole transport conditions and mobility values in measured temperature range, differential scanning calorimetry measurement were conducted (data can be found in Fig. S8 in Appendix 2). Energetic disorder parameter σ in PBDTTPD blends with PCBM was reported before, where authors reported σ = 65 meV and σ = 81 meV for different configurations of PBDTTPD molecule **[146]**. In OFET structures with neat PBDTTPD material disorder parameter σ of interface DOS in OFET channel near dielectric surface is smaller than its blend with PCBM (63 meV to 81 meV) and treating SiO_2 surface with OTS decreases disorder parameter σ from 63 meV to 50 meV.

CONCLUSIONS

It was shown that in FTO/TiO_2/$CH_3NH_3PbI_3$/Spiro-OMeTAD/Au solar cell structure photogenerated holes extraction is obstructed by morphology of perovskite and organic layers. The disorder of Spiro-OMeTAD layer, disorder and grain boundaries of polycrystalline perovskite film and the interface between perovskite and Spiro-OMeTAD layers impede hole transport by increasing density of trap states and therefore lowering hole mobility in comparison with hole mobilities reported before in each single layer separately.

Hole mobility in PCPDTBT layer employed in OFET structure is 800 times larger at room temperature in parallel to the substrate direction than in perpendicular to the substrate direction. Small difference in energetic disorder parameters $\sigma_=$ and $\sigma_\perp$ in each of the directions accordingly indicates that the difference in mobility comes from the mobility prefactor μ_0 (probability for the holes to hop). Therefore, in parallel to the substrate direction there are lower average coordinate intersite distance and better molecular orientation for the hole transport. Due to morphological changes at higher temperature (above 72 °C) the mobility of holes, moving near PCPDTBT/SiO_2 interface in parallel to the substrate direction decreases.

In OFET structures with PBDTTPD active layer hole mobility increases from $\mu_{tr} = 9.3*10^{-5}$ cm^2/Vs to $\mu_{tr} = 1.5*10^{-4}$ cm^2/Vs at room temperature after treating SiO_2 surface with OTS. The increase in hole mobility can be attributed to the decrease of energetic disorder parameter σ of organic/dielectric layers interface DOS from 63 meV to 50 meV as it reduced dielectric surface defects influence on hole transport and improved hole hopping conditions.

Investigation of the recombination of photogenerated charge carriers in PBDTTPD sandwich structure points to bimolecular-type recombination with coefficient $B_{exp} = 4.2*10^{-11}$ cm^3/s in the whole measured time range (more than 3 orders of magnitude). It is 6 times lower than calculated Langevin recombination coefficient, which shows that part of holes with higher mobility are escaping from photogeneration area before they can recombine and holes with lower mobility are mainly participating in recombination, therefore reducing recombination rate. Hole mobility decreases with time holes spend in the layer, because of holes relaxation through DOS after photogeneration.

SANTRAUKA LIETUVIŲ KALBA

Įvadas

Organiniai puslaidininkiai jau dabar yra labai svarbi gaminamų elektronikos prietaisų gausos dalis. Pavyzdžiui, beveik visa elektrofotografija šiuo metu veikia organinių medžiagų pagrindu, o vis daugiau pramoninių gamintojų siūlo organinių šviestukų pagrindu veikiančius ekranus (didžiausi gamintojai: Samsung, LG, BOE). Mechaninis organinių medžiagų lankstumas buvo ne kartą minimas kaip didelis privalumas moksliniuose straipsniuose **[1-3]**, o dabar pirmieji komerciškai prieinami produktai su pilnai lankstomais ekranais (ne lenktais) jau yra parduodami parduotuvėse visame pasaulyje (išmanieji telefonai, planšetės, nešiojami kompiuteriai). Tai parodo pasiteisinusį didžiulį organinių puslaidininkių potencialą ir šios medžiagos tampa vis svarbesnėmis ir kituose pritaikymuose, pavyzdžiui, organiniuose lauko tranzistoriuose (OLT) ir organiniuose saulės elementuose (žiūrėti 1 pav.). Mokslinės grupės, dirbančios su organiniais saulės elementais, gana neseniai pradėjo tyrinėti ir perovskitus, kurie kartu su organiniais puslaidininkiais yra labai potencialūs pasiekti naujas aukštumas saulės elementų efektyvume **[4, 5]**. Perovskitų medžiagos tapo labai populiarios ne tik jų pritaikyme saulės energetikoje, o susidomėjimas jomis vis auga, atrandant vis naujas medžiagų variacijas ir naujus pritaikymus (žiūrėti 2 pav.).

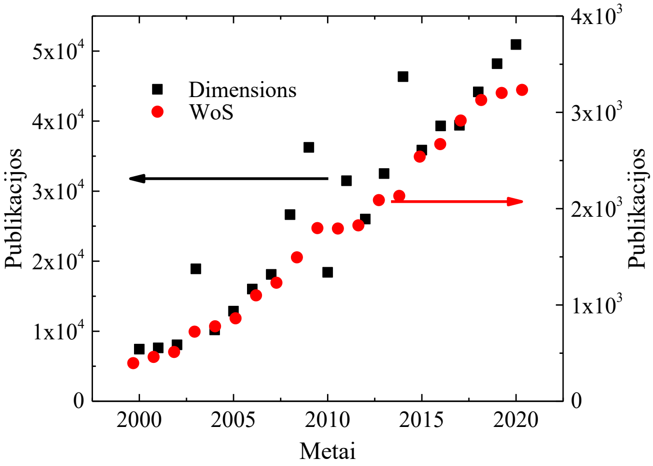

1 pav. Mokslinių publikacijų skaičius pagal raktažodį „organic semiconductor“ duomenų bazėse „Dimensions“ (juodi kvadratai) ir „Web of Science“ (raudoni taškai) **[7, 8]**.

Krūvininkų pernaša organiniuose puslaidininkiuose yra vienas iš svarbiausių faktorių, lemiančių šių medžiagų pritaikymą įvairiose srityse ir prietaisuose, todėl krūvininkų transportas yra vienas iš labiausiai studijuojamų dalykų organinių puslaidininkių tyrimų srityje. Augantis susidomėjimas organinėmis medžiagomis privilioja vis daugiau žmonių ir pinigų į šį tyrimų lauką, todėl per paskutinį dešimtmetį smarkiai išaugo su organinėmis medžiagomis dirbančių mokslinių grupių skaičius **[6]**. Į šį augimą įeina ir vasaros mokyklos studentams, stipendijos antros ir trečios pakopos studentams, taip pat ir podoktorantūros stažuočių programos.

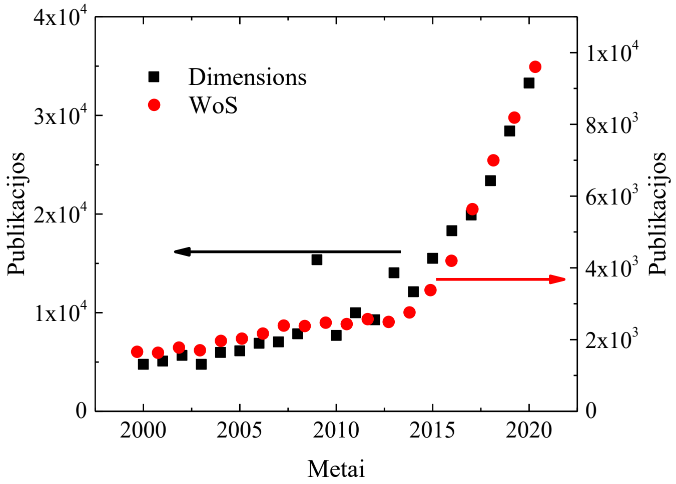

2 pav. Mokslinių publikacijų skaičius pagal raktažodį „perovskite“ duomenų bazėse „Dimensions“ (juodi kvadratai) ir „Web of Science“ (raudoni taškai) **[7, 8]**.

Didžiausias dėmesys šioje disertacijoje buvo skiriamas krūvininkų pernašai ir rekombinacijai įvairiose iš organinių puslaidininkių suformuotose struktūrose. Nuo tada, kai pasirodė pirmasis mokslinis straipsnis apie iš perovskitų pagamintą saulės elementą **[9]**, buvo atlikta nemažai tyrimų aiškinantis krūvininkų pernašą šio naujo tipo medžiagose. Tačiau nepaisant itin greito progreso saulės elementų, pagamintų su perovskitų tipo medžiagomis, efektyvume, dar nėra tikslios teorijos, paaiškinančios visus perovskitų sluoksniuose vykstančius elektroninius procesus. Be to, tyrimų duomenys stipriai priklauso nuo perovskito sluoksnio gamybos metodo, nuo medžiagų grynumo ir šie veiksniai gali nulemti nekontroliuojamus morfologinius pokyčius sluoksnyje ir prastą rezultatų atsikartojimą.

Teoriniai krūvininkų pernašos modeliavimų hibridiniuose perovskituose rezultatai rodo labai aukštą krūvininkų judrį, o tai yra kiek neįprasta organinių saulės elementų srityje, kurioje paprastai dominuoja mažos judrio vertės. Tačiau eksperimentų metų gautos krūvininkų judrio vertės perovskitų sluoksniuose buvo gerokai mažesnes ir stipriai priklausė nuo morfologijos ir temperatūros **[10-12]**. Šiame darbe skylių judris organinio saulės elemento struktūroje su $CH_3NH_3PbI_3$ perovskito sluoksniu buvo išmatuotas foto-CELIV metodu norint geriau suprasti krūvininkų pernašą tokio tipo saulės elementų struktūroje.

Vienas didžiausių skirtumų tarp organinių puslaidininkių ir neorganinių puslaidininkių yra tai, kad organinės medžiagos paprastai sudaro amorfinės struktūros sluoksnius dėl silpnos molekulių tarpusavio sąveikos. Tai gali būti ir privalumu (lankstumas, lengvi ir greiti gamybos procesai), ir trūkumu (mažas krūvininkų judris, prastas atsikartojamumas). Keičiant organinių puslaidininkinių sluoksnių morfologiją, galima stipriai pagerinti elektronines sluoksnių savybes **[13]**. Kai kurių organinių puslaidininkinių polimerų sluoksnių morfologija gali būti ženkliai pakeista sluoksnio formavimo metu. Tai parodo ne tik stiprią organinių medžiagų elektrinių savybių priklausomybę nuo morfologijos, bet ir galimybę iš vienos medžiagos suformuoti įvairios vidinės struktūros sluoksnius **[14]**. Šiame darbe buvo nagrinėjamas krūvininkų transportas OLT struktūros bandiniuose pagamintuose su grynos PCPDTBT (poly[2,6-(4,4-bis-(2-ethylhexyl)-4H-cyclopenta [2,1-b;3,4-b′]dithiophene)-alt-4,7(2,1,3-benzothiadiazole)]) medžiagos sluoksniu. Šis polimeras yra dažnai naudojamas kartu su PCBM ([6,6]-Phenyl C61 (arba C71) butyric acid methyl ester) medžiaga tūrinių heterosandūrų saulės elementuose **[15, 16]**. Tačiau šiame darbe PCPDTBT medžiaga buvo panaudota OLT struktūros bandiniuose, kurie leido tyrinėti krūvininkų pernašą skirtingomis OLT struktūros kryptimis ir aiškintis krūvininkų pernašos anizotropiją. Šiam tikslui buvo pritaikyti i-CELIV ir lauko tranzistorių srovių kinetikų metodai.

Organiniuose lauko tranzistoriuose dielektriko paviršius yra itin svarbus krūvininkų pernašai, nes jis yra pagrindas, su kuriuo organinis sluoksnis sudaro sandūrą, kuri turi stiprią įtaką organinio sluoksnio morfologijai ir taip pat krūvininkų pernašai OLT kanale. Dielektriko paviršius gali būti modifikuojamas prieš formuojant organinį sluoksnį ir taip gali būti pagerinta krūvininkų pernaša **[17, 18]**. Taigi tyrinėjant organinius puslaidininkius OLT struktūros bandiniuose yra svarbu aiškintis, kaip dielektriko paviršius daro įtaką krūvininkų pernašai. Šiame darbe organinė skylių transportinė medžiaga PBDTTPD, su kuria dažnai formuojamos tūrinių heterosandūrų saulės elementai kartu su PCBM **[19]**, buvo panaudota OLT struktūros bandiniuose norint ištirti krūvininkų pernašą grynoje PBDTTPD medžiagoje ir kaip dielektriko sluoksnis daro įtaką krūvininkų pernašai.

Fotogeneruotų krūvininkų rekombinacija yra vienas svarbiausių organinių puslaidininkių, naudojamų saulės elementuose, parametrų. Taigi šiame darbe iš grynos PBDTTPD medžiagos buvo pagaminti diodinės struktūros bandiniai krūvininkų pernašos ir rekombinacijos tyrimams. Grynos medžiagos tyrinėjimas suteikia daugiau informacijos apie pačią medžiagą ir jos parametrus, o įvairių mišinių tyrimai yra labiau nukreipti į optimalių santykių, optimalių storių ir panašių parametrų tyrinėjimą, kad būtų gautos geriausios įmanomos tokios bandinių charakteristikos kaip efektyvumas, stabilumas ir bendras našumas **[20, 21]**. Šiame darbe PBDTTPD diodinės struktūros bandiniai buvo tiriami lėkio trukmės ir foto-CELIV metodais. Abu metodai skirti tyrinėti krūvininkų pernašą, tačiau foto-CELIV metodas taip pat gali būti pritaikytas rekombinacijos spartos tyrimui ir rekombinacijos koeficientų nustatymui fotogeneruotų krūvininkų tankio mažėjimo eksperimento metu **[22-24]**.

PAGRINDINIAI DISERTACIJOS TIKSLAI IR UŽDAVINIAI

Pagrindiniai šios disertacijos tikslai yra krūvininkų pernašos tyrimas saulės elemento struktūros bandiniuose su $CH_3NH_3PbI_3$ perovskito sluoksniu, organinio lauko tranzistoriaus struktūros bandiniuose su grynų PCPDTBT ir PBDTTPB medžiagų sluoksniais ir rekombinacijos tyrimas diodinės struktūros bandiniuose su PBDTTPD medžiaga. Įgyvendinant tikslus reikėjo atlikti tokius uždavinius, kaip skirtingų struktūrų bandinių gamyba, tinkamų tyrimo metodų pasirinkimas ir pritaikymas, norint išsiaiškinti krūvininkų pernašos parametrus, būdingus tiriamoms medžiagoms. Taigi, atsižvelgiant į problematiką, atitinkamai buvo suformuoti pagrindiniai disertacijos uždaviniai:

1. Pritaikyti foto-CELIV metodą krūvininkų judrio tyrimui saulės elemento struktūros bandiniuose su $CH_3NH_3PbI_3$ perovskito sluoksniu.
2. Pagaminti OLT struktūros bandinius su gryna PCPDTBT medžiaga, pritaikyti i-CELIV ir lauko tranzistorių srovių kinetikų metodus krūvininkų transporto tyrimui skirtingomis OLT struktūros bandinio kryptimis.
3. Pagaminti OLT struktūros bandinius su gryna PBDTTPD medžiaga ant skirtingai paruoštų dielektriko paviršių ir ištirti dielektriko paviršiaus įtaką krūvininkų pernašai.
4. Pagaminti diodinės struktūros bandinius su gryna PBDTTPD medžiaga ir ištirti fotogeneruotų krūvininkų transportą ir rekombinaciją.

DARBO NAUJUMAS IR AKTUALUMAS

Kiekviename iš šiame darbe atliktų eksperimentų yra pademonstruotas mokslinio darbo naujumas:

- Pirmą kartą pritaikius foto-CELIV metodą krūvininkų judrio matavimams $CH_3NH_3PbI_3$ perovskito saulės elementų struktūros bandinyje, buvo parodyta, kad bandinio sluoksnių morfologija apsunkina skylių ištraukimą.
- Išmatavus krūvininkų pernašą skirtingomis kryptimis OLT struktūros bandinyje su gryna PCPDTBT medžiaga i-CELIV ir lauko tranzistorių srovių kinetikų metodais buvo parodyta, kad PCPDTBT sluoksnis pasižymi krūvininkų pernašos anizotropija.

- Pirmą kartą tyrinėjant krūvininkų pernašą PBDTTPD medžiagoje OLT struktūros bandinyje i-CELIV ir lauko tranzistorių srovių kinetikų metodais buvo pademonstruota dielektriko paviršiaus įtaka skylių pernašai OLT kanale.
- Pirmą kartą tyrinėjant krūvininkų pernašą ir rekombinaciją grynoje PBDTTPD medžiagoje diodinės struktūros bandinyje foto-CELIV metodu buvo nustatyta, kad medžiaga pasižymi redukuota bimolekuline rekombinacija.

GINAMIEJI TEIGINIAI

1. $CH_3NH_3PbI_3$ perovskito sluoksnio polikristališkumas ir viduje polikristalinio sluoksnio netvarkingai išsidėstę kristalitai bei perovskito ir organinio sluoksnių tarpusavio sandūra apsunkina skylių ištraukimą iš saulės elemento struktūros bandinio dėl padidėjusio pagavimų lygmenų tankio.
2. OLT struktūros bandiniai su gryna PCPDTBT medžiaga pasižymi skylių transporto anizotropija lygiagrečia ir statmena padėklui kryptimis, o PCPDTBT sluoksnio morfologija pakinta prie aukštesnių nei kambario temperatūrų ir taip daro įtaką skylių pernašai.
3. SiO_2 paviršiaus modifikavimas OLT struktūros bandiniuose su gryna PBDTTPD medžiaga sumažina sandūros energetinės netvarkos parametrą σ dėl sumažėjusios SiO_2 paviršiaus defektų įtakos skylių pernašai ir taip pagerina skylių transporto sąlygas netoli dielektriko paviršiaus.
4. Diodinės struktūros bandiniai su gryna PBDTTPD medžiaga pasižymi bimolekuline rekombinacija, kurios sparta yra šešis kartus mažesnė nei Lanževeno rekombinacijos sparta, apskaičiuota pagal gautas krūvininkų judrio vertes, dėl dalies skylių pabėgimo iš rekombinacijos zonos.

PUBLIKACIJŲ SĄRAŠAS IR AUTORIAUS INDĖLIS

Publikacijų sąrašas

1. Andrius Aukštuolis, Mihaela Girtan, George A. Mousdis, Romain Mallet, Marcela Socol, Mohamed Rasheed, Anca Stanculescu. Measurement of charge carrier mobility in perovskite nanowire films by photo-CELIV method, *Proceedings of the Romanian Academy, Series A*, 18, 1, 34–41 (2017).
2. Andrius Aukštuolis, Nerijus Nekrašas, Kristijonas Genevičius, Jūratė Jonikaitė-Švėgždienė. Anisotropy of charge carrier transport in PCPDTBT field-effect transistor structures, *Synthetic Metals*, 264, 116382 (2020), https://doi.org/10.1016/j.synthmet.2020.116382.
3. Andrius Aukštuolis, Nerijus Nekrašas, Kristijonas Genevičius, Giedrius Juška, Investigation of charge carrier mobility and recombination in PBDTTPD thin layer structures, *Organic Electronics*, 90, 106066 (2021), https://doi.org/10.1016/j.orgel.2021.106066.

Autoriaus indėlis

1-oji publikacija. Autorius foto-CELIV metodu išmatavo bendraautorių pagamintus bandinius, surinko eksperimentinius duomenis, atliko jų analizę ir paruošė publikacijai. Taip pat autorius prisidėjo prie kelių publikacijos dalių rašymo ir redagavo publikacijos tekstą.

2-oji publikacija. Autorius pagamino bandinius, reikalingus eksperimentams, atliko matavimus i-CELIV ir lauko tranzistorių srovių kinetikų metodais, surinko eksperimentinius duomenis, atliko jų analizę ir paruošė publikacijai. Autorius kartu su bendraautoriumi N. Nekrašu parašė pirmąjį juodraštį ir drauge su bendraautoriais K. Genevičiumi ir N. Nekrašu atliko reikiamus pataisymus juodraštyje.

3-ioji publikacija. Autorius pagamino bandinius, reikalingus eksperimentams, atliko matavimus i-CELIV ir lauko tranzistorių srovių kinetikų metodais. Kartu su bendraautoriumi N. Nekrašu atliko matavimus lėkio trukmės ir foto-CELIV metodais. Autorius surinko eksperimentinius duomenis, atliko jų analizę ir paruošė publikacijai. Autorius drauge su bendraautoriais N. Nekrašu ir K. Genevičiumi parašė pirmąjį juodraštį ir atliko reikiamus pataisymui juodraštyje.

PRANEŠIMAI TARPTAUTINĖSE KONFERENCIJOSE

1. Mihaela Girtan*, G. Mousdis, A. Aukštuolis, M. Rasheed, R. Mallet, Studies of the physical properties $CH_3NH_3PbI_3$ nanowires thin films prepared by spin-coating, EMRS 2016 (gegužės 2-6), Lilis, Pracūzija. Stendinis pranešimas.
2. Andrius Aukštuolis*, George A. Mousdis, Romain Mallet, Mihaela Girtan*, Measurement of charge carrier mobility in $CH_3NH_3PbI_3$ perovskite thin films systems by photo-CELIV method, 3èmes Journées Pérovskites Hybrides (JPH) 2017 (gegužės 9-10), Anžė, Prancūzija. Stendinis pranešimas.
3. A. Aukštuolis*, N. Nekrašas, K. Genevičius, M. Girtan, G. Juška, Charge carrier transport properties in PBDTTPD organic solar cell structure, 12th Conference on Hybrid and Organic Photovoltaics, HOPV20 Virtuali konferencija, 2020 (gegužės 26-29). Stendinis pranešimas.
4. Andrius Aukštuolis*, Nerijus Nekrašas, Kristijonas Genevičius, Jūratė Jonikaitė-Švėgždienė, Giedrius Juška, Charge carrier transport properties in thin film hybrid field effect transistor structures, 28th in the series of Condensed Matter General conferences, CMD2020GEFES, 2020 (rugpjūčio 31 – rugsėjo 4), virtuali konferencija. Pranešimas žodžiu.
5. Andrius Aukštuolis*, Nerijus Nekrašas, Kristijonas Genevičius, Jūratė Jonikaitė-Švėgždienė, Giedrius Juška, Charge carriers transport properties in PCPDTBT thin film transistor structures, Functional materials and Nanotechnologies – 2020 (Lapkričio 23-25), Virtuali konferencija. Stendinis pranešimas.

* Pranešėjas

TIRIAMASIS DARBAS

Šiame skyriuje bus aptarti visi šiame darbe pritaikyti tyrimo metodai, naudotos medžiagos ir aprašyti bandinių gamybos procesai.

Medžiagos

Šiame darbe buvo tirtos kelios organinės puslaidininkinės medžiagos ir viena perovskito struktūrą turinti medžiaga (3 pav.). Spiro-MeOTAD yra skyles pernešanti puslaidininkinė medžiaga kartu su $CH_3NH_3PbI_3$ perovskitu buvo naudojamos saulės elementų bandiniam formuoti. PCPDTBT yra skyles pernešantis organinis puslaidininkinis polimeras, kuris buvo naudojamas formuojant organinio lauko tranzistoriaus struktūros bandinius. PBDTTPD yra skyles pernešantis organinis puslaidininkinis polimeras, kuris buvo naudojamas formuojant organinio lauko tranzistoriaus struktūros bandinius bei organinius diodinės struktūros bandinius.

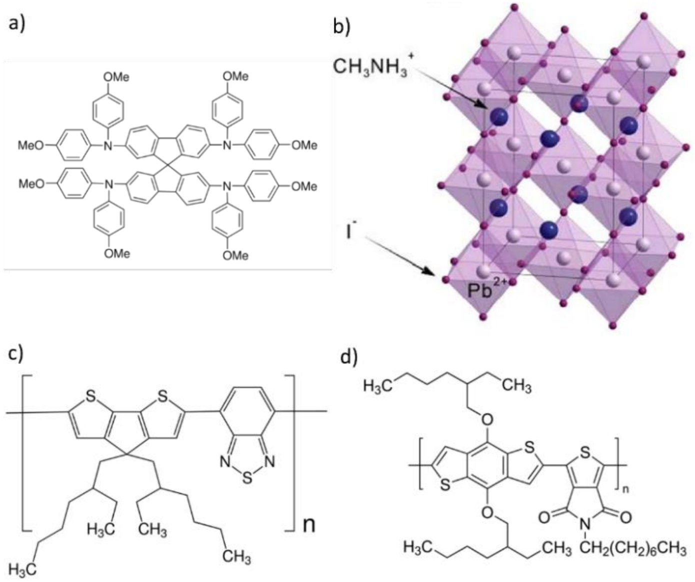

3 pav. Naudotų medžiagų scheminiai paveikslai. a) Spiro-MeOTAD molekulė; b) $CH_3NH_3PbI_3$ perovskito kubinė gardelė; c) PCPDTBT molekulė; d) PBDTTPD molekulė **[120]**.

Bandiniai

Saulės elemento bandinys su $CH_3NH_3PbI_3$ perovskito sluoksniu, naudotas foto-CELIV matavimuose, yra pavaizduotas 4 pav. Sluoksniai buvo formuojami ant nupirktų stiklo padėklų su FTO sluoksniu, kuris atliko ir peršviečiamo elektrodo funkciją eksperimento metu. Tankus 30 nm storio titano dioksido (TiO_2) sluoksnis buvo suformuotas reaktyvaus dulkinimo metodu, panaudojus titano taikinį deguonies atmosferoje. Ant suformuoto TiO_2 sluoksnio padėklo sukimo būdu (1600 rpm, 30 s) buvo suformuotas perovskito sluoksnis iš dviejų prieš pat formuojant sumaišytų vienodų molinių kiekių tirpalų: 0,1983 gramo (1,25 mmol) CH_3NH_3I medžiagos ištirpintos 0,25 ml DMF tirpiklyje ir 0,5785 gramo (1,25 mmol) PbI_2 medžiagos ištirpintos 25 ml DMF tirpiklyje.

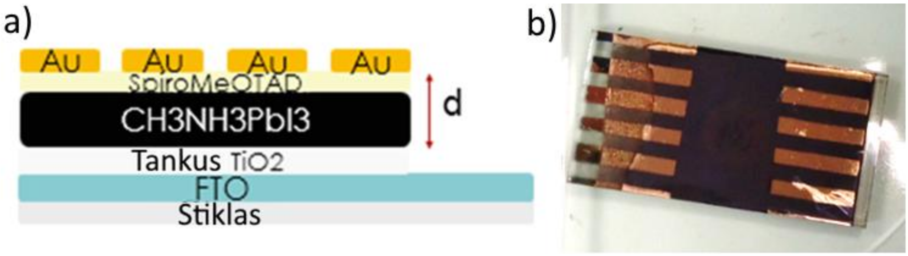

4 pav. a) Scheminis saulės elemento bandinio su $CH_3NH_3PbI_3$ perovskito sluoksniu vaizdas; b) bandinio nuotrauka.

CH_3NH_3I medžiaga buvo paruošta pagal receptą:

- 20 ml metilamino tirpalo (pirkas Ferak 40% w/v), kuriame buvo 8 g metilamino (257 mmol), atskiesta su 80 ml etanoliu;
- į šį maišomą tirpalą buvo pamažu pilamas hidrojodo rūgšties (HI) vandenyje tirpalas (pirkas Merck 57% w/v) kol tirpalo pH pasikeitė į rūgštinį (iš viso buvo panaudota apie 60 ml hidrojodo rūgšties);
- tirpalas toliau buvo maišomas kambario temperatūroje iki kol visi tirpikliai išgaravo;
- likusios nuosėdos sudėtos į dietileterį ir po to išfiltruotos;
- po filtravimo buvo gauti balti CH_3NH_3I kristalai, kurie buvo palikti džiūti 60 °C temperatūroje per naktį.

PbI_2 medžiaga buvo paruošta pagal receptą:

- 3,3 gramo (10 mmol) $Pb(NO_3)_2$ (pirkas Serva) buvo ištirpinta 50 ml distiliuoto vandens;

- šį tirpalą maišant, į jį buvo lėtai pilamas tirpalas, pagamintas iš 3,3 g (20 mmol) kalio jodido (pirkas Merck) ištirpinto 50 ml distiliuoto vandens;
- gautos aukso geltonumo nuosėdos buvo perfiltruotos ir gauti aukso geltonumo PbI_2 kristalai;
- kristalai buvo palikti džiūti 60 °C temperatūroje per naktį.

Ant suformuoto perovskito sluoksnio Spiro-MeOTAD (pirktas Merck) sluoksnis buvo formuojamas padėklo sukimo būdu (3500 rpm, 20 s) iš tirpalo, kuriame 75 mg Spiro-MeOTAD medžiagos ištirpinta 0,3 ml chlorbenzene. Galiausiai auksinis elektrodas (40 nm storio) buvo suformuotas dulkinimo būdu vakuume.

PCPDTBT organinio lauko tranzistoriaus struktūros bandiniai buvo formuojami ant nupirktų Si/SiO_2 padėklų, kuriuose SiO_2 sluoksnio storis buvo 100 nm ir kuris buvo naudojamas kaip dielektrikas, o smarkiai legiruotas silicis (n tipas) buvo naudojamas kaip užtūros elektrodas i-CELIV ir lauko tranzistorių srovės kinetikų matavimuose (5 pav.). Prieš liejant organinį sluoksnį padėklai buvo valomi ultragarsinėje vonelėje po 15 minučių paeiliui kiekviename iš šių tirpiklių: distiliuotas vanduo, acetonas, izopropanolis. Po valymo tirpikliuose padėklai buvo 2 minutėms įdėti į deguonies plazmos kamerą, kad būtų pašalintos visos likusios organinės liekanos ir kad SiO_2 paviršius taptų hidrofiliškesnis.

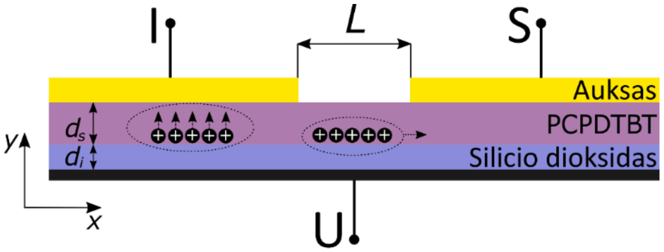

5 pav. Scheminis PCPDTBT lauko tranzistoriaus bandinio vaizdas.

PCPDTBT medžiagos (pirkta Sigma-Aldrich) pradinė forma buvo sausi milteliai, o jos molekulinės masė buvo M_w 7000-20000 g/mol. Prieš medžiagą ištirpinant chloroforme su 10 mg/ml koncentracija inertinių dujų atmosferoje nebuvo atlikta jokių medžiagos gryninimo procedūrų, ji buvo naudota tokia, kokia buvo atsiųsta gamintojo. Chloroformas kaip tirpiklis buvo pasirinktas dėl gero PCPDTBT medžiagos tirpumo jame **[121]** ir dėl didelio tirpiklio garavimo greičio, kuris užtikrina pakankamą susiformavusio sluoksnio storį, reikalingą i-CELIV matavimams. Tirpalas buvo liejamas padėklo sukimo būdu inertinių dujų atmosferoje. Formavimas buvo padalintas į du žingsnius:

pirmasis (500 rpm, 60 s) suformavo sluoksnį, o antrasis (2000 rpm, 40 s) pašalino tirpiklio likučius iš jau susiformavusio sluoksnio. Taip buvo gautas d_s = 160 nm sluoksnio storis. Po to auksiniai ištakos ir santakos elektrodai buvo užgarinti ant PCPDTBT sluoksnio paviršiaus vakuuminio garinimo būdu. Organinio lauko tranzistoriaus struktūros bandinio kanalo ilgis buvo L = 30 µm. Bandiniai prieš matavimus nebuvo atkaitinti.

PBDTTPD medžiaga buvo panaudota dviejų skirtingų tipų bandinių formavime: organinio lauko tranzistoriaus struktūros bandiniuose ir organinės diodinės struktūros bandiniuose. Diodinės struktūros bandiniai buvo gaminami ant stiklo/IAO (indžio alavo oksido) padėklų, o lauko tranzistoriaus struktūros bandiniai buvo gaminami ant Si/SiO_2 padėklų, kurių SiO_2 sluoksnis (d_i = 100 nm) buvo naudojamas kaip dielektrikas, o stipriai legiruotas silicis (n tipas) kaip užtūros elektrodas (žiūrėti 6 pav. ir 7 pav.). Prieš liejant organinį sluoksnį visi padėklai buvo valomi ultragarsinėje vonelėje po 15 minučių paeiliui kiekviename iš šių tirpiklių: distiliuotas vanduo, acetonas, izopropanolis. Po valymo tirpikliuose padėklai buvo 2 minutėms įdėti į deguonies plazmos kamerą, kad būtų pašalintos visos likusios organinės liekanos ir padėklų paviršius taptų hidrofiliškesnis. Po valymo procedūrų dalis Si/SiO_2 padėklų buvo 15-kai minučių panardinti į 60 °C temperatūros OTS/tolueno tirpalą, kurio koncentracija buvo 10 mmol. Išmirkyti padėklai buvo plaunami heksane (taip pašalinami pertekliniai OTS sluoksniai nuo paviršiaus), acetone, izopropanolyje.

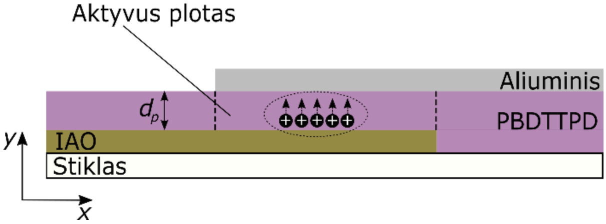

6 pav. Scheminis PBDTTPD diodinės struktūros bandinio vaizdas.

PBDTTPD medžiaga (pirka Sigma-Aldrich) buvo gauta sausų miltelių pavidalo ir prieš naudojimą nebuvo atliekama jokių gryninimo procedūrų. Formuojant diodinės struktūros bandinius PBDTTPD buvo ištirpintas chlorbenzene 10 mg/ml koncentracija. Tirpalas inertinių dujų atmosferoje buvo lašinamas ant stiklo/IAO padėklo, kol buvo padengtas visas paviršiaus plotas, o tirpikliui išgaravus, susiformavusio sluoksnio storis buvo d_p = 1.2 µm. Tuomet bandinys buvo perkeltas į vakuuminę kamerą, kurioje vakuuminio garinimo būdu pro kaukę buvo užgarinti aliuminio elektrodai.

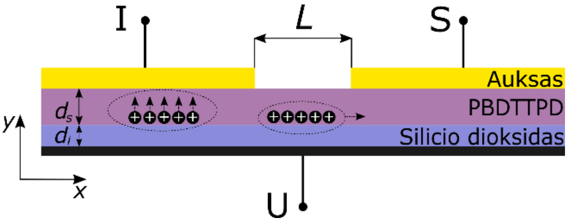

7 pav. Scheminis PBDTTPD lauko tranzistoriaus struktūros bandinio vaizdas.

Lauko tranzistoriaus struktūros bandinių gamybai PBDTTPD medžiaga buvo ištirpinta chloroforme 10 mg/ml koncentracija. Tirpalas buvo liejamas padėklo sukimo būdu inertinių dujų atmosferoje. Formavimas buvo padalintas į du žingsnius: pirmasis (500 rpm, 60 s) suformavo sluoksnį, o antrasis (2000 rpm, 40 s) pašalino tirpiklio likučius iš jau susiformavusio sluoksnio. Taip buvo gautas d_s = 135 nm sluoksnio storis. Po to auksiniai ištakos ir santakos elektrodai buvo užgarinti ant PBDTTPD sluoksnio paviršiaus vakuuminio garinimo būdu. Organinio lauko tranzistoriaus struktūros bandinio kanalo ilgis buvo L = 30 µm. Bandiniai prieš matavimus nebuvo atkaitinti.

Matavimų metodai

Naujos sintetinamos ir vis tobulinamos organinės puslaidininkinės medžiagos reikalauja ir naujesnių bei tikslesnių matavimo metodų, kurie taip pat yra tobulinami arba kuriami nauji ir pritaikomi organinių puslaidininkių tyrimų srityje. Įvairių struktūrų organinių puslaidininkių bandiniai suteikia galimybę išmatuoti medžiagų savybes skirtingose organinio sluoksnio konfigūracijose, tačiau tuomet iškyla gautų rezultatų palyginimo tarp skirtingų laboratorijų problema. Organinių puslaidininkių sluoksniai yra itin jautrūs gamybos sąlygoms, kurios gali daryti didelę įtaką matavimų rezultatams, tačiau ir atliekamo eksperimento sąlygos gali taip pat turėti įtakos matavimų rezultatams. Šiame skyriuje bus aptarti visi pagrindiniai naudoti matavimo metodai, jų privalumai ir trūkumai, jie bus palyginti tarpusavyje norint parodyti, kokiomis sąlygomis kiekvienas iš metodų yra tinkamas naudoti ir kokios organinių puslaidininkių savybės gali būti ištirtos.

Lėkio trukmės (TOF) metodas

Pirmą kartą lėkio trukmės (ang. time of flight – TOF) metodą pademonstravo mokslininkas W. E. Spear‘as 1957 metais **[122]**. Šis metodas greitai tapo plačiai naudojamas krūvio pernašos tyrimuose puslaidininkių ir organinių puslaidininkių sluoksniuose ir yra naudojamas ir iki dabar kaip paprastas metodas krūvininkų pernašos tyrimuose **[123, 124]**. Metodo paprastumas slypi nesudėtingoje įrangoje, kuri yra reikalinga eksperimentui atlikti: šviesos šaltinis, gebantis generuoti trumpalaikius šviesos impulsus, stačiakampio impulso generatorius ir oscilografas (8 pav.). Svarbu, kad šviesos šaltinis gebėtų generuoti impulsus, kurių trukmė būtų mažesnė nei tiriamos medžiagos krūvininkų relaksacijos laikas, tačiau didžioji dalis šiuo metu gaminamų lazerių geba generuoti gerokai trumpesnių už krūvininkų relaksaciją trukmių šviesos impulsus.

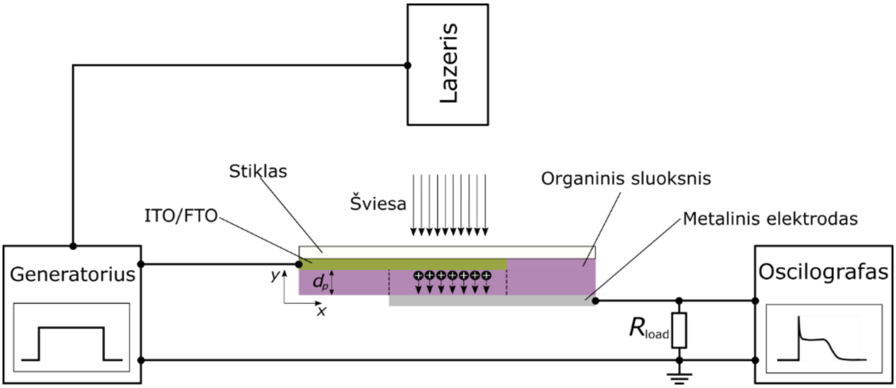

8 pav. Lėkio trukmės metodo scheminis vaizdas.

Vienas svarbiausių dalykų atliekant eksperimentą yra paruošti bandinį taip, kad jis būtų tinkamas matuoti pasirinktu metodu. Lėkio trukmės metodui tinkamo bandinio scheminis vaizdas pavaizduotas 8 pav. Bent vienas bandinio elektrodas turi būti skaidrus eksperimente naudojamai šviesai, matuojamos organinės medžiagos sluoksnis turi būti pakankamo storio, kad būtų išpildyta paviršinės sugerties ($\alpha d > 1$) sąlyga. Tai yra pirmasis lėkio trukmės metodo trūkumas – bandinys negali būti labai plonas. Paprastai organiniai puslaidininkiai pasižymi stipria sugertimi regimajame šviesos ruože, tačiau norint išlaikyti $\alpha d > 1$ sąlygą, reikia, kad sluoksnio storis būtų ne plonesnis nei keli šimtai nanometrų, priklausomai nuo naudojamų medžiagos ir šviesos **[125]**. Taip pat medžiagos Maksvelo relaksacijos trukmė τ_σ turi būti ilgesnė nei krūvininkų tranzito per bandinį laikas t_{tr}. Taigi Lėkio trukmės metodas nėra tinkamas organinių medžiagų tyrimui, kurios pasižymi santykinai dideliu laidumu.

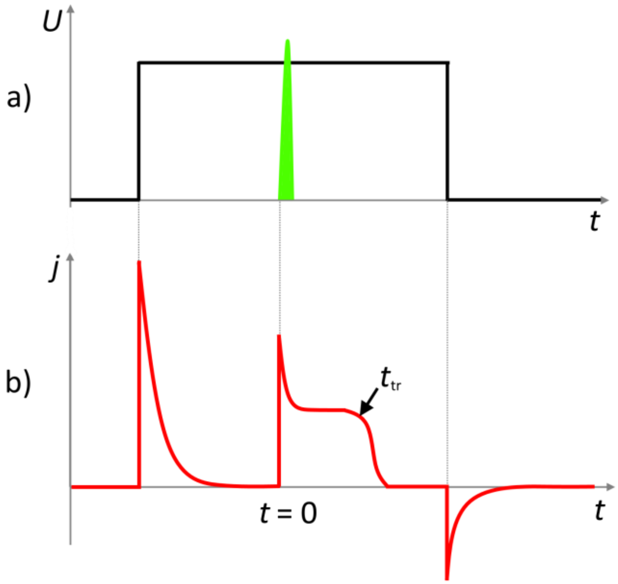

9 pav. Teorinės Lėkio trukmės metodo srovės kinetikos. a) Šviesos impulsas ir stačiakampis impulsas; b) bandinio atsakas į impulsus.

Po fotosužadinimo yra sukuriami krūvininkai ir jie keliauja bandiniu elektriniame lauke, sukurtame prijungto stačiakampio impulso (9 pav.). Didelis Lėkio trukmės metodo privalumas yra tai, kad galima nesudėtingai išmatuoti elektronų ir skylių judrius vien tik pakeitus prijungto stačiakampio impulso poliarumą. Sugeneruoti krūvininkai juda per bandinį ir pasiekia metalinį elektrodą po tranzito laiko t_{tr}, kuris po to panaudojamas krūvininkų judriui rasti:

$$\mu = \frac{d_{\mathrm{p}}^{2}}{U t_{\mathrm{tr}}} \quad , \tag{2.1}$$

kur d_p yra matuojamos medžiagos sluoksnio storis, o U yra stačiakampio impulso įtampa.

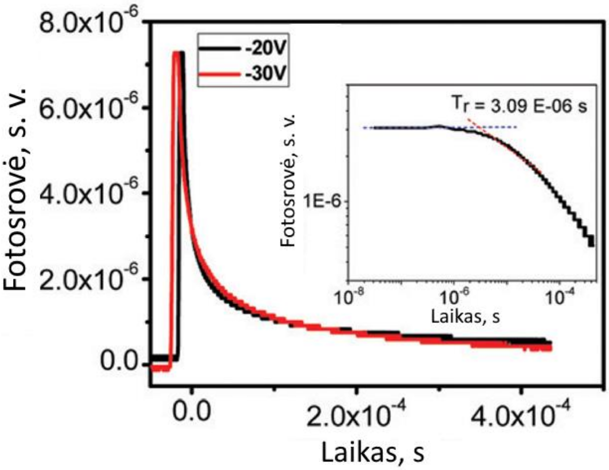

10 pav. Lėkio trukmės metodo fotosrovės kinetika be aiškiai išreikštos krūvininkų tranzito vietos. Pridėtinėje diagramoje pateikta log-log skalė, kurioje randamas tranzito laikas t_{tr}. Pritaikyta iš **[124]**.

Paprastai srovės kinetikoje yra aiškiai matoma krūvininkų tranzito vieta ir nekyla sunkumų rasti tranzito laiką t_{tr}, tačiau kartais organinės medžiagos pasižymi labai dispersine krūvininkų pernaša ir tuomet srovės kinetikoje krūvininkų tranzito vietos gali ir nesimatyti. Tokiu atveju galima srovės kinetiką atvaizduoti log(j)-log(t) koordinatėse, tuomet krūvininkų tranzito vieta matoma aiškiau (10 pav.).

Foto-CELIV metodas

Pirmą kartą krūvio ištraukimo tiesiškai kylančia įtampa (ang. charge extraction by linearly increasing voltage) metodas (toliau CELIV) buvo pademonstruotas mokslininko A. Petravičiaus 1975 metais kaip alternatyva lėkio trukmės metodui **[126]**. Vėliau buvo pademonstruota, kad šis metodas puikiai tinka tyrinėjant krūvininkų pernašą mikrokristalinio silicio sluoksniuose ir π-konjuguotų organinių puslaidininkių sluoksniuose **[61, 127]**. Modifikuotas CELIV metodas buvo pritaikytas šviesa generuotų krūvininkų pernašos ir rekombinacijos šviesai jautriose medžiagose tyrimuose ir pavadintas foto-CELIV **[55, 128]**. Įranga, reikalinga foto-CELIV matavimams atlikti yra identiška lėkio trukmės metodo įrangai: generatorius, gebantis generuoti trikampio formos impulsus, šviesos šaltinis ir oscilografas (11 pav.). Šviesos šaltinis ir generatorius yra sinchronizuoti taip, kad būtų galima valdyti užlaikymo trukmę t_{del} tarp šviesos impulso ir generatoriaus impulso. Varijuojant užlaikymo trukmę foto-CELIV metodu galima tyrinėti krūvininkų judrio priklausomybę nuo laiko ir krūvininkų rekombinaciją.

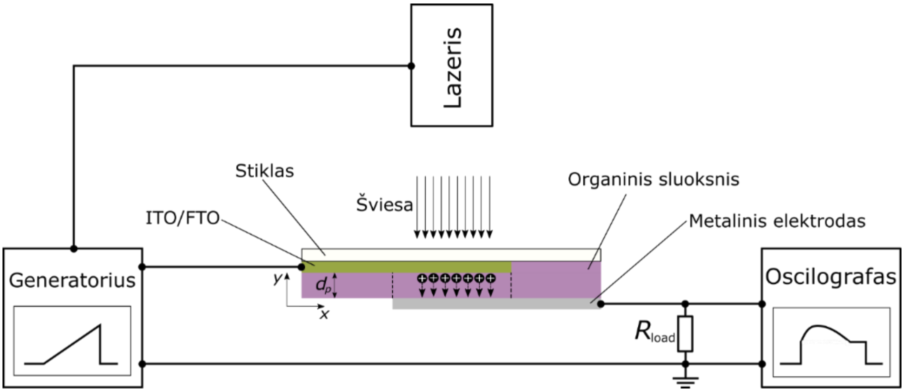

11 pav. Foto-CELIV metodo scheminis vaizdas.

Bandinio, tinkamo tyrinėti foto-CELIV metodu, struktūra yra panaši (kartais ir identiška) į bandinio, tinkamo tyrinėti lėkio trukmės metodu, ir yra sudaryta iš kelių sluoksnių (11 pav.). Paprasčiausia įmanoma struktūra yra diodinė struktūra – vienas sluoksnis tarp dviejų elektrodų, kurių vienas yra peršviečiamas eksperimente naudojamai šviesai. Tokio bandinio geometrinė talpa:

$$C = \frac{\varepsilon_0 \varepsilon_{\mathrm{s}} S}{d_{\mathrm{p}}} \tag{2.2}$$

arba

$$C = \frac{Q}{U} \quad , \tag{2.3}$$

kur S yra elektrodų persiklojimo plotas, ε_{s} ir ε_0 yra atitinkamai tiriamo sluoksnio ir vakuumo dielektrinės skvarbos, d_{p} yra tiriamo sluoksnio storis, Q yra krūvis tiriamame sluoksnyje.

Iš dviejų talpos lygčių išreiškiame krūvį:

$$Q = \frac{U \varepsilon_0 \varepsilon_{\mathrm{s}} S}{d_{\mathrm{p}}} \quad . \tag{2.4}$$

Bandinys kartu su R_{load} sudaro diferencijuojančią *RC* grandinę, kurios atsakas į tiesiškai kylančią įtampą yra stačiakampio formos signalas (žiūrėti 12 pav.). Pirminis srovės tankio šuolis $j(0)$ tuomet gali būti išreikštas atitinkamai:

$$j(0)=\frac{I}{S}=\frac{1}{S}\frac{dQ}{dt}=\frac{1}{S}\frac{d(U\varepsilon_0\varepsilon_\mathrm{s}S/d_\mathrm{p})}{dt}=\frac{\varepsilon_0\varepsilon_\mathrm{s}}{d_\mathrm{p}}\frac{dU}{dt}=\frac{\varepsilon_0\varepsilon_\mathrm{s}A}{d_\mathrm{p}}=\frac{CA}{S}\quad, \qquad (2.5)$$

kur *I* yra srovė, o *A* yra trikampio formos impulso įtampos kilimo greitis.

Jeigu šviesos impulsas yra sugeriamas organinės medžiagos paviršiuje ($\alpha d > 1$), tuomet sugeneruoti krūvininkai yra traukiami per visą bandinio storį d_p dėl atsiradusio elektrinio lauko nuo prijungto trikampio formos impulso.

$$\begin{aligned} d_\mathrm{p}&=\int_0^{t_{tr}} v_{dr}\,dt=\int_0^{t_{tr}}\frac{\mu U}{d_\mathrm{p}}dt=\frac{\mu}{d_\mathrm{p}}\int_0^{t_{tr}}U\,dt=\frac{\mu}{d_\mathrm{p}}\int_0^{t_{tr}}At\,dt=\\ &=\frac{\mu A}{d_\mathrm{p}}\int_0^{t_{tr}}t\,dt=\frac{\mu A t_{tr}^2}{2d_\mathrm{p}}\end{aligned}\quad, \qquad (2.6)$$

kur μ yra krūvininkų judris, v_{dr} yra krūvininkų dreifo greitis, o t_{tr} yra krūvininkų tranzito per bandinį laikas.

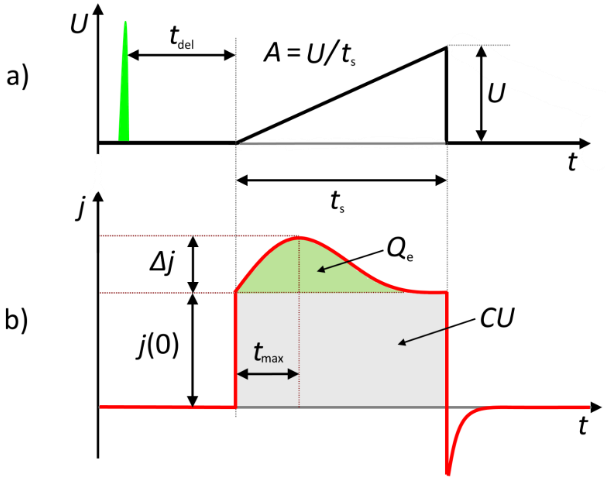

12 pav. Scheminis foto-CELIV metodo srovės kinetikų vaizdas. a) šviesos impulsas ir generatoriaus trikampio formos impulsas; b) foto-CELIV srovės tankio kinetika.

Foto-CELIV metodo srovės tankio kinetika turi ištrauktų krūvininkų suformuotą iškilimą Δj virš pirminio srovės tankio šuolio $j(0)$ (12 pav.). Ištrauktas krūvis suformuoja viršūnę srovės tankio kinetikoje laiko momentu t_{max}, kuris yra lygus krūvininkų tranzito laikui t_{tr}. Tuomet lygtis (2.6) gali būti perrašyta ir gali būti apskaičiuojamas krūvininkų judris:

$$\mu = \frac{2d_{\mathrm{p}}^2}{At_{\mathrm{max}}^2} \quad . \tag{2.7}$$

Ši lygtis tinkama naudoti tik esant tam tikromis eksperimentinėmis sąlygomis. Nuo foto-CELIV sukūrimo buvo atlikta daug eksperimentų naudojant šį metodą ir pasinaudojant surinktais duomenimis kartu su teorinio modeliavimo duomenimis krūvininkų judrio ir krūvininkų tranzito laiko t_{max} sąryšis buvo patikslintas ir pritaikytas įvairioms eksperimentinėms sąlygoms, pavyzdžiui, įvairiems sugerties profiliams **[128]**. Tuomet (2.7) lygtis gali būti perrašyta:

$$\mu = K^2 \frac{2d_{\mathrm{p}}^2}{At_{\mathrm{max}}^2\left(1 + 0.36\left(\frac{\Delta j}{j(0)}\right)\right)} \quad , \tag{2.8}$$

kur $K = t_{\mathrm{max}}/t_{\mathrm{tr}}$ yra korekcijos koeficientas. Priklausomai nuo matuojamo sluoksnio sugerties profilio αd koeficientas K gali įgyti reikšmes nuo $1/\sqrt{3}$ ($\alpha d < 1$) iki 1 ($\alpha d > 1$) (13 pav.).

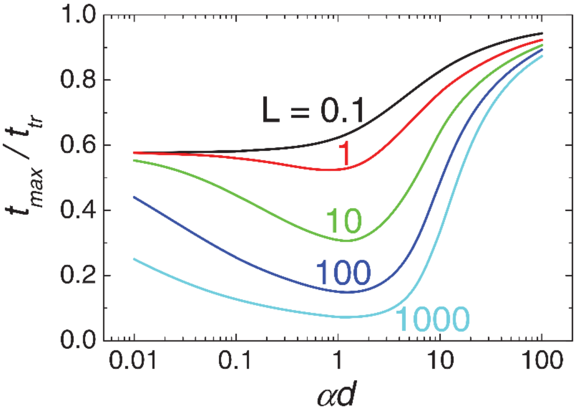

13 pav. Korekcijos koeficiento K priklausomybės nuo sugerties profilio esant skirtingiems šviesos šaltinio intensyvumams teoriniai skaičiavimai. Pritaikyta iš **[128]**.

Vienas didžiausių foto-CELIV metodo pranašumų prieš lėkio trukmės metodą yra galimybė matuoti santykinai dideliu laidumu pasižyminčias medžiagas. Medžiagos, matuojamos lėkio trukmės metodu, krūvininkų relaksacijos laikas τ_σ turi būti didesnis už krūvininkų tranzito laiką t_{tr}, kad būtų išvengta elektrinio lauko persiskirstymo matuojamame bandinyje. Tačiau matuojant foto-CELIV metodu krūvininkų relaksacijos laikas τ_σ gali būti randamas iš srovės kinetikos ir yra lygus laikui, kuriam esant foto-CELIV srovės kinetika pasiekia dvigubą $j(0)$ vertę. Tuomet, pasinaudojant rasta krūvininkų relaksacijos trukme, krūvininkų judris gali būti apskaičiuojamas lygtimi:

$$\mu = \frac{\tau_\sigma d_\mathrm{p}^2}{t_\mathrm{max}^3 A} \quad . \tag{2.9}$$

Foto-CELIV metodas turi dar vieną matavimams naudingą detalę – galimybę keisti užlaikymo trukmę t_del tarp šviesos impulso ir trikampio formos impulso (12 pav.). Ilginant užlaikymo trukmę galima tyrinėti krūvininkų judrio priklausomybę nuo laiko. Tokio pobūdžio tyrinėjimai yra svarbūs netvarkiems organiniams puslaidininkiams, nes juose vysta šuolinė krūvio pernaša per būsenų tankio (DOS) energijos būsenas ir su laiku krūvininkai gali klimpti į gilesnius būsenų tankio lygmenis ir taip gali kisti jų judris ir rekombinacijos sparta.

Krūvininkų rekombinacijos spartos tyrimas foto-CELIV metodu atliekamas stebint, kaip fotogeneruotas krūvis bandinyje gęsta didinant užlaikymo trukmę t_del. Ištrauktas krūvis Q_e randamas atėmus tamsinę srovės kinetiką iš tos, kuri buvo gauta bandinį apšvietus $j - j(0) = \Delta j$. Tuomet suintegravus skirtumą Δj ir žinant geometrinius bandinio parametrus, galima apskaičiuoti krūvininkų tankį n ir taip rasti krūvininkų tankio gesimą $n(t)$. Bimolekulinės rekombinacijos koeficientą B galima rasti pritaikius lygtį:

$$n(t) = \frac{1}{Bt + \frac{1}{n(0)}} \tag{2.10}$$

prie eksperimentiškai gautų krūvininkų tankio gesimo duomenų.

i-CELIV metodas

Visi prieš tai aprašyti tyrimo metodai buvo skirti tyrinėti diodinės struktūros arba saulės elementų struktūros bandinius, kuriuose tiriamasis sluoksnis yra tarp dviejų elektrodų. Tačiau vienos iš dažniausiai naudojamų ir kartais patogiausių bandinio struktūrų krūvininkų pernašos tyrimams yra lauko tranzistoriaus ir metalo-izoliatoriaus-puslaidininkio struktūros, kurios turi izoliatoriaus (dielektriko) sluoksnį. Tiriamasis bandinys, tokiu atveju, turi tik vieną elektrodą arba lauko tranzistoriaus atveju du tokius pačius elektrodus. Būtent struktūroms su izoliatoriaus sluoksniu G. Juška 2012 metais pademonstravo naują metodą pavadinimu i-CELIV krūvininkų pernašai organiniuose puslaidininkiuose tyrinėti **[129]**. Šiuo metodu galima rasti krūvininkų judrį ir tyrinėti krūvininkų pernašą statmena dielektrikui kryptimi (y ašies kryptimi 14 pav.).

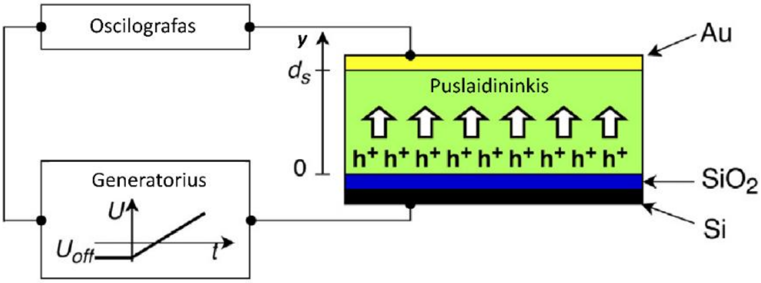

14 pav. Metalo-izoliatoriaus-puslaidininkio struktūros bandinys su skylių transportine medžiaga ir i-CELIV metodo pavyzdinė schema. Pritaikyta iš **[130]**.

Prie bandinio su dielektriko sluoksniu prijungus injektuojančią įtampą U_{off} (14 pav. ir 15 pav.) krūvininkai keliaus per visą bandinio ilgį ir susirinks prie pat dielektriko paviršiaus. Pusiausvyros būsenoje krūvininkų pasiskirstymas gali būti išreikštas:

$$j = \mu kT \frac{dp(x)}{dx} + ep(x)\mu F(x) = 0 \quad , \tag{2.11}$$

kur μ yra krūvininkų judris, k yra Boltzmano konstanta, p yra krūvininkų tankis (šiuo atveju skylių), F yra elektrinis laukas, T yra temperatūra, o e yra elementarusis krūvis.

Pagal Gauss‘o dėsnį:

$$\frac{dF(x)}{dx} = \frac{ep(x)}{\varepsilon_s \varepsilon_0} \quad , \tag{2.12}$$

kur ε_0 ir ε_s yra vakuumo ir puslaidininkio dielektrinės skvarbos, galime perrašyti lygtį:

$$\frac{d^2F(x)}{dx^2} + \frac{e}{kT}F(x)\frac{dF(x)}{dx} = 0 \quad . \tag{2.13}$$

Tuomet randame lygties sprendinius:

$$F(x) = \left(\frac{d_i}{U_{\text{off}}} + \frac{e}{2kT}x\right)^{-1} \tag{2.14}$$

ir

$$p(x) = p(0)\left(1 + \frac{eU_{\text{off}}x}{2kTd_i}\right)^{-2} \quad , \tag{2.15}$$

kur d_i yra dielektriko storis.

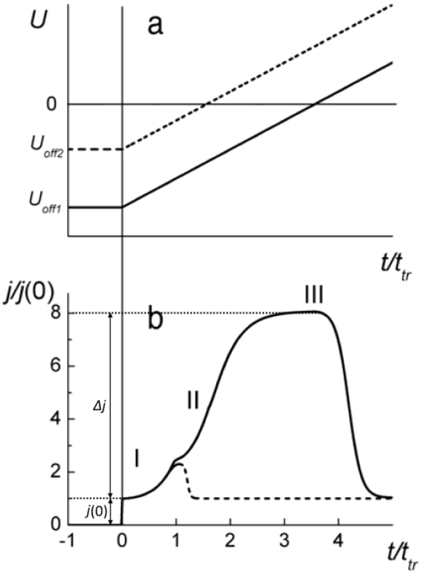

15 pav. Prijungiamos įtampos impulsas i-CELIV metode (a) ir teorinės srovės tankio kinetikos (b). Pritaikyta iš **[129]**.

Kai $eU_{\mathrm{off}} >> kT$ ir dielektriko talpa yra didesnė už puslaidininkio talpą, krūvininkai susirinks prie pat dielektriko paviršiaus. Šis krūvininkų rezervuaras gali būti ištraukiamas tiesiškai kylančia įtampa, kurios kilimo greitis $A = dU/dt$. Erdvinio krūvio ribotos srovės tankis tuomet gali būti išreikštas atitinkamai:

$$j(t) = e\mu p(x,t) + \varepsilon_{\mathrm{s}}\varepsilon_0 \frac{dF(x,t)}{dt} \quad . \tag{2.16}$$

Norint supaprastinti lygtį, suvidurkiname erdvinio krūvio ribotos srovės tankį puslaidininkio sluoksnyje koordinatėse $0<x<d_{\mathrm{s}}$ iki laiko momento t_{sc} (laiko momentas, reikalingas krūvininkams pasiekti elektrodą) su duotomis sąlygomis $F = 0$ ir $x = 0$:

$$j(t) = \frac{\varepsilon_{\mathrm{s}}\varepsilon_0 A}{d_{\mathrm{s}}} + \frac{\varepsilon_{\mathrm{s}}\varepsilon_0 \mu}{2d_{\mathrm{s}}} F^2(d_s,t) = \varepsilon_{\mathrm{s}}\varepsilon_0 \frac{dF(d_{\mathrm{s}},t)}{dt} \quad , \tag{2.17}$$

kur d_{s} yra puslaidininkio sluoksnis.

Kaip matyti 15 pav. (b), yra trys skirtingi regionai i-CELIV metodo srovės tankio kinetikoje. Sprendžiant (2.17) lygtį pirmajame regione, gauname sprendinius:

$$\frac{\Delta j(t)}{j(0)} = \tan^2\left(\frac{t}{t_{\mathrm{tr}}}\right) \quad , \tag{2.18}$$

$$t_{\mathrm{sc}} = 0.92 t_{\mathrm{tr}} \quad , \tag{2.19}$$

kur $j(0)$ yra pirminis srovės tankio šuolis nuo įtampos impulso, Δj yra ištrauktų krūvininkų srovės tankis, o t_{tr} yra krūvininkų tranzito laikas. Mažo krūvio ištraukimo atveju turime:

$$t_{\mathrm{tr}} = d_{\mathrm{s}} \sqrt{\frac{2}{\mu A}\left(1 + \frac{\varepsilon_{\mathrm{s}} d_{\mathrm{i}}}{\varepsilon_{\mathrm{i}} d_{\mathrm{s}}}\right)} \quad , \tag{2.20}$$

kur ε_{i} yra dielektriko sluoksnio dielektrinė skvarba.

Tuomet antrajame srovės tankio kinetikos regione (15 pav. (b)) turime:

$$\frac{\Delta j(t)}{j(0)} = \frac{9}{4}\frac{t^2}{t_{\mathrm{tr}}^2} \quad . \tag{2.21}$$

Ištraukto krūvio srovė visada įsisotins ties dielektriko talpos C_i įkrovimo srovės riba (trečias srovės tankio kinetikos regionas 15 pav. (b)) ir taip galime išreikšti srovės tankį:

$$j_{\mathrm{sat}} = \varepsilon_\mathrm{i}\varepsilon_0 A/d_\mathrm{i} \quad . \tag{2.22}$$

Jeigu visas skylių rezervuaras yra ištraukiamas, srovės tankis pradės mažėti iki kol pasieks pirminio šuolio vertę $j(0)$.

Mažo ištraukto krūvio atveju ($\Delta j \leq j(0)$) srovės tankio kinetika turės viršūnę laiko momentu t_tr (žiūrėti punktyrinę liniją 15 pav. (b)) ir krūvininkų judris gali būti paskaičiuojamas naudojantis (2.20) lygtimi. Jeigu krūvininkų rezervuaras yra didesnis nei krūvis elektrode laiko momentu t_tr, turime EKRS sąlygas ir srovės kinetika aprašoma (2.18) lygtimi. Srovės tankio kinetikos linkis, atskiriantis pirmąjį ir antrąjį regionus, paprastai nėra stebimas dėl dispersinės pernašos organiniuose puslaidininkiuose. Taigi esant $\Delta j >> j(0)$ sąlygai, galima pasirinkti laiko momentą t_1, kuomet srovė pasiekia dvigubą $j(0)$ vertę (žiūrėti 16 pav.), krūvininkų judrio skaičiavimui:

$$t_1 = \frac{\pi}{4} t_{\mathrm{tr}} \quad . \tag{2.23}$$

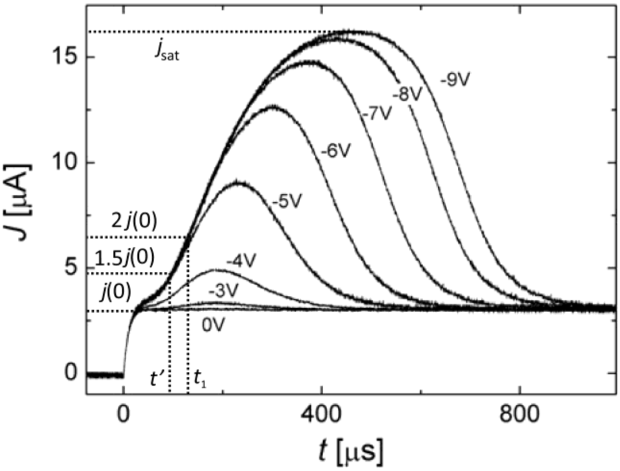

16 pav. Eksperimento metu gautos i-CELIV srovės tankio kinetikos bandinyje su MEH-PPV sluoksniu esant skirtingoms injekcinėms įtampoms. Pritaikyta iš **[129]**.

Jeigu *Δj* yra dydžiu palyginamas su $j(0)$ (dažniausiai tai reiškia, kad organinio puslaidininkio sluoksnis ir dielektriko sluoksnis yra panašaus storio), tuomet laiko momentas t_1 netinkamas judrio skaičiavimui, nes tuo metu jau būna prasidėjęs srovės sotinimasis ir laikas, kada srovė pasiekia dvigubą $j(0)$ vertę yra netikslus. Tuomet geriau pasirinkti laiko momentą *t*’, kada srovės pasiekia 1,5 karto didesnę srovės vertę nei $j(0)$ (žiūrėti 16 pav.). Tuomet tranzito laikas t_{tr} randamas pagal lygtį:

$$t' = \tan^{-1}\left(\frac{1}{\sqrt{2}}\right) t_{\mathrm{tr}} \quad . \tag{2.24}$$

Srovės tankio kinetikos taip pat suteikia informacijos apie geometrinę bandinio talpą $j(0) = C_g A$. Pasinaudojus organinio puslaidininkio sluoksnio ir dielektriko sluoksnio talpų santykiu galima surasti organinio puslaidininkio sluoksnio storį be papildomų matavimų:

$$d_{\mathrm{s}} = \varepsilon_0 \varepsilon_{\mathrm{s}} A \left(\frac{1}{j(0)} - \frac{1}{j_{\mathrm{sat}}}\right) \quad . \tag{2.25}$$

Lauko tranzistorių srovių kinetikų metodas

Pirmą kartą santakos srovės I_D užlaikymo laikas t_d po prijungto stačiakampio įtampos impulso lauko tranzistoriuose buvo aprašytas 1969 metais **[131]**. Vėliau šis srovių kinetikų metodas buvo pritaikytas OLT dariniuose plonų organinių puslaidininkių sluoksnių tyrimams **[132-135]**. Pasinaudojus šiuo metodu galima tyrinėti krūvininkų, judančių prie pat dielektriko ir organinio puslaidininkio sluoksnių sandūros, pernašą (x ašies kryptimi 17 pav (a).)

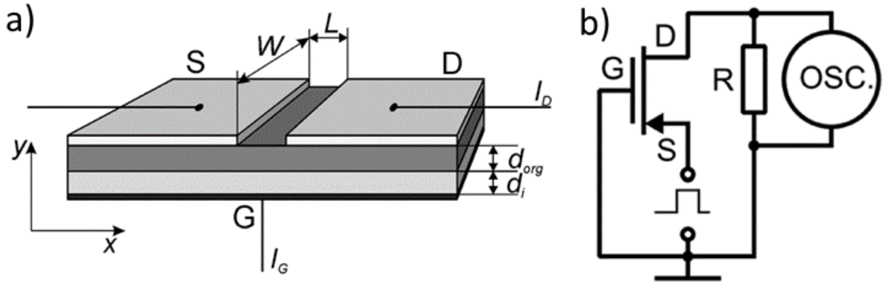

17 pav. a) scheminis OLT struktūros bandinio vaizdas; b) lauko tranzistorių srovių kinetikų metodo sujungimo schema. Pritaikyta iš **[135, 136]**.

Kuomet organinio lauko tranzistoriaus užtūra yra įžeminta, o ištaka yra sujungta su žeme per varžą (17 pav. (b)), stačiakampis įtampos impulsas, prijungtas prie ištakos, įkrovinės užtūros talpą srove:

$$I_{\mathrm{D}}(x,t) = \rho(x,t)\mu F(x,t)W \quad , \tag{2.26}$$

kur $\rho(x,t)$ yra paviršiaus krūvio tankis OLT kanale, $F(x,t)$ yra elektrinio lauko x komponentė, W yra kanalo plotis, o μ yra krūvininkų judris. Kanalas yra suformuojamas iš santakos elektrodo injektuotų krūvininkų. Tuomet galime užrašyti:

$$\rho(x,t) = \frac{\varepsilon_{\mathrm{i}}\varepsilon_0}{d_{\mathrm{i}}}U(x,t) \quad , \tag{2.27}$$

kur $U(x,t)$ yra potencialas, ε_{i} ir ε_0 yra dielektriko ir vakuumo dielektrinės skvarbos, o d_{i} yra dielektriko sluoksnio storis. Iš tęstinumo lygties:

$$\frac{d\rho(x,t)}{dt} = -\frac{dj_{\mathrm{D}}(x,t)}{dx} = -\mu\frac{d}{dt}\big(\rho(x,t)F(x,t)\big) \quad , \tag{2.28}$$

kur $j_{\mathrm{D}}(x,t)$ yra srovės tankis lauko tranzistoriaus kanale. Perrašius iš abiejų lygčių gauname:

$$\mu\frac{d}{dx}\left(U\frac{dU}{dx}\right) = \frac{dU}{dt} \quad . \tag{2.29}$$

Patogumui galime sunormalizuoti kintamus dydžius: $x^* = x/L$, $t^* = t\mu U_{\mathrm{SD}}/L^2$, $U^* = U/U_{\mathrm{SD}}$. Tuomet galime paprasčiau perrašyti lygtį:

$$\frac{1}{2}\frac{d^2U^{*2}}{dx^{*2}} = \frac{dU^*}{dt^*} \quad . \tag{2.30}$$

Skaitinis (2.30) lygties sprendinys parodo erdvinį potencialo $U^*(x)$ pasiskirstymą skirtingais laiko momentais (18 pav. (b)) esant $U^*(0,0) = 1$ pradinei sąlygai. Santakos srovės kinetika pavaizduota 18 pav. (a). Joje matomas laiko momentas t_{d}, kada krūvininkai pasieka santakos elektrodą, kuris naudojamas krūvininkų, judančių išilgai dielektriko paviršiaus, judrio apskaičiavime:

$$\mu = 0.38 \frac{L^2}{t_\mathrm{d} U_\mathrm{SD}} \quad . \tag{2.31}$$

Krūvininkų judris, apskaičiuotas pasinaudojus (2.31) lygtimi, parodo krūvininkų judrį mažo krūvio tankio lauko tranzistoriaus kanale sąlygomis, nes apskaičiuojamas iš pirmųjų kanalu prabėgusių ir santaką pasiekusių krūvininkų.

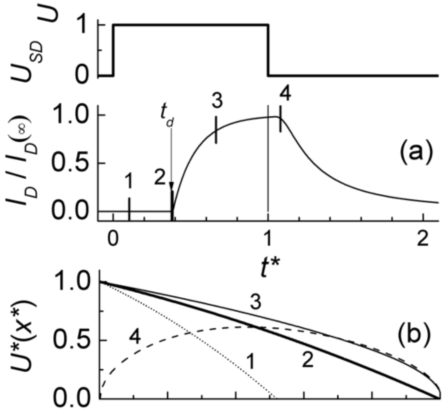

18 pav. Srovės kinetikos lauko tranzistoriaus kanale (a) ir potencialo pasiskirstymo (b) įvairiais laiko momentais, nurodytais (a) dalyje, teoriniai skaičiavimai. Pritaikyta iš **[135]**.

Lauko tranzistorių srovių kinetikų metodas yra patogus ir tuo, kad juo naudojantis gaunama ir įsisotinusios srovės I_D vertė, kuri taip pat gali būti panaudojama krūvininkų judrio skaičiavimui. Srovei lauko tranzistoriaus kanale pasiekus savo soties vertę (žiūrėti 18 pav. (a) 4 dalį) esant tam tikrai prijungtai įtampai, srovę sudarančių krūvininkų judris gali būti paskaičiuojamas atitinkamai:

$$\mu = \frac{d_\mathrm{i} L}{\varepsilon_\mathrm{i} \varepsilon_0 U_\mathrm{SD} W} \frac{\partial I_\mathrm{D}}{\partial U_\mathrm{GS}} \quad , \tag{2.32}$$

kur U_GS yra įtampa tarp ištakos ir užtūros. Kuomet srovė I_D įsisotina, lauko tranzistoriaus kanale turime didelę krūvininkų tankio sąlygą, todėl ir krūvininkų judris, paskaičiuotas iš I_D soties vertės pagal (2.32) lygtį yra judris esant didelio krūvio kanale sąlygomis.

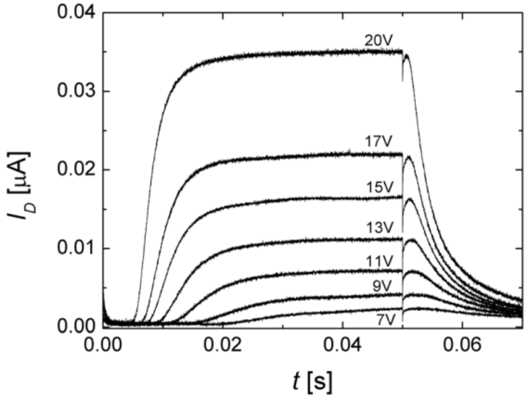

19 pav. Eksperimento metu gautos srovės kinetikos prie skirtingų U_{SD} įtampų RR-P3HT lauko tranzistoriuose. Pritaikyta iš **[135]**.

19 pav. nubrėžtos kelios eksperimento metu gautos santakos srovės kinetikos iš RR-P3HT medžiagos pagamintame lauko tranzistoriuje. Paveiksle aiškiai matosi kaip krūvininkų prabėgimo laikas t_d ir srovės soties vertė keičiasi prijungus didesnę įtampą U_{SD}.

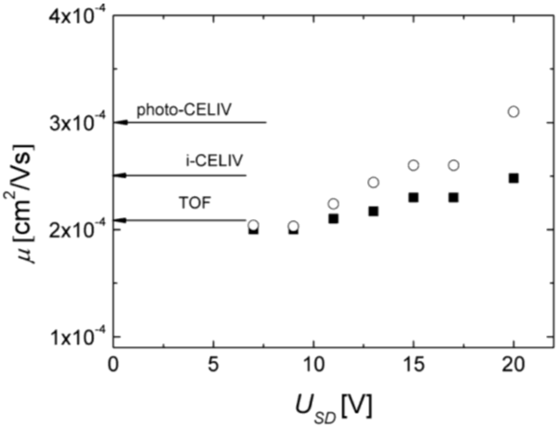

20 pav. Skylių judrio priklausomybė nuo prijungtos įtampos tarp ištakos ir santakos. Juodi kvadratai žymi judrį, paskaičiuotą iš skylių prabėgimo trukmės t_d, o balti apskritimai žymi skylių judrį, paskaičiuotą iš srovės soties vertės. Rodyklės žymi skylių judrį, gautą kitais metodais. Pritaikyta iš **[135]**.

G. Juška eksperimento metu palygino skylių judrį, gautą srovių kinetikų metodu, su skylių judriu, gautu kitais matavimo metodais, RR-P3HT medžiagoje (žiūrėti 20 pav.) **[135]**. Srovių kinetikų metodu gautas judris yra lygiagrečia padėklui kryptimi judančių skylių judris (x ašies kryptimi 17 pav.), kuomet kiti metodai rodo skylių judrį statmena padėklui kryptimi (y ašies kryptimi 17 pav.). Gauti eksperimentiniai rezultatai rodo, kad srovių kinetikų metodas yra patikimas ir patogus metodas krūvininkų pernašos tyrimams organinių puslaidininkių sluoksniuose.

PAGRINDINIAI REZULTATAI IR DISKUSIJA

Krūvininkų pernaša organinių saulės elementų bandiniuose su $CH_3NH_3PbI_3$ perovskito sluoksniu

Perovskitų taikymas organiniuose saulės elementuose vis auga (žiūrėti 2 pav.), tačiau aiškaus supratimo apie krūvio pernašą šiose medžiagose vis dar trūksta. Atrodo, kad kiekvienas naujas pasirodantis straipsnis po truputį augina supratimą, kaip veikia perovskitų medžiagos, ir taip po truputį yra dėliojami blokeliai tiesiamame kelyje į dar efektyvesnius saulės elementus.

Keletas prieš tai publikuotų straipsnių parodė, kad halogenidų perovskitai pasižymi ilgu krūvininkų difuzijos nuotoliu **[78, 79, 81]**. $CH_3NH_3PbI_3$ (arba MAPbI) perovskitų sluoksniai, paruošti pagal receptą, aprašytą skyriuje Bandiniai, turi labai ilgus siaurus kristalus (ilgis didesnis nei 200 µm, žiūrėti 21 pav. c)). Ilgi krūvininkų difuzijos nuotoliai gali būti iš dalies paaiškinti galimybe perovskitų sluoksniuose suformuoti ilgus kristalus. Tačiau, kaip matyti 21 pav. b), perovskito sluoksnio šoninis pjūvis parodo, kad tas pats perovskito sluoksnis pasižymi ir polikristaline sandara. Tokio tipo struktūra, kuri turi polikristalinę struktūrą ir ilgus kristalus paviršiuje, daro stiprią įtaką kitiems ant perovskito paviršiaus liejamiems sluoksniams, kaip tai matyti 21 pav. c). Ant perovskito sluoksnio paviršiaus užlietas Spiro-OMeTAD sluoksnis parodo, koks netolygus yra perovskito sluoksnis ir kaip netolygiai pasiskirsto Spiro-OMeTAD sluoksnis jį užliejus.

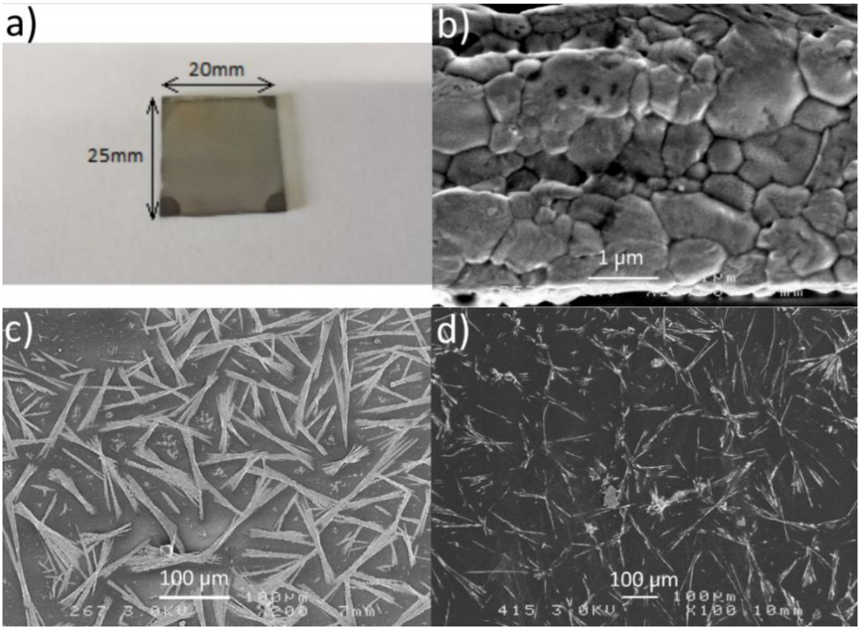

21 pav. $MAPbI_3$ perovskito sluoksnis ant stiklo padėklo: a) bandinio nuotrauka; b) skenuojančio elektronų mikroskopo gautas šoninio pjūvio vaizdas; c) skenuojančio elektronų mikroskopo gautas paviršiaus vaizdas; d) skenuojančio elektronų mikroskopo gautas paviršiaus vaizdas po ant perovskito užlietos Spiro-OMeTAD medžiagos.

Jau anksčiau buvo parodyta, kad metilamonio švino jodido ($MAPbI_3$) perovskitai yra kubinės Pm3m fazės būsenoje temperatūrose, aukštesnėse nei 330 K, žemiau kurios perovskitas patiria fazinį perėjimą į tetragonalinę I4/mcm fazę, o esant žemesnei nei 170 K temperatūrai, tas pats perovskitas pereina į ortorombinę Pnma fazę **[12]**. Skirtumai tarp tetragonalinės ir kubinės fazių yra nežymus PbI_6 oktaedro pasisukimas aplink c ašį ir mažas energijos lygmenų skirtumas. Rentgeno spindulių difrakcijos tetragonalinės ir kubinės perovskito fazių spektrai yra panašūs su keliais skirtumais, kuriuos pagrinde sudaro kubinės fazės spektro viršūnių ties 100 ir 200 išskyrimas į tetragonalinės fazės spektro viršūnes ties atitinkamai 002, 110 ir 004, 220. Taip pat tetragonalinėje fazėje atsiranda dvi naujos viršūnės ties 211 ir 213. Aiškiausias būdas atskirti dvi minėtąsias viršūnes rentgeno spindulių difrakcijos spektre yra mažas nuokrypis nuo 211 plokštumos ties $2\theta \sim 23.5°$.

Toliau šiame darbe $CH_3NH_3PbI_3$ perovskito sluoksniai buvo tiriami rentgeno spindulių difrakcijos spektroskopija (žiūrėti 22 pav.). Spektre esanti viršūnė ties $2\theta = 23.68°$ rodo, kad sluoksnis yra tetragonalinės I4/mcm fazės būsenoje. Viršūnė, esanti ties $2\theta = 14.29°$ gali būti išskaidyta į du komponentus ties $2\theta = 14.14°$ ir $2\theta = 14.29°$, kurie gali būti atitinkamai priskiriami 002 ir 110 plokštumoms **[137]**. Rentgeno spindulių difrakcijos $CH_3NH_3PbI_3$ perovskito sluoksnių, išlietų ant įvairių paviršių (stiklo, FTO ir TiO_2), spektrai parodo, kad minėtieji sluoksniai yra 3D tetragonalinės I4/mcm fazės struktūros. Nesant nė vienos viršūnės rentgeno spindulių difrakcijos spektre, kurios priklausytų PbI_2, rodo, kad perovskito sluoksnyje nėra PbI_2 likučių ir kad perovskito formavimosi reakcijos, metu prekursoriai pilnai sureagavo.

Kai kurių rentgeno spindulių difrakcijos spektro viršūnių intensyvumo padidėjimas tirtame perovskito sluoksnyje, suformuotame ant tankaus TiO_2 sluoksnio, lyginant su perovskito sluoksniais, suformuotais ant stiklo arba FTO sluoksnio, rodo, kad perovskito sluoksnyje ant TiO_2 sluoksnio galimai susiformavo didesni kristalai. Paprastai didesni kristalai lemia geresnę krūvio pernašą dėl taip susidariusių geresnių sąlygų krūvininkų judėjimui.

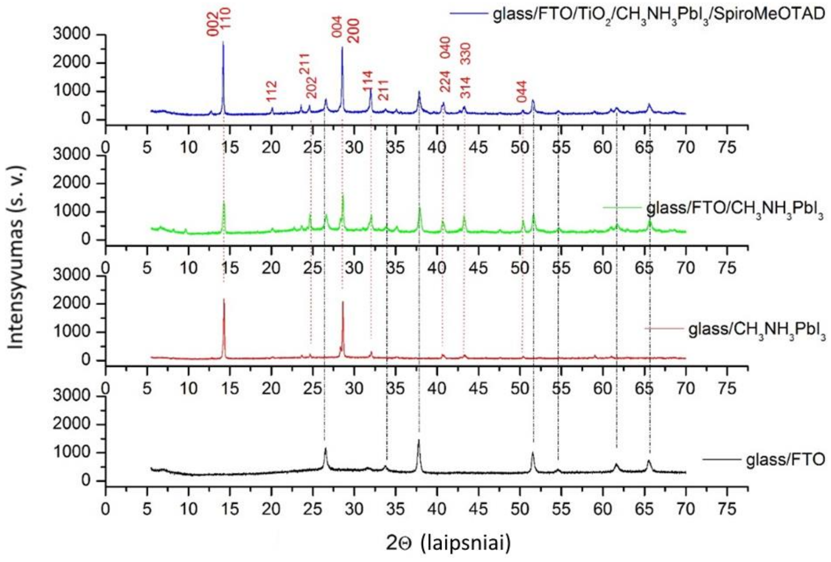

22 pav. $MAPbI_3$ plonų sluoksnių ant įvairių paviršių rentgeno spindulių difrakcijos spektrai. Palyginimui pateiktas ir stiklo/FTO rentgeno spindulių difrakcijos spektras.

Tolimesni saulės elemento struktūros su $MAPbI_3$ perovskito sluoksniu tyrimai buvo nukreipti į krūvininkų pernašą ir šiam tikslui buvo panaudotas foto-CELIV metodas. Prie bandinio prijungus tiesiškai kylančios įtampos impulsą buvo pastebėta, kad srovės tankio kinetikos forma yra būdinga medžiagoms, kurios yra santykinai laidžios elektros srovei. Tuomet iš gautos srovės tankio kinetikos nustatytas Maksvelo relaksacijos laikas τ_σ, kuris yra randamas srovės tankiui pasiekus dvigubą pirminio talpinio šuolio vertę $j(0)$ (žiūrėti 23 pav.)

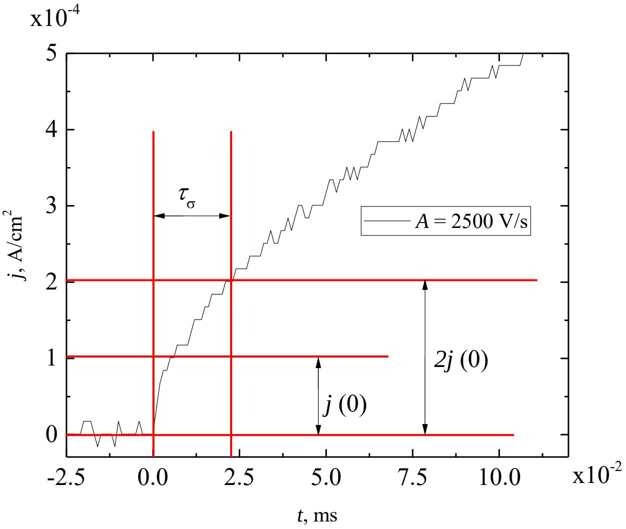

23 pav. Priartinta foto-CELIV metodu gautos srovės tankio kinetikos pradžia saulės elemento bandinyje su $MAPbI_3$ perovskito sluoksniu.

$MAPbI_3$ perovskito sluoksnis pasižymi stipria sugertimi λ = 532 nm bangos ilgio šviesai **[71]**, kuri ir buvo naudojama foto-CELIV matavimuose. Tirto bandinio storis buvo d = 1,2 μm (perovskito sluoksnis kartu su Spiro-OMeTAD sluoksniu), taigi sugerties stipris eksperimente naudotai šviesai buvo atitinkamai $\alpha d \sim 9{,}6$. Kuomet sluoksnis pasižymi tokia stipria sugertimi, šviesa yra sugeriama ir krūvininkai yra generuojami sluoksnio paviršiuje, taigi turime paviršinės sugerties sąlygas, o generuoti krūvininkai yra ištraukiami per visą bandinį ir keliauja per visą jo storį d = 1,2 μm. Foto-CELIV matavimo metu prijungta įtampa buvo parinkta atitinkamai, kad būtų ištraukinėjamos šviesa sugeneruotos skylės per perovskito ir Spiro-OMeTAD sluoksnius.

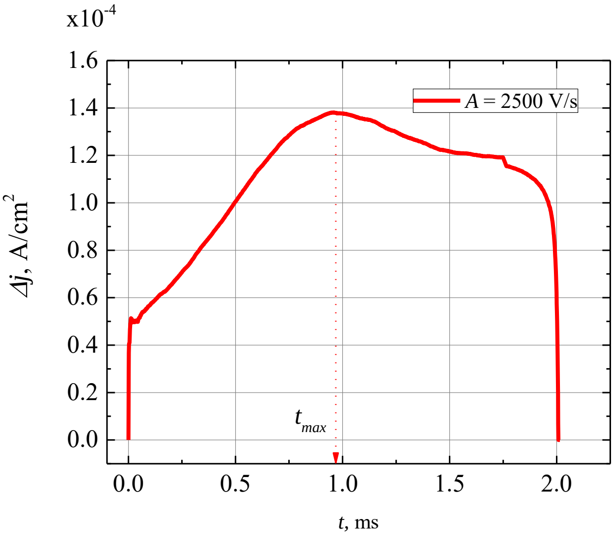

24 pav. Foto-CELIV srovės tankio kinetika *Δj* saulės elemento bandinyje su $MAPbI_3$ perovskito sluoksniu.

24 pav. nubrėžta foto-CELIV metodu gauta fotogeneruotos srovės tankio kinetika $\Delta j = j - j(0)$, kai įtampos kilimo greitis buvo A = 2500 V/s. Skylių tranzito laikas buvo nustatytas iš laiko momento $t_{\max}$, kada susiformavo viršūnė srovės tankio kinetikoje. Skylių judris buvo apskaičiuotas pagal formulę (2.9), nes sluoksnis buvo santykinai laidus ir skaičiavime buvo panaudotas tuo pačiu metodu gauta Maksvelo relaksacijos trukmė τ_σ. Foto-CELIV metodu gautos skylių judrio vertės variavo nuo $\mu = 5.2*10^{-7}$ cm^2/Vs iki $\mu = 8.5*10^{-7}$ cm^2/Vs, priklausomai nuo įtampos kilimo greičio A (žiūrėti 25 pav.). Vien tik Spiro-OMeTAD medžiagoje išmatuotas skylių judris siekia nuo $\mu = 1.69*10^{-6}$ cm^2/Vs iki $\mu = 4*10^{-5}$ cm^2/Vs, priklausomai nuo sluoksnio struktūros ir naudoto matavimo metodo **[138, 139]**.

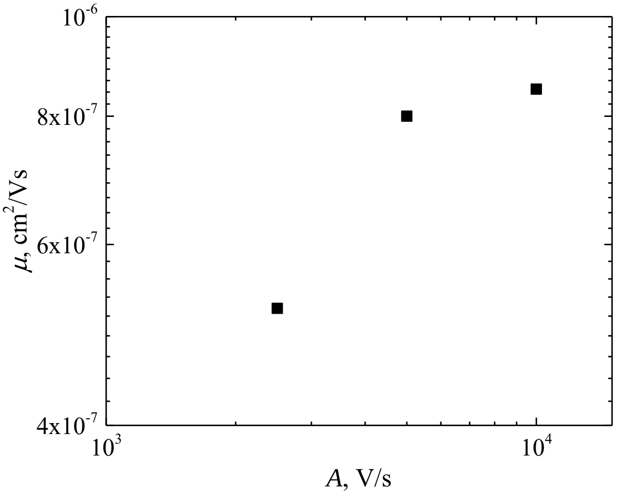

25 pav. Skylių judris $CH_3NH_3PbI_3$ perovskito ir Spiro-OMeTAD sluoksniuose, gautas foto-CELIV metodu esant keliems skirtingiems įtampos kilimo greičiams *A*.

Skylių judris $CH_3NH_3PbI_3$ perovskitų sluoksniuose siekia net 500-800 cm^2/Vs teoriniuose modeliavimuose, tačiau eksperimentuose gautos skylių judrių vertės yra gerokai mažesnės, o kartais siekia tik $4.8*10^{-6}$ cm^2/Vs, kaip buvo parodyta lauko tranzistoriaus bandiniuose anksčiau, kaip buvo aptarta šios disertacijos 1.4 skyriuje. Taigi skylių judris perovskitų sluoksniuose labai priklauso nuo tiriamos struktūros ir jos vidinės morfologijos.

Šiame darbe skylių judris $CH_3NH_3PbI_3$ perovskito ir Spiro-OMeTAD sluoksniuose siekė $\mu = 8.5*10^{-7}$ cm^2/Vs. Ši vertė yra mažesnė nei prieš tai publikuotos vertės tiek $CH_3NH_3PbI_3$ perovskito sluoksniuose, tiek Spiro-OMeTAD medžiagoje. Kelios priežastys nulėmė šią mažesnę skylių judrio vertę matuotose saulės elementų bandiniuose: Spiro-OMeTAD sluoksnio netvarka, $CH_3NH_3PbI_3$ perovskito sluoksnio polikristališkumas ir netvarkingai išsidėstę kristalitai polikristalinės sandaros sluoksnyje bei Spiro-OMeTAD ir perovskito sluoksnio sandūra (žiūrėti 21 pav.). Šios sluoksnių morfologijos ypatybės nulėmė padidėjusį prilipimo lygmenų tankį ir taip sumažino skylių judrį.

Krūvininkų pernašos anizotropijos tyrimas PCPDTBT lauko tranzistorių bandiniuose

Organiniai lauko tranzistorių bandiniai su PCPDTBT medžiaga buvo pagaminti su viršutiniais ištakos ir santakos elektrodais, kad būtų galima krūvininkų pernašą tyrinėti dviem kryptimis: lygiagrečia ir statmena padėklui kryptimis (dielektriko sluoksnis šiuo atveju ir yra padėklas). Statmena padėklui kryptimi krūvininkų pernašos tyrimui buvo naudojamas i-CELIV metodas, o lygiagrečia padėklui kryptimi – lauko tranzistorių srovių kinetikų metodas. Eksperimento metu naudota įranga leido atlikti matavimus aukštesnėse temperatūrose siekiančiose iki 200 °C, todėl ja naudojantis taip pat buvo ištirta krūvininkų pernašos priklausomybė nuo temperatūros. PCPDTBT medžiaga yra dažnai naudojama kaip skylių pernašos medžiaga tūrinėse heterosandūrose kartu su PCBM **[15, 16]**, todėl tyrinėti skylių pernašą PCPDTBT yra aktualu ir šiame darbe pagamintuose organiniuose lauko tranzistoriaus bandiniuose tiek i-CELIV metodu, tiek lauko tranzistorių srovių kinetikų metodu buvo tyrinėjama skylių pernaša atitinkamai parenkant įtampų poliarumus, kad į bandinį būtų injektuojamos ir po to iš jo ištraukiamos skylės.

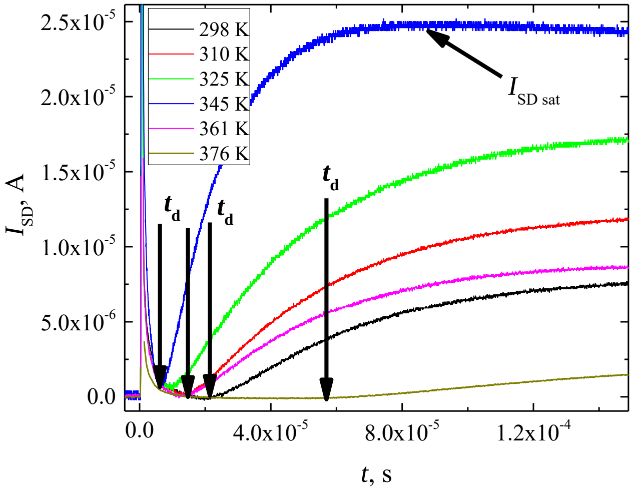

26 pav. PCPDTBT organinio lauko tranzistoriaus bandinio srovės kinetikos prie kelių skirtingų temperatūrų, gautos naudojant lauko tranzistorių srovių kinetikų metodą.

Kelios lauko tranzistorių srovių kinetikų eksperimento metu prie skirtingų temperatūrų gautos srovės kinetikos pavaizduotos 26 pav. Juodomis rodyklėmis pažymėtos vietos rodo įsisotinusios srovės $I_{\mathrm{SD\ sat}}$ tranzistoriaus kanale vertę ir laiko momentus t_{d}, kuomet į ištaką injektuotos skylės pasiekia santakos elektrodą. Srovės I_{SD} augimas kanale po laiko momento t_{d} vyksta dėl skylių tankio didėjimo iki kol srovė pasiekia savo maksimalią vertę $I_{\mathrm{SD\ sat}}$. Lauko tranzistorių srovių kinetikų metodas turi kelis privalumus, lyginant jį su standartinėmis voltamperinėmis lauko tranzistoriaus charakteristikomis. Visų pirma krūvininkų judris, surastas naudojantis t_{d} vertėmis nėra paveiktas didelio krūvininkų tankio lauko tranzistoriaus kanale, todėl galimas palyginimas su krūvininkų judriu, gautu naudojant i-CELIV metodą. Taip pat pirmieji kanalu keliaujantys krūvininkai yra jautresni prilipimo lygmenims, kurių tankis sluoksnyje gali kisti besikeičiant sluoksnio morfologijai.

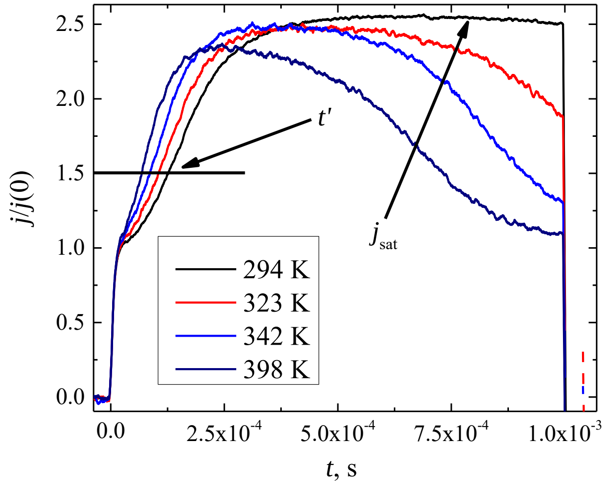

27 pav. PCPDTBT organinio lauko tranzistoriaus bandinio srovės kinetikos prie kelių skirtingų temperatūrų, gautos naudojant i-CELIV metodą.

Kelios srovės tankio kinetikos gautos i-CELIV metodu prie skirtingų temperatūrų pavaizduotos 27 pav. Po pirminio talpinio šuoliuko $j(0)$ dėl prie bandinio prijungto tiesiškai kylančios įtampos impulso, srovės tankis toliau auga dėl iš bandinio ištraukiamų skylių ir laiko momentas t' randamas srovės tankio kinetikoje, kuomet srovės tankio vertė pasiekia 1,5*$j(0)$ vertę. Srovės tankio kinetikos pradžia yra supertiesinė, o tai rodo, kad matavimo metu buvo EKRS sąlygos ir visos injektuotos skylės buvo pasiekusios organinio sluoksnio ir dielektriko sandūrą, o ištraukimo metu jos keliavo per visą organinio sluoksnio storį d_{s} **[129]**.

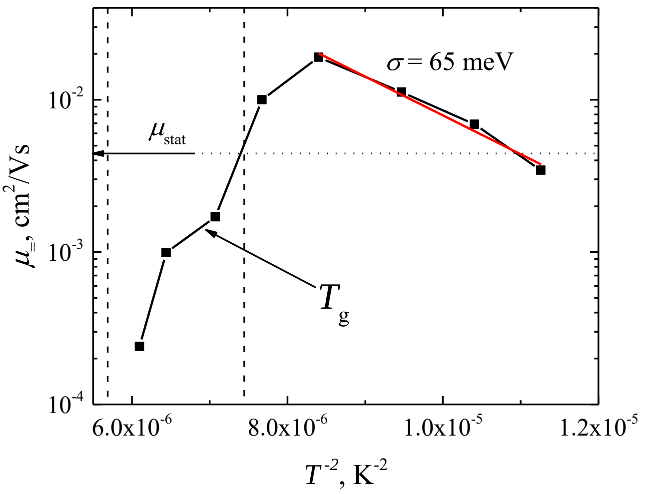

28 pav. Skylių judrio lygiagrečia padėklui kryptimi priklausomybė nuo temperatūros.

28 pav. pavaizduota, kokią įtaką skylių judriui lygiagrečia padėklui kryptimi $\mu_=$ daro aukštesnė nei kambario temperatūra. Atvaizduotos judrio priklausomybės ašys parinktos atitinkamai tokios, kad būtų galima rasti energetinės netvarkos parametrą σ, pagal Bässler‘io šuolinės pernašos modelį **[32]**. PCPDTBT medžiagoje skylių judris lygiagrečia padėklui kryptimi pradžioje didėja kartu su kylančia temperatūra (žiūrėti 28 pav.). Toks judrio didėjimas didėjant temperatūrai yra normalus organinėms netvarkioms medžiagoms, pasak Bässler‘io modelio, dėl temperatūra aktyvuojamos skylių pernašos **[32]**. Temperatūrai pasiekus 72 °C tiek skylių judris lygiagrečia padėklui kryptimi, tiek srovė $I_{\rm SD\ sat}$ OLT bandinio kanale pasiekia savo didžiausias vertes ir toliau didėjant temperatūrai pradeda mažėti (srovės mažėjimas matomas 26 pav.). Saulės elemento, pagaminto iš PCPDTBT:PCBM heterosandūros, efektyvumo sumažėjimas panašioje temperatūroje publikuotas ir anksčiau **[140]**. Minėtame straipsnyje autoriai nurodo, kad trumpo jungimo srovė ir efektyvumas saulės elemente sumažėjo dėl sumažėjusio sluoksnio laidumo. Iš rezultatų, pavaizduotų 28 pav., galime teigti, kad laidumas heterosandūroje galėjo sumažėti dėl skylių judrio sumažėjimo PCPDTBT medžiagoje. Skylių judrio lygiagrečia padėkui kryptimi sumažėjimas prie aukštesnių temperatūrų įvyksta dėl PCPDTBT sluoksnio morfologijos pakitimų ir tai bus aptarta vėlesnėse pastraipose. Taip pat palyginimui skylių judris $\mu_{\rm stat}$ buvo paskaičiuotas pasinaudojant turimomis

$I_{\mathrm{SD\ sat}}$ vertėmis (žiūrėti 28 pav.). Panašios skylių judrio vertės kambario temperatūroje rodo, kad skylių judris neturi žymios priklausomybės nuo skylių tankio OLT bandinio kanale.

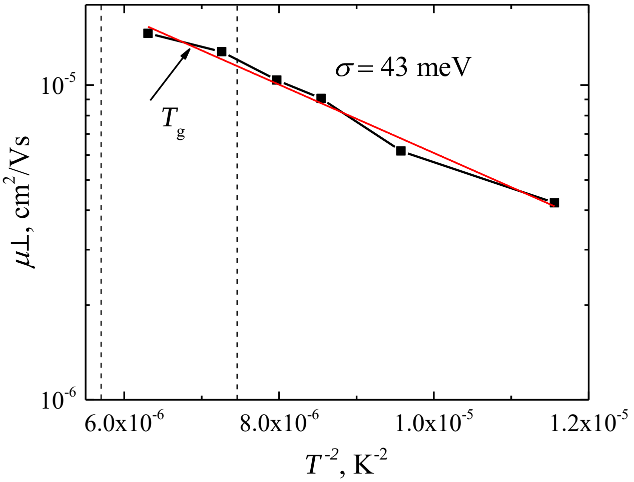

29 pav. Skylių judrio statmena padėklui kryptimi priklausomybė nuo temperatūros.

Priešingai nei skylių judris lygiagrečia padėklui kryptimi, skylių judris statmena padėklui kryptimi $\mu_{\perp}$ didėja visame kaitinimo diapazone (žiūrėti 29 pav.). Taip pat skylių judrio vertė statmena padėklui kryptimi yra 800 kartų mažesnė nei lygiagrečia padėklui kryptimi kambario temperatūroje. Toks didelis judrio skirtumas parodo, kad skylės keliauja skirtingomis sąlygomis skirtingomis kryptimis, o taip pat skiriasi ir sluoksnio morfologija priklausomai nuo krypties. Norint ištirti netvarką kiekvienai iš skylių judėjimo krypčių, buvo suskaičiuoti energetinės netvarkos parametrai σ kiekvienai judėjimo krypčiai pagal Bässler‘io modelio formules netvarkioms medžiagoms.

Lygtyje (1.3) yra du pagrindiniai parametrai, nuo kurių priklauso krūvininkų judris: elektrinis laukas ir temperatūra. Energetinės netvarkos parametrai σ buvo rasti atidėjus tiesę skylių judrio priklausomybėje nuo temperatūros (žiūrėti 28 pav. ir 29 pav.). Patikimos pozicinės netvarkos parametro Σ vertės negalima rasti dėl to, kad nei lauko tranzistorių srovių kinetikų metode, nei i-CELIV metode negalima apskaičiuoti tikslios elektrinio lauko stiprio vertės. Elektrinio lauko įtaka skylių pernašai buvo nepaisoma, nes skylių judrio vertės buvo apskaičiuotos esant silpnam arba nuliniam elektriniam laukui. Skylių judrio lygiagrečia padėklui kryptimi vertės buvo ekstrapoliuotos iš skylių judrio priklausomybės nuo tarp ištakos ir santakos prijungtos įtampos U_{SD}, taip buvo rasta judrio vertė prie nulinio elektrinio lauko (judrio priklausomybė nuo prijungtos įtampos pateikta Fig. S1 Appendix 1). Skylių judrio priklausomybė nuo prijungtos įtampos U_{SD} taip pat rodo, kad judris neturi žymios priklausomybės nuo elektrinio lauko matuotame diapazone. Lauko tranzistorių srovių kinetikų metode prijungta įtampa yra proporcinga elektriniam laukui bandinyje, tačiau negalima apskaičiuoti konkrečios vertės, nes elektrinis laukas kinta su laiku ir su koordinate iki kol srovė kanale įsisotina. Elektrinio lauko įtaka skylių judriui statmena padėklui kryptimi buvo atmesta dėl to, kad didelė elektrinio lauko dalis buvo sukoncentruota ant dieletriko sluoksnio, be to kuomet yra ištraukiamos pirmosios skylės laiko momentu t_{tr}, įtampa, krentanti ant bandinio yra žema dėl to, kad tai yra tik pati tiesiškai kylančios įtampos impulso pradžia, taigi elektrinis laukas PCPDTBT sluoksnyje yra labai silpnas.

Paprastai yra laikoma, kad krūvininkų judėjimas OLT kanale yra 2D judėjimas, nes krūvininkai yra labai prispausti prie dielektriko paviršiaus. Tačiau E.V. Emelianova **[141]** savo teoriniame modeliavime parodė, kad kuomet krūvininkai OLT kanale šuoliuoja per Gausinį pasiskirstymą turintį būsenų tankį (DOS) ir krūvininkų koncentracija yra žema, krūvininkų judrio priklausomybė nuo temperatūros yra labai panaši į priklausomybę 3D atveju temperatūrose, artimose kambario temperatūrai, esant tam pačiam energetiniam netvarkos parametrui σ. Lauko tranzistorių srovių kinetikų metodas atitinka žemos krūvininkų koncentracijos sąlygas, o apskaičiuota energinės netvarkos parametro vertė σ (2D atvejis) yra tik <10% mažesnė nei 3D atveju, pasak E.V. Emelianova teorinio modeliavimo rezultatų. Taigi šioje disertacijoje apskaičiuotos energinės netvarkos parametrų vertės $\sigma_{=} = 65$ meV lygiagrečia padėklui kryptimi ir $\sigma_{\perp} = 43$ meV statmena padėklui kryptimi gali būti lyginamos tarpusavyje.

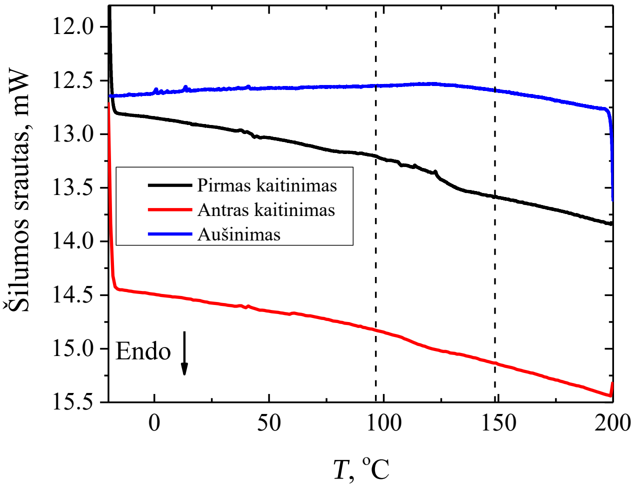

30 pav. PCPDTBT medžiagos diferencinės skenuojančios kalorimetrijos termogramos.

Norint išsiaiškinti, kodėl skylių judris lygiagrečia padėklui kryptimi pasiekus tam tikrą temperatūrą pradėjo mažėti, buvo atlikti diferencinės skenuojančios kalorimetrijos (DSK) matavimai PCPDTBT medžiagai temperatūrų ruože nuo -20 °C iki 200 °C (253 K to 473 K). Pokytis termogramose prasideda prieš 100 °C ir baigiasi virš 120 °C, o iš antro kaitinimo termogramos buvo nustatyta stiklėjimo temperatūra $T_g = 112{,}5$ °C (žiūrėti 30 pav. ir 31 pav.). Nežymus ir lėtas pokytis DSK termogramoje ties stiklėjimo temperatūra yra tikėtinas rezultatas polimerams dėl jų didelės molekulinės masės, tačiau skylių judrio matavimai rodo, kad pasikeitimas morfologijoje yra itin svarbus skylių pernašai PCPDTBT medžiagoje (žiūrėti 28 pav.). Iš skylių judrio lygiagrečia padėklui kryptimi $\mu_=$ galima spręsti, kad struktūriniai pokyčiai išlietame PCPDTBT sluoksnyje įvyksta net žemesnėse temperatūrose nei stiklėjimo temperatūra T_g ir kad tie pokyčiai morfologijoje daro stiprią įtaką skylių pernašai. Mažas pokytis DSK termogramose nereiškia, kad sluoksnio morfologija pakito nežymiai, nes po kaitinimo DSK matavimų metu buvo matyti pokyčiai polimero medžiagoje. Prieš kaitinimą polimero būsena buvo paskiri grūdeliai, o po kaitinimo polimeras susiliejo į vieną didesnį gabalą medžiagos ir atrodė lyg būtų sulydytas. Nors ir buvo matomi pokyčiai PCPDTBT medžiagoje po DSK matavimų, tačiau skylių pernašos matavimuose naudotame bandinyje nebuvo matoma jokių pasikeitimų išlietame polimero sluoksnyje. i-CELIV metodas leidžia sekti bandinio sluoksnio storį (žiūrėti lygtį (2.25)) kiekvieną kartą, kai tik yra atliekamas skylių judrio matavimas. Matuojant i-CELIV metodu nebuvo pastebėta jokių PCPDTBT sluoksnio storio pasikeitimų skirtingose temperatūrose, todėl galima teigti, kad temperatūra nesukėlė jokių įtrūkimų ar pažeidimų sluoksnyje, kurie būtų atsispindėję sluoksnio talpos pakitime.

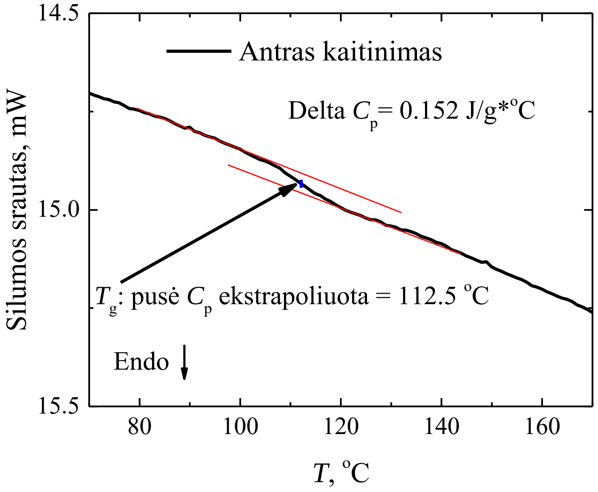

31 pav. Priartinta antro kaitinimo PCPDTBT medžiagos diferencinės skenuojančios kalorimetrijos termograma, iš kurios nustatyta stiklėjimo temperatūra T_g.

DSK matavimai rodo, kad skylių judrio mažėjimas lygiagrečia padėklui kryptimi yra sluoksnio morfologijos pakitimų aukštesnėje nei 72 °C temperatūroje padarinys. Papildomai atominės jėgos mikroskopo matavimai buvo atlikti PCPDTBT OLT bandiniuose prieš ir po matavimų, kurių metu bandinys buvo kaitinamas. Sluoksnio paviršius buvo labai lygus prieš matavimus ir po matavimų ($\Delta z \leq 5$ nm) ir nebuvo pastebėta jokių žymių pasikeitimų sluoksnio paviršiuje po kaitinimo, tik tai, kad po kaitinimo sluoksnis tapo dar lygesnis (paviršiaus vidutinis nelygumas prieš kaitinimą buvo 1,2 nm, o po kaitinimo 0,3 nm), tačiau tai yra tikėtina didžiajai daliai organinių puslaidininkinių medžiagų, kurios buvo pakaitintos virš savo stiklėjimo temperatūros (atominės jėgos mikroskopo nuotraukos yra pateiktos Fig. S2 Appendix 1). Taigi PCPDTBT sluoksnio vidinė morfologija ir jo pokyčiai nebuvo matomi sluoksnio paviršiuje. Taip pat buvo atlikti papildomi rentgeno spindulių difrakcijos matavimai sluoksnio kristališkumui įvertinti. Ir kaitintas, ir nekaitintas sluoksniai turėjo tik vieną plačią viršūnę ties maždaug

2θ ~ 20° (duomenys pateikti Fig. S3 Appendix 1). Iš šių duomenų galima teigti, kad abu sluoksniai buvo gana amorfinės būsenos ir neturėjo aiškios kristalinės sandaros.

Kylant temperatūrai, kyla ir skylių šuoliavimo per būsenas dažnis dėl temperatūra aktyvuojamo skylių transporto prigimties, tačiau dėl temperatūros pakitusi PCPDTBT sluoksnio morfologija kartu pakeičia ir būsenų tankį medžiagoje ir taip daro stiprią įtaką skylių pernašai. Todėl skylių judris lygiagrečia padėklui kryptimi pradeda mažėti (žiūrėti 28 pav.). Pakartotiniai kaitinimai ir skylių judrio matavimai buvo atlikti norint įsitikinti, kad judrio vertė pakito dėl morfologijos pokyčių (duomenys pateikti Fig. S4 Appendix 1). Skylių judris statmena padėklui kryptimi didėja visame kaitinimo diapazone, tačiau skylių judrio vertės yra ženkliai mažesnės (žiūrėti 29 pav.). Šie rezultatai rodo, kad PCPDTBT sluoksnyje skirtingomis kryptimis (lygiagrečia ir statmena padėklui kryptimis) keliaujančios skylės tai daro skirtingomis sąlygomis. Tai gali būti paaiškinta išlieto sluoksnio morfologija, kuri nulėmė kad dėl sąveikos su SiO_2 sluoksniu susiformavo geresnės sąlygos skylių transportui netoli dielektriko sluoksnio nei visame sluoksnio tūryje. Tokiu atveju vidutinis π jungčių atstumas sumažėja ir todėl skylių judris ženkliai padidėja. Skylių judrio skirtumas skirtingomis kryptimis yra paslėptas judrio daugiklyje μ_0, kuris nurodo skylių šuolių tikimybę. Daugiklis μ_0 yra proporcingas pernašos integralo kvadratui ir yra nulemtas vidutinio erdvinio būsenų tarpusavio atstumo ir molekulių sluoksnyje orientacijos **[142]**. Galima daryti išvadą, kad lygiagrečia padėklui kryptimi vidutinis erdvinis būsenų tarpusavio atstumas ir PCPDTBT molekulių orientacija sluoksnyje nulemia geresnes sąlygas skylių pernašai nei statmena padėklui kryptimi. Eksperimentiniai rezultatai taip pat rodo, kad šios geresnės skylių pernašai sąlygos yra gerokai jautresnės aukštesnei temperatūrai. Temperatūra morfologiją paveikia taip, kad molekulės sluoksnyje keičia savo padėtį arčiau dielektriko sluoksnio nei visame sluoksnio tūryje. Panaši tendencija, kuomet skirtinga morfologija susiformuoja skirtingomis sluoksnio kryptimis jau buvo pastebėta ir kitose medžiagose **[13]**. Viename straipsnyje **[143]** autoriai parodė, kad esant tam tikroms sąlygoms PCPDTBT medžiaga chloroforme gali suformuoti tam tikrus nanodalelių dydžio kristalus, o tai galėtų daryti įtaką iš tokio tirpalo išlieto sluoksnio morfologijai. Šiame disertacijos skyriuje pristatyti rezultatai suderinami su kitų autorių rezultatais PCPDTBT ar panašios struktūros medžiagoms **[13, 14, 144]**. Taip pat turėtų būti atkreiptas dėmesys į morfologijos pokyčius PCPDTBT medžiagoje, jeigu iš šios medžiagos bus gaminami įtaisai, kurie bus naudojami aplinkoje, kurioje bus aukštesnės nei kambario temperatūros.

Krūvininkų pernaša ir rekombinacija plonasluoksnėse PBDTTPD struktūrose

Šiame darbe buvo tiriami dviejų tipų bandiniai su gryna PBDTTPD medžiaga: OLT struktūros bandiniai ir diodinės struktūros bandiniai (žiūrėti 6 pav. ir 7 pav.). PBDTTPD medžiaga yra dažnai naudojama kaip skylių transporto medžiaga kartu su PCBM tūrinių heterosandūrų saulės elementų tyrimuose **[19]**, todėl yra svarbu plačiau patyrinėti skylių pernašą šioje medžiagoje. Taigi tiek OLT struktūros bandiniuose, tiek diodinės struktūros bandiniuose įtampos buvo parinktos atitinkamai, kad į tiriamus sluoksnius būtų injektuojamos ir iš jų ištraukiamos skylės.

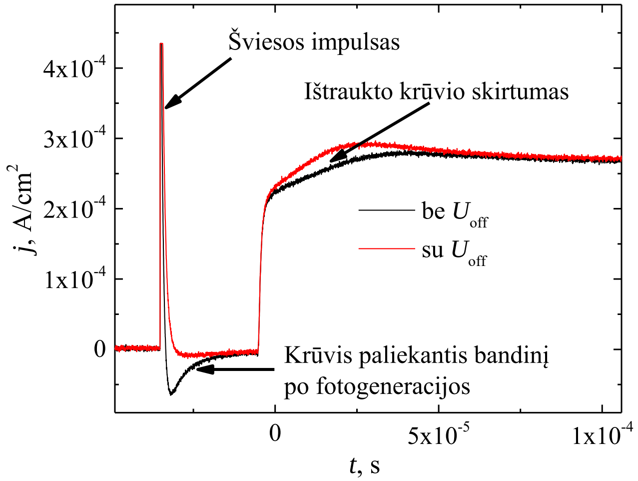

32 pav. Foto-CELIV metodu gautos srovės tankio kinetikos be prijungto priešįtampio ir su prijungtu priešįtampiu U_{off}.

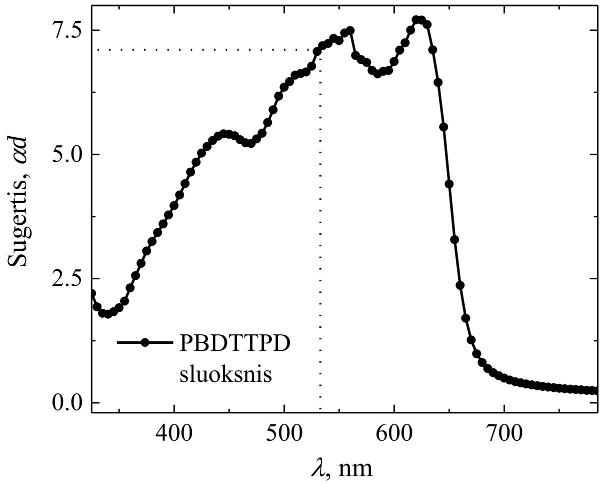

33 pav. PBDTTPD sluoksnio sugerties spektras. Taškinių linijų susikirtimo vieta žymi bangos ilgį, kuris buvo naudojamas foto-CELIV ir lėkio trukmės eksperimentų metu.

Pirmasis šio darbo tikslas buvo ištirti skylių judrį ir rekombinaciją diodinės struktūros bandiniuose su gryna PBDTTPD medžiaga ir tam buvo panaudoti lėkio trukmės ir foto-CELIV metodai. Foto-CELIV eksperimento metu prie bandinio buvo prijungta išorinė įtampa U_{off} = 0,7 V, kad būtų kompensuotas bandinyje esantis vidinis elektrinis laukas ir šviesa generuoti krūvininkai neišeitų iš bandinio iki ištraukimo tiesiškai kylančia įtampa momento (žiūrėti 32 pav.). Taip pat svarbu paminėti, kad suformuotas PBDTTPD sluoksnis turi stiprią sugertį šviesai (žiūrėti 33 pav.), kuri buvo naudota lėkio trukmės ir foto-CELIV matavimuose, ir į tai buvo atsižvelgta apskaičiuojant skylių judrį. Kelios foto-CELIV metodu gautos srovės tankio kinetikos prie skirtingų užlaikymo trukmių t_{del} atvaizduotos 34 pav. Juodu apskritimu apibrėžtos srovės tankio kinetikų „uodegos“, kurios net ir pasibaigus ištraukiančiai įtampai nenusileidžia iki pirminio srovės tankio šuolio $j(0)$, parodo, kad bandinyje egzistuoja skylės, kurias labai sunku ištraukti tiesiškai kylančia įtampa iš jų užimtų būsenų. Šios „uodegos“ yra stebimos net ir prie skirtingų užlaikymo trukmių t_{del} ir tai yra dispersinės skylių pernašos PBDTTPD medžiagoje požymis, kuris susijęs su šviesa generuotų skylių persiskirstymu su laiku per energijos būsenų tankį (DOS) **[145]**.

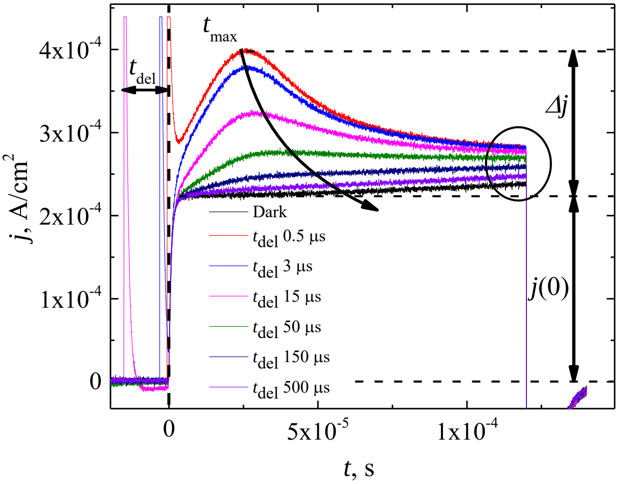

34 pav. Kelios foto-CELIV srovės tankio kinetikos prie skirtingų užlaikymo trukmių t_{del}.

Skylių judris PBDTTPD sluoksnyje gautas foto-CELIV metodu buvo lygus $\mu_{\mathrm{ph}} = 4{,}8*10^{-4}$ cm^2/Vs ir tai yra panaši vertė į anksčiau publikuotas šios medžiagos skylių judrio vertes ($1{,}4*10^{-4}$ cm^2/Vs – $7{,}5*10^{-4}$ cm^2/Vs) **[146-149]**. Tačiau reikia atkreipti dėmesį į tai, kad anksčiau publikuotos vertės buvo gautos PBDTTPD medžiagos mišiniuose su kitomis medžiagomis ir taip pat skyrėsi matavimo metodai. Šiame darbe matuotas skylių judris grynoje PBDTTPB medžiagoje mažėjo didėjant užlaikymo trukmei t_{del} (žiūrėti 35 pav. ir atitinkamai didėjantis skylių tranzito laikas t_{max} matomas 34 pav.). Skylių judris mažėja dėl skylių persiskirstymo per energijos būsenų tankį su laiku. Kol užlaikymo trukmės t_{del} yra santykinai mažos (iki kelių µs) turime gana didelį skylių skaičių, kurios keliauja per bandinį didesniu greičiu ($\mu_{\mathrm{ph}} = 4{,}8*10^{-4}$ cm^2/Vs) ir kurios sudaro foto-CELIV srovės tankio kinetikoje matomą smailę (žiūrėti raudonos ir mėlynos spalvos srovės tankio kinetikas 34 pav.), ir santykinai mažą kiekį lėtesnių skylių, kurios neištraukiamos su tiesiškai kylančia įtampa (žiūrėti „uodegas“ 34 pav.). Toliau didėjant užlaikymo trukmei t_{del} dėl rekombinacijos mažėja bendras skylių skaičius bandinyje (žiūrėti kinetikų plotą virš tamsinės srovės tankio kinetikos 34 pav.), tačiau taip pat didėja ir lėtesnių skylių indėlis į fotosrovę, lyginant su greitesnių skylių skaičiumi. Galima daryti išvadą, kad be užlaikymo trukmės skylių judris būtų artimas skylių judriui išmatuotam TOF metodika $\mu_{\mathrm{tof}} = 10^{-3}$ cm^2/Vs (TOF matavimo duomenys pateikti Fig. S5 ir Fig. S6 Appendix 2), nes judrio vertės gautos foto-CELIV metodu artėja link TOF metodu gautos vertės (žiūrėti mėlyną punktyrinę liniją 35 pav.). Šie duomenys rodo, kad iš grynos PBDTTPD medžiagos pagamintame diodinės struktūros bandinyje energijos būsenų tankio uodega mažėja gerokai lėčiau nei Gausinio pasiskirstymo atveju. Skylės, esančios gilesniuose lygmenyse nėra stebimos TOF srovės kinetikoje, tačiau stebimos foto-CELIV srovės tankio kinetikoje, kai užlaikymo trukmė t_{del} yra pakankamai ilga, kad didžioji dalis didesnio judrio skylių jau yra arba rekombinavusios, arba relaksavusios į gilesnius lygmenis. Medžiagos, kuriose yra dviejų energijos būsenų tankių pasiskirstymų superpozicija, pavyzdžiui, Gausinio ir eksponentinio pasiskirstymų, buvo tirtos ir anksčiau **[47]**. Verta paminėti, kad TOF ir foto-CELIV metodų naudojimas kartu išryškina tokias skylių pernašos savybes, kurios kitu atveju liktų nepastebėtos, ir tai parodo, kokie svarbūs yra krūvininkų pernašos tyrimai plačiame laikų diapazone.

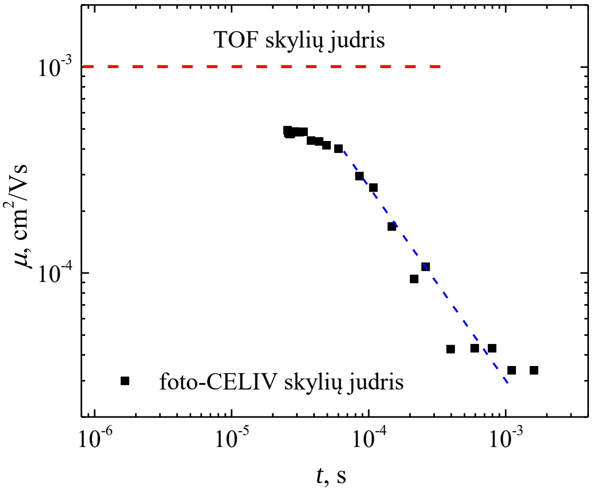

35 pav. Skylių judris diodinės PBDTTPD struktūros bandinyje. Laiko ašis yra t_{del} + t_{max}, o tai yra didžiosios skylių dalies gyvavimo trukmė nuo fotogeneracijos iki ištraukimo iš bandinio.

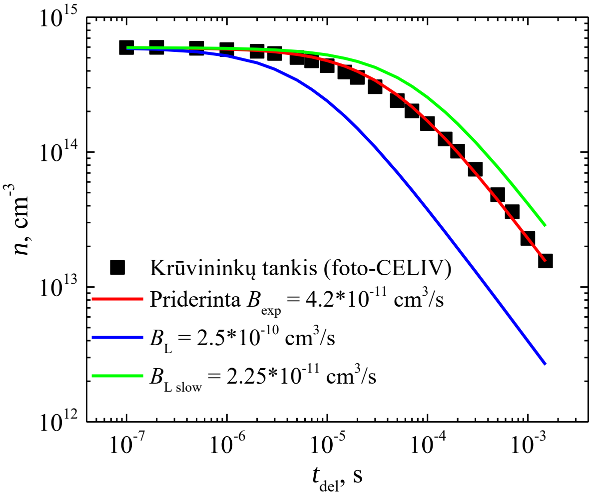

36 pav. Ištrauktų skylių tankio priklausomybė nuo užlaikymo trukmės t_{del}.

Krūvininkų tankio mažėjimas, kuris gali būti matuojamas foto-CELIV metodu keičiant užlaikymo trukmę t_{del}, leidžia tyrinėti krūvininkų rekombinaciją diodinės PBDTTPD struktūros bandinyje (36 pav.). Naudojantis (2.10) lygtimi bimolekulinės rekombinacijos koeficientas B_{exp} gali būti įvertintas priderinus lygtį prie eksperimento metu gautų rezultatų (žiūrėti raudoną liniją 36 pav.). Per visą t_{del} intervalą matuotas skylių judris sumažėja dešimt kartų, tačiau priderintas bimolekulinės rekombinacijos koeficientas B_{exp} tinka visame matuotame intervale. Priderinto bimolekulinės rekombinacijos koeficiento vertė buvo B_{exp} = 4,2*10^{-11} cm^3/s, tačiau apskaičiuotas Lanževeno rekombinacijos koeficientas buvo B_L = 2,5 * 10^{-10} cm^3/s (skaičiavimui buvo panaudotas skylių judris μ_{ph} = 4,8*10^{-4} cm^2/Vs), o tai rodo, kad rekombinacijos sparta bandinyje buvo 6 kartus mažesnė nei rodo skylių judris. Paprastai redukuota Lanževeno rekombinacija yra stebima organinių puslaidininkių heterosandūrose ir yra aiškinama atskirtomis viena nuo kitos skylių ir elektronų keliavimo trajektorijomis **[150, 151]** arba mažiausio judrio krūvininkų įtaka rekombinacijos spartai **[57]**, arba skylių ir elektronų krūvio delokalizacijos ištįsimu energijos būsenose, dalyvaujančiose krūvio pernašoje **[22]**. Tačiau šie aiškinimai dažniausiai pateikiami bandiniams su tūrinėmis heterosandūromis ir aiškinama keliomis eilėmis redukuota Lanževeno rekombinacijos sparta, kai šiame darbe buvo tirta gryna medžiaga, o rekombinacijos sparta mažesnė 6 kartais. Kaip jau buvo minėta, 34 pav. ir 35 pav. rodo, kad šviesa generuotos skylės su laiku relaksuoja, užima gilesnes energijos būsenas, per kurias šuoliavimas yra apsunkintas, todėl ir stebimas skylių judrio mažėjimas. Lanževeno rekombinacijos koeficientas, apskaičiuotas naudojantis mažiausiu skylių judriu $\mu_{ph} = 4{,}35{*}10^{-5}$ cm^2/Vs, gautu matuojant foto-CELIV metodu, buvo lygus $B_{L\ slow} = 2{,}25{*}10^{-11}$ cm^3/s (žiūrėti žalią liniją 36 pav.) ir yra tik du kartus mažesnis nei rekombinacijos koeficientas B_{exp}. Galima manyti, kad rekombinacijos koeficientas B_{exp} yra susietas su efektiniu skylių judriu, kuris yra artimas mažiausiam skylių judriui foto-CELIV matavime, nes dalis skylių su didesniu judriu pabėga iš rekombinacijos zonos prieš joms rekombinuojant, o skylės su mažesniu judriu pasilieka ir dalyvauja rekombinacijos procese, todėl ir gaunama redukuota bimolekulinės rekombinacijos koeficiento vertė.

Skylių judris PBDTTPD OLT struktūros bandiniuose su viršutiniais ištakos ir santakos auksiniais elektrodais buvo tirtas lauko tranzistorių srovių kinetikų ir i-CELIV metodais. Nors PBDTTPD medžiaga yra perspektyvi skylių transportinė medžiaga, tačiau buvo publikuotas tik vienas straipsnis, kuriame buvo tyrinėjama skylių pernaša OLT struktūros bandinyje **[152]**. Straipsnio autoriai tyrinėjo PBDTTPD medžiagos ir P3HT mišinį, kuriame išmatuotas skylių judris variavo nuo $4{,}36{*}10^{-4}$ cm^2/Vs iki $8{,}69{*}10^{-3}$ cm^2/Vs kambario temperatūroje. Aukštesnės skylių judrio vertės straipsnyje gautos bandiniuose su didesne P3HT dalimi mišinyje.

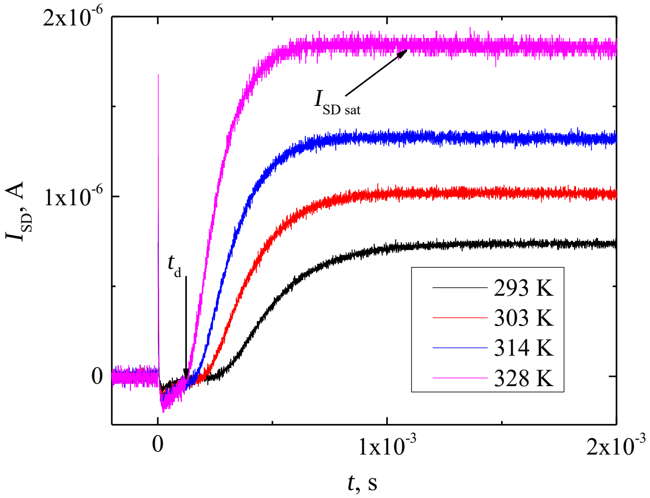

37 pav. I_{SD} srovės kinetikos prie skirtingų temperatūrų OLT struktūros bandinyje su OTS pasluoksniu (U_{SD} = 80 V).

Pasinaudojant eksperimento metu gauta t_d verte (žiūrėti 37 pav.) apskaičiuotas skylių judris kambario temperatūroje siekė $\mu_{tr} = 9.3*10^{-5}$ cm^2/Vs bandinyje be OTS pasluoksnio ir $\mu_{tr} = 1.5*10^{-4}$ cm^2/Vs bandinyje su OTS pasluoksniu. Pateiktos skylių judrio vertės yra ekstrapoliuotos vertės iš judrio priklausomybės nuo prijungtos įtampos U_{SD}, kad būtų gautas skylių judris prie nulinio elektrinio lauko (duomenys pateikti Fig. S7 Appendix 2). Skylių judris taip pat gali būti randamas ir iš $I_{SD\ sat}$ vertės ir palyginimui kambario temperatūroje OLT struktūros bandinyje su OTS pasluoksniu apskaičiuotas skylių judris siekė $\mu_{sat} = 1{,}1*10^{-4}$ cm^2/Vs (žiūrėti 38 pav.). Iš t_d vertės apskaičiuotas judris atitinka mažo krūvininkų tankio OLT kanale sąlygas, o iš $I_{SD\ sat}$ vertės apskaičiuotas judris atitinka didelio krūvininkų tankio OLT kanale sąlygas. Kadangi abejomis sąlygomis gautas skylių judris buvo labai panašus, galima teigti, kad PBDTTPD medžiagoje skylių judris neturi stiprios priklausomybės nuo skylių tankio ir tai patvirtina, kad foto-CELIV metodu gautas skylių judrio mažėjimas yra dėl skylių persiskirstymo per energijos būsenų tankį, o ne dėl skylių mažėjimo dėl rekombinacijos.

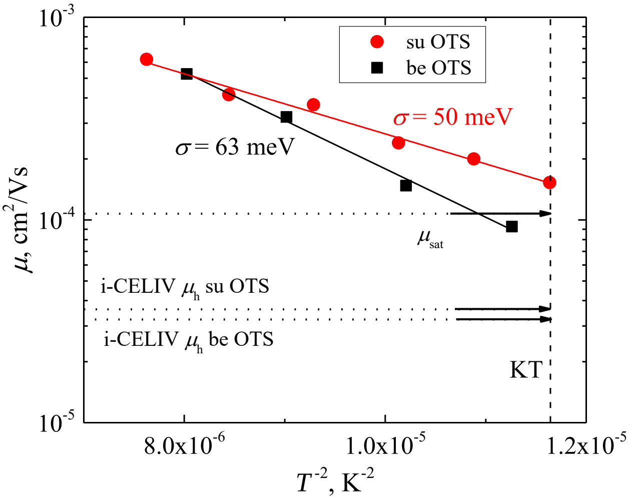

38 pav. Skylių judrio, gauto lauko tranzistorių srovių kinetikų metodu, priklausomybė nuo temperatūros. Rodyklės žymi skylių judrį, gautą i-CELIV metodu, ir skylių judrį, gautą iš voltamperinės charakteristikos. Brūkšninė linija žymi kambario temperatūrą.

i-CELIV metodu gautas skylių judris ženkliai nesiskyrė tarp OLT struktūros bandinių be OTS pasluoksnio ir su OTS pasluoksniu, o skylių judrio vertės buvo atitinkamai lygios $\mu_h = 3{,}2*10^{-5}$ cm^2/Vs ir $\mu_h = 3{,}4*10^{-5}$

cm^2/Vs (žiūrėti 38 pav.). i-CELIV eksperimento metu skylės nekeliauja OLT kanalu netoli dielektriko ir organinio sluoksnių sandūros, todėl skylių judrio vertės yra panašios bandiniuose be OTS pasluoksnio ir bandiniuose su OTS pasluoksniu, kai OLT kanalu keliaujančių skylių judris bandiniuose su OTS pasluoksniu buvo didesnis nei bandiniuose be OTS pasluoksnio. Skylių judrio vertė, gauta i-CELIV metodu yra artima mažiausiai skylių judrio vertei, gautai foto-CELIV metodu, tačiau bendrai yra mažesnė už skylių judrį, apskaičiuotą pasinaudojus t_d verte (palyginimui žiūrėti 35 pav. ir 38 pav.). Skirtumas tarp i-CELIV skylių judrio ir lauko tranzistorių srovių kinetikų skylių judrio atsiranda todėl, kad i-CELIV eksperimento metu injektuotos skylės yra laikomos ilgai (net ilgiau nei didžiausia t_{del} vertė foto-CELIV eksperimente) prieš jas ištraukiant, o lauko tranzistorių srovių kinetikų eksperimento metu skylės juda iš karto jas injektavus į bandinį.

Iš skylių judrio priklausomybės nuo temperatūros nustatyti dielektriko ir PBDTTPD sluoksnių sandūros būsenų tankio energetinės netvarkos parametrai σ parodė, kad energetinė netvarka OLT struktūros bandinio su OTS pasluoksniu σ = 50 meV yra mažesnė nei bandinio be OTS pasluoksnio σ = 63 meV (žiūrėti 38 pav.). Taigi, galima teigti, kad dėl sumažėjusios energetinės netvarkos bandinyje (sumažėjusios dielektriko paviršiaus defektų įtakos skylių pernašai) su OTS pasluoksniu pagerėjo sąlygos skylių pernašai OLT kanale, todėl skylių judris buvo didesnis. Norint įsitikinti, kad skylių judriui įtakos nedarė sluoksnio morfologijos pokyčiai aukštesnėje temperatūroje, buvo atlikti diferencinės skenuojančios kalorimetrijos matavimai, kuriuose nebuvo stebimas joks pasikeitimas PBDTTPD medžiagoje kaitinimo diapazone (DSK duomenys pateikti Fig. 8 Appendix 2). Būsenų tankio energetinės netvarkos parametras σ PBDTTPD medžiagos mišinyje su PCBM jau buvo matuotas anksčiau ir gautos vertės buvo σ = 65 meV ir σ = 81 meV dviems skirtingoms PBDTTPD medžiagos molekulinėms konfigūracijoms **[146]**. OLT struktūros bandiniuose su gryna PBDTTPD medžiaga būsenų tankio energetinės netvarkos parametras σ = 63 meV dielektriko ir organinio sluoksnių sandūroje yra mažesnis nei mišinio su PCBM σ = 81 meV. Taip pat dielektriko SiO_2 paviršiaus modifikavimas OTS medžiaga sumažina būsenų tankio energetinės netvarkos parametrą σ nuo 63 meV iki 50 meV.

IŠVADOS

Šiame darbe buvo parodyta, kad FTO/TiO_2/$CH_3NH_3PbI_3$/Spiro-OMeTAD/Au struktūros saulės elemento bandinyje fotogeneruotų skylių ištraukimas yra apsunkintas dėl perovskito ir organinio sluoksnių morfologijos ypatumų. Spiro-OMeTAD sluoksnio netvarka, $CH_3NH_3PbI_3$ perovskito sluoksnio polikristališkumas ir viduje polikristalinio sluoksnio netvarkingai išsidėstę kristalitai bei perovskito ir organinio sluoksnių tarpusavio sandūra apsunkina skylių transportą po fotogeneracijos dėl padidėjusio prilipimo lygmenų tankio ir dėl to sumažėjusio skylių judrio, lyginant su skylių judriu kiekvienoje iš šių medžiagų atskirai.

Skylių judris kambario temperatūroje PCPDTBT sluoksnyje OLT struktūros bandinyje yra 800 kartų didesnis lygiagrečia padėklui kryptimi nei statmena padėklui kryptimi. Nedidelis būsenų tankio energetinės netvarkos parametrų $\sigma_{=}$ ir $\sigma_{\perp}$ skirtumas atitinkamomis kryptimis rodo, kad skylių judrio skirtumas yra nulemtas judrio daugiklio μ_0, kuris nurodo skylių šuolių tikimybę. Taigi lygiagrečia padėklui kryptimi vidutinis erdvinis būsenų tarpusavio atstumas ir molekulių orientacija sluoksnyje yra gerokai palankesnė skylių pernašai nei statmena padėklui kryptimi. Dėl morfologinių sluoksnio pokyčių aukštesnėje nei kambario temperatūroje (virš 72 °C) skylių, judančių OLT kanalu netoli PCPDTBT/SiO_2 sandūros, judris sumažėja.

OLT struktūros bandinyje pagamintame su PBDTTPD sluoksniu skylių judris kambario temperatūroje padidėja nuo μ_{tr} = 9,3*10^{-5} cm^2/Vs iki μ_{tr} = 1,5*10^{-4} cm^2/Vs po to, kai SiO_2 dielektriko paviršius yra modifikuojamas OTS medžiaga. Skylių judris padidėja dėl dielektriko ir organinių sluoksnių sandūros būsenų tankio energetinės netvarkos parametro σ sumažėjimo nuo 63 meV iki 50 meV dėl sumažėjusios dielektriko paviršiaus defektų įtakos ir dėl to pagerėjusių sąlygų skylių pernašai šuoliuojant per būsenas.

Fotogeneruotų krūvininkų rekombinacijos tyrimas diodinės PBDTTPD struktūros bandinyje rodo, kad sluoksnyje vyksta bimolekulinė rekombinacija, kurios koeficientas yra B_{exp} = 4,2*10^{-11} cm^3/s visame matuotame laiko intervale, ilgesniame nei trys eilės. Šis koeficientas yra 6 kartus mažesnis nei iš skylių judrio apskaičiuotas Lanževeno rekombinacijos koeficientas ir tai parodo, kad rekombinacijos sparta bandinyje yra redukuota. Redukcija vyksta dėl skylių su didesniu judriu pabėgimu iš rekombinacijos zonos prieš joms rekombinuojant, o tik likusios lėtesnės skylės dalyvauja rekombinacijos procese, taip sumažindamos rekombinacijos spartą. Skirtingų judrių skylės bandinyje egzistuoja dėl to, kad fotogeneruotos skylės su laiku lėtėja dėl skylių persiskirstymo per energijos būsenų tankį PBDTTPD sluoksnyje.

REFERENCES

[1] Samuel E. Root, Suchol Savagatrup, Adam D. Printz, Daniel Rodriquez, Darren J. Lipomi, Mechanical Properties of Organic Semiconductors for Stretchable, Highly Flexible, and Mechanically Robust Electronics, *Chemical Reviews*, **117**, 9, 6467−6499 (2017).

[2] Mark A. M. Leenen, Volker Arning, Heiko Thiem, Jürgen Steiger, Ralf Anselmann, Printable electronics: flexibility for the future, *Physica Status Solidi A*, **206**, 4, 588–597 (2009).

[3] Yan Qian, Xinwen Zhang, Dianpeng Qi, Linghai Xie, Bevita K. Chandran, Xiaodong Chen, Wei Huang, Thin-film organic semiconductor devices: from flexibility to ultraflexibility, *Science China Materials*, **59**, 589–608 (2016).

[4] Shida Yang, Weifei Fu, Zhongqiang Zhang, Hongzheng Chen, Chang-Zhi Li, Recent advances in perovskite solar cells: efficiency, stability and lead-free perovskite, *Journal of Materials Chemistry A*, **5**, 23, 11462–11482 (2017).

[5] Federico Bella, Gianmarco Griffini, Juan-Pablo Correa-Baena, Guido Saracco, Michael Grätzel, Anders Hagfeldt, Stefano Turri, Claudio Gerbaldi, Improving efficiency and stability of perovskite solar cells with photocurable fluoropolymers, *Science*, **354**, 6309, 203–206 (2016).

[6] Anna Köhler, Heinz Bässler, Electronic Processes in Organic Semiconductors, Wiley-VCH Verlag GmbH & Co., (2015).

[7] The number of publications was calculated in “Dimensions” online database (https://app.dimensions.ai/discover/publication), date of checking [2020-09-14].

[8] The number of publications was calculated in “Web of Science” online database (https://app.webofknowledge.com/author/search), date of checking [2020-09-14].

[9] A. Kojima, K. Teshima, Y. Shirai, T. Miyasaka, Organometal halide perovskites as visible-light sensitizers for photovoltaic cells, *Journal of the American Chemical Society*, **131**, 17, 6050–6051 (2009).

[10] Y. Chen, H. T. Yi, X. Wu, R. Haroldson, Y. N. Gartstein, Y. I. Rodionov, K. S. Tikhonov, A. Zakhidov, X. -Y. Zhu, V. Podzorov, Extended carrier lifetimes and diffusion in hybrid perovskites revealed by Hall effect and photoconductivity measurements, *Nature Communications*, **7**, 12253 (2016).

[11] Xin Yu Chin, Daniele Cortecchia, Jun Yin, Annalisa Bruno, Cesare Soci, Lead iodide perovskite light-emitting field-effect transistor, *Nature Communications*, **6**, 7383 (2015).

[12] Tom Baikie, Yanan Fang, Jeannette M. Kadro, Martin Schreyer, Fengxia Wei, Subodh G. Mhaisalkar, Michael Graetzel, Tim J. White, Synthesis and crystal chemistry of the hybrid perovskite $(CH_3NH_3)PbI_3$ for solid-state sensitised solar cell applications, *Journal of Materials Chemistry A*, **1**, 18, 5628–5641 (2013).

[13] Colin R. Bridges, Michael J. Ford, Elayne M. Thomas, Christian Gomez, Guillermo C. Bazan, Rachel A. Segalman, Effects of Side Chain Branch Point on Self Assembly, Structure, and Electronic Properties of High Mobility Semiconducting Polymers, *Macromolecules*, **51**, 21, 8597–8604 (2018).

[14] Florian S. U. Fischer, Daniel Trefz, Justus Back, Navaphun Kayunkid, Benjamin Tornow, Steve Albrecht, Kevin G. Yager, Gurpreet Singh, Alamgir Karim, Dieter Neher, Martin Brinkmann, Sabine Ludwigs, Highly Crystalline Films of PCPDTBT with Branched Side Chains by Solvent Vapor Crystallization: Influence on Opto-Electronic Properties, *Advanced Materials*, **27**, 7, 1223–1228 (2015).

[15] M. Wright, R. Lin, M. J. Y. Tayebjee, X. Yang, B. P. Veettil, X. Wen, A. Uddin, Effect of Blend Composition on Binary Organic Solar Cells Using a Low Band Gap Polymer, *Journal of Nanoscience and Nanotechnology*, **15**, 3, 2204–2211 (2015).

[16] Mauro Morana, Matthias Wegscheider, Alberta Bonanni, Nikos Kopidakis, Sean Shaheen, Markus Scharber, Zhengguo Zhu, David Waller, Russell Gaudiana, Christoph Brabec, Bipolar Charge Transport in PCPDTBT-PCBM Bulk-Heterojunctions for Photovoltaic Applications, *Advanced Functional Materials*, **18**, 12, 1757–1766 (2008).

[17] Young-Se Jang, Hoon-Seok Seo, Ying Zhang, Jong-Ho Choi, Characteristics of tetracene-based field-effect transistors on pretreated surfaces, *Organic Electronics*, **10**, 2, 222–227 (2009).

[18] Jungyoon Seo, Seungtaek Oh, Giheon Choi, Hyun Ho Choi, Hwa Sung Lee, Polymeric Conformation of Organic Interlayers as a Determining Parameter for the Charge Transport of Organic Field-Effect Transistors, *Macromolecular Research*, **28**, 670–676 (2020).

[19] Serge Beaupré, Ahmed Najari, Mario Leclerc, High open-circuit voltage solar cells using a new thieno[3,4-c] pyrrole-4,6-dione based copolymer, *Synthetic Metals*, **182**, 1, 9–12 (2013).

[20] Jonathan A. Bartelt, Jessica D. Douglas, William R. Mateker, Abdulrahman El Labban, Christopher J. Tassone, Michael F. Toney, Jean M. J. Fréchet, Pierre M. Beaujuge, Michael D. McGehee, Controlling Solution-Phase Polymer Aggregation with Molecular Weight and Solvent Additives to Optimize Polymer-Fullerene Bulk Heterojunction Solar Cells, *Advanced Energy Materials*, **4**, 9, 1301733 (2014).

[21] Jonathan A. Bartelt, Zach M. Beiley, Eric T. Hoke, William R. Mateker, Jessica D. Douglas, Brian A. Collins, John R. Tumbleston, Kenneth R. Graham, Aram Amassian, Harald Ade, Jean M. J. Fréchet, Michael F. Toney, Michael D. McGehee, The Importance of Fullerene Percolation in the Mixed Regions of Polymer–Fullerene Bulk Heterojunction Solar Cells, *Advanced Energy Materials*, **3**, 3, 364–374 (2013).

[22] D. H. K. Murthy, A. Melianas, Z. Tang, G. Juška, K. Arlauskas, F. Zhang, L. D. A. Siebbeles, O. Inganas, T. J. Savenije, Origin of reduced bimolecular recombination in blends of conjugated polymers and fullerenes, *Advanced Functional Materials*, **23**, 34, 4262–4268 (2013).

[23] R. Österbacka, A. Pivrikas, G. Juška, K. Genevičius, K. Arlauskas, H. Stubb, Mobility and density relaxation of photogenerated charge carriers in organic materials, *Current Applied Physics*, **4**, 5, 534-538 (2004).

[24] N. Nekrašas, K. Genevičius, M. Viliūnas, G. Juška, Features of current transients of photogenerated charge carriers, extracted by linearly increased voltage, *Chemical Physics*, **404**, 24, 56–59 (2012).

[25] Jianhui Hou, Hsiang-Yu Chen, Shaoqing Zhang, Gang Li, Yang Yang, Synthesis, Characterization, and Photovoltaic Properties of a Low Band Gap Polymer Based on Silole-Containing Polythiophenes and 2,1,3-Benzothiadiazole, *Journal of the American Chemical Society*, **130**, 48, 16144–16145 (2008).

[26] J. Stark, W. Steubing, Fluorescence and light electrical sensitivity of organic substances, *Physikalische Zeitschrift*, **9**, 481 (1908).

[27] A. Bernanose, M. Comte, P. Vouaux, A new method of emission of light by certain organic compounds, *Journal de Chimie Physique*, **50**, 64 (1953).

[28] C. K. Chiang, C. R. Fincher Jr., Y. W. Park, A. J. Heeger, H. Shirakawa, E. J. Louis, S. C. Gau, Alan G. MacDiarmid, Electrical Conductivity in Doped Polyacetylene, *Physical Review Letters*, **39**, 17, 1098 (1977).

[29] P. W. Atkins, Molecular Quantum Mechanics, 2nd edition, Oxford University Press (1983).

[30] K. Mullen, G. Wegner, Electronic Materials: The Oligomer Approach, Wiley-VCH Verlag GmbH & Co. (1998).

[31] Sabine Ludwigs, P3HT Revisited – From Molecular Scale to Solar Cell Devices, Springer-Verlag Berlin Heidelberg (2014).

[32] H. Bässler, Charge Transport in Disordered Organic Photoconductors. A Monte Carlo Simulation Study, *Physica Status Solidi B*, **175**, 1, 15–56 (1993).

[33] Wolfgang Brütting, Chihaya Adachi, Physics of Organic Semiconductors, Wiley-VCH Verlag GmbH & Co. (2012).

[34] Gregor Meller, Tibor Grasser, Organic Electronics, Springer-Verlag Berlin Heidelberg (2010).

[35] Peter Atkins, Julio de Paula, Atkins' Physical Chemistry, Oxford University Press (2006).

[36] Number of citations was provided by CrossRef (https://www.crossref.org/services/cited-by/), date of checking [2020-11-13].

[37] Sergey Novikov, Two-dimensional bimolecular recombination in amorphous organic semiconductors, *Physical Chemistry Chemical Physics*, **22**, 3, 1174–1180 (2020).

[38] S. D. Baranovskii, Theoretical description of charge transport in disordered organic semiconductors, *Physica Status Solidi B*, **251**, 3, 487–525 (2014).

[39] A. Miller, E. Abrahams, Impurity conduction at low concentrations, *Physical Review*, **120**, 3, 745 (1960).

[40] O. Rubel, S. D. Baranovskii, P. Thomas, S. Yamasaki, Concentration dependence of the hopping mobility in disordered organic solids, *Physical Review B*, **69**, 1, 014206 (2004).

[41] Jean-Luc Brédas, David Beljonne, Veaceslav Coropceanu, Jérôme Cornil, Charge-Transfer and Energy-Transfer Processes in π-Conjugated Oligomers and Polymers: A Molecular Picture, *Chemical Reviews*, **104**, 11, 4971–5004 (2004).

[42] S. D. Baranovskii, T. Faber, F. Hensel, P. Thomas, The applicability of the transport-energy concept to various disordered materials, *Journal of Physics: Condensed Matter*, **9**, 13, 2699 (1997).

[43] Ling Li, Gregor Meller, Hans Kosin, Transport energy in organic semiconductors with partially filled localized state, *Applied Physics Letters*, **92**, 1, 013307 (2008).

[44] S. D. Baranovskii, H. Cordes, F. Hensel, G. Leising, Charge-carrier transport in disordered organic solids, *Physical Review B*, **62**, 12, 7934 (2000).

[45] V. I. Arkhipov, P. Heremans, E. V. Emelianova, G. J. Adriaenssens, H. Bässler, Weak-field carrier hopping in disordered organic semiconductors: the effects of deep traps and partly filled density-of-states distribution, *Journal of Physics: Condensed Matter*, **14**, 42, 9899–9911 (2002).

[46] M. M. Mandoc, B. de Boer, G. Paasch, P. W. M. Blom, Trap-limited electron transport in disordered semiconducting polymers, *Physical Review B*, **75**, 19, 193202 (2007).

[47] S. L. M. van Mensfoort, J. Billen, S. I. E. Vulto, R. A. J. Janssen, R. Coehoorn, Electron transport in polyfluorene-based sandwich-type devices: Quantitative analysis of the effects of disorder and electron traps, *Physical Review B*, **80**, 3, 033202 (2009).

[48] Chaudhary Vivek, Pandey Rajiv K, Prakash Rajiv, Kumar Naresh, Singh Arun Kumar, Highly aligned and crystalline poly(3-hexylthiophene) thin films by off-center spin coating for high performance organic field-effect transistors, *Synthetic Metals*, **258**, 116221 (2019).

[49] M. Kitamura, Y. Arakawa, Pentacene-based organic field-effect transistors, *Journal of Physics: Condensed Matter*, **20**, 18, 184011 (2008).

[50] A. Pivrikas, G. Juška, A. J. Mozer, M. Scharber, K. Arlauskas, N. S. Sariciftci, H. Stubb, R. Österbacka, Bimolecular Recombination Coefficient as a Sensitive Testing Parameter for Low-Mobility Solar-Cell Materials, *Physical Review Letters*, **94**, 17, 176806 (2005).

[51] C. Soci, D. Moses, A. J. Heeger, Effects of bimolecular recombination and charge-trapping on the transient photoconductivity of poly (p-phenylene vinylene), *Synthetic Metals*, **153**, 145–148 (2005).

[52] C.G. Shuttle, B. O’Regan, A. M. Ballantyne, J. Nelson, D. D. C. Bradley, J. R. Durrant, Bimolecular recombination losses in polythiophene: fullerene solar cells, *Physical Review B*, **78**, 11, 113201 (2008).

[53] P. Langevin, Recombinaison et mobilites des ions dans les gaz, *Annales de chimie et de physique*, **28**, 433 (1903).

[54] M. Pope, C. E. Swenberg, Electronic Processes in Organic Crystals and Polymers, 2nd edition, Oxford University Press, USA (1999).

[55] A. J. Mozer, N. S. Sariciftci, L. Lutsen, D. Vanderzande, R. Österbacka, M. Westerling, G. Juška, Charge transport and recombination in bulk heterojunction solar cells studied by the photoinduced charge extraction in linearly increasing voltage technique, *Applied Physics Letters*, **86**, 11, 112104 (2005).

[56] C. Deibel, A. Baumann, V. Dyakonov, Polaron recombination in pristine and annealed bulk heterojunction solar cells, *Applied Physics Letters*, **93**, 16, 163303 (2008).

[57] L. J. A. Koster, V. D. Mihailetchi, P. W. M. Blom, Bimolecular recombination in polymer/fullerene bulk heterojunction solar cells, *Applied Physics Letters*, **88**, 5, 052104 (2006).

[58] Gert-Jan A. H. Wetzelaer, Niels J. van der Kaap, L. Jan Anton Koster, Paul W. M. Blom, Quantifying Bimolecular Recombination in Organic Solar Cells in Steady State, *Advanced Energy Materials*, **3**, 9, 1130–1134 (2013).

[59] H. Ohkita, S. Cook, Y. Astuti, W. Duffy, S. Tierney, W. Zhang, M. Heeney, I. McCulloch, J. Nelson, D. D. C. Bradley, J. R. Durrant, Charge carrier formation in polythiophene/fullerene blend films studied by transient absorption spectroscopy, *Journal of the American Chemical Society*, **130**, 10, 3030–3042 (2008).

[60] T. M. Clarke, F. C. Jamieson, J. R. Durrant, Transient absorption studies of bimolecular recombination dynamics in polythiophene/fullerene blend films, *The Journal of Physical Chemistry C*, **113**, 49, 20934–20941 (2009).

[61] G. Juška, K. Arlauskas, M. Viliūnas, J. Kočka, Extraction Current Transients: New Method of Study of Charge Transport in Microcrystalline Silicon, *Physical Review Letters*, **84**, 21, 4946 (2000).

[62] Carsten Deibel, Vladimir Dyakonov, Polymer–fullerene bulk heterojunction solar cells, *Reports on Progress in Physics*, **73**, 9, 096401 (2010).

[63] Robert M. Metzger, Unimolecular and Supramolecular Electronics I, Springer-Verlag Berlin Heidelberg (2012).

[64] Richard J. D. Tilley, Perovskites: Structure-Property Relationships, John Wiley & Sons Ltd (2016).

[65] D. Weber, CH3NH3SnBrxI3-x (x = 0–3), a Sn(II)-System with the Cubic Perovskite Structure, *Zeitschrift für Naturforschung B*, **33**, 12, 862–865 (1978).

[66] D. Weber, CH3NH3PbX3, a Pb(II)-System with Cubic Perovskite Structure, *Zeitschrift für Naturforschung B*, **33**, 12, 1443–1445 (1978).

[67] A. Poglitsch, D. Weber, Dynamic disorder in methylammonium trihalogenoplumbates (II) observed by millimeter-wave spectroscopy, *The Journal of Chemical Physics*, **87**, 11, 6373 (1987).

[68] N. Onoda-Yamamuro, T. Matsuo, H. Suga, Calorimetric and IR spectroscopic studies of phase transitions in methylammonium trihalogenoplumbates (II), *Journal of Physics and Chemistry of Solids*, **51**, 12, 1383–1395 (1990).

[69] R. E. Wasylishen, O. Knop, J. B. Macdonald, Cation rotation in methylammonium lead halides. *Solid State Communications*, **56**, 7, 581–582 (1985).

[70] Best Research-Cell Efficiency Chart, https://www.nrel.gov/pv/cell-efficiency.html, date of checking [2021-01-12].

[71] Guichuan Xing, Nripan Mathews, Shuangyong Sun, Swee Sien Lim, Yeng Ming Lam, Michael Grätzel, Subodh Mhaisalkar, Tze Chien Sum, Long-Range Balanced Electron- and Hole-Transport Lengths in Organic-Inorganic $CH_3NH_3PbI_3$, *Science*, **342**, 6154, 344–347 (2013).

[72] Ajay Kumar Jena, Ashish Kulkarni, Tsutomu Miyasaka, Halide Perovskite Photovoltaics: Background, Status, and Future Prospects, *Chemical Reviews*, **119**, 5, 3036–3103 (2019).

[73] A. Walsh, Principles of chemical bonding and band gap engineering in hybrid organic-inorganic halide perovskites, *The Journal of Physical Chemistry C*, **119**, 11, 5755–5760 (2015).

[74] S. D. Stranks, G. E. Eperon, G. Grancini, C. Menelaou, M. J. P. Alcocer, T. Leijtens, L. M. Herz, A. Petrozza, H. J. Snaith, Electron-Hole Diffusion

Lengths Exceeding 1 Micrometer in an Organometal Trihalide Perovskite Absorber, *Science*, **342**, 6156, 341−342 (2013).

[75] K. Galkowski, A. Mitioglu, A. Miyata, P. Plochocka, O. Portugall, G. E. Eperon, J. T. W. Wang, T. Stergiopoulos, S. D. Stranks, H. J. Snaith, R. J. Nichola, Determination of the exciton binding energy and effective masses for methylammonium and formamidinium lead tri-halide perovskite semiconductors, *Energy & Environmental Science*, **9**, 3, 962−970 (2016).

[76] Tze-Chien Sum, Nripan Mathews, Halide Perovskites Photovoltaics, Light Emitting Devices, and Beyond, Wiley-VCH Verlag GmbH & Co. (2019).

[77] K. Tanaka, T. Takahashi, T. Ban, T. Kondo, K. Uchida, N. Miura, Comparative study on the excitons in lead-halide-based perovskite-type crystals CH3NH3PbBr3 CH3NH3PbI3, *Solid State Communications*, **127**, 9–10, 619–623 (2003).

[78] D. Shi, V. Adinolfi, R. Comin, M. Yuan, E. Alarousu, A. Buin, Y. Chen, S. Hoogland, A. Rothenberger, K. Katsiev, Y. Losovyj, X. Zhang, P. A. Dowben, O. F. Mohammed, E. H. Sargent, O. M. Bakr, Low trap-state density and long carrier diffusion in organolead trihalide perovskite single crystals, *Science*, **347**, 6221, 519–522 (2015).

[79] Wanyi Nie, Hsinhan Tsai, Reza Asadpour, Jean-Christophe Blancon, Amanda J. Neukirch, Gautam Gupta, Jared J. Crochet, Manish Chhowalla, Sergei Tretiak, Muhammad A. Alam, Hsing-Lin Wang, Aditya D. Mohite, High-efficiency solution-processed perovskite solar cells with millimeter-scale grains, *Science*, **347**, 6221, 522–525 (2015).

[80] P. M. Beaujuge, J. M. J. Fréchet, Molecular Design and Ordering Effects in π-Functional Materials for Transistor and Solar Cell Applications, *Journal of the American Chemical Society*, **133**, 50, 20009–20029 (2011).

[81] Guichuan Xing, Nripan Mathews, Shuangyong Sun, Swee Sien Lim, Yeng Ming Lam, Michael Grätzel, Subodh Mhaisalkar, Tze Chien Sum, Long-Range Balanced Electron- and Hole-Transport Lengths in Organic-Inorganic $CH_3NH_3PbI_3$, *Science*, **342**, 6156, 344–347 (2013).

[82] Nam-Gyu Park, Michael Grätzel, Tsutomu Miyasaka, Organic-Inorganic Halide Perovskite Photovoltaics, Springer International Publishing (2016).

[83] C. C. Stoumpos, C. D. Malliakas, M. G. Kanatzidis, Semiconducting Tin and Lead Iodide Perovskites with Organic Cations: Phase Transitions, High Mobilities, and Near-Infrared Photoluminescent Properties, *Inorganic Chemistry*, **52**, 15, 9019–9038 (2013).

[84] Eric Diau, Peter Chen, Perovskite Solar Cells: Principle, Materials and Devices, World Scientific Publishing Co. Pte. Ltd. (2018).

[85] Milos Petrovic, Vijila Chellappan, Seeram Ramakrishna, Perovskites: Solar cells & engineering applications – materials and device developments, *Solar Energy*, **122**, 678–699 (2015).

[86] M. Thirumoorthi, J. Thomas Joseph Prakash, Structure, optical and electrical properties of indium tin oxide ultra thin films prepared by jet nebulizer spray pyrolysis technique, *Journal of Asian Ceramic Societies*, **4**, 1, 124–132 (2016).

[87] D. J. Kwak, B. H. Moon, D. K. Lee, C. S. Park, Y. M. Sung, Comparison of transparent conductive indium tin oxide, titanium-doped indium oxide, and fluorine-doped tin oxide films for dye-sensitized solar cell application, *Journal of Electrical Engineering and Technology*, **6**, 5, 684–687 (2011).

[88] Zhu Yun, Wan Pengfei, Wang Yue, Yan Dali, Wang Shouyu, Comparison Study of Optical, Electrical and Mechanical Properties between Transparent Conductive ZnO:Ga and SnO2:F Films, *Rare Metal Materials and Engineering*, **41**, 471–474 (2012).

[89] Cheng-Kuang Lee, Chun-Wei Pao, Solubility of [6,6]-Phenyl-C61-butyric Acid Methyl Ester and Optimal Blending Ratio of Bulk Heterojunction Polymer Solar Cells, *The Journal of Physical Chemistry C*, **116**, 23, 12455–12461 (2012).

[90] Fangming Jin, Bei Chu, Wenlian Li, Zisheng Su, Bo Zhao, Tianyou Zhang, Xingwu Yan, Yuan Gao, Hairuo Wu, C.S. Lee, Jianzhuo Zhu, Huachun Pi, Junbo Wang, The influence of donor material on achieving high photovoltaic response for organic bulk heterojunction cells with small ratio donor component, *Organic Electronics*, **14**, 4, 1130–1135 (2013).

[91] Cheng-Kuang Lee, Chun-Wei Pao, Chih-Wei Chu, Multiscale molecular simulations of the nanoscale morphologies of P3HT:PCBM blends for bulk heterojunction organic photovoltaic cells, *Energy & Environmental Science*, **4**, 10, 4124–4132 (2011).

[92] Ye Huang, Edward J. Kramer, Alan J. Heeger, Guillermo C. Bazan, Bulk Heterojunction Solar Cells: Morphology and Performance Relationships, *Chemical Reviews*, **114**, 14, 7006–7043 (2014).

[93] Marco Notarianni, Kristy Vernon, Alison Chou, Muhsen Aljada, Jinzhang Liu, Nunzio Motta, Plasmonic effect of gold nanoparticles in organic solar cells, *Solar Energy*, **106**, 23–37 (2014).

[94] Jingjing Chang, Hai Zhu, Juanxiu Xiao, Furkan Halis Isikgor, Zhenhua Lin, Yue Hao, Kaiyang Zeng, Qing-Hua Xuc, Jianyong Ouyang, Enhancing the planar heterojunction perovskite solar cell performance through tuning the precursor ratio, *Journal of Materials Chemistry A*, **4**, 20, 7943–7949 (2016).

[95] Manuel Salado, Laura Calio, Rüdiger Berger, Samrana Kazim, Shahzada Ahmad, Influence of the mixed organic cation ratio in lead iodide based perovskite on the performance of solar cells, *Physical Chemistry Chemical Physics*, **18**, 39, 27148–27157 (2016).

[96] Yafei Wang, Jiang Wu, Peng Zhang, Detao Liu, Ting Zhang, Long Ji, Xiangling Gu, Zhi David Chen, Shibin Li, Stitching triple cation perovskite by a mixed anti-solvent process for high performance perovskite solar cells, *Nano Energy*, **39**, 616–625 (2017).

[97] Zhengyang Bin, Jiangwei Li, Liduo Wang, Lian Duan, Efficient n-type dopants with extremely low doping ratios for high performance inverted perovskite solar cells, *Energy & Environmental Science*, **9**, 11, 3424–3428 (2016).

[98] Mingyang Cha, Peimei Da, Jun Wang, Weiyi Wang, Zhanghai Chen, Faxian Xiu, Gengfeng Zheng, Zhong-Sheng Wang, Enhancing Perovskite Solar Cell Performance by Interface Engineering Using

$CH_3NH_3PbBr_{0.9}I_{2.1}$ Quantum Dots, *Journal of the American Chemical Society*, **138**, 27, 8581–8587 (2016).

[99] D. Bi, P. Gao, R. Scopelliti, E. Oveisi, J. Luo, M. Grätzel, A. Hagfeldt, M. K. Nazeeruddin, High-Performance Perovskite Solar Cells with Enhanced Environmental Stability Based on Amphiphile-Modified $CH_3NH_3PbI_3$, *Advanced Materials*, **28**, 15, 2910–2915 (2016).

[100] Chih-Hung Tsai, Chia-Ming Lin, Cheng-Hao Kuei, Improving the performance of perovskite solar cells by adding 1,8-diiodooctane in the CH3NH3PbI3 perovskite layer, *Solar Energy*, **176**, 178–185 (2018).

[101] Anick M. van de Craats, John M. Warman, Matthijs P. de Haas, Dieter Adam, Jürgen Simmerer, Dietrich Haarer, Peter Schuhmacher, The mobility of charge carriers in all four phases of the columnar discotic material hexakis(hexylthio)triphenylene: Combined TOF and PR-TRMC results, *Advanced Materials*, **8**, 10, 823–826 (1996).

[102] O. Semeniuk, G. Juska, J. O. Oelerich, M. Wiemer, S. D. Baranovskii, A. Reznik, Charge transport mechanism in lead oxide revealed by CELIV technique, *Scientific Reports*, **6**, 33359 (2016).

[103] C. A. Amorim, M. R. Cavallari, G. Santos, F. J. Fonseca, A. M. Andrade, S. Mergulhão, Determination of carrier mobility in MEH-PPV thin-films by stationary and transient current techniques, *Journal of Non-Crystalline Solids*, **358**, 3, 484–491 (2012).

[104] Attila J. Mozer, Niyazi Serdar Sariciftci, Almantas Pivrikas, Ronald Österbacka, Gytis Juška, Lutz Brassat, Heinz Bässler, Charge carrier mobility in regioregular poly(3-hexylthiophene) probed by transient conductivity techniques: A comparative study, *Physical Review B*, **71**, 3, 035214 (2005).

[105] A. Tsumura, H. Koezuka, T. Ando, Macromolecular electronic device: Field-effect transistor with a polythiophene thin film, *Applied Physics Letters*, **49**, 18, 1210–1212 (1986).

[106] Yoon Ho Lee, Moonjeong Jang, Moo Yeol Lee, O. Young Kweon, Joon Hak Oh, Flexible Field-Effect Transistor-Type Sensors Based on Conjugated Molecules, *Chem*, **3**, 5, 724–763 (2017).

[107] S. P. Tiwari, E. B. Namdas, V. Ramgopal Rao, D. Fichou, S. G. Mhaisalkar, Solution-Processed n-Type Organic Field-Effect Transistors With High on/off Current Ratios Based on Fullerene Derivatives, *IEEE Electron Device Letters*, **28**, 10, 880–883 (2007).

[108] J. Veres, S. Ogier, G. Lloyd, D. de Leeuw, Gate Insulators in Organic Field-Effect Transistors, *Chemistry of Materials*, **16**, 23, 4543–4555 (2004).

[109] Kouji Suemori, Sei Uemura, Manabu Yoshida, Satoshi Hoshino, Noriyuki Takada, Takehito Kodzasa, Toshihide Kamata, Influence of fine roughness of insulator surface on threshold voltage stability of organic field-effect transistors, *Applied Physics Letters*, **93**, 3, 033308 (2008).

[110] S. Oku, T. Nagase, S. Nagamatsu, W. Takashima, K. Kaneto, Comparative Study on Gate Insulators of Polymers and SiO2 in Transport Properties of p- and n-Type Organic Field-Effect Transistors, *Japanese Journal of Applied Physics*, **49**, 1, 01AB14 (2010).

[111] Takeo Minari, Takashi Nemoto, Seiji Isoda, Temperature and electric-field dependence of the mobility of a single-grain pentacene field-effect transistor, *Journal of Applied Physics*, **99**, 3, 034506 (2006).

[112] Pawel Miskiewicz, Marta Mas-Torrent, Jaroslaw Jung, Sylwia Kotarba, Ireneusz Glowacki, Elba Gomar-Nadal, David B. Amabilino, Jaume Veciana, Bärbel Krause, Dina Carbone, Concepció Rovira, Jacek Ulanski, Efficient High Area OFETs by Solution Based Processing of a π-Electron Rich Donor, *Chemistry of Materials*, **18**, 20, 4724–4729 (2006).

[113] U. Bielecka, P. Lutsyk, K. Janus, J. Sworakowski, W. Bartkowiak, Effect of solution aging on morphology and electrical characteristics of regioregular P3HT FETs fabricated by spin coating and spray coating, *Organic Electronics*, **12**, 11, 1768–1776 (2011).

[114] I. G. Hill, A. Rajagopal, A. Kahn, Y. Hu, Molecular level alignment at organic semiconductor-metal interfaces, *Applied Physics Letters*, **73**, 5, 662–664 (1998).

[115] L.A. Majewski, M. Grell, Organic field-effect transistors with ultrathin modified gate insulator, *Synthetic Metals*, **151**, 2, 175–179 (2005).

[116] T. D. Tsai, J. W. Chang, T. C. Wen, T. F. Guo, Manipulating the Hysteresis in Poly(vinyl alcohol)-Dielectric Organic Field-Effect Transistors Toward Memory Elements, *Advanced Functional Materials*, **23**, 34, 4206–4214 (2013).

[117] S. W. Lee, H. J. Lee, J. H. Choi, W. G. Koh, J. M. Myoung, J. H. Hur, U. Jeong, Periodic Array of Polyelectrolyte-Gated Organic Transistors from Electrospun Poly(3-hexylthiophene) Nanofibers, *Nano Letters*, **10**, 1, 347–351 (2010).

[118] N. Benson, M. Schidleja, C. Melzer, R. Schmechel, H. von Seggern, Complementary organic field effect transistors by ultraviolet dielectric interface modification, *Applied Physics Letters*, **89**, 18, 182105 (2006).

[119] B. Kumar, B. K. Kaushik, Y. S. Negi, Organic Thin Film Transistors: Structures, Models, Materials, Fabrication, and Applications: A Review, *Polymer Reviews*, **54**, 1, 33–111 (2014).

[120] Zhenhua Chen, Hui Li, Yongbing Tang, Xing Huang, Derek Ho, Chun-Sing Lee, Shape-controlled synthesis of organolead halide perovskite nanocrystals and their tunable optical absorption, *Materials Research Express*, **1**, 1, 015034 (2014).

[121] Heewon Hwang, Hoyeon Lee, Shafidah Shafian, Wooseop Lee, Jeesoo Seok, Ka Yeon Ryu, Du Yeol Ryu and Kyungkon Kim, Thermally Stable Bulk Heterojunction Prepared by Sequential Deposition of Nanostructured Polymer and Fullerene, *Polymers*, **9**, 9, 456 (2017).

[122] W. E. Spear, Transit time measurement of charge carriers in amorphous selenium films, *Proceedings of the Physical Society B*, **70**, 669 (1957).

[123] Tengzhou Yang, Fuhua Dai, Hiroaki Iino, Masayuki Kanehara, Xuying Liu, Takeo Minari, Chuan Liu, Solution-processable liquid crystalline chrysene semiconductors with wide band gap: Self-organization and carrier transport properties, *Organic Electronics*, **63**, 184–193 (2018).

[124] Indu Bala, Nitya Singh, Rohit Ashok Kumar Yadav, Joydip De, Santosh Prasad Gupta, Dharmendra Pratap Singh, Deepak Kumar Dubey, Jwo-Huei Jou, Redouane Doualid, Santanu Kumar Pal, Room temperature perylene based columnar liquid crystals as solid-state fluorescent emitters in solution-processable organic light-emitting diodes, *Journal of Materials Chemistry C*, **8**, 36, 12485 (2020).

[125] Maher Al-Ibrahim, H. Klaus Roth, M. Schroedner, Alexander Konkin, Uladzimir Zhokhavets, Gerhard Gobsch, Peter Scharff, Steffi Sensfuss, The influence of the optoelectronic properties of poly(3-alkylthiophenes) on the device parameters in flexible polymer solar cells, *Organic Electronics*, **6**, 65–77 (2005).

[126] A. Petravičius, G. Juška, R. Baubinas, Drift of holes in high-resistivity p-type CdSe crystal plates, *Soviet physics. Semiconductors*, **9**, 1530 (1975).

[127] G. Juška, K. Arlauskas, M. Viliūnas, K. Genevičius, R. Österbacka, H. Stubb, Charge transport in π-conjugated polymers from extraction current transients, *Physical Review B*, **62**, 24, R16235 (2000).

[128] G. Juška, N. Nekrašas, V. Valentinavičius, P. Meredith, A. Pivrikas, Extraction of photogenerated charge carriers by linearly increasing voltage in the case of Langevin recombination, *Physical Review B*, **84**, 15, 155202 (2011).

[129] G. Juška, N. Nekrašas, K. Genevičius, Investigation of charge carriers transport from extraction current transients of injected charge carriers, *Journal of Non-Crystalline Solids*, **358**, 4, 748–750 (2012).

[130] J. Važgėla, K. Genevičius, G. Juška, i-CELIV technique for investigation of charge carriers transport properties, *Chemical Physics*, **478**, 20, 126–129 (2016).

[131] J. R. Burns, Large-signal transit-time effects in the MOS transistor, *RCA Review*, **30**, 15 (1969).

[132] D. Basu, L. Wang, L. Dunn, B. Yoo, S. Nadkarni, A. Dodabalapur, M. Heeney, I. McCulloch, Direct measurement of carrier drift velocity and mobility in a polymer field-effect transistor, *Applied Physics Letters*, **89**, 24, 242104 (2006).

[133] L. Dunn, D. Basu, L. Wang, A. Dodabalapur, Organic field effect transistor mobility from transient response analysis, *Applied Physics Letters*, **88**, 6, 063507 (2006).

[134] M. Weis, J. Lin, D. Taguchi, T. Manaka, M. Iwamoto, Analysis of Transient Currents in Organic Field Effect Transistor: The Time-of-Flight Method, *The Journal of Physical Chemistry C*, **113**, 43, 18459 (2009).

[135] G. Juška, N. Nekrašas, K. Genevičius, A. Pivrikas, Current transients in organic field effect transistors, *Applied Physics Letters*, **102**, 16, 163306 (2013).

[136] G. Juška, N. Nekrašas, K. Genevičius, T. Grigaitis, The determination of charge carrier mobility from the current transients in organic field effect transistor, *Journal of Applied Physics*, **116**, 2, 023702 (2014).

[137] Zhaoning Song, Suneth C. Watthage, Adam B. Phillips, Brandon L. Tompkins, Randy J. Ellingson, Michael J. Heben, Impact of Processing Temperature and Composition on the Formation of Methylammonium Lead Iodide Perovskites, *Chemistry of Materials*, **27**, 13, 4612–4619 (2015).

[138] Tomas Leijtens, I-Kang Ding, Tommaso Giovenzana, Jason T. Bloking, Michael D. McGehee, Alan Sellinger, Hole Transport Materials with Low Glass Transition Temperatures and High Solubility for Application in Solid-State Dye-Sensitized Solar Cells, *ACS Nano*, **6**, 2, 1455–1462 (2012).

[139] Dong Shi, Xiang Qin, Yuan Li, Yao He, Cheng Zhong, Jun Pan, Huanli Dong, Wei Xu, Tao Li, Wenping Hu, Jean-Luc Brédas, Osman M. Bakr, Spiro-OMeTAD single crystals: Remarkably enhanced charge-carrier transport via mesoscale ordering, *Science Advances*, **2**, 4, e1501491 (2016).

[140] Zubair Ahmad, Farid Touati, Fahmi F. Muhammad, Mansoor Ani Najeeb, R. A. Shakoor, Effect of ambient temperature on the efficiency of the PCPDTBT:PC71BM BHJ solar cells, *Applied Physics A*, **123**, 486 (2017).

[141] E. V. Emelianova, M. van der Auweraer, G. J. Adriaenssens, A. Stesmans, Carrier mobility in two-dimensional disordered hopping systems, *Organic Electronics*, **9**, 1, 129–135 (2008).

[142] M. Paul Borsenberger, David S. Weiss, Organic Photoreceptors for Xerography, CRC Press LLC, p485 (1998).

[143] Dongkyun Seo, Jonghyup Park, Tae Joo Shin, Pil J. Yoo, Juhyun Park, Kyungwon Kwak, Bathochromic shift in absorption spectra of conjugated polymer nanoparticles with displacement along backbones, *Macromolecular Research*, **23**, 6, 574–577 (2015).

[144] F. S. U. Fischer, K. Tremel, A.-K. Saur, S. Link, N. Kayunkid, M. Brinkmann, D. Herrero-Carvajal, J. T. Lopez Navarrete, M. C. Ruiz Delgado, S. Ludwigs, Influence of Processing Solvents on Optical Properties and Morphology of a Semicrystalline Low Bandgap Polymer in the Neutral and Charged States, *Macromolecules*, **46**, 12, 4924−4931 (2013).

[145] Tracey M. Clarke, Jeff Peet, Andrew Nattestad, Nicolas Drolet, Gilles Dennler, Christoph Lungenschmied, Mario Leclerc, Attila J. Mozer, Charge carrier mobility, bimolecular recombination and trapping in polycarbazole copolymer:fullerene (PCDTBT:PCBM) bulk heterojunction solar cells, *Organic Electronics*, **13**, 11, 2639–2646 (2012).

[146] Iordania Constantinou, Tzung-Han Lai, Erik D. Klump, Subhadip Goswami, Kirk S. Schanze, Franky So, Effect of Polymer Side Chains on Charge Generation and Disorder in PBDTTPD Solar Cells, *ACS Applied Materials & Interfaces*, **7**, 48, 26999−27005 (2015).

[147] Long Ye, Wei Jiang, Wenchao Zhao, Shaoqing Zhang, Yong Cui, Zhaohui Wang, Jianhui Hou, Toward efficient non-fullerene polymer solar cells: Selection of donor polymers, *Organic Electronics*, **17**, 295–303 (2015).

[148] Xue-Qiang Chen, Xiang Yao, Xuan Xiang, Long Liang, Wei Shao, Fu-Gang Zhao, Zhengquan Lu, Wenwu Wang, Jingjing Li, Wei-Shi Li, Long-Term Thermally Stable Organic Solar Cells Based on Cross-linkable Donor-Acceptor Conjugated Polymers, *Journal of Materials Chemistry A*, **4**, 23, 9286–9292 (2016).

[149] Wisnu Tantyo Hadmojo, Febrian Tri Adhi Wibowo, Du Yeol Ryu, In Hwan Jung, Sung-Yeon Jang, Fullerene-Free Organic Solar Cells with an Efficiency of 10.2% and an Energy Loss of 0.59 eV Based on a Thieno[3,4-c]Pyrrole-4,6-dione Containing Wide Band Gap Polymer Donor, *ACS Applied Materials & Interfaces*, **9**, 38, 32939−32945 (2017).

[150] G. J. Adriaenssens, V. I. Arkhipov, Non-Langevin recombination in disordered materials with random potential distributions, *Solid State Communications*, **103**, 9, 541–543 (1997).

[151] I. Balberg, R. Naidis, M. K. Lee, J. Shinar, L. F. Fonseca, Bipolar phototransport in p-conjugated polymer/C60 composites, *Applied Physics Letters*, **79**, 2, 197–199 (2001).

[152] Sungho Nam, Hwajeong Kim, Donal D. C. Bradley, Youngkyoo Kim, All-polymer phototransistors with bulk heterojunction sensing layers of thiophene-based electron-donating and thienopyrroledione-based electron-accepting polymers, *Organic Electronics*, **39**, 199–206 (2016).

PADĖKA/ACKNOWLEDGEMENTS

Šiame kelyje, kurio tik dalį atspindi prirašyti puslapiai ir kuris prasidėjo dar Kietojo Kūno Elektronikos katedroje ir tęsiasi Cheminės Fizikos institute, sutikau daugybę žmonių, kurie prisidėjo, padėjo ar tiesiog keliavo kartu. Pirmiausia noriu padėkoti savo darbo vadovui Nerijui Nekrašui, kuris buvo vadovas nuo pat bakalauro studijų laikų ir nesibodėdavo atsakinėti į klausimus ne tik iš fizikos srities. Taip pat noriu išreikšti dėkingumą Kristijonui Genevičiui už nuolatinę pagalbą ruošiant bandinius ir ieškant vis pasislepiančios sidabro pastos. Dėkoju Gyčiui Juškai, kurio, atrodo, niekada nesibaigiančios žinios pasitikdavo kiekvieną kartą, kai reikėjo interpretuoti gautus rezultatus, Kęstučiui Arlauskui už paskaitas, istorijas ir patarimus, Julijai Gorbaniovai už nenuilstančią energiją ir pagalbą bėgiojant biurokratijos koridoriais bei už tai, kad nebuvo nė vienos problemos, kuriai nebūtų pasiūlytas sprendimas, Mindaugui Viliūnui, kurio surinkta elektronikos įtaisų kolekcija leido konstruoti, kurti, ieškoti, ir už konsultacijas elektronikos klausimais.

Džiaugiuosi, kad šiuo laikotarpiu buvau ne vienas, ne vienišas, nepaliktas. Noriu padėkoti Jonui Nekrasovui, su kuriuo dalinamės kabinetu ir istorijomis, Tomui Grigaičiui už ekskursijas po Fizikos Fakulteto rūsį ir humoro jausmą netelpantį į ne tik į fizikos mokslo ribas, bet taip pat ir metafizines, Giedriui Juškai už auksinius nanometrus ir mikroskopinius tyrinėjimus. Per šį laikotarpį pasitaikė ne vienas atvejis, kada netikėtai prireikė greitos pagalbos, todėl noriu padėkoti tą pagalbą suteikusiems Martynui Veličkai, Sandrai Stanionytei, Linai Mikoliūnaitei.

Esu be galo dėkingas savo tėvams Gitai ir Ričardui Aukštuoliams, kurie išleido į Vilniaus universitetą, palaikė renkantis fiziko kelią ir įvairiapusiškai padėjo juo keliaujant. Taip pat dėkoju sesei Rasai Aukštuolytei ir broliui Pauliui Aukštuoliui už laiką kartu ir pademonstruotą supratingumą. Dėkoju visiems savo draugams, kurie labai stengėsi per dažnai neužduoti klausimo: „Tai kada baigsi?“ Nuoširdžiai dėkoju Rho nano komandos nariams, kurie šiltai priėmė ir parodė, kaip atrodo mokslininkų bendruomenė ne akademinėje aplinkoje. Dėkoju savo partnerei Monikai, kuri kantriai laukė kartu su manimi.

I would like to express big gratitude to Mihaela Girtan who not only guided my internship in Angers, but also helped in every way possible. I will never forget conversations, constant searching and hiding of the keys, all the door codes and the time in France. I am very grateful to Michael O'Connor who helped me to adapt myself to French culture and who helped me to improve my French language skills and table manners during lovely suppers.

APPENDIX 1

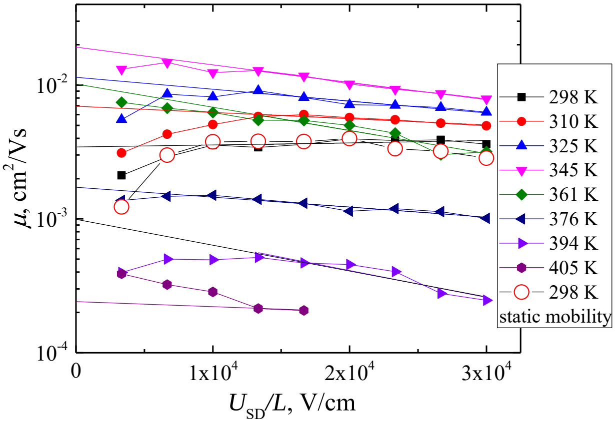

Fig. S1. PCPDTBT OFET structure hole mobility dependence on applied voltage obtained by OFET current transients method. Open red circles show mobility calculated from I-V characteristics at room temperature.

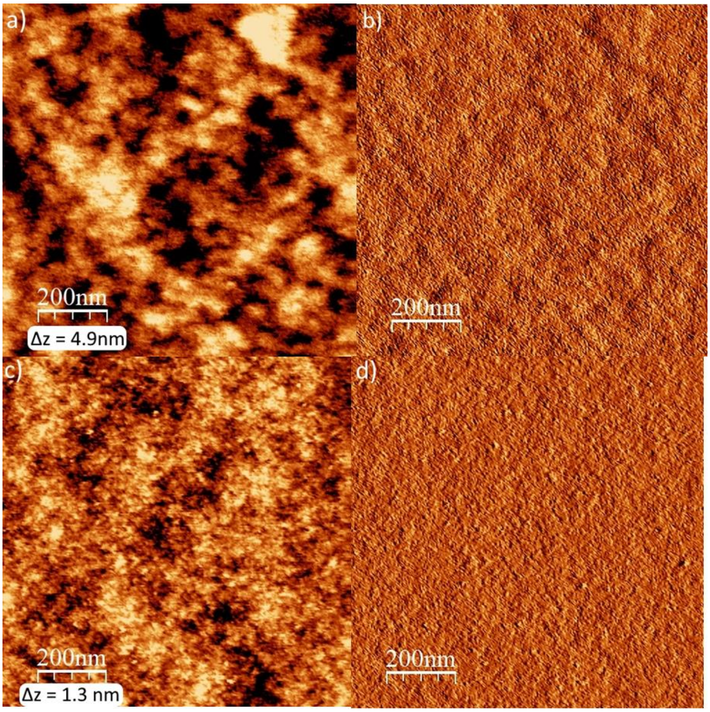

Fig. S2. AFM images of PCPDTBT OFET structure surfaces. a) and b) images are from unheated structure, RMS = 1.2 nm c) and d) images are from heated structure, RMS = 0.3 nm (after measurements).

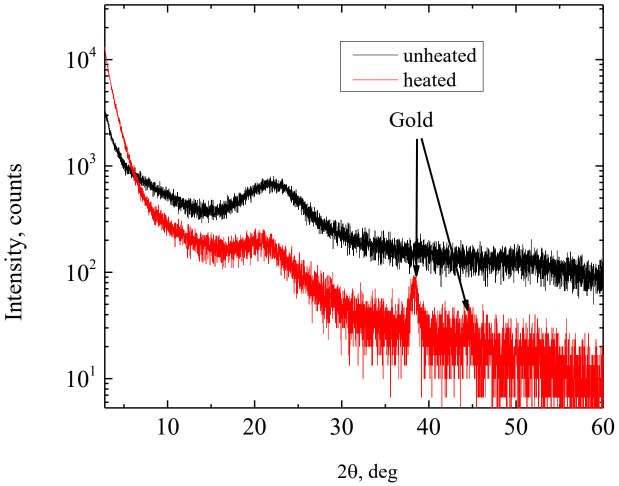

Fig. S3. Grazing incidence XRD results of heated (after measurements) and unheated PCPDTBT layers in OFET structure. Arrows mark response from the gold contacts on the top of PCPDTBT.

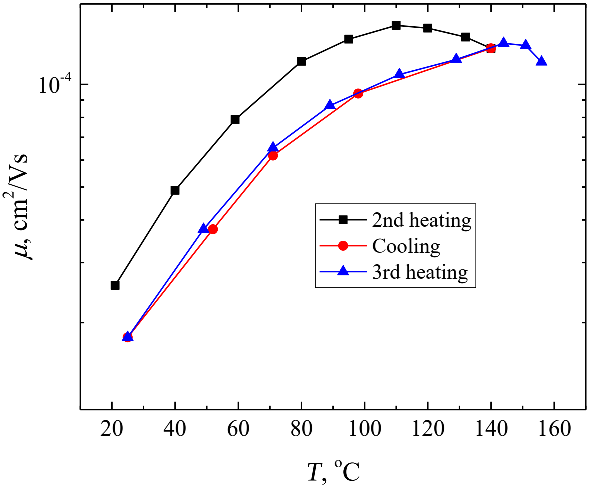

Fig. S4. Hole mobility in parallel to the substrate direction at different temperatures after repeated heating cycles (obtained by OFET current transients technique).

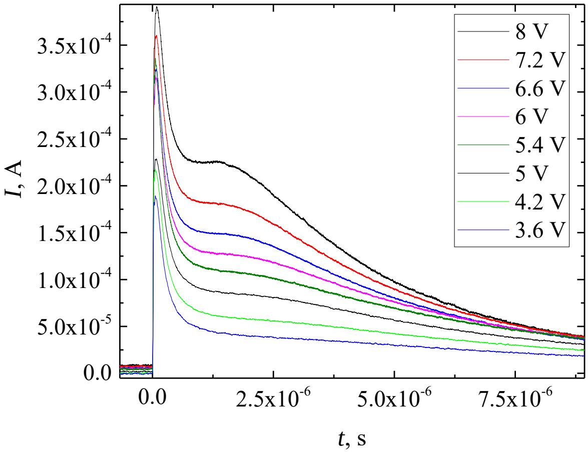

Fig. S5. TOF current transients of PBDTTPD sandwich structure.

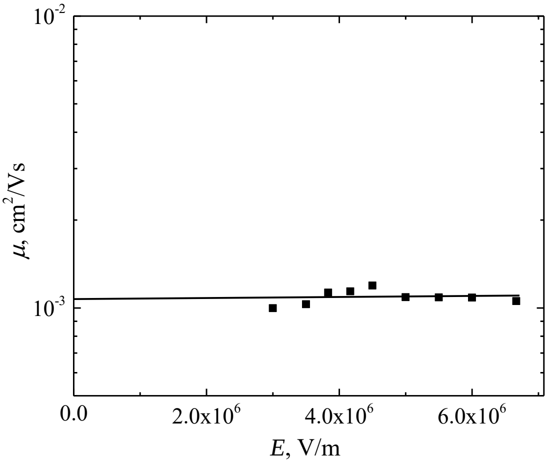

Fig. S6. Hole mobility in PBDTTPD sandwich structure obtained by TOF technique.

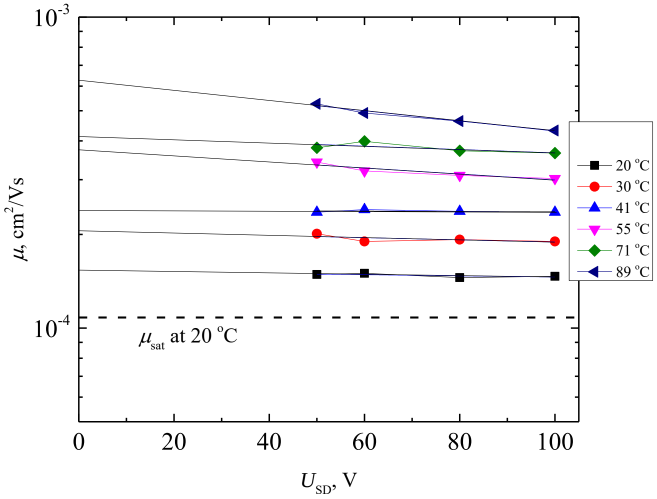

Fig. S7. Hole mobility dependence on U_{SD} in OFET structures with OTS treatment and PBDTTPD as active layer. Dashed line marks hole mobility obtained from $I_{SD\ sat}$ values in OFET current transients method.

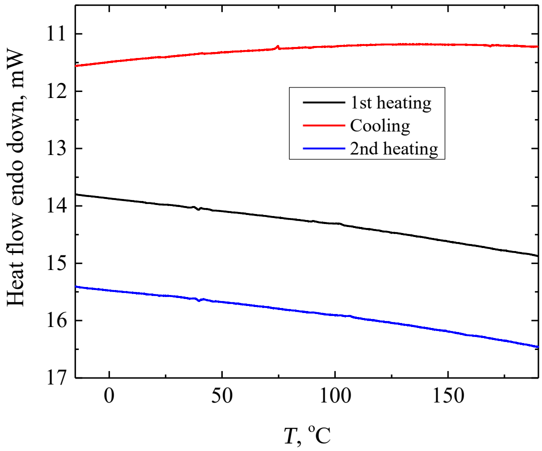

Fig. S8. Differential scanning calorimetry thermograms of PBDTTPD.

CURRICULUM VITAE

Name: Andrius
Surname: Aukštuolis
Date of birth: 1988-05-09
Place of birth: Panevėžys, Lithuania
E-mail: andrius.aukstuolis@ff.vu.lt

Education:

2014-2020	Vilnius University, Faculty of Physics *Ph. D. studies*.
2011-2013	Vilnius University, Faculty of Physics *Master's degree*
2007-2011	Vilnius University, Faculty of Physics *Bachelor's degree*
2003-2007	Juozas Balčikonis Gymnasium
1999-2003	Panevėžys Secondary School "Vyturys"
1995-1999	Kazimieras Paltarokas Secondary School

Work experience:

2017-now	Vilnius University, Institute of Chemical Physics, *Junior Researcher*
2018-2020	UAB Rho nano, *Senior Researcher*
2014-2017	Vilnius University, Institute of Chemical Physics, *Senior Engineer*

LIST OF PUBLICATIONS AND THEIR COPIES / PUBLIKACIJŲ SĄRAŠAS IR JŲ KOPIJOS

1. Andrius Aukštuolis, Mihaela Girtan, George A. Mousdis, Romain Mallet, Marcela Socol, Mohamed Rasheed, Anca Stanculescu. Measurement of charge carrier mobility in perovskite nanowire films by photo-CELIV method, *Proceedings of the Romanian Academy*, *Series A*, 18, 1, 34–41 (2017).

2. Andrius Aukštuolis, Nerijus Nekrašas, Kristijonas Genevičius, Jūratė Jonikaitė-Švėgždienė. Anisotropy of charge carrier transport in PCPDTBT field-effect transistor structures, *Synthetic Metals*, 264, 116382, (2020) https://doi.org/10.1016/j.synthmet.2020.116382.

3. Andrius Aukštuolis, Nerijus Nekrašas, Kristijonas Genevičius, Giedrius Juška, Investigation of charge carrier mobility and recombination in PBDTTPD thin layer structures, *Organic Electronics*, 90, 106066, (2021) https://doi.org/10.1016/j.orgel.2021.106066.

1st publication / 1-oji publikacija

Measurement of charge carrier mobility in perovskite nanowire films by photo-CELIV method

Andrius Aukštuolis, Mihaela Girtan, George A. Mousdis, Romain Mallet,
Marcela Socol, Mohamed Rasheed, Anca Stanculescu

Proceedings of the Romanian Academy, Series A, 18, 1, 34–41 (2017)

THE PUBLISHING HOUSE
OF THE ROMANIAN ACADEMY

PROCEEDINGS OF THE ROMANIAN ACADEMY, Series A,
Volume 18, Number 1/2017, pp. 34–41

MEASUREMENT OF CHARGE CARRIER MOBILITY IN PEROVSKITE NANOWIRE FILMS BY PHOTO-CELIV METHOD

Andrius AUKŠTUOLIS[1, 2], Mihaela GIRTAN[1], George A. MOUSDIS[3], Romain MALLET[4],
Marcela SOCOL[5], Mohamed RASHEED[1], Anca STANCULESCU[5]

[1] Angers University, Photonics Laboratory (LPHIA), France
[2] Vilnius University, Faculty of Physics, Department of Solid State Electronics, Lithuania
[3] National Hellenic Foundation, Athens, Greece
[4] SCIAM, Angers University, France
[5] National Institute of Materials Physics, Bucharest, Magurele, Romania
Corresponding author: Mihaela GIRTAN, E-mail: `mihaela.girtan@univ-angers.fr`

Abstract. In this paper the holes' mobility for the configuration FTO/TiO_2/$CH_3NH_3PbI_3$/Spiro-MeOTAD/Au was measured for the first time by the Photo-CELIV method. The TiO_2 dense film was deposited by reactive sputtering at room temperature on FTO glass substrates. High crystalized perovskite films were deposited from solutions in one step by spin coating. Spiro-MeOTAD molecular glass was used as holes transporting layer. The highest holes' mobility from TiO_2 thin film through the perovskite and Spiro MeOTAD film to the top gold electrode was of order 8.5×10^{-7} cm^2/Vs.

Key words: perovskites, holes' mobility, photo-CELIV, solar cells, titanium oxide, $CH_3NH_3PbI_3$.

1. INTRODUCTION

The organic-inorganic perovskite solar cells have attracted much attention during the last five years and became the most promising material for the new generation of solar cells [1–5]. In particular, the organic-inorganic halide perovskites have several features such as: long charge carrier lifetime, long diffusion length and ambipolar charge transport capability, which made them very attractive materials for solar cells. Also their facile synthesis directly on the substrate at low temperature made them very suitable for applications on plastics substrates. Within the last six years the efficiencies of a typical solar cell: FTO/TiO_2dense/TiO_2mes/Perovskite/HTM/Au rapidly increased from 4% to 21%.

However, despite the extremely fast progress, the materials' electronic properties that are crucial to the photovoltaic performance are relatively little understood. It is still under debate whether the photo-generated charges have an excitonic or a free-carrier character. Also, is not completely clear how the charge carriers' mobility of the active layer influences the overall performance and the origin of the high efficiencies of perovskite-based solar cell devices. Moreover the results strongly depend on the preparation method, the purity of the material and the film treatment, which can result to uncontrolled morphological variations and poor reproducibility of photovoltaic performance.

The theoretical calculations of mobility of charge carriers in hybrid perovskite, using the density functional theory including van der Waals interaction and the Boltzmann theory for diffusive transport in the relaxation time approximation, indicate that the mobility of electrons in MAPI perovskite crystals ranges from 5 to 10 $cm^2V^{-1}s^{-1}$ and that for holes within 1–5 $cm^2V^{-1}s^{-1}$, where the variations depend on the crystal structure investigated and the level of doping [6]. In the case of devices, the perovskite films are composed of microcrystals, or nanowires, hence the experimental values of mobility of charge carriers in perovskites films may differ from theoretical calculation by many orders of magnitude. On the other side the charge carrier's mobility in the Spiro-Me-O-TaD holes transporter layer is much lower, which can globally conduct to a lower charge carrier's mobility through the whole device multilayer structure.

In this paper we investigate the mobility of holes through the interface $CH_3NH_3PbI_3$/Spiro-MeOTAD by using the Photo-generated Charge Extraction by Linearly Increasing Voltage (Photo-CELIV) method. Photo-CELIV is a new and powerful technique for studying charge transport physics, particularly in disordered systems such as organic semiconductors [7]. We considered here the multi-layer structure based on methyl-ammonium lead-iodide perovskite: FTO/TiO_2/$CH_3NH_3PbI_3$/Spiro-MeOTAD/Au.

The TiO_2 film may be deposited by different methods such as spin coating [8–9], spray pyrolysis [10-13], and PLD [14–16]. Different from the most common studied system using MAPI perovskite, in this study the TiO_2 dense film was deposited by sputtering and not by spray pyrolysis. The advantage of sputtering method comparing to spray pyrolysis is the very high reproducibility and deposition at room temperature. There is no need to heat the substrate FTO/glass films. In our previous studies [17–33] we have demonstrated that heating of transparent conducting electrodes at more than 300 °C conduct to irreversible changes of the electrical properties.

2. EXPERIMENTAL SETTING

The configuration of studied samples is described in Fig.1. Commercial FTO covered glasses were used as transparent electrodes. A dense titanium oxide (TiO_2) film of 30 nm was deposited by reactive sputtering using a metallic titanium target in oxygen atmosphere. Two equimolar solutions of 0.1983 g (1.25 mmole) CH_3NH_3I at 0.25 ml dry DMF 0.5785 g (1.25 mmole) PbI_2 at 25 ml dry DMF, were mixed, just before the spin coating. The CH_3NH_3I was prepared as follows: 20 ml of a methylamine solution (Ferak 40/% w/v) containing 8 g methylamine (257 mmol) was diluted with 80 ml of ethanol. To this solution a Hydroiodic acid solution in water (Merck 57 % w/v) was added slowly under stirring until the PH of solution turns to acidic (about 60 ml). The solution was stirred for 2 h at room temperature and evaporated to dryness. The solid was dispersed to anhydrous diethylether and filtrated. It washed copiously with anhydrous diethylether to obtain white crystals. The CH_3NH_3I crystals were dried at 60 ^{0}C in a vacuum oven overnight. The PbI_2 was prepared as follows: 3.3 g (10 mmol) of $Pb(NO_3)_2$ (Serva anal. Grade) were diluted to 50 ml of distilled water. To this solution, a solution of 3.3 g (20 mmol) of KI (Merck Reag. Ph. Eur.) in 50 ml distilled water was added under stirring, slowly at room temperature. The gold-yellow precipitate was filtered and recrystallized from water to give golden-yellow crystals. The PbI_2 crystals were dried at 60 ^{0}C in a vacuum oven overnight. The perovskite film was prepared, in one step, by spin coating. The solution was spin on the top of TiO_2 dense film at 1 600 RPM during 30 s. For the Hole Transporting Material (HTM) thin films preparation was used the Spiro-MeOTAD purchased from MERCK. A solution of (75 mg in 0.3 ml CB) was spin coat at 3 500 RPM during 20 s. The top gold electrode (of about 40 nm) was deposited by sputtering under vacuum.

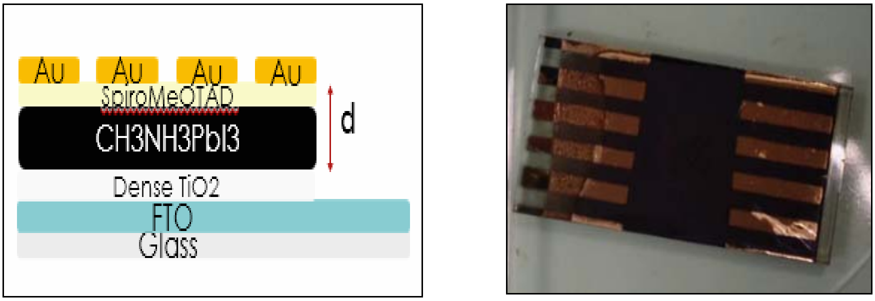

a) b)

Fig. 1 – a) Multi-layer solar cells perovskite configuration; b) sample photo.

The principle of charge carriers' mobility measurements by Photo-CELIV method is described briefly in Fig. 2.

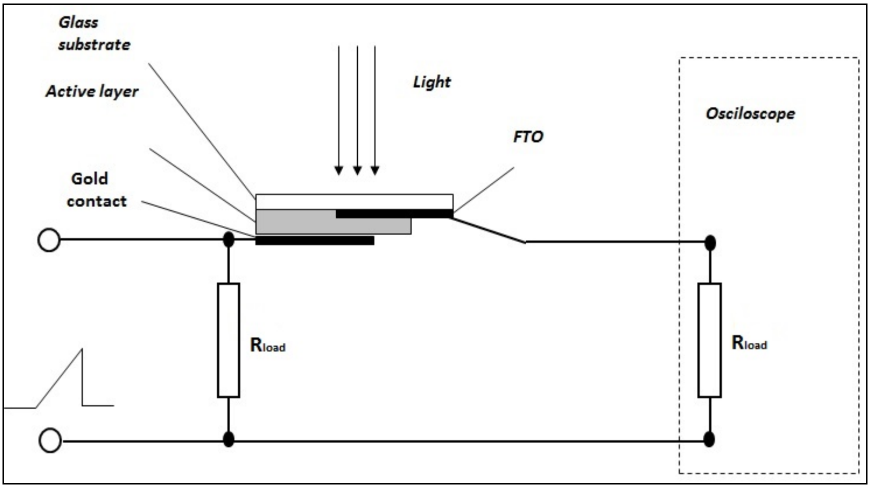

Fig. 2 – Photo-CELIV setup.

The method is based on the analysis of the extraction of photo-generated charge carriers current transients when a ramp voltage pulse is applied to a sample with a blocking contact (Fig. 3). The time t_{max} corresponding to the maximal current density depends on the mobility of charge carriers (μ). The initial slope of the current density transient depends on the bulk conductivity, σ, of the sample. The concentration of photo-generated charge carriers Δn or Δp can be estimated by integration of the extracted part of current density transients (above $j(0)$). So the carriers' concentration and the mobility of equilibrium charge carriers may be estimated independently. A short laser pulse ($\lambda = 532$ nm) of 250 ms is applied before starting the current density measurement (moment $t = 0$ see Fig. 3). This short light pulse will create more charge carriers and we will call j_{light} the density of current after the exposure of the sample to this short light pulse. j_{dark} is the current density measured in the absence of the light pulse (in dark). The density of photo-generated current, $j_{photogen}$ is given by the difference between j_{light} and j_{dark}: $j_{photogen} = j_{light} - j_{dark}$.

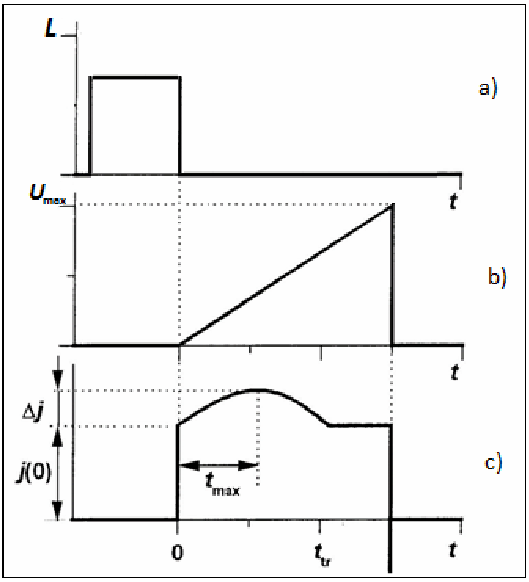

Fig. 3. – Schematic illustration of CELIV a) light pulse; b) ramp voltage pulse applied to sample; c) current density in the sample after ramp voltage is applied [12].

By varying A – the voltage slope, the best conditions can be achieved to get the initial step $j(0)$.

In the case of samples with low electrical conductivities, the extracted charge carriers do not significantly affect the electric field inside the samples and the charge carriers mobility can be calculated easily using the following formula:

$$t_{\max} = \sqrt{\frac{2d^2}{3\mu A}} \quad . \tag{1}$$

If the electrical conductivity of the samples is high, then the mobility can be calculated by the formula:

$$t_{\max} = \sqrt[3]{\frac{3\tau_\sigma d^2}{\mu A}}. \tag{2}$$

Here τ_σ is Maxwell's relaxation time. In most of the cases, τ_σ could be determined from the period of time between the moment of the signal start and the moment when the current density transient reaches the double initial step value: $2j(0)$.

In this paper the mobility of holes through the perovskite and Spiro MeOTAD film was determined. The thickness (*d*), corresponding to this transversal region (see Fig. 1) was determined by profilometry and was 1.2 µm. The value of $t_{\max}$ was determined from the graph of photogenerated current density.

3. RESULTS AND DISCUSSIONS

Figure 4b–c depicts the SEM micrographs for the methylamonium-lead triodine (MAPI) thin films deposited on glass. As one can see the prepared perovskite films presented long crystals (more than 200 µm). Several studies have established that halide perovskite exhibits unusually long diffusion excitons lengths reaching over 100 nm. This could be explained for the extremely long dimension of these perovskite crystals. Figure 4d presents the SEM micrograph of top Spiro-MeOTAD layer deposited on nanowires perovskite film.

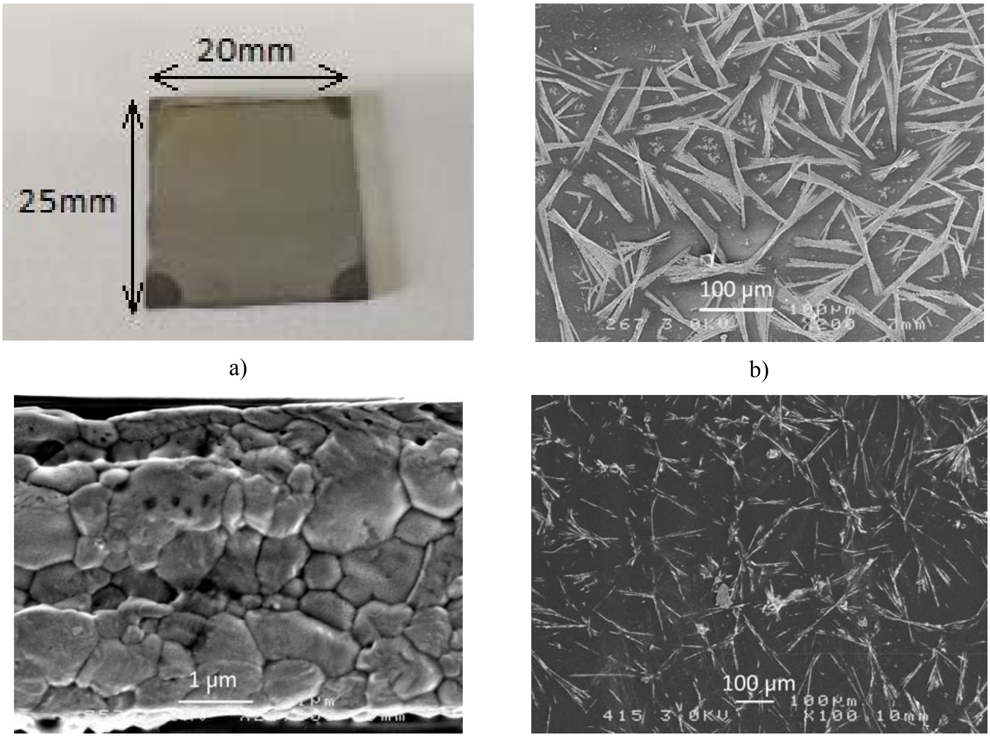

a) b)

c) d)

Fig. 4 – Perovskite nanowire film on glass substrate: a) sample photo; b), c), SEM micrograph of films deposited on glass substrates; d) top view after Spiro-MeOTAD film deposition.

The XRD analysis for the perovskite films deposited on glass, FTO, and TiO_2 films, respectively, are given in Fig. 5.

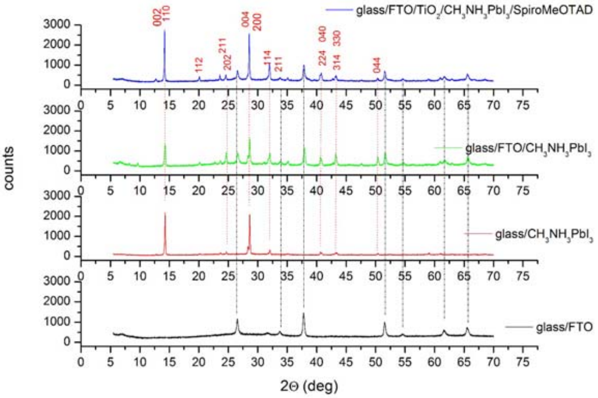

Fig. 5 – XRD spectra for MAPI thin films deposited on glass, FTO/glass, and TiO_2 dense films, respectively. The XRD spectra of the reference FTO/glass is also given.

It was found through powdered X-ray diffraction (XRD) that the methylammonium lead iodide ($MAPbI_3$) perovskite exists in the cubic Pm3m phase at high temperature above 330 K, below which it undergoes a phase transition to the tetragonal I4/mcm phase and then to the orthorhombic Pnma phase below 170 K [34]. There are no critical differences between the tetragonal and cubic phases, except a slight rotation of PbI_6 octahedra along the *c*-axis and a small difference in energy. The XRD spectra of the cubic and tetragonal phases are similar with slight differences that consist mainly from splitting of the peaks 100 and 200 of cubic phase to the 002, 110 and 004, 220 of the tetragonal phase, respectively. Moreover two new peaks (211) and (213) appear in the tetragonal phase. The most safe criterion of XRD spectra to distinguish between them is the minor diffraction from the (211) planes at $2\theta \sim 23.5°$.

In our case the presence of a peak at 23.68° in the XRD spectra indicates the presence of the tetragonal I4/mcm phase. The peak at $2\theta = 14.29°$ can be deconvoluted [35] into two peak components at 14.14° and 14.29° attributed to the 002 and 110 diffractions, respectively.

The X-ray diffraction patterns of $CH_3NH_3PbI_3$ films on different substrates (glass, FTO, and TiO_2) confirm the tetragonal 3D structure and the space group I4/mcm. No peaks of PbI_2 are observed indicating that is no excess of PI2 and the reaction of perovskite formation was completed. The peaks intensity increase in the case of the deposition of perovskite film on TiO_2 dense films indicating a better crystallisation comparing to films deposited on FTO or glass. The crystallite size influences the transport of charge carriers. A better crystallization and large crystalline size are favourable to a higher transport of charge carriers.

In Fig. 6 is given the current density J_{light} after laser pulse excitation. From this graph the value of τ_σ could be extracted.

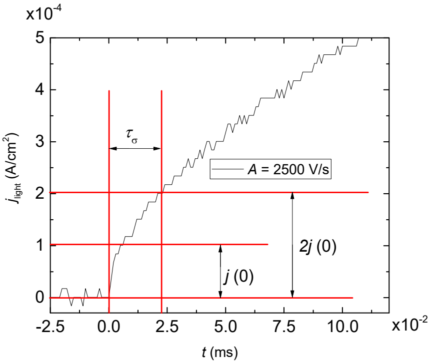

Fig. 6 – The light current density; τ_σ is Maxwell's relaxation time.

The value of t_{max} was determined from the maximum of the photo-generated current (see Fig.7).

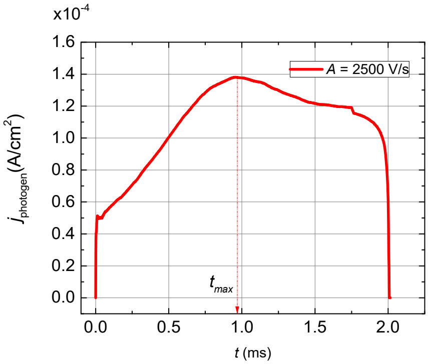

Fig. 7 – The photo-generated current density.

The form of current density kinetics suggests that the investigated layers were highly conductive. Hence, from the values of τ_σ and t_{max} the holes mobility μ_h was calculated according to eq. (2):

$$\mu_h = \frac{3\tau_\sigma d^2}{A t_{\max}^{3}}. \tag{3}$$

The obtained values for different slopes of increasing voltage are given in Table 1. This mobility corresponds to the charge transport between the TiO_2 interface and top gold contact.

The experimental values of Spiro-OMeTAD, one of the hole transporting material (HTM) with the highest hole mobility, is of about 4×10^{-5} $cm^2V^{-1}s^{-1}$ [36].

The high reported values of the holes mobility correspond only to theoretical calculation for $CH_3NH_3PbI_3$ nanocrystals. In practical cases the measured values of mobility of holes are much smaller, of order of 10^{-5} $cm^2V^{-1}s^{-1}$ and this could be explained by the disorder and grain boundaries in the case of polycrystalline films, or due to the interfaces between the perovskite nanowires and Spiro-MeOTAD molecular glass material in this case.

Table 1

The calculated values of holes' mobility
in $CH_3NH_3PbI_3$/Spiro-MeOTAD thin film by using Photo-CELIV

U_{max} (V)	t_{ramp} (s)	ramp A (V/s)	τ_σ (s)	$t_{\max}$ (s)	μ_h (cm²/Vs)
5	2×10^{-3}	2 500	2.2×10^{-5}	9.6×10^{-4}	5.2×10^{-7}
5	1×10^{-3}	5 000	2.0×10^{-5}	6.3×10^{-4}	8.0×10^{-7}
5	0.5×10^{-3}	10 000	1.3×10^{-5}	4.3×10^{-4}	8.5×10^{-7}

4. CONCLUSIONS

The mobility of holes for the configuration FTO/TiO2/CH3NH3PbI3/Spiro-MeOTAD/Au was measured by the Photo-CELIV method. Structural and morphological properties was analysed by X-ray diffraction and Scanning Electron Microscopy. The holes' mobility was determined by photo-CELIV method using a green laser (λ = 532 nm). The highest holes' mobility from TiO2 thin film through the perovskite and Spiro MeOTAD film to the top gold electrode was of order 8.5×10^{-7} cm²/Vs. The electrical properties were correlated with the morphological and structural properties of the perovskite film.

ACKNOWLEDGEMENTS

One of the authors (G.A. Mousdis) would like to acknowledge the financial support from the Hellenic General Secretariat for Research and Technology through project Polynano-Kripis 447963.

REFERENCES

1. M. GRATZEL, *The light and shade of perovskite solar cells*, Nat. Mater., **13**, *9*, pp. 838–842, 2014.
2. M.A. GREEN, A. HO-BAILLIE, H.J. SNAITH, *The emergence of perovskite solar cells*, Nat. Photonics, **8**, *7*, pp. 506–514, 2014.
3. H.J. SNAITH, *Perovskites: The Emergence of a New Era for Low-Cost, High-Efficiency Solar Cells*, J. Phys. Chem. Lett., **4**, *21*, pp. 3623–3630, 2013.
4. N.G. PARK, *Organometal Perovskite Light Absorbers Toward a 20% Efficiency Low-Cost Solid-State Mesoscopic Solar Cell*, J. Phys. Chem. Lett., **4**, *15*, pp. 2423–2429, 2013.
5. Q.F. DONG, Y.J. FANG, Y.C. SHAO, P. MULLIGAN, J. QIU, L. CAO, J.S. HUANG, *Electron-hole diffusion lengths > 175 mu m in solution-grown $CH_3NH_3PbI_3$ single crystals*, Science, **347**, *6225*, pp. 967–970, 2015.
6. CARLO MOTTA, FEDWA EL-MELLOUHI, STEFANO SANVITO, *Charge carrier mobility in hybrid halide perovskites*, Scientific Reports, **5**, *12746*, 2015.
7. N. NEKRAŠAS, K. GENEVIČIUS, M. VILIŪNAS, G. JUŠKA, *Features of current transients of photogenerated charge carriers, extracted by linearly increased voltage*, Chemical Physics, **404**, pp. 56–59, 2012.
8. N. IFTIMIE, D. LUCA, F. LACOMI, M. GIRTAN, D. MARDARE, *Gas sensing materials based on TiO_2 thin films*, J. Vac. Sci. Amp Technol. B, **27**, *1*, pp. 538–541, 2009.
9. A.V. MANOLE, M. DOBROMIR, M. GIRTAN, R. MALLET, G. RUSU, D. LUCA, *Optical properties of Nb-doped TiO_2 thin films prepared by sol-gel method*, Ceram. Int., **39**, *5*, pp. 4771–4776, 2013.
10. I. VAICIULIS, M. GIRTAN, A. STANCULESCU, L. LEONTIE, F. HABELHAMES, S. ANTOHE, *On titanium oxide spray deposited thin films for solar cells applications*, Proc. Romanian Acad. A, **13**, *4*, pp. 335–342, 2012.
11. C. ADOMNITEI, D. LUCA, M. GIRTAN, I. SANDU, V. NICA, A.V. SANDU, D. MARDARE, *Nb-doped TiO_2 thin films deposited by spray pyrolysis method*, J. Optoelectron. Adv. Mater., **15**, *5–6*, pp. 519–522, 2013.
12. D. MARDARE, F. IACOMI, N. CORNEI, M. GIRTAN, D. LUCA, *Undoped and Cr-doped TiO_2 thin films obtained by spray pyrolysis*, Thin Solid Films, **518**, *16*, pp. 4586–4589, 2010.
13. D. CHAPRON, M. GIRTAN, J.Y. LE POMMELEC, A. BOUTEVILLE, *Droplet dispersion calculations for ultrasonic spray pyrolysis depositions*, J. Optoelectron. Adv. Mater., **9**, *4*, pp. 902–906, 2007.
14. A. STANCULESCU, M. SOCOL, G. SOCOL, I.N. MIHAILESCU, M. GIRTAN, F. STANCULESCU, *Maple prepared organic heterostructures for photovoltaic applications*, Appl. Phys. -Mater. Sci. Process., **104**, *3*, pp. 921–928, 2011.
15. F. STANCULESCU, O. RASOGA, A.M. CATARGIU, L. VACAREANU, M. SOCOL, C. BREAZU, N. PREDA, G. SOCOL, A. STANCULESCU, *MAPLE prepared heterostructures with arylene based polymer active layer for photovoltaic applications*, Appl. Surf. Sci., **336**, pp. 240–248, 2015.
16. A. STANCULESCU, L. VACAREANU, M. GRIGORAS, M. SOCOL, G. SOCOL, F. STANCULESCU, N. PREDA, E. MATEI, I. IONITA, M. GIRTAN, I.N. MIHAILESCU, *Thin films of arylenevinylene oligomers prepared by MAPLE for applications in non-linear optics*, Appl. Surf. Sci., **257**, *12*, pp. 5298–5302, 2011.
17. S. IFTIMIE, R. MALLET, J. MERIGEON, L. ION, M. GIRTAN, S. ANTOHE, *On the structural, morphological and optical properties of ITO, ZnO, ZnO: Al and NiO thin films obtained by thermal oxidation*, Dig. J. Nanomater. Biostructures, **10**, *1*, pp. 221–229, 2015.
18. M. GIRTAN, A. BOUTEVILLE, G.G. RUSU, M. RUSU, *Preparation and properties of SnO_2: F thin films*, J. Optoelectron. Adv. Mater., **8**, *1*, pp. 27–30, 2006.
19. M. GIRTAN, R. MALLET, *On the electrical properties of transparent electrodes*, Proc. Romanian Acad. A, **15**, *2*, pp. 146–150, 2014.
20. F.Z. GHOMRANI, S. IFTIMIE, N. GABOUZE, A. SERIER, M. SOCOL, A. STANCULESCU, F. SANCHEZ, S. ANTOHE, M. GIRTAN, *Influence of Al doping agents nature on the physical properties of Al:ZnO films deposited by spin-coating technique*, Optoelectron. Adv. Mater.-Rapid Commun., **5**, *3–4*, pp. 247–251, 2011.
21. M. RUSU, G.G. RUSU, M. GIRTAN, S.D. SEIGNON, *Structural and optical properties of ZnO thin films deposited onto ITO/glass substrates*, J. Non-Cryst. Solids, **354**, *35–39*, pp. 4461–4464, 2008.
22. M. GIRTAN, *Investigations on the optical constants of indium oxide thin films prepared by ultrasonic spray pyrolysis*, Mater. Sci. Eng. B-Solid State Mater. Adv. Technol., **118**, *1–3*, pp. 175–178, 2005.
23. M. GIRTAN, A. VLAD, R. MALLET, M.A. BODEA, J.D. PEDARNIG, A. STANCULESCU, D. MARDARE, L. LEONTIE, S. ANTOHE, *On the properties of aluminium doped zinc oxide thin films deposited on plastic substrates from ceramic targets*, Appl. Surf. Sci., **274**, pp. 306–313, 2013.
24. M. GIRTAN, G.G. RUSU, S. DABOS-SEIGNON, M. RUSU, *Structural and electrical properties of zinc oxides thin films prepared by thermal oxidation*, Appl. Surf. Sci., **254**, *13*, pp. 4179–4185, 2008.
25. G.G. RUSU, M. GIRTAN, M. RUSU, *Preparation and characterization of ZnO thin films prepared by thermal oxidation of evaporated Zn thin films*, Superlattices Microstruct., **42**, 1–*6*, pp. 116–122, 2007.
26. M. GIRTAN, *The influence of post-annealing treatment on the electrical properties of In_2O_3 thin films prepared by an ultrasonic spray CVD process*, Surf. Coat. Technol., **184**, *2–3*, pp. 219–224, 2004.
27. M. GIRTAN, G. FOLCHER, *Structural and optical properties of indium oxide thin films prepared by an ultrasonic spray CVD process*, Surf. Coat. Technol., **172**, *2–3*, pp. 242–250, 2003.
28. M. GIRTAN, H. CACHET, G. I. RUSU, *On the physical properties of indium oxide thin films deposited by pyrosol in comparison with films deposited by pneumatic spray pyrolysis*, Thin Solid Films, **427**, *1–2*, pp. 406–410, 2003.
29. M. GIRTAN, G.I. RUSU, G.G. RUSU, *The influence of preparation conditions on the electrical and optical properties of oxidized indium thin films*, Mater. Sci. Eng. B-Solid State Mater. Adv. Technol., **76**, *2*, pp. 156–160, 2000.
30. M. GIRTAN, G.I. RUSU, G.G. RUSU, S. GURLUI, *Influence of oxidation conditions on the properties of indium oxide thin films*, Appl. Surf. Sci., **162**, pp. 492–498, 2000.

31. M. GIRTAN, M. SOCOL, B. PATTIER, M. SYLLA, A. STANCULESCU, *On the structural, morphological, optical and electrical properties of sol-gel deposited ZnO In films*, Thin Solid Films, **519**, *2*, pp. 573–577, 2010.
32. M. GIRTAN, R. MALLET, D. CAILLOU, G.G. RUSU, M. RUSU, *Thermal stability of poly(3,4-ethylenedioxythiophene)-polystyrenesulfonic acid films electrical properties*, Superlattices Microstruct., **46**, *1–2*, pp. 44–51, 2009.
33. M. GIRTAN, M. KOMPITSAS, R. MALLET, I. FASAKI, *On physical properties of undoped and Al and In doped zinc oxide films deposited on PET substrates by reactive pulsed laser deposition*, Eur. Phys. J.-Appl. Phys., **51**, *3*, 2010.
34. T. BAIKIE, Y. FANG, J.M. KADRO, M. SCHREYER, F. WEI, S.G. MHAISALKAR, M. GRAETZEL, T.J. WHITE, *Synthesis and Crystal Chemistry of the Hybrid Perovskite* $(CH_3NH_3)PbI_3$ *for Solid-State Sensitised Solar Cell Applications*, J. Mater. Chem. A, **18**, *1*, pp. 5628–5641, 2013.
35. ZHAONING SONG, SUNETH C. WATTHAGE, ADAM B. PHILLIPS, BRANDON L. TOMPKINS, RANDY J. ELLINGSON, MICHAEL J. HEBEN., *Impact of Processing Temperature and Composition on the Formation of Methylammonium Lead Iodide Perovskites*, Chem. Mater., **27**, *13*, pp. 4612–4619, 2015.
36. TOMAS LEIJTENS, I-KANG DING, TOMMASO GIOVENZANA, JASON T. BLOKING, MICHAEL D. MCGEHEE, ALAN SELLINGER, *Hole Transport Materials with Low Glass Transition Temperatures and High Solubility for Application in Solid-State Dye-Sensitized Solar Cells*, ACS Nano, **6**, *2*, pp.1455–1462, 2012.

Received June 17, 2016

2nd publication / 2-oji publikacija

Anisotropy of charge carrier transport in PCPDTBT field-effect transistor structures

Andrius Aukštuolis, Nerijus Nekrašas, Kristijonas Genevičius, Jūratė Jonikaitė-Švėgždienė

Synthetic Metals, 264, 116382 (2020)
https://doi.org/10.1016/j.synthmet.2020.116382

Reprinted with permission from the *Elsevier*
Perspausdinta su *Elsevier* leidimu

Synthetic Metals 264 (2020) 116382

Contents lists available at ScienceDirect

Synthetic Metals

journal homepage: www.elsevier.com/locate/synmet

Anisotropy of charge carrier transport in PCPDTBT field-effect transistor structures

Andrius Aukštuolis[a,*], Nerijus Nekrašas[a], Kristijonas Genevičius[a], Jūratė Jonikaitė-Švėgždienė[b]

[a] Vilnius University, Faculty of Physics, Institute of Chemical Physics, Vilnius, Lithuania
[b] Vilnius University, Faculty of Chemistry and Geosciences, Institute of Chemistry, Vilnius, Lithuania

ARTICLE INFO

Keywords:
PCPDTBT
OFET
i-CELIV
DSC
Mobility
Morphology

ABSTRACT

In this paper we are analyzing anisotropy of hole mobility in the organic field-effect transistor structures with an active layer of PCPDTBT (poly[2,6-(4,4-bis-(2-ethylhexyl)-4H-cyclopenta [2,1-b;3,4-b′]dithiophene)-alt-4,7(2,1,3-benzothiadiazole)]). Hole mobility and its dependence on the temperature was measured by i-CELIV and current transients methods. The combination of both techniques allowed us to obtain results of hole mobilities in perpendicular and parallel to the substrate directions. In the same temperature range differential scanning calorimetry (DSC) measurements were performed to detect morphological changes in the active layer of the field-effect transistor structure. From obtained results of mobility dependence on temperature, energetic disorder parameter of Bässler's Gaussian Disorder Model (GDM) was estimated. DSC data and hole transport data demonstrated that the change in PCPDTBT's morphology is responsible for the abrupt decrease of hole mobility on temperature in the field-effect transistor structure.

1. Introduction

Organic semiconductors are getting more attention as they are replacing traditional inorganic semiconductors in the applications like solar cells, light emitting diodes, thin film transistors. Replacement comes from the main advantages of the organic semiconductors, which are: low weight, simpler fabrication procedure, flexibility and potentially low costs in mass production in comparison with traditional inorganic semiconductors [1,2]. However, organic semiconductors have still to overcome some issues to be used more widely. The most important of those problems are low efficiency, degradation from oxygen, humidity or light, low charge carrier mobility [3]. One of the biggest difference between traditional semiconductors and organic semiconductors is that organics usually are in the amorphous state due to weak interaction between the molecules. This feature can be considered as an advantage (flexibility, easy manufacturing) as well as a disadvantage (low mobility). By manipulating the morphology of the organic semiconductors the performance in devices can be significantly increased [4]. The morphology and its influence on the devices' performance is one of the most relevant study areas for organic semiconductors. In this work we investigate charge carrier transport in the polymer PCPDTBT (Fig. 1) which could have different morphology (of lower disorder or of higher disorder) [5] therefore investigation of anisotropy in PCPDTBT films is important. Unlike the Ref. [5] our aim was to investigate charge carrier transport properties influenced by morphology differences. The change in the temperature of the material can affect charge carrier transport by increasing energy of charge carriers and by changing the morphology. A good example of how temperature affects morphology and charge carrier transport is typical bulk heterojunction solar cells made of P3HT:PCBM [6].

In this work we focused on PCPDTBT morphology's influence on hole mobility in the field-effect transistor (OFET) structure with top contacts (Fig. 2). In OFETs the channel of charge carriers is located near dielectric layer where morphology is different in comparison with bulk material, so temperature could affect each region differently. Investigation of charge carrier transport anisotropy is important because it gives information about the performance of the OFET and the inner structure of the material and how dielectric's surface affects transport of the charge carriers.

There are few conventional methods to measure charge carrier mobility of organic semiconductors. Depending on the structure of the sample time of flight (TOF), I–V characteristics, space charge limited current (SCLC), charge extraction by linearly increasing voltage (CELIV) and others can be used, but only few of them are applicable for OFET structure. For example, TOF method is not suitable for structures with dielectric layer or with planar electrodes, while I–V characteristics are suitable but the density of charge carriers in the channel can significantly influence the values of obtained mobility. Two different

---

* Corresponding author at: Saulėtekio al. 3, Vilnius, Lithuania.
E-mail address: andrius.aukstuolis@ff.vu.lt (A. Aukštuolis).

https://doi.org/10.1016/j.synthmet.2020.116382
Received 3 January 2020; Received in revised form 22 March 2020; Accepted 1 April 2020

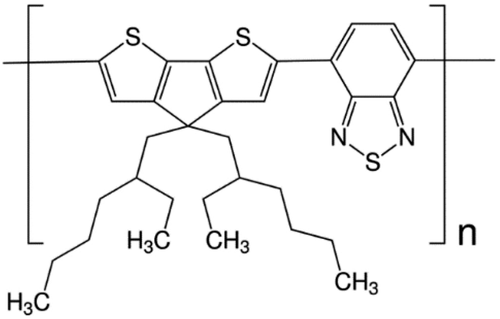

Fig. 1. Chemical structure of PCPDTBT.

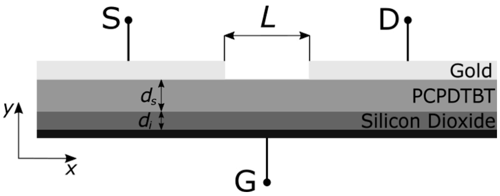

Fig. 2. Schematic drawing of an OFET structure employed in our work.

methods were used by us to measure hole mobility in different directions in PCPDTBT layer. The first one is a modified CELIV method for structures with dielectric layer and it is called i-CELIV [7]. In this method mobility of charge carriers moving in perpendicular to the substrate direction (along y axis in Fig. 2) is measured. The second method is based on current transients in field-effect transistor structures [8]. This method allows us to investigate transport of the charge carriers in parallel to the substrate direction (along x axis in Fig. 2). The combination of two methods allows us to investigate anisotropy of charge carrier movement in the active layer. In this work we used Gaussian disorder model proposed by Bässler [9] and we evaluated disorder parameters of density of states (DOS) in the PCPDTBT layer. Estimation of disorder parameters were performed at higher than room temperatures because this temperature range is typical for operating OFETs.

2. Experimental

2.1. Sample preparation

In this work we used Si/SiO_2 substrates which were single side polished, polished side had thermally grown SiO_2 layer on top. Silicon layer was heavily doped (n type) and used as gate electrode in our measurements. The thickness of SiO_2 layer was 100 nm. Substrates were cleaned in ultrasonic bath for 15 min in each of the solvents: distilled water, acetone and isopropanol. Before spin-coating PCPDTBT substrate was treated by oxygen plasma for two minutes to remove organic residuals and to make surface more hydrophilic.

Poly[2,6-(4,4-bis-(2-ethylhexyl)-4H-cyclopenta [2,1-b;3,4-b′]dithiophene)-alt-4,7(2,1,3-benzothiadiazole)] PCPDTBT material was bought from Sigma-Aldrich in form of dry powder with the average molecular weight M_w $7000-20000$ g/mol. PCPDTBT was used as it is, without any additional purification. It was dissolved in chloroform with the concentration of 10 mg/mL under dry nitrogen atmosphere. Chloroform was chosen because of a good solubility of PCPDTBT [10] and high evaporation rate, which are needed to produce thick enough layer for i-CELIV measurements. However, high evaporation rate can result in more amorphous layer. Solution was spincoated on Si/SiO_2 substrate under the same nitrogen atmosphere conditions as solution was made. First spincoating step was 500 rpm for 60 s to cast the layer and second step was 2000 rpm for 40 s to completely dry the sample and remove residuals of a solvent. These parameters resulted in getting 160 nm thickness d_s of active layer. After spincoating the polymer, gold source and drain contacts with OFET's channel length L of 30 μm were formed via evaporation. Structure with top contacts was required for investigations of hole transport in perpendicular to the substrate direction by i-CELIV. Samples were not annealed prior to measurements.

2.2. DSC measurements

Differential scanning calorimetry (DSC) measurements were performed on a DSC 8500 (Perkin Elmer). Small sample of PCPDTBT powder $4-7$ mg were filled into standart aluminium pan. The temperature range was from -20 °C to 200 °C (273 K–493 K) with a heating and cooling rate of 10 °C/min. All measurements were done in dry nitrogen atmosphere. Glass transition temperature T_g of polymer was calculated from the heating thermogram.

2.3. Experimental setup

Sample with the thermocouple attached was put in the dedicated electrically shielded holder on the hot plate. Measurements were conducted in temperature range from 20 °C to 160 °C. In both methods (current transients and i-CELIV) polarity of voltage was chosen to inject holes into PCPDTBT layer through the golden source contact.

Current transients measurement setup was set accordingly to the report [8]. In this setup voltage pulse U_{SD} is applied while gate electrode is grounded and drain electrode is grounded via load resistor. At very first, injected through the source electrode holes move towards dielectric layer, because the y-component of electric field is much larger than x-component (due to $d_s < < L$). After reaching dielectric and PCPDTBT interface they move along the dielectric layer towards the drain contact until time t_d when first holes reach drain contact (Fig. 4). Time t_d is much larger than drift time of holes from source to dielectric layer (because $d_s < < L$), so latter can be neglected. Thus, while channel is not formed yet and voltage drop on load resistance is negligible, from t_d and U_{SD} values the mobility of holes $\mu_=$ in parallel to the substrate direction can be calculated [8]:

$$\mu_= = 0.38\frac{L^2}{t_d U_{SD}}, \tag{1}$$

i-CELIV method allows us to investigate charge carrier transport in the perpendicular to the substrate direction. In this setup voltage is connected between source and gate and all injected holes accumulate near dielectric surface. Later they are extracted by ramp voltage and move backwards the entire thickness of the organic layer (Figs. 2 and 3). In this work we call it perpendicular to the substrate direction. During extraction the first holes move in SCLC conditions and reach the source at transit time t_{tr}. In the original paper [11] authors used time t_1 defined at double the value of j_0 for the t_{tr} estimation. However, we used a slightly smaller value of t' - when j_0 reaches 1.5 of its value, to avoid inaccuracy in transit time evaluation by saturation of the extraction current. In our case t_{tr} can be recalculated by [11]:

$$t' = \tan^{-1}\left(\frac{1}{\sqrt{2}}\right)t_{tr}\ . \tag{2}$$

Hole mobility in perpendicular to the substrate direction can be found:

$$\mu_\perp = \frac{2d_s^2}{At_{tr}^2}\left(1 + \frac{\varepsilon_s d_i}{\varepsilon_i d_s}\right) \tag{3}$$

where A is voltage increase rate, ε_i is dielectric's permittivity, d_i is the

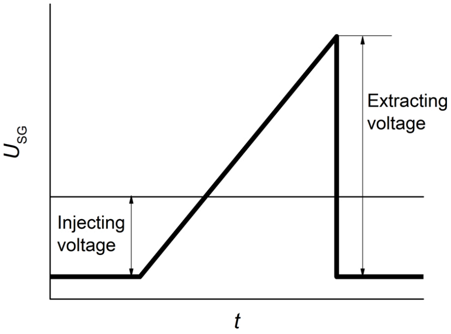

Fig. 3. Schematic view of i-CELIV ramp signal.

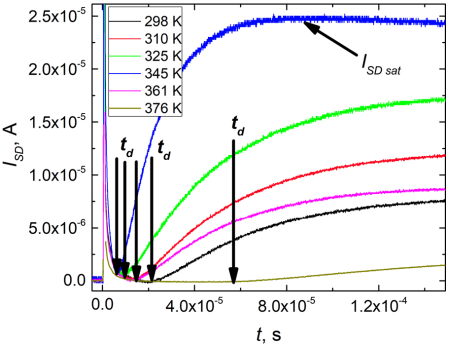

Fig. 4. Current transients at different temperatures (obtained from current transient method).

thickness of the dielectric layer, ε_s is PCPDTBT's permittivity and d_s is the thickness of PCPDTBT layer.

During the i-CELIV measurements the injecting voltage was high enough to get the saturation of extraction current density j_{sat} for d_s calculation and control at different temperatures. The thickness of the layer d_s can be calculated accordingly [7]:

$$d_s = \varepsilon_0 \varepsilon_s A \left(\frac{1}{j_0} - \frac{1}{j_{sat}} \right) \tag{4}$$

where ε_0 is vacuum permittivity, j_0 is current density value of initial capacitance step of i-CELIV and j_{sat} is current density saturation value. All the data of i-CELIV measurement is given in supplementary information Table S1.

3. Results and discussion

Our experimental setup allows to measure hole mobilities in temperatures up to 200 °C. In Fig. 4 few typical current transients of organic field effect transistor structure with PCPDTBT active layer at different temperatures are presented. Black arrows mark the saturated value of $I_{SD\ sat}$ and time t_d when holes reach drain contact. Further increase of the current after t_d is caused by increasing density of charge carriers in the OFET channel until the current reaches saturation $I_{SD\ sat}$. In our investigation the current transients technique has advantages over I–V characteristics. Firstly, mobility values obtained from t_d are not affected by high charge carrier density, so comparison with i-CELIV results is more relevant. Secondly, first traveling holes are more sensitive to trapping states which can be affected by morphological changes in the film. However, for verification and comparison we calculated hole mobility μ_{stat} (Fig. 6) from measured $I_{SD\ sat}$ current values at room temperature (hole mobility values obtained from I–V characteristics can be found in supplementary information Figure S1).

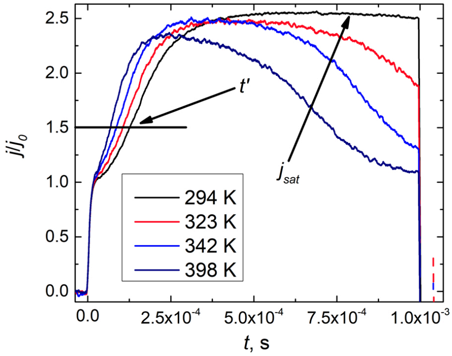

Fig. 5. Normalized current density transients at different temperatures (obtained from i-CELIV method).

Few examples of i-CELIV current density transients at different temperatures are presented In Fig. 5. After initial step j_0 attributed to source-gate capacitance of the sample, extraction current density rises and the time value t' can be found for hole mobility estimation. The line marks time t' when the current density reaches 1.5 of the value of the initial capacitance step j_0. The beginning of i-CELIV transients is superlinear. This faster than linear increase shows that the extraction current density is space charge limited (eq. (2)) and this mean that holes are accumulated near the dielectric layer and that they travel the entire thickness of the layer during extraction [7].

In the Fig. 6 we see how temperature affects the hole mobility in parallel to the substrate direction. The axes in the mobility dependence plot was chosen according to Bässler's model of hopping through energy states in order to obtain disorder parameters of the PCPDTBT [9]. In PCPDTBT hole mobility in parallel to the substrate direction increases in the beginning of heating (see fitted region in Fig. 6). This is generally expected result in disordered materials according to Bässler's model [9], because of temperature activated hopping rate. When the temperature reaches certain point of 72 °C the mobility and saturated current starts to decrease (the decrease of saturated current can be seen in the Fig. 4). A decrease of the PCPDTBT:PCBM solar cell's performance in higher than room temperatures was reported before [12]. In

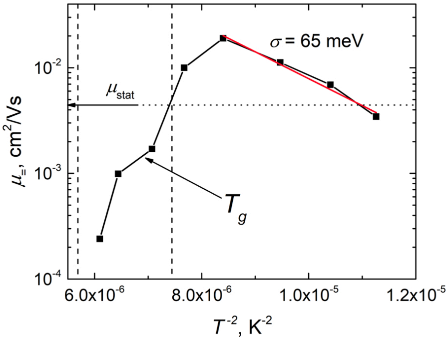

Fig. 6. Hole mobility dependence on temperature obtained by current transients measurement method.

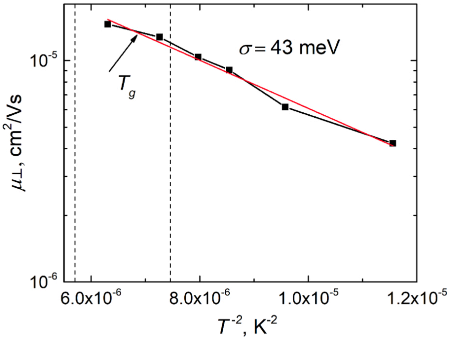

Fig. 7. Hole mobility dependence on temperature obtained by i-CELIV measurement method.

the article authors state that short circuit current and efficiency had decreased due to the decrease of the conductivity of the layer. Our results suggest that the conductivity could have been decreased because of the decrease in hole mobility. Mobility's decrease is attributed to the change in PCPDTBT layer's morphology as it could be seen from secondary measurements of hole mobility after the sample was cooled (supplementary information Fig. S4).

In contrast to the dependence of mobility in parallel to the substrate direction, hole mobility obtained by i-CELIV increases through the all heating range (Fig. 7). The values of hole mobility in perpendicular to the substrate direction are lower 800 times at room temperature. These results suggest different conditions of movement of holes in different directions as well as different morphologies. To investigate the disorder of each direction the energetic disorder parameters σ were calculated using Bässler's formalism for disordered systems [9]:

$$\mu(T,\ E) = \mu_0 \exp\left(-\left(\frac{2}{3}\frac{\sigma}{kT}\right)^2\right)\begin{cases}\exp C\left(\left(\frac{\sigma}{kT}\right)^2 - \Sigma^2\right)E^{\frac{1}{2}};\ \Sigma \geq 1.5\\ \exp C\left(\left(\frac{\sigma}{kT}\right)^2 - 2.25\right)E^{\frac{1}{2}};\ \Sigma < 1.5\end{cases}, \qquad (5)$$

where μ_0 is mobility prefactor, σ is energetic disorder parameter, k is Boltzmann constant, T is temperature, C is numeric constant, Σ is positional disorder parameter and E is electric field. In eq. (5) there are two main parameters influencing charge carrier mobility: the temperature and the electric field. Energetic disorder parameters were found from the fit of hole mobility dependence on temperature (Figs. 6 and 7). Reliable value of positional disorder parameter Σ from our measurement techniques cannot be found because the exact value of electric field cannot be found neither in i-CELIV, nor current transients techniques. Electric field's influence was neglected because the values of hole mobility were close to zero electric field condition in both cases. For the parallel to the substrate direction zero electric field mobility values was extrapolated from mobility dependence on the voltage between source and drain (supplementary information Fig. S1). The mobility dependence on the voltage U_{SD} also indicates that hole mobility has a weak dependence on the electric field in the measured range. In current transients measurement applied voltage U_{SD} is proportional to the electric field in the layer but the exact value of the electric field cannot be found because the electric field changes in time and in coordinate until $I_{\mathrm{SD\ sat}}$ is reached. In the perpendicular to the substrate direction electric field can be neglected because a significant part of the electric field is concentrated on the dielectric layer. Also when the first holes are extracted at the time t_{tr} the voltage from the ramp signal is still low and the electric field in PCPDTBT layer is very weak.

Charge carrier movement in the channel of the OFET is usually considered as 2D movement. E.V. Emelianova et al. [13] reported their numerical calculations of the charge carrier movement in the channel and showed that when charge carriers are hopping through Gaussian DOS and their concentration is low, mobility dependence on the temperature is very similar to 3D case around the room temperature for the same energetic disorder parameter σ. Our current transients measurements are performed at low concentration condition and in 2D case calculated value of σ would be < 10 % smaller than in 3D case according to the Fig. 2 in the report [13]. Our found value of $\sigma_{=}$ for parallel to the substrate direction was 65 meV. The value of $\sigma_{\perp}$ for perpendicular to the substrate direction was substantially lower than $\sigma_{=}$ and equal to 43 meV.

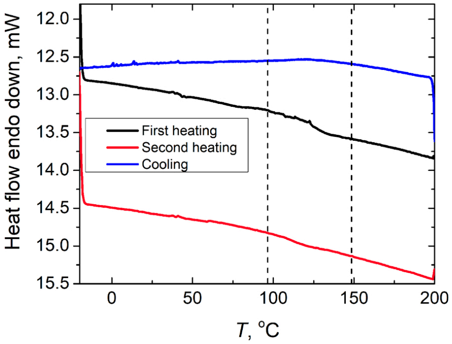

Fig. 8. DSC thermograms of PCPDTBT material.

To explain abrupt change in mobility's values with the increasing temperature, DSC measurements were performed in temperature range from -20 °C to 200 °C (253 K–473 K). Visible change in thermogram starts before 100 °C and ends above 120 °C and from the most abrupt change in the second heating curve the glass transition temperature T_g was found to be around 112.5 °C (Figs. 8 and 9). Indistinct and slow change in the thermogram is common for polymer materials because of their molecular weight, but mobility's measurements show (Fig. 6) that the change in the morphology is crucial for hole transport. From mobility $\mu_{=}$ measurements we can make assumption that structural changes in the PCPDTBT layer occurs at even lower temperatures than T_g and that these changes in morphology affects transport of the holes. Small shift in the DSC curve around glass transition temperature does not mean that morphological transition in PCPDTBT is small. After

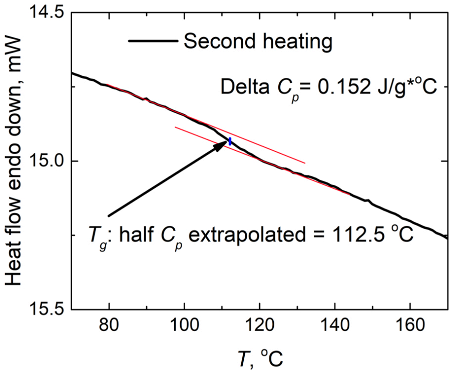

Fig. 9. Second heating thermogram with calculated glass transition temperature T_g.

heating there were visible changes in polymer state: from powder form before heating it changed to one piece glass/film type material after heating. Even though there were visible changes in PCPDTBT after heating in DSC measurements, spincoated layer did not have any visible changes. i-CELIV method allows to register active layer's thickness (see eq. (4)) with every measurement made. We did not register any thickness or capacitance change in the PCPDTBT layer during the hole mobility measurements in different temperatures thus heating did not cause any discontinuities in the layer. DSC measurements indicate that the decrease of mobility in higher temperatures obtained by current transients' measurement was caused by morphology changes in the film. Additional Atomic Force Microscopy measurements were performed on manufactured OFET structures before and after heating. The surface of spincoated PCPDTBT layer was very smooth before and after heating ($\Delta z \leq 5$ nm) and did not show any significant changes in the surface topology (supplementary information Fig. S2), only that heated layer became even smoother (roughness 1.2 nm of unheated layer to 0.3 nm of heated layer) which is expected result when heating material above T_g. Thus the inner morphological changes were not reflected on the surface of PCPDTBT. Also additional measurement of the structure were done by grazing incidence X-ray diffraction technique (supplementary information Fig. S3). Both heated and unheated PCPDTBT layers have single broad peaks around 20 degrees of 2θ. Thus both layers are rather amorphous and do not have clear crystal structure.

At higher temperatures holes temperature activated hopping rate increases, but the change in PCPDTBT morphology causes modification of the DOS and affects hole transport also. As a result we observed decrease in the hole mobility at higher temperatures in the parallel to the substrate direction (Fig. 6). In the perpendicular to the substrate direction we see steady increase in the hole mobility but the values of the mobility are much lower (Fig. 7). These results suggest that in PCPDTBT layer holes move in the different conditions in different directions (parallel and perpendicular to the substrate). This could be explained by morphology of polymer, in which (because of the interaction with SiO_2) the better conditions for the holes to move by the polymer/SiO_2 interface have formed (presumably, similar to "edge on" orientation). In this case the average π stacking distance decreases and therefore mobility of the holes is significantly higher. This difference in the mobility is hidden in the prefactor μ_0 which contains the probability for the holes to hop. Prefactor μ_0 is proportional to square of transfer integral and is determined by average coordinate intersite distance and molecular orientation [14]. We conclude that in parallel to the substrate direction average coordinate intersite distance and molecular orientation leads to more favorable conditions for the hole transport. From our experimental results it follows, that these conditions are more susceptible to the heat. Higher temperature affects morphology in the way that molecules change their orientation more in the vicinity to the dielectric layer than in the volume. Similar difference in morphology in different directions was reported before [4]. In [15] report authors showed that under some circumstances PCPDTBT could form nanoparticle quasicrystal structures in the chloroform solvent which could then result in similar morphology of the layer. In our work demonstrated results are in agreement with other authors' works [4,5,16] and we prove, that triggered by heating changes in morphology of PCPDTBT should be considered constructing devices, especially those, which are intended to work in higher ambient temperature.

4. Conclusions

Hole transport properties of OFET structures with PCPDTBT active layer were investigated by current transients and i-CELIV methods in different directions (parallel and perpendicular to the substrate) and at different temperatures. In PCPDTBT layer hole mobility is much larger (800 times at room temperature) in parallel to the substrate direction than in perpendicular to the substrate direction. Small difference in energetic disorder parameters $\sigma_{=}$ and $\sigma_{\perp}$ indicates that the difference in mobility comes from the mobility prefactor μ_0 (probability for the holes to hop). Thus in parallel to the substrate direction there are lower average coordinate intersite distance and better molecular orientation for the hole transport. Due to morphological changes in higher temperature (above 72 °C) the mobility of holes, moving near PCPDTBT/SiO_2 interface in parallel to the substrate direction is decreased. Morphological changes and decrease in hole mobility in PCPDTBT at higher temperature should be carefully addressed when making devices with this charge carrier transporting material.

CRediT authorship contribution statement

Andrius Aukštuolis: Conceptualization, Data curation, Formal analysis, Writing - original draft, Writing - review & editing, Visualization. **Nerijus Nekrašas:** Methodology, Validation, Writing - review & editing, Project administration. **Kristijonas Genevičius:** Validation, Formal analysis, Writing - original draft, Writing - review & editing, Funding acquisition. **Jūratė Jonikaitė-Švėgždienė:** Conceptualization, Investigation, Writing - original draft.

Declaration of Competing Interest

The authors declare that there are no conflicts of interest.

Appendix A. Supplementary data

Supplementary material related to this article can be found, in the online version, at doi:https://doi.org/10.1016/j.synthmet.2020.116382.

References

[1] Y. Yang, F. Wudl, Organic electronics: from materials to devices, Adv. Mater. 21 (2009) 1401–1403, https://doi.org/10.1002/adma.200900844.

[2] A.J. Oostra, E.C.P. Smits, D.M. de Leeuw, P.W.M. Blomc, J.J. Michels, On the short circuit resilience of organic solar cells: prediction and validation Phys, Chem. Chem. Phys. 17 (2015) 21501–21506, https://doi.org/10.1039/c5cp03156g.

[3] F. Laquai, D. Andrienko, C. Deibel, D. Neher, Charge carrier generation, recombination, and extraction in polymer fullerene bulk heterojunction organic solar cells, in: K. Leo (Ed.), Elementary Processes in Organic Photovoltaics. Advances in Polymer Science, Springer, Cham, 2017, pp. 267–291.

[4] Colin R. Bridges, Michael J. Ford, Elayne M. Thomas, Christian Gomez, Guillermo C. Bazan, Rachel A. Segalman, Eff ;ects of side chain branch point on self assembly, structure, and electronic properties of high mobility semiconducting polymers, Macromolecules 51 (2018) 8597–8604, https://doi.org/10.1021/acs.macromol.8b01906.

[5] Florian S.U. Fischer, Daniel Trefz, Justus Back, Navaphun Kayunkid, Benjamin Tornow, Steve Albrecht, Kevin G. Yager, Gurpreet Singh, Alamgir Karim, Dieter Neher, Martin Brinkmann, Sabine Ludwigs, Highly crystalline films of PCPDTBT with branched side chains by solvent vapor crystallization: influence on opto-electronic properties, Adv. Mater. 27 (7) (2015) 1223–1228, https://doi.org/10.1002/adma.201403475.

[6] Yunzhang Lu, Yan Wang, Zhihui Feng, Yu Ning, Xiaojun Liu, Yanwu Lü, Yanbing Hou, Temperature-dependent morphology evolution of P3HT:PCBM blend solar cells during annealing processes, Synth. Met. 162 (23) (2012) 2039–2046, https://doi.org/10.1016/j.synthmet.2012.10.012.

[7] G. Juška, N. Nekrašas, K. Genevičius, Investigation of charge carriers transport from extraction current transients of injected charge carriers, J. Non. Solids 358 (2012) 748–750, https://doi.org/10.1016/j.jnoncrysol.2011.12.016.

[8] G. Juška, N. Nekrašas, K. Genevičius, A. Pivrikas, Current transients in organic field effect transistors, Appl. Phys. Lett. 102 (2013) 163306, , https://doi.org/10.1063/1.4803054.

[9] H. Bässler, Charge transport in disordered organic photoconductors. A Monte Carlo simulation study, Phys. Stat. Sol. (B) 175 (15) (1993), https://doi.org/10.1002/pssb.2221750102.

[10] Heewon Hwang, Hoyeon Lee, Shafidah Shafian, Wooseop Lee, Jeesoo Seok, Yeon Ryu Ka, Du Yeol Ryu, Kyungkon Kim, Thermally stable bulk heterojunction prepared by sequential deposition of nanostructured polymer and fullerene, Polymers 9 (2017) 456, https://doi.org/10.3390/polym9090456.

[11] J. Važgėla, K. Genevičius, G. Juška, i-CELIV technique for investigation of charge carriers transport properties, Chem. Phys. 478 (2016) 126–129, https://doi.org/10.1016/j.chemphys.2016.04.005.

[12] Zubair Ahmad, Farid Touati, Fahmi F. Muhammad, Mansoor Ani Najeeb, R.A. Shakoor, Effect of ambient temperature on the efficiency of the PCPDTBT:PC71BM BHJ solar cells, Appl. Phys. A (2017) 123 486; https://DOI:

10.1007/s00339-017-1098-8.

[13] E.V. Emelianova, M. van der Auweraer, G.J. Adriaenssens, A. Stesmans, Carrier mobility in two-dimensional disordered hopping systems, Org. Electron. 9 (1) (2008) 129–135, https://doi.org/10.1016/j.orgel.2007.09.004.

[14] M. Borsenberger Paul, David S. Weiss, Organic Photoreceptors for Xerography, Marcel Dekker, New York, 1998 p 485.

[15] Dongkyun Seo, Jonghyup Park, Tae Joo Shin, Pil J. Yoo, Juhyun Park, Kyungwon Kwak, Bathochromic shift in absorption spectra of conjugated polymer nanoparticles with displacement along backbones, Macromol. Res. 23 (6) (2015) 574–577, https://doi.org/10.1007/s13233-015-3078-1.

[16] F.S.U. Fischer, K. Tremel, A.-K. Saur, S. Link, N. Kayunkid, M. Brinkmann, D. Herrero-Carvajal, J.T. Lopez Navarrete, M.C. Ruiz Delgado, S. Ludwigs, Influence of processing solvents on optical properties and morphology of a semicrystalline low bandgap polymer in the neutral and charged states, Macromolecules 46 (2013) 4924–4931, https://doi.org/10.1021/ma400939z.

3rd publication / 3-oji publikacija

Investigation of charge carrier mobility and recombination in PBDTTPD thin layer structures

Andrius Aukštuolis, Nerijus Nekrašas, Kristijonas Genevičius, Giedrius Juška

Organic Electronics, 90, 106066 (2021)
https://doi.org/10.1016/j.orgel.2021.106066

Organic Electronics 90 (2021) 106066

Contents lists available at ScienceDirect

Organic Electronics

journal homepage: http://www.elsevier.com/locate/orgel

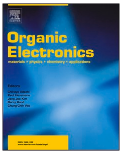

Investigation of charge carrier mobility and recombination in PBDTTPD thin layer structures

Andrius Aukštuolis [*], Nerijus Nekrašas, Kristijonas Genevičius, Giedrius Juška

Vilnius University, Faculty of Physics, Institute of Chemical Physics, Vilnius, Lithuania

ARTICLE INFO

Keywords:
PBDTTPD
OFET
Photo-CELIV
Recombination
Charge transport
Organic semiconductors

ABSTRACT

In this paper we present investigation of hole transport properties in sandwich and OFET structures with single active layer of PBDTTPD (Poly[(5,6-dihydro-5-octyl-4,6-dioxo-4H-thieno[3,4-c]pyrrole-1,3-diyl)[4,8-bis[(2-ethylhexyl)oxy]benzo[1,2-b:4,5-b′]dithiophene-2,6-diyl]]). Sandwich structures were investigated by photo-CELIV and TOF techniques, obtained results showed strongly time dependent hole mobility and non-Gaussian DOS tail. Photogenerated charge carrier decay experiment demonstrated that bimolecular recombination coefficient is smaller than calculated Langevin recombination coefficient and this was explained by faster holes escaping recombination area and not participating in Langevin recombination process. Organic field-effect transistor structure was investigated by current transients technique to find hole mobility near the dielectric layer and to study OTS treatment influence on hole transport. The study of hole mobility dependence on temperature was performed in order to evaluate energetic disorder of interface DOS in the channel of OFET structures.

1. Introduction

Organic semiconductors are gaining more popularity as active materials in electronic devices because of their advantages against traditional semiconductors: low weight, simpler fabrication procedure, flexibility, lower cost in mass production [1]. However, due to their main drawbacks like low mobility, degradation in the atmosphere conditions, low performance of charge carrier transport new organic semiconductors are still under intensive studies [2]. As morphology of organic materials is closely tied with the performance of the final device [3], every small change in manufacturing procedure should be considered carefully because fabrication conditions affect the characteristics of the formed structure [4,5].

Typical structure of organic solar cell usually contains few different layers or bulk heterojunction of at least two charge transporting materials and PBDTTPD is commonly used as hole transport material in blends with PCBM ([6,6]-phenyl-C61 butyricacidmethylester) in solar cell structures [6]. There are as well organic field-effect transistor (OFET) structures containing two materials in the active layer [7]. Studies of structures with blended materials bring useful information about optimal ratios of the materials to get the best possible characteristics, efficiencies, stabilities [8,9]. However, investigating single layer structures gives more detailed information about the material itself and there are only few studies where structures with single PBDTTPD (Fig. 1) layer were investigated [10–12].

In this work we focused on two mono layer structures with PBDTTPD as active material: sandwich structure (Fig. 2) and organic field-effect transistor structure with top source-drain electrodes (Fig. 3). These structures are convenient as they allow to apply few methods and study hole transport from different approaches: in sandwich structure holes are moving in the bulk of the material to reach the electrode while in OFET structure holes are moving alongside dielectric layer thus hole transport conditions are different in each case. The interface of dielectric and active layers is essential to hole transport in the OFET channel and it can be improved via modification of dielectric layer surface before casting active layer [13,14].

Few convenient techniques were used for the investigation of hole transport. Sandwich structures were investigated by time of flight (TOF) and photo generated charge extraction by linearly increasing voltage (photo-CELIV) technique [15,16]. Both techniques can be used for evaluation of hole mobility, moreover photo-CELIV technique also allows to estimate recombination rate and Langevin recombination coefficient in photogenerated charge decay experiment [17–19]. OFET structures were investigated by currents transients and i-CELIV (injection CELIV) techniques as these techniques evaluate hole mobility in different directions of the sample (along x axis and along y axis in Fig. 3)

---

[*] Corresponding author. Saulėtekio al. 3, Vilnius, Lithuania.
E-mail address: andrius.aukstuolis@ff.vu.lt (A. Aukštuolis).

https://doi.org/10.1016/j.orgel.2021.106066
Received 11 August 2020; Received in revised form 30 November 2020; Accepted 4 January 2021

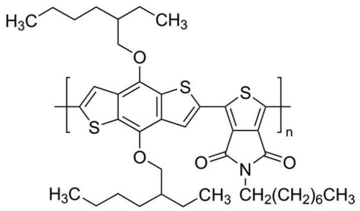

Fig. 1. Schematic view of PBDTTPD molecule.

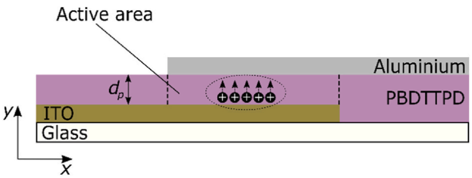

Fig. 2. Schematic drawing of sandwich structure used for photo-CELIV and TOF measurements.

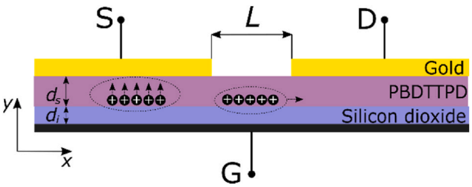

Fig. 3. Schematic drawing of an OFET structure employed in our work.

[20,21]. Mobility dependence on temperature allows to estimate energetic disorder parameter σ of interface density of states (DOS) and link hole transport improvement with improved disorder along the dielectric layer [22].

2. Experimental

2.1. Sample preparation

Two types of substrates were used for the preparation of the samples. Sandwich structures were made on glass/ITO (glass/Indium Tin Oxide) substrates and OFET structures were made on Si/SiO$_2$ substrates on polished SiO$_2$ ($d_i = 100$ nm) side. Silicon layer was heavily doped (n type) and used as gate electrode in OFET structures. All substrates were cleaned in ultrasonic bath for 15 min in each of the solvents: distilled water, acetone and isopropanol. Cleaned substrates were treated by oxygen plasma for 2 min to remove organic residuals and to make surface more hydrophilic. Part of Si/SiO$_2$ substrates were submerged in 60 °C OTS/toluene solution of 10 mmol concentration for 15 min (OTS – trichloro(octyl)silane purchased from Sigma-Aldrich). After it they were washed in each of the solvents: hexane (removing additional OTS layers), acetone, isopropanol.

PBDTTPD was bought from Sigma-Aldrich in form of dry powder and was used as it is, without any additional purification. For sandwich structures PBDTTPD was dissolved in chlorobenzene with 10 mg/mL concentration. Layer was dropcasted under the dry nitrogen atmosphere conditions and the thickness of layer was $d_p = 1.2$ μm. After deposition aluminum electrodes were formed via thermal evaporation under vacuum. For OFET structures PBDTTPD was dissolved in chloroform with 10 mg/mL concentration. Solution then was spincoated on Si/SiO$_2$ substrates under the dry nitrogen atmosphere conditions. The first spincoating step was 500 rpm for 60 s to cast the layer and the second step was 2000 rpm for 40 s to completely dry the sample and remove residuals of solvent. These parameters resulted in getting $d_s = 135$ nm thickness of active layer. Gold source and drain electrodes were subsequently evaporated, resulting in OFET's channel length L of 30 μm. None of the samples were annealed prior to the measurements.

2.2. Experimental setup and theory

TOF measurements were conducted using short pulses (~4 ns) of 532 nm wavelength laser. Samples were illuminated through ITO electrode and external voltage was applied prior illumination to create electric field in the layer in which holes move and are extracted through aluminium electrode (Fig. 2). PBDTTPD layer absorption was measured with Perkin Elmer Lambda 1050 spectrophotometer and it had strong absorption for 532 nm wavelength light with optical density of $\alpha d_p > 7$ (Fig. 6), where α is absorption coefficient. Thus the region of photogeneration is near the surface and from experiment results hole mobility was calculated [15]:

$$\mu_{\mathrm{tof}} = \frac{d_{\mathrm{p}}^2}{U t_{\mathrm{tr}}} \tag{1}$$

where U is applied voltage and t_{tr} is hole transit time.

photo-CELIV measurements were conducted under the same illumination conditions as in TOF measurements. External voltage $U_{\mathrm{off}} = 0.7$ V was applied prior illumination to compensate built-in electric field and to stop photogenerated charge carriers from leaving the sample (Fig. 4). During the experiment extracting ramp voltage was 8 V and the duration of signal was 120 μs. From experiment results hole mobility μ_{ph} was calculated accordingly [16]:

$$\mu_{\mathrm{ph}} = \frac{2d_{\mathrm{p}}^2}{A t_{\max}^2 \left(1 + 0.36\left(\frac{\Delta j}{j(0)}\right)\right)} \tag{2}$$

where A is voltage increment rate, $t_{\max}$ is the time when extracted charge current density reaches peak value, Δj is extracted charge current density peak value, $j(0)$ is initial current density step (Fig. 5).

Recombination in organic materials is one of the key process which describes how material will perform in electronic devices and photo-CELIV technique allows to investigate recombination by altering time t_{del} between light pulse and applied ramp voltage. Also at each different t_{del} value mobility of holes can be calculated using eq. (2) and energy relaxation influence on mobility and recombination can be investigated. The decay of extracted photogenerated charge carrier density $n(t)$ due to

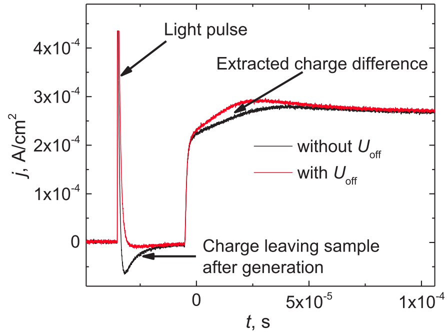

Fig. 4. photo-CELIV current density transients with and without U_{off}.

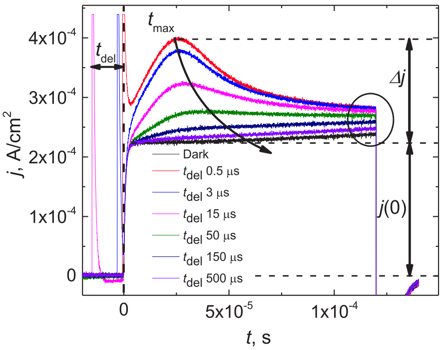

Fig. 5. photo-CELIV current density transients with increasing t_{del}.

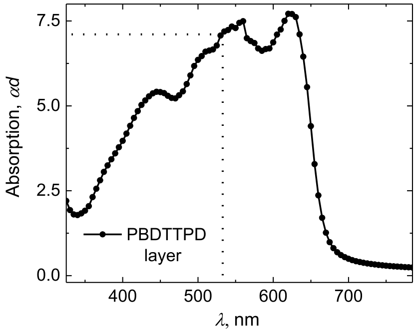

Fig. 6. Absorption spectrum of PBDTTPD layer. Dotted lines crossing marks absorption of wavelength used in photo-CELIV and TOF measurements.

bimolecular recombination is described by equation:

$$n(t) = \frac{1}{B_{\exp}t + \frac{1}{n(0)}} \tag{3}$$

where $n(0)$ is the initial charge carrier density and $B_{\exp}$ is bimolecular recombination coefficient.

Recombination in organic semiconductor materials is usually described as Langevin type bimolecular recombination [23]. Langevin recombination coefficient B_L depends on the mobility of charge carriers in the material and it can be calculated (if mobility values of different types of charge carriers differs significantly, lower mobility can be neglected):

$$B_L = \frac{e(\mu_{ph} + \mu_e)}{\varepsilon_s \varepsilon_0} \tag{4}$$

where μ_e is electron mobility, ε_s and ε_0 are PBDTTPD layer and vacuum permittivities respectively and e is elementary charge.

Current transients measurement setup was set accordingly to the report [20]. In this setup voltage pulse U_{SD} is applied while gate electrode is grounded and drain electrode is grounded via load resistor. At very first, injected through the source electrode holes move towards dielectric layer, because the y-component of electric field (Fig. 3) is much larger than x-component (because $d_s \ll L$). After reaching dielectric and PBDTTPD interface they move along the dielectric layer towards the drain electrode until time t_d when first holes reach drain electrode (Fig. 9). Time t_d is much larger than drift time of holes from source to dielectric layer (because $d_s \ll L$), so latter can be neglected. Thus, while channel is not formed yet and voltage drop on load resistance is negligible, from t_d and U_{SD} values the mobility of injected holes μ_{tr} in OFET structure can be calculated [20]:

$$\mu_{tr} = 0.38\frac{L^2}{t_d U_{SD}} \tag{5}$$

During i-CELIV measurements in OFET structure voltage is connected between source and gate and all injected holes accumulate near dielectric surface. Later they are extracted by ramp voltage and move backwards the entire thickness of the organic layer (Fig. 2) [21]. During extraction the first holes move in SCLC conditions and reach the source at transit time t_{tr} from which hole mobility μ_h can be calculated [21]:

$$\mu_h = \frac{2d_s^2}{At_{tr}^2}\left(1 + \frac{\varepsilon_s d_i}{\varepsilon_i d_s}\right) \tag{6}$$

where A is voltage increase rate, ε_i is dielectric layer permittivity and ε_s is semiconductor layer permittivity. In i-CELIV technique injected holes before extraction are kept near dielectric surface for a period of time longer than t_{del} in photo-CELIV experiment, thus mobility values are measured in similar conditions as in photo-CELIV experiment at the longest t_{del} values.

Disorder parameters of organic materials is usually described by Bässler's model and energetic disorder parameter σ of DOS is related to charge carrier hopping mobility and temperature via formula [22]:

$$\mu_{tr} = \mu_0 \exp\left(-\frac{4}{9}\left(\frac{\sigma}{kT}\right)^2\right) \tag{7}$$

where μ_0 is mobility prefactor, k is Boltzmann constant and T is the temperature. Thus, mobility dependence on temperature allows to evaluate energetic disorder of DOS in the layer.

3. Results and discussion

The first goal of this study was to investigate hole mobility in sandwich structure with single PBDTTPD layer and to achieve it photo-CELIV and TOF methods were employed. Fig. 5 displays few typical photo-CELIV current density transients with different t_{del} values. Black circle marks the "tails" where transients do not reach the initial capacitance step $j(0)$ indicating that some holes are very hard to extract by increasing ramp voltage from their occupied states. These "tails" are seen throughout the whole delay time t_{del} range and point to the dispersive character of holes transport in PBDTTPD layer which is connected to the redistribution of photogenerated holes in DOS with time [24].

Hole mobility in PBDTTPD layer obtained by photo-CELIV method is $\mu_{ph} = 4.8{*}10^{-4}$ cm^2/Vs and similar to already reported results elsewhere ($1.4{*}10^{-4}$ cm^2/Vs – $7.5{*}10^{-4}$ cm^2/Vs) [25–28]. It should be considered that in mentioned reports blends of PBDTTPD were measured and different methods were used. With increasing t_{del} value we observed decrease of hole mobility in PBDTTPD (see Fig. 7 and corresponding t_{max} increasing in Fig. 5). The decrease of hole mobility is caused by photogenerated holes redistribution in their states with time. With low t_{del} value (up to few μs) we have significant part of holes travelling relatively fast ($\mu_{ph} = 4.8{*}10^{-4}$ cm^2/Vs), forming pronounced current density peak with low t_{max} value (for example, see red and blue curves in Fig. 5) and relatively small amount of slower holes part of which cannot be extracted by applied ramp voltage (see "tails" of transients above $j(0)$). The increase of t_{del}, in addition to lowering the amount of holes (due to recombination; see area of photo-transient above "dark" transient in Fig. 5), also causes the increased contribution of slower holes to the photo current with respect to the faster ones. We can assume that without t_{del} hole mobility would be higher and close to hole mobility $\mu_{tof} = 10^{-3}$ cm^2/Vs measured by TOF method (measurement data in supplementary information Figs. S1 and S2) as mobility by photo-CELIV

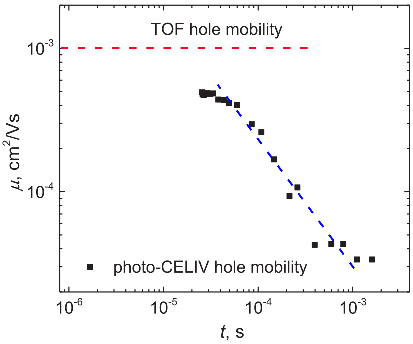

Fig. 7. Hole mobility in PBDTTPD sandwich structure. Time t in the bottom axis is $t_{del} + t_{max}$ which is the lifetime of the most holes from photogeneration to extraction.

tends to saturate to TOF value (Fig. 7 blue dashed line). These results suggest that PBDTTPD material employed in sandwich structure exhibits much slower decay of DOS tail than in Gaussian DOS model. The holes in deep energy states barely contribute to the non-dispersive TOF current, but become "visible" in the photo-CELIV current when t_{del} is large and the most of photogenerated higher mobility holes have recombined or relaxed to deep energy states. Systems which exhibit superposition of two different DOS distributions (for example, Gaussian + exponential) was reported before [29]. It is worth mentioning, that combination of TOF and photo-CELIV techniques exposes hole transport properties discussed above that otherwise would be undetected and this emphasizes the importance of measurements in broad time scale.

Charge carrier density decay measured by photo-CELIV allows to investigate recombination rate in PBDTTPD sandwich structure (Fig. 8). Using eq. (2) bimolecular recombination coefficient B_{exp} can be found by fitting extracted charge density dependence on time (Fig. 8 red line). Even though hole mobility changes by one order of magnitude with respect to t_{del}, the fitting of n(t_{del}) assuming B_{exp} = const is appropriate in all measured t_{del} range. From the experimental results we obtained bimolecular recombination coefficient $B_{exp} = 4.2{*}10^{-11}$ cm^3/s. However, calculated Langevin recombination coefficient was $B_L = 2.5 * 10^{-10}$ cm^3/s (for calculation we used $\mu_{ph} = 4.8{*}10^{-4}$ cm^2/Vs) which means that recombination in the PBDTTPD sandwich structure was slowed down by almost 6 times. Usually, reduction of Langevin type recombination is observed in organic semiconductor blends and is explained by the separation of the hole and electron pathways [30,31], by the influence of the lowest mobility charge carriers [32], by the extent of charge delocalization of holes and electrons in charge transfer state [17]. However, these reasons explain reduction of recombination by few orders of magnitude in blends while in our case we have pure polymer layer and recombination is slowed down by 6 times only. As mentioned above, Figs. 5 and 7 indicate that photogenerated holes with the time relax and occupy lower energy states, hopping gets more difficult and average mobility decreases. Langevin recombination coefficient calculated by using the lowest measured hole mobility (μ_{ph} = $4.35{*}10^{-5}$ cm^2/Vs) is $B_{L\ slow} = 2.25{*}10^{-11}$ cm^3/s (Fig. 8 green line) and is about two times smaller than experimentally obtained recombination coefficient B_{exp}. We can assume that B_{exp} is tied to effective hole mobility in the layer which is close to the slowest measured mobility in photo-CELIV experiment, because part of holes with higher mobility escapes from photogeneration area before they can recombine and letting holes with lower mobility recombine, therefore reduced recombination coefficient is obtained.

Hole mobility in OFET structures with top source – drain gold electrodes (Fig. 2) was measured by current transients and i-CELIV methods. Though PBDTTPD is considered to be a promising hole transport polymer, only single work has been reported about using it in the OFET structure [7]. Authors investigated PBDTTPD mixed with P3HT (poly (3-hexylthiophene-2,5-diyl)) in the active layer and found hole mobilities to be in range $4.36{*}10^{-4}$ cm^2/Vs – $8.69{*}10^{-3}$ cm^2/Vs at room temperature, mainly addressing higher mobility values to the P3HT part. By using t_d value (Fig. 9) we estimated hole mobility at room temperature $\mu_{tr} = 9.3{*}10^{-5}$ cm^2/Vs in OFET structure without OTS treatment and $\mu_{tr} = 1.5{*}10^{-4}$ cm^2/Vs in OFET structure with OTS treatment. Hole mobility values were extrapolated from hole mobility dependence on applied voltage U_{SD} to get zero field hole mobility (experiment data is presented in supplementary information Fig. S3). Current transients method also gives opportunity to estimate hole mobility from IV characteristics using $I_{SD\ sat}$ value (Fig. 9) and for comparison and verification we calculated hole mobility at room temperature of OFET structure with OTS treatment ($\mu_{sat} = 1.1{*}10^{-4}$ cm^2/Vs, Fig. 10). Hole mobility calculated using t_d value represents mobility in low charge carrier density conditions and hole mobility calculated using $I_{SD\ sat}$ value represents mobility in the high charge carrier density in OFET channel conditions. With both hole mobility values being similar we can assume that charge carrier density does not affect mobility in PBDTTPD layers and our measured photo-CELIV hole mobility dependency on delay time t_{del} is caused by holes redistributing through energy states of DOS with the time and not by charge carrier density reduction due to recombination.

i-CELIV results of hole mobility do not show any significant difference between OFET structure without OTS treatment and OFET structure with OTS treatment ($\mu_h = 3.2{*}10^{-5}$ cm^2/Vs and $\mu_h = 3.4{*}10^{-5}$ cm^2/Vs respectively, Fig. 10). In i-CELIV experiment holes do not travel via

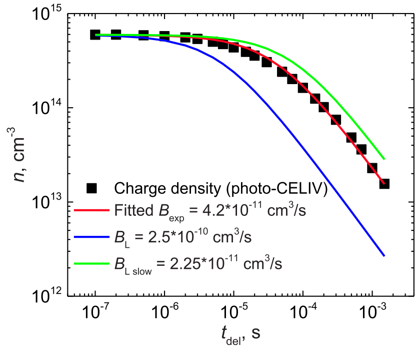

Fig. 8. Extracted charge carrier density decay in PBDTTPD sandwich structure.

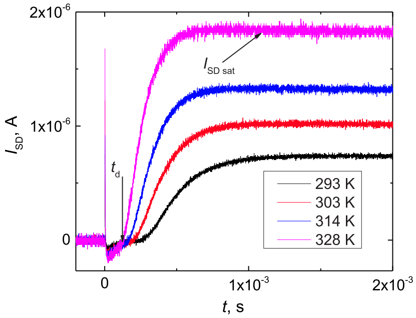

Fig. 9. Current I_{SD} transients at different temperatures obtained by current transients technique in OFET structure with OTS treatment (U_{SD} = 80 V).

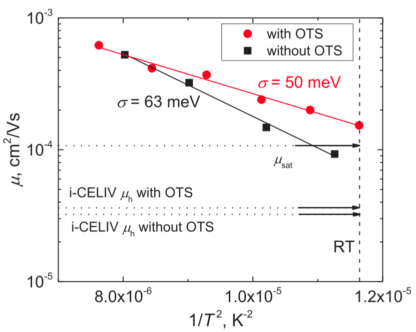

Fig. 10. Hole mobility dependence on temperature obtained from current transients measurements. Arrows mark hole mobility values obtained from i-CELIV and IV characteristics at room temperature. Dashed line marks room temperature.

OFET structure channel near dielectric/polymer interface, thus hole mobility is equal with and without OTS treatment, while we see improved hole mobility in OFET structure channel with OTS treatment. i-CELIV hole mobility is similar to the lowest photo-CELIV hole mobility, but is lower than calculated from t_d value (compare Figs. 7 and 10), because in i-CELIV injected holes are kept in the sample for a while before extraction, just as under photo-CELIV conditions with the highest t_{del} values, while in current transients experiment holes travel instantly after voltage is applied.

In mobility dependence on temperature (Fig. 10) we observe that energetic disorder parameter of dielectric/polymer interface DOS σ is smaller in OFET structure channel with OTS treatment than in OFET structure channel without OTS treatment (50 meV–63 meV), thus via reduced interface disorder hole transport conditions were improved and hole mobility increased. For verification that PBDTTPD does not have any phase shift which can also modify hole transport conditions and mobility values in measured temperature range, differential scanning calorimetry measurement were conducted (supplementary information Fig. S4). Energetic disorder parameter σ in PBDTTPD blends with PCBM was reported before, where authors reported $\sigma = 65$ meV and $\sigma = 81$ meV for different configurations of PBDTTPD molecule [25]. Our results show that pure PBDTTPD material has smaller disorder parameter σ of interface DOS in OFET channel near dielectric surface than its blend with PCBM (63 meV–81 meV) and that treating SiO_2 surface with OTS decreases disorder parameter σ to 50 meV.

4. Conclusions

It was found that in pure PBDTTPD sandwich structure the time that non-equilibrium holes have spent in the layer reduces their mobility by one order of magnitude. Hole mobility dependence on time in photo-CELIV and non-dispersive hole transport TOF results combined show that holes with time redistribute in non-Gaussian DOS tail in pure PBDTTPD volume. Investigation of the recombination of charge carriers points to bimolecular-type recombination with coefficient $B_{exp} = 4.2*10^{-11}$ cm^3/s in the whole measured time range (more than 3 orders of magnitude). It corresponds to the hole mobility, which is close to the lowest value measured by photo-CELIV technique, showing that part of holes with higher mobility are escaping from photogeneration area before they can recombine and holes with lower mobility are mainly participating in recombination.

OTS treatment of SiO_2 surface leads to hole mobility increase from $\mu_{tr} = 9.3*10^{-5}$ cm^2/Vs to $\mu_{tr} = 1.5*10^{-4}$ cm^2/Vs, as measured by current transients technique. The increase in hole mobility can be attributed to the decrease of energetic disorder parameter of interface DOS σ from 63 meV to 50 meV of the energy states near the dielectric layer as it improved hole hopping conditions. Similar hole mobility values obtained by current transients technique and obtained by IV characteristics show that hole mobility is independent from the density of holes in PBDTTPD.

Declaration of competing interest

The authors declare that they have no known competing financial interests or personal relationships that could have appeared to influence the work reported in this paper.

Appendix A. Supplementary data

Supplementary data to this article can be found online at https://doi.org/10.1016/j.orgel.2021.106066.

References

[1] Samuel E. Root, Suchol Savagatrup, Adam D. Printz, Daniel Rodriquez, Darren J. Lipomi, Mechanical properties of organic semiconductors for stretchable, highly flexible, and mechanically Robust electronics, Chem. Rev. 117 (2017) 6467–6499, https://doi.org/10.1021/acs.chemrev.7b00003.

[2] Sergi Riera-Galindo, Francesca Leonardi, Raphael Pfattner, Marta Mas-Torrent, Organic semiconductor/polymer blend films for organic field-effect transistors, Adv. Mater. Technol. (2019) 1900104, https://doi.org/10.1002/admt.201900104.

[3] Chengliang Wang, Huanli Dong, Lang Jiang, Wenping Hu, Organic semiconductor crystals, Chem. Soc. Rev. 47 (2018) 422, https://doi.org/10.1039/c7cs00490g.

[4] Hongseok Youn, Joon Hui, Park, L. Jay Guo, Organic photovoltaic cells: from performance improvement to manufacturing processes, Small 11 (19) (2015) 2228–2246, https://doi.org/10.1002/smll.201402883.

[5] Monika M. Voigt, Roderick C.I. Mackenzie, Simon P. King, Chin P. Yau, Atienzar Pedro, Justin Dane, Panagiotis E. Keivanidis, Ivan Zadrazil, Donal D. C. Bradley, Jenny Nelson, Gravure printing inverted organic solar cells: the influence of ink properties on film quality and device performance, Sol. Energy Mater. Sol. Cells 105 (2012) 77–85, https://doi.org/10.1016/j.solmat.2012.04.025.

[6] Serge Beaupré, Najari Ahmed, Mario Leclerc, High open-circuit voltage solar cells using a new thieno[3,4-c] pyrrole-4,6-dione based copolymer, Synth. Met. 182 (2013) 9–12, https://doi.org/10.1016/j.synthmet.2013.08.022.

[7] Sungho Nam, Hwajeong Kim, Donal D.C. Bradley, Youngkyoo Kim, All-polymer phototransistors with bulk heterojunction sensing layers of thiophene-based electron-donating and thienopyrroledione-based electron-accepting polymers, Org. Electron. 39 (2016) 199–206, https://doi.org/10.1016/j.orgel.2016.09.034.

[8] Jonathan A. Bartelt, D. Jessica, Douglas, R. William, Mateker, Abdulrahman El Labban, Christopher J. Tassone, Michael F. Toney, M. Jean, J. Fréchet, Pierre M. Beaujuge, Michael D. McGehee, Controlling solution-phase polymer aggregation with molecular weight and solvent additives to optimize polymer-fullerene bulk heterojunction solar cells, Adv. Energy Mater. (2014) 1301733, https://doi.org/10.1002/aenm.201301733.

[9] Jonathan A. Bartelt, M. Zach, Beiley, Eric T. Hoke, William R. Mateker, Jessica D. Douglas, Brian A. Collins, John R. Tumbleston, Kenneth R. Graham, Aram Amassian, Harald Ade, M. Jean, J. Fréchet, Michael F. Toney, Michael D. McGehee, The importance of fullerene percolation in the mixed regions of polymer–fullerene bulk heterojunction solar cells, Adv. Energy Mater. 3 (2013) 364–374, https://doi.org/10.1002/aenm.201200637.

[10] Yingping Zou, Najari Ahmed, Philippe Berrouard, Serge Beaupre, Badrou Reda Aich, Tao Ye, Mario Leclerc, A thieno[3,4-c]pyrrole-4,6-dione-based copolymer for efficient solar cells, J. Am. Chem. Soc. 132 (2010) 5330–5331, https://doi.org/10.1021/ja101888b.

[11] Abdulrahman El Labban, Julien Warnan, Cabanetos Clement, Olivier Ratel, Christopher Tassone, Michael F. Toney, Pierre M. Beaujuge, Dependence of crystallite formation and preferential backbone orientations on the side chain pattern in PBDTTPD polymers, ACS Appl. Mater. Interfaces 6 (2014) 19477–19481, dx.doi.org/10.1021/am505280a.

[12] Aurelien Tournebize, Jean-Luc Gardette, Christine Taviot-Gueho, Didier Begu, Marc Alexandre Arnaud, Christine Dagron-Lartigau, Hussein Medlej, C. Roger, Hiorns, Serge Beaupre, Mario Leclerc, Agnes Rivaton, Is there a photostable conjugated polymer for efficient solar cells? Polym. Degrad. Stabil. 112 (2015) 175e184, https://doi.org/10.1016/j.polymdegradstab.2014.12.018.

[13] Young-Se Jang, Hoon-Seok Seo, Ying Zhang, Jong-Ho Choi, Characteristics of tetracene-based field-effect transistors on pretreated surfaces, Org. Electron. 10 (2009) 222–227, https://doi.org/10.1016/j.orgel.2008.11.002.

[14] Jungyoon Seo, Seungtaek Oh, Giheon Choi, Hyun Ho Choi, Hwa Sung Lee, Polymeric conformation of organic interlayers as a determining parameter for the charge transport of organic field-effect transistors, Macromol. Res. 28 (2020) 670–676, https://doi.org/10.1007/s13233-020-8112-2.

[15] W.E. Spear, Transit time measurement of charge carriers in amorphous selenium films, Proc. Phys. Soc. 70 (1957) 669. London.

[16] G. Juška, K. Arlauskas, M. Viliūnas, K. Genevičius, R. Osterbacka, H. Stubb, Charge transport in p-conjugated polymers from extraction current transients, Phys. Rev. B 62 (2000) 24.

[17] D.H.K. Murthy, A. Melianas, Z. Tang, G. Juška, K. Arlauskas, F. Zhang, L.D. A. Siebbeles, O. Inganas, T.J. Savenije, Origin of reduced bimolecular recombination in blends of conjugated polymers and fullerenes, Adv. Funct. Mater. 23 (2013) 4262–4268, https://doi.org/10.1002/adfm.201203852.

[18] R. Osterbacka, A. Pivrikas, G. Juška, K. Genevičius, K. Arlauskas, H. Stubb, Measuring the time relaxation of photogenerated charge carriers in organic materials, Curr. Appl. Phys. 415 (2004) 534–538, https://doi.org/10.1016/j.cap.2004.01.013.

[19] N. Nekrašas, K. Genevičius, M. Viliūnas, G. Juška, Features of current transients of photogenerated charge carriers, extracted by linearly increased voltage, Chem. Phys. 404 (2012) 56–59, https://doi.org/10.1016/j.chemphys.2012.01.008.

[20] G. Juška, N. Nekrašas, K. Genevičius, A. Pivrikas, Current transients in organic field effect transistors, Appl. Phys. Lett. 102 (2013) 163306, https://doi.org/10.1063/1.4803054.

[21] G. Juška, N. Nekrašas, K. Genevičius, Investigation of charge carriers transport from extraction current transients of injected charge carriers, J. Non-Cryst. Solids 358 (2012) 748–750. https://doi:10.1016/j.jnoncrysol.2011.12.016.

[22] H. Bässler, Charge transport in disordered organic photoconductors. A Monte Carlo simulation study, Phys. State solid. 175 (1993) 15, https://doi.org/10.1002/pssb.2221750102.

[23] P. Langevin, Ann. Chem. Phys. 28 (1903) 433.

[24] M. Tracey, Clarke, Jeff Peet, Nattestad Andrew, Drolet Nicolas, Dennler Gilles, Lungenschmied Christoph, Leclerc Mario, Attila J. Mozer, Charge carrier mobility, bimolecular recombination and trapping in polycarbazole copolymer:fullerene (PCDTBT:PCBM) bulk heterojunction solar cells, Org. Electron. 13 (2012) 2639–2646, https://doi.org/10.1016/j.orgel.2012.07.037.

[25] Iordania Constantinou, Tzung-Han Lai, Erik D. Klump, Subhadip Goswami, Kirk S. Schanze, Franky So, Effect of polymer side chains on charge generation and disorder in PBDTTPD solar cells, ACS Appl. Mater. Interfaces 7 (2015) 26999–27005, https://doi.org/10.1021/acsami.5b09497.

[26] Long Ye, Wei Jiang, Wenchao Zhao, Shaoqing Zhang, Yong Cui, Zhaohui Wang, Jianhui Hou, Toward efficient non-fullerene polymer solar cells: selection of donor polymers, Org. Electron. 17 (2015) 295–303, https://doi.org/10.1016/j.orgel.2014.12.020.

[27] Xue-Qiang Chen, Xiang Yao, Xuan Xiang, Long Liang, Wei Shao, Fu-Gang Zhao, Zhengquan Lu, Wenwu Wang, Jingjing Li, Wei-Shi Li, Long-term thermally stable organic solar cells based on cross-linkable donor-acceptor conjugated polymers, J. Mater. Chem. A 4 (2016) 9286, https://doi.org/10.1039/c6ta01450j.

[28] Tantyo Hadmojo Wisnu, Tri Adhi Wibowo Febrian, Yeol Ryu Du, Fullerene-free organic solar cells with an efficiency of 10.2% and an energy loss of 0.59 eV based on a thieno[3,4-c]Pyrrole-4,6-dione containing wide band gap polymer donor, in: Jung Hwan, Jang Sung-Yeon (Eds.), ACS Appl. Mater. Interfaces 9 (2017) 32939–32945, https://doi.org/10.1021/acsami.7b09757.

[29] S.L.M. van Mensfoort, J. Billen, S.I.E. Vulto, R.A.J. Janssen, R. Coehoorn, Electron transport in polyfluorene-based sandwich-type devices: quantitative analysis of the effects of disorder and electron traps, Phys. Rev. B 80 (2009), 033202, https://doi.org/10.1103/PhysRevB.80.033202.

[30] G.J. Adriaenssens, V.I. Arkhipov, Non-Langevin recombination in disordered materials with random potential distributions, Solid State Commun. 103 (1997) 541e543, https://doi.org/10.1016/S0038-1098(97)00233-0.

[31] I. Balberg, R. Naidis, M.K. Lee, J. Shinar, L.F. Fonseca, Bipolar phototransport in p-conjugated polymer/C60 composites, Appl. Phys. Lett. 79 (2001) 197–199, https://doi.org/10.1063/1.1383801.

[32] L.J.A. Koster, V.D. Mihailetchi, P.W.M. Blom, Bimolecular recombination in polymer/fullerene bulk heterojunction solar cells, Appl. Phys. Lett. 88 (2006), 052104, https://doi.org/10.1063/1.2170424.

Vilniaus universiteto leidykla
Saulėtekio al. 9, III rūmai, LT-10222 Vilnius
El. p. info@leidykla.vu.lt, www.leidykla.vu.lt
Tiražas 25 egz.